UNIVERSITY OF
FORWARD
THINKING
WESTMINSTER⌗

Analysis and Design of Low-Cost Waveguide Filters for Wireless Communications

Jankovic, U.

Analysis and Design of Low-Cost Waveguide Filters for Wireless Communications

Uros Jankovic

A thesis submitted in partial fulfilment of the requirements

for the degree of Doctor of Philosophy

University of Westminster

January 2018

Abstract

The area of research of this thesis is built around advanced waveguide filter structures. Waveguide filters and the waveguide technology in general are renowned for high power capacity, low losses and excellent electromagnetic shielding. Waveguide filters are important components in fixed wireless communications as well as in satellite and radar systems. Furthermore, their advantages and utilization become even greater with increase in frequency, which is a trend in modern communication systems because upper frequency bands offer larger channel capacities.

However, waveguide filters are relatively bulky and expensive. To comply with more and more demanding miniaturization and cost-cutting requirements, compactness and economical design represent some of the main contemporary focuses of interest. Approaches that are used to achieve this include use of planar inserts to build waveguide discontinuities, additive manufacturing and substrate integration. At the same time, waveguide filters still need to satisfy opposed stringent requirements like small insertion loss, high selectivity and multiband operation. Another difficulty that metal waveguide components face is integration with other circuitry, especially important when solid-state active devices are included. Thus, improvements of interconnections between waveguide and other transmission interfaces are addressed too.

The thesis elaborates the following aspects of work:

- Further analysis and improved explanations regarding advanced waveguide filters with E-plane inserts developed by the Wireless Communications Research Group, using both cross coupled resonators and extracted pole sections (Experiments with higher filter orders, use of tuning screws, degrees of freedom in design, etc. Thorough performance comparison with competing filter technologies)
- Proposing novel E-plane filter sections with I-shaped insets
- Extension of the E-plane filtering structures with metal fins to new compact dual band filters with high frequency selectivity and miniaturized diplexers.
- Introduction of easy-to-build waveguide filters with polymer insert frames and high-performance low-profile cavity filters, taking advantage of enhanced fabrication capabilities when using additive manufacturing
- Developing new substrate integrated filters, as well as circuits used to transfer signals between different interfaces
  Namely, these are substrate integrated waveguide to metal waveguide planar transitions that do not require any modifications of the metal waveguides. Such novel transitions have been designed both for single and orthogonal signal polarizations.

Contents

List of Abbreviations

2D	two-dimensional
3D	three-dimensional
CAD	computer-aided design
CAM	computer-aided manufacturing
DC	direct current
EM	electromagnetic
EPS	extracted pole section
FDD	frequency-division duplex
FDM	fused deposition modelling / frequency-division multiplexing
FDMA	frequency-division multiple access
FIR	frequency-invariant reactance
GHz	gigahertz
LLFPB	lumped, linear, finite, passive and bilateral
NRN	non-resonating node
OMT	orthomode transducer
PCB	printed circuit board
PLA	polylactic acid
POTS	plain old telephone service
RF	radio frequency
RWG	rectangular waveguide
PR	positive real
SICL	substrate integrated coaxial line
SIW	substrate integrated waveguide
TE	transverse electric
TEM	transverse electric and magnetic
TM	transverse magnetic
TP	transmission pole
TZ	transmission zero

List of Figures

1. Introduction

Many different types of filters are used in practice to remove unwanted components from a compound input entity (ex. water, air, optical and email filters). As such, electronic filters are typically used to pass input signals at frequencies of interest and to reject the signals at undesirable frequencies. Electronic filters are very common components in electronic circuits, such as those used after nonlinear modules in RF chains. For example, anti-aliasing filters (AAFs) are used to avoid distortion (aliasing) in sampling process of analog-to-digital converters (ADCs) as the result of not satisfying the sampling theorem. They are not easily recognizable from the outside, although prevalent in equipment like computers, telephones, video, audio and photography gear. Some frequently found and more visible electronic filters include those in microfilters for ADSL Internet and audio equalizers.

According to the relation between frequency bands they pass or reject, electronic filters are categorized as lowpass, highpass, bandpass and bandstop filters. (E.g. AAFs are lowpass filters that supress analog input signal before AD conversion at frequencies greater than the Nyquist frequency, which is half of the sampling rate; Microfilters have a simple lowpass LC filter on the telephone side of a splitter, as telephones preceded the Internet and originally there had not been need for their filtering; In audio equalizers, decreasing bass is done by highpass filtering and decreasing highs by lowpass filtering.) Although additional processes like phase corrections and equalization using allpass networks to reverse phase and amplitude signal distortions sustained through communication channel are feasible, they come at the cost of increased insertion loss. Similar penalty occurs with predistorted microwave filters[1], which compensate for dissipation effects inside the filter - frequency responses having more rounded look and be less selective. Since for realizable systems holds the fundamental property of causality, which means that the output depends on the past and current inputs but not on future ones, it should be noted that real-time filters with zero-width frequency transition between passband and stopband (infinite selectivity) do not exist.

Filters considered in this thesis are analog filters. Unlike digital filters, which are divided into two large groups of finite impulse response (FIR) and infinite impulse response (IIR) ones, analog filters are almost exclusively IIR[2]. Digital electronic circuits have had great success in previous decades. One of their key advantages is scalability, i.e. ability to handle growing amount of work, since large building blocks are not constructed from scratch, but rather composed of smaller building blocks. This property allows effects like rapid progress of microprocessor power following the Moore's law. For analog circuits that kind of

---

[1] To account for dissipation, predistorted microwave filters have positions of their ideal transfer function poles in the complex plane shifted in positive real direction prior to the synthesis of filter elements. The desired lossless-equivalent response shape is utilized after filter loss is included. However, the compensation is usually made only partially because of high insertion loss. Thus, resulting response looks like one of a less lossy filter, but still not lossless.

[2] FIR filters have inherent characteristic of being stable, satisfying the criterion $\int |h(t)| dt < \infty$, whereas IIR are not. In fact, analog filters that are of concern in practise are indeed stable, as it is intuitively well expected. However, since for their easier description are used idealised mathematical objects, they reach limiting stability characteristics. Moreover, we are interested in realisability analysis to determine which set of functions represents idealised realisable structures. For their speed, FIR filters are used in Network Analyzers (NAs) as intermediate frequency (IF) filters.

scalability is not possible and that is why we have never seen analog designs of similar complexity. Nevertheless, this is at the same time an advantage of analog circuit design. Analog microwave filters as fundamental segment of RF front ends are not endangered of becoming obsolete due to their close relation with the channel medium, which is inherently analog. They are now equally being applied to pass/reject signals initially digital in the baseband, as they were used before for signals initially analog in the baseband. Moreover, there is resurgence of analog technology in terahertz components owing to better energy efficiency. And due to the fact that analog circuit design is considered more demanding, average salaries of analog engineers are higher than those of digital engineers. Interestingly, with their periodical nature, filters in the form of commensurate distributed networks share similarities with digital filters, yet using different transformation of the (complex) frequency variable from the lumped filter networks.

Here specifically, the focus of attention are microwaves, which are attractive for wide range of applications, offering possibilities for high channel capacities, small size structures and sometimes suitable propagation characteristics. The term microwave is originally more used by the military, whereas the term RF more by the civil community. Microwave technology is prevalent today, with majority of applications in communications (like ubiquitous cellular telephony and WLANs), radar and medical systems as well as environmental remote sensing, by virtue of its focus moving over time from specialised to commercial. For a layperson, the word microwave is probably best associated with microwave ovens. Using water resonances at ISM 2.4 GHz band, they can quickly and evenly heat food in a metal cavity fed with microwave energy produced by a magnetron. Interestingly, in our time even the background cosmic radiation left from the Big Bang is in the microwave frequency range. After it was accidently measured by a giant horn-reflector antenna, background cosmic radiation served as the final support for the wide acceptance of the Big Bang theory.

Microwave components are typically on the order of microwave wavelengths, meaning that the phase of quantities like voltage, current, electric and magnetic field change significantly over the physical extent of the device. Hence, their analysis requires specific electromagnetic treatment, since standard circuit theory approximations at much lower frequencies or geometrical optics approximations at much higher frequencies in general fail to give results of sufficient accuracy. Likewise, practical designs possess distinctivenesses such as use of elements with distributed parameters. From today's popular IT and computer science viewpoint, microwave filters are part of telecommunication/network hardware and belong to the physical layer (layer 1) of the OSI model.

Naturally, the literature review here starts with general books on the topic of microwave engineering [1-1]-[1-6]. References [1-7]-[1-9] extend the list with the books aimed to bridge the gap between RF/microwave and telecommunication engineers, inspired by the aforementioned rapid application of microwave technology in wireless and satellite systems. These systems are implied here as the target applications as well.

Further on and more specifically, waveguide technology has its strengths in terms of high power handling capability, low losses, excellent isolation as well as for its special appropriateness for high frequency operation. These properties directly relate to merits of waveguide filters. (We are restricting ourselves to waveguide in the usual sense of the word,

as a hollow metallic tube, though it is also used in connection with a wider variety of wave-guiding structures.) Standard waveguide filter applications include satellite communications, terrestrial point-to-point microwave links (fixed wireless communications, such as between different sites in mobile phone backhaul networks or between locations of programme production and distanced TV towers in broadcast television systems), defence navigation and communication systems and radar systems.

From a designer's point of view, waveguides are distinguishable from transmission lines for that they do not support propagation of TEM mode. In transmission lines (taken with certain tolerance for the effects of losses and inhomogeneous dielectric), TEM mode propagates from the zero frequency, is not dispersive, and usually all the phenomena of interest can be described exclusively considering it. By contrast, propagation in waveguides is represented by dispersive TE and TM modes, which emerge as propagating modes only starting from relatively high frequencies, called the cutoff frequencies of those modes. The most important one is the mode with the lowest cutoff frequency - the dominant mode. Generally, it is desirable to transport signals through a waveguide component and manage couplings with it with just one mode. For instance, in the most frequently used waveguides, rectangular waveguides, the dominant mode cutoff frequency is the one at which the wider side of the waveguide's rectangular cross section is half wavelength wide. However, higher order modes are relatively close, limiting the usable bandwidth. On the other side, as it will soon be briefly explained, higher order modes are used in some waveguide filters to improve filter properties like enabling size and loss reduction at the cost of structure complexity (hence, they are more difficult to be fabricated). The topic of waveguides is, other than in general books about microwave engineering, extensively covered in a specialized book for guided waves [1-10] and specifically waveguides [1-11]. Furthermore, the papers [1-12]-[1-14] cover the subject of ridged waveguides, which geometry is of special interest in this work, apart from the most used, rectangular and circular waveguides. Since electromagnetic wave theory has the central underlying position here, to the current reference list is added [1-15]. It deals with advanced electromagnetics for engineering problems, with topics arranged by mathematical techniques that are used.

The story of waveguide filters is traced here starting with WWII years and activity of the MIT Radiation Laboratory, formed mainly for development of radar systems[3]. Although the Rad Lab lasted for just a couple of years, it hosted many of the greatest scientists and engineers of the time and beyond. Their abundant highly valuable results in electronics and telecommunications (especially for microwave engineering) were published during years after the laboratory closure within the MIT Radiation Laboratory Series. Its 28 volumes are now available online at the Jefferson Lab web address [1-16]. The chapter 10 of the volume 9 [1-17], written by Fano and Lawson, is the first fundamental text treating waveguide filters[4].

Apart from electromagnetic analysis, microwave filter design relies on circuit theory, which had already been well developed for low-frequency passive analog filters. They revolutionized early years of telecommunications and were arguably the most advanced branch of electrical engineering at that time. Classical passive analog filter theory evolution

---

[3] Development of a long-range radio navigation system was also targeted, from which the well-known LORAN emerged.
[4] Note that Marcuvitz's Waveguide Handbook [1-11] also originates from this series.

had very intense period around the first half of the 20th century. It was marked by works of scientists and engineers like Zobel, Foster, Cauer, Brune, Darlington and others[5] with progression in theoretical concepts from simple filters, over image impedance filters, to network synthesis filters, making it, together with later development and refinements, one of the best studied and understood areas of electronics. Nevertheless, a simple relation between lumped and distributed circuits yet had to be provided by Richards [1-23], describing commensurate distributed networks. A new distributed-circuit element in the form of a transmission line (waveguide) section, without its equal in lumped circuits, appeared. More accurate microwave filter designs reaching wider bandwidths have started being developed with the use of distributed prototypes [1-24]. Further about circuit theory for electrical networks with filtering characteristics, especially synthesis of these networks, can be searched for in the books [1-25]-[1-32]. Network synthesis is reversed process to the network analysis in the sense that the problem now is to construct a network from a prescribed external behaviour bounded by realisability theory limitations and shaped by approximation theory.

Some of Seymour Cohn's papers were of great help in explaining principal microwave filter configurations, such as [1-33] about direct-coupled-resonator filters for narrowband waveguide filters. The same author introduced the often used waffle-iron filter, basically a low-pass design made by corrugating waveguide walls both in longitudinal and transverse directions, giving the filter its name. It is suitable for use when both a wide passband and a wide stopband free of spurious transmission modes (waveguide low-pass filters are important for harmonic rejection) are looked for. The first filters used to be designed applying solely all-pole filter approximations by minimum-phase networks. It started with the employment of Butterworth approximation function utilizing maximally flat passband (derivatives up to the order of the filter are zero at the zero frequency of a low-pass prototype function), whereas now more popular Chebyshev approximation function appeared somewhat later. Chebyshev filters utilize equiripple passband with the steepest passband to stopband transition of all the filters without finite transmission zeros.

Even higher selectivities than those of Chebyshev filters are possible when finite transmission zeros are introduced. Symmetrical response elliptic approximation function or more general pseudo-elliptic approximation function, also known as generalized Chebyshev, are used when this is expected. In the most general case of transmission zero positions in the complex plane, filters are implemented via non-minimum-phase networks. These networks with more than one signal path between the input and the output ports can be designed by cross-coupling filter resonators [1-34]. Cross couplings do not need to be physical, but can also be modal, using higher or lower order, propagating or evanescent modes as separate signal paths [1-35]. Another way of realizing finite real frequency transmission zeroes is by having extracted pole sections [1-36], containing resonators dedicated for this role.

---

[5] George A. Campbell and Otto J. Zobel had significant contributions in image method filter design (k-type sections, m-type sections, etc.) for frequency-division multiplexing in POTS. Ronald M. Foster and Wilhelm Cauer were pioneers of filter synthesis method, and canonical filter forms were named after them. Ernst Guillemin was professor at MIT whose explanations and dissemination of network analysis and synthesis theory had great impact. A number of future leading circuit theorists and electronics engineers working in other fields were students of his. Otto Brune in his doctoral thesis proved positive-real function being sufficient condition for driving-point impedance realisability using transformers. Sidney Darlington developed insertion loss synthesis approach, now also known as Darlington synthesis. Some prominent examples of their work are listed in [1-18]-[1-22].

Dual-mode cavities offer great potential for size reduction by cutting down the number of filter resonators by half. A great advancement for waveguide filters came with development of effective dual-mode filter designs [1-37]. These compact high-Q filters have become very common in satellite transponders. Filters with even more simultaneously excited modes per cavity are available, but are rarely used in practice because of their complexity. Certain unconventional waveguide modes appearing in regions of the mode chart that are not cramped and preferably supporting dual-mode operation are also sometimes used for having good Q factor to volume ratio [1-38]. Another application of distinguishable properties of wave propagation inside waveguide structures can be seen in evanescent mode filters [1-39], which operating frequencies are below the cutoff frequency of the dominant mode, leading to another method of size reduction. To keep wave propagating inside below-cutoff waveguide sections, which are of smaller cross sections than those supporting dominant mode propagation, they are periodically loaded with obstacles like capacitive screws or dielectric inserts perturbing the field. Extremely compact and high-Q filters are now being made by inserting dielectric resonators (called pucks) inside waveguide cavities [1-40]. Dielectric resonator filters could not have been immediately used in practice, but had to wait for emergence of low-loss and more thermally stable dielectric materials [1-41].

In this regard, there are several recent and ongoing investigations considering application of materials with enhanced properties in waveguide and other microwave filters, which have added a lot to research activity in these fields. Superconductivity has a potential of achieving immensely high Q factors [1-42], which applicability has made big advancements with development of London, Ginzburg-Landau and BCS theories, followed by discovery of high-temperature superconductivity (HTS) in some ceramic materials. HTS microwave filters have characteristics attractive for use in satellites and cellular base stations. One of challenges is to implement as many superconductive components as possible within the same cooled module. Another popular approach concerns electromagnetic metamaterials [1-43],[1-44] – materials engineered to have electromagnetic properties not found in nature, with particular interest in media with negative values of both their permittivity and permeability. They are known as double-negative, left-handed or negative index metamaterials, having negative refractive index. Electromagnetic metamaterials are made to be effectively homogenous by repetitive pattern of structures like split-ring resonators (SRRs), significantly smaller than the guided wavelength. Metamaterials can provide greater variety of EM wave propagation possibilities, and one of numerous target applications is to reduce size of waveguide filters [1-45]. Carbon based structures have been one of the most vibrant scientific and technological areas of interest for a while and incredibly auspicious new horizons have opened with experimental verification of flat monolayer carbon allotrope [1-46], which is a basic building block for other graphitic allotropes including fullerenes and graphite itself in the free state. Among a number of superlatives related to graphene, its electronic properties are considered as maybe the most valuable ones. Though not in the focus, applications in passive microwave devices have been considered so far as well [1-47][6].

Concerning books about microwave filters, [1-48] is still the most famous one, although it was written more than half a century ago. (For example, previously mentioned waffle-iron filter is described in it.) More modern microwave filter books covering the topic of waveguide

---

[6] It is interesting to mention that there are plans for using graphene in processes of water filtration and its desalination.

filters [1-49]-[1-52] include later developments in design procedures, facilitating computer calculations and optimization, as well as newer waveguide filter structures. There is a number of active engineers and researchers whose work has had continued impact on development of waveguide filter theory and practice: Smain Amari, Jens Bornemann, Uwe Rosenberg [1-53], Ming Yu [1-54], Simone Bastioli [1-55], Giuseppe Macchiarella [1-56], Vicente Boria [1-57], to name a few. University of Westminster Wireless Communications Research Group (WCRG) has its own tradition in this field [1-58]-[1-61].

1.1 Aims and Objectives of the Thesis

The main aim of this work is developing more cost-effective and compact waveguide filters and related components, otherwise known as expensive and bulky, in order to keep them as competitive technology in the modern market dominated by low cost mass production of items. However, this comes with constraint that superior properties of waveguide technology, low losses and power handling capacity, should not be drastically compromised. In addition, the filters should be able to utilize complex response functions to satisfy very stringent requirements of communication system designers.

More precisely, the chief idea is to use affordable fabrication technologies like waveguide E-plane planar inserts, additive manufacturing and substrate integrated waveguides for this goals, but at the same time to keep structure characteristics as close as possible to the conventional waveguide ones.

The first goal was to improve understanding of currently most advanced E-plane waveguide filters and experiment with their performances under different requirements such as amplitude characteristics with different transmission zero positions, different relative bandwidths and such. Further objective was to develop a novel geometry of E-plane filters being able to take advantage of using a thin dielectric support along the centre E-plane.

The study of modal nature of E-plane extracted pole filters produced the goal to apply independent control of different modes using only different geometries within the centre E-plane of a filter further to the modes used at different frequency bands.

Incredible rise of additive manufacturing on one side, but problems with easy metal plating of polymers on the other, inspired the target to take best of both additive and subtractive manufacturing and design filters with least obstacles regarding fabrication. In addition, the clear strength of 3D printing regarding ease of fabricating high performance resonators opened the question of solutions under constrained specifications that cannot be satisfied by optimal structures for general unconstrained case.

Finally, potential of substrate integrated waveguides to be universal intermediate element between hollow metal waveguides and planar transmission lines was noticed and it set the aim to design structures utilizing this property. Further investigation divided it into a single polarization objective and orthogonal polarization objective, driven by needs to feed versatile waveguide filters.

1.2 Outline of the Thesis

Since the main subject of the thesis are waveguide structures, although fabricated in different ways and upgraded with elements to shape them for particular applications, the further text opens with chapter 2 dedicated to waveguides and waveguide resonators. Using classical electromagnetic field theory, it is first shown that TE and TM waves propagate along waveguides rather than TEM waves. Electric and magnetic field distributions are found step-by-step, starting with Maxwell's equations as the fundamental laws of electromagnetism. Characteristic physical quantities connected with waveguides like cutoff frequency, guide wavelength and wave impedance are derived as well. Special treatment is given to rectangular waveguides, as they are the most common type of waveguides seen in practice. Different standards regarding rectangular waveguides and their connections are mentioned. The next step is short circuiting waveguide sections at both ends to form resonators, which are in turn building blocks of waveguide filters. Furthermore, losses in waveguides and waveguide resonators that can be caused by dissipation both in dielectrics and metals are investigated.

Chapter 3 gives introduction to the circuit theory. The starting question asks which filter structures are feasible at all, having available just limited number of elements to build filter circuits. It turns out that filter realizability theory is very well studied field and that transfer functions of filters are rational functions with some additional limitations. Next topic is generation of mathematical functions that approximate desirable filter responses, but can also be implemented using physical filter networks. Important topic in filter theory are transformations between different types of filters, and here is of biggest concern relationship between lowpass and bandpass filters. Most filter synthesis start with lowpass prototype, and frequency-invariant reactance is introduced as a virtual element needed to keep the same mathematical apparatus for asymmetric bandpass filters.

Chapter 4 finally deals with modern waveguide filters, in particular with those using E-plane technology. That way, fabrication is simplified because filter is composed of a reusable housing parts and insert, which is implemented as a planar circuit. Although properties of two visually similar recently proposed classes of filters with metal fins are considered, they work in slightly different ways as one utilizes finite transmissions zeros through cross coupled resonators and the other one through elements (fins) specifically dedicated for that purpose. These filters have been considered from many aspects, from sensitivity analysis and mechanical tuning to comparing resonator Q factors and analysing resonating modes. Finally, a new type of balanced E-plane sections are introduced, which have resonators realising transmission zeros that do not require electric contact with waveguide housing.

In chapter 5, the scope of E-plane filters is extended to dual band filters and diplexers. The notion of fins inside filters having different effect on even and odd degree modes is used here to independently control resonances in two different frequency bands. Furthermore, ultra compact filters are used for diplexers in order to drastically reduce size and weight of these bulky components.

Chapter 6 concerns additive manufacturing application in fabrication of microwave waveguide and cavity filters. First filter type uses 3D printing only for filter insert dielectric. This hybrid method is aimed to be one of the easiest filter fabrications, with a lot of added

freedom regarding structure complexity. The second type has aim to be high performance planar filter.

Chapter 7 considers substrate integrated waveguide circuits. It begins with a new variation ow SIW filters using dual mode cavities. Finally, very effective transitions from SIW to metal waveguide are proposed. The second type is an orthomode transducer, as it is able to work as polarization duplexer. It has outstanding broadband quality for a planar device of that kind.

The appendix considers in great details materials and fabrication processes essential for modern microwave filters. Firstly, fabrication of PCBs is covered, both using in-house circuit board plotter and sending Gerber files to external fabricators. After that, just basic ideas about CNC machining are touched as it still a gold standard for quality fabrication, before having very detailed overview of up-and-coming 3D printing technologies and materials they use. Right after, equally important topic of realising metal surfaces in microwave structures is again thoroughly covered.

References

[1-1]   D. M. Pozar, *Microwave engineering*, 4th ed., New York: John Wiley & Sons, 2012.

[1-2]   R. E. Collin, *Foundations for microwave engineering*, 2nd ed. New York: Wiley-IEEE Press, 2001.

[1-3]   P. A. Rizzi, *Microwave engineering: passive circuits*. Englewood Cliffs, NJ: Prentice Hall PTR, 1988.

[1-4]   A. R. Djordjevic, D. V. Tosic, *Mikrotalasna tehnika*. Belgrade: Akademska misao, 2006.

[1-5]   V. V. Petrovic, D. V. Tosic, A. R. Djordjevic, *Mikrotalasna pasivna kola*. Belgrade: Elektrotehnički fakultet, 2010.

[1-6]   R. Sorrentino, G. Bianchi, *Microwave and RF Engineering*, John Wiley & Sons, 2010.

[1-7]   D. M. Pozar, *Microwave and RF wireless systems*. New York; Chichester: John Wiley & Sons, 2001.

[1-8]   K. Chang, *RF and Microwave Wireless Systems*. Hoboken: John Wiley & Sons, 2000.

[1-9]   L. E. Larson, *RF and microwave circuit design for wireless communications*. Boston, Mass.; London: Artech House, 1996.

[1-10]   R. E. Collin, *Field theory of guided waves*, 2nd ed. New York: Wiley-IEEE Press, 1991.

[1-11]   N. Marcuvitz, *Waveguide handbook*. London: Peter Peregrinus on behalf of the Institution of Electrical Engineers, 1993.

[1-12]   S. B. Cohn, "Properties of Ridge Wave Guide," *Proc. IRE*, vol. 35, no. 8, pp. 783–788, Aug. 1947.

[1-13]   J. P. Montgomery, "On the Complete Eigenvalue Solution of Ridged Waveguide," *IEEE Trans. Microw. Theory Tech.*, vol. 19, no. 6, pp. 547–555, Jun. 1971.

[1-14]   W. J. R. Hoefer and M. N. Burton, "Closed-Form Expressions for the Parameters of Finned and Ridged Waveguides," *IEEE Trans. Microw. Theory Tech.*, vol. 30, no. 12, pp. 2190–2194, Dec. 1982.

[1-15]   R. F. Harrington, *Time-harmonic electromagnetic fields*. New York: Wiley-IEEE Press, 2001.

[1-16]   http://www.jlab.org/ir/MITSeries.html

[1-17]   G. L. Ragan (Editor), *Microwave Transmission Circuits*, M.I.T Rad. Lab Series, vol. 9. New York: McGraw-Hill, 1948.

[1-18]   O. J. Zobel, "Theory and design of uniform and composite electric wave-filters," *The Bell System Technical Journal*, vol. 2, no. 1, pp. 1-46, Jan. 1923.

[1-19]   R. M. Foster, "A reactance theorem," *Bell System Technical Journal*, vol. 3, pp. 259-67, 1924.

[1-20]   W. Cauer, *Synthesis of Linear Communication Networks*. New York: McGraw-Hill, 1958.

[1-21] O. Brune, "Synthesis of finite two terminal network whose driving point impedance is a prescribed function of frequency," *Journal of Mathematics and Physics*, vol. 10, pp. 191-236, 1931.

[1-22] S. Darlington, "Synthesis of reactance 4-poles with prescribed insertion loss characteristics," *Journal of Mathematics and Physics*, vol. 18, pp. 257-353, 1939.

[1-23] P. I. Richards, "Resistor-Transmission-Line Circuits," *Proc. IRE*, vol. 36, no. 2, pp. 217–220, Feb. 1948.

[1-24] L. Young, "Direct-Coupled Cavity Filters for Wide and Narrow Bandwidths," *IEEE Trans. Microw. Theory Tech.*, vol. 11, no. 3, pp. 162–178, May 1963.

[1-25] E. A. Guillemin, *Synthesis of passive networks: theory and methods appropriate to the realization and approximation problems*. John Wiley & Sons, 1957.

[1-26] D, F. Tuttle, *Network synthesis*, vol. I, John Wiley & Sons, New York, 1958.

[1-27] N. Balabanian, *Network synthesis*, Prentice-Hall, Englewood Cliffs, N. J., 1958.

[1-28] M. E. Van Valkenburg, *Modern Network Synthesis*. New York: John Wiley & Sons, 1960.

[1-29] L. Weinberg, *Network analysis and synthesis*, second edition, McGraw-Hill, 1962.

[1-30] F. F. Kuo, *Network analysis and synthesis*, second edition, John Wiley & Sons, 1966.

[1-31] J. D. Rhodes, *Theory of electrical filters*. London: John Wiley & Sons, 1976.

[1-32] H. Baher, *Synthesis of electrical networks*. Wiley, New York, 1984.

[1-33] S. B. Cohn, "Direct-Coupled-Resonator Filters," *Proc. IRE*, vol. 45, no. 2, pp. 187–196, Feb. 1957.

[1-34] J. R. Pierce, "Paralleled-Resonator Filters," *Proc. IRE*, vol. 37, no. 2, pp. 152–155, Feb. 1949.

[1-35] F. Arndt, T. Duschak, U. Papziner and P. Rolappe, "Asymmetric iris coupled cavity filters with stopband poles," *IEEE International Digest on Microwave Symposium*, Dallas, TX, 1990, pp. 215-218 vol.1.

[1-36] J. D. Rhodes and R. J. Cameron, "General Extracted Pole Synthesis Technique with Applications to Low-Loss TE_{011} Mode Filters," *IEEE Transactions on Microwave Theory and Techniques*, vol. 28, no. 9, pp. 1018-1028, Sep 1980.

[1-37] A. E. Atia, A. E. Williams, "Narrow-Bandpass Waveguide Filters," *IEEE Trans. Microw. Theory Tech.*, vol.20, no.4, pp.258-265, Apr 1972.

[1-38] E. L. Griffin and F. A. Young, "A Comparison of Four Overmoded Canonical Narrow Bandpass Filters at 12 GHz," *Microwave Symposium Digest, 1978 IEEE-MTT-S International*, 1978, pp. 47–49.

[1-39] G. F. Craven and C. K. Mok, "The Design of Evanescent Mode Waveguide Bandpass Filters for a Prescribed Insertion Loss Characteristic," *IEEE Trans. Microw. Theory Tech.*, vol. 19, no. 3, pp. 295–308, Mar. 1971.

[1-40] S. B. Cohn, "Microwave Bandpass Filters Containing High-Q Dielectric Resonators," *IEEE Trans. Microw. Theory Tech.*, vol. 16, no. 4, pp. 218–227, Apr. 1968.

[1-41] W. Wersing, "Microwave ceramics for resonators and filters," *Current Opinion on Solid State and Materials Science*, vol. 1, pp. 715-29, 1996.

[1-42] M. J. Lancaster, *Passive Microwave Device Applications of High Temperature Superconductors*, MA, Cambridge:Cambridge Univ. Press, 1997.

[1-43] C. Caloz, T. Itoh, *Electromagnetic Metamaterials: Transmission Line Theory and Microwave Applications*. Hoboken, N.J.: John Wiley & Sons, 2006

[1-44] N. Engheta, R. W. Ziolkowski, *Metamaterials: Physics and Engineering Explorations*. Hoboken, N.J.: Wiley-Interscience, 2006.

[1-45] Y. Dong and T. Itoh, "Promising Future of Metamaterials," *IEEE Microwave Magazine*, vol. 13, no. 2, pp. 39-56, March-April 2012.

[1-46] A. K. Geim and K. S. Novoselov, "The rise of graphene," *Nat. Mater.*, vol. 6, no. 3, pp. 183–191, Mar. 2007.

[1-47] J. Perruisseau-Carrier, "Graphene for antenna applications: Opportunities and challenges from microwaves to THz," in *Antennas and Propagation Conference (LAPC), 2012 Loughborough*, 2012, pp. 1–4.

[1-48] G. L. Matthaei, L. Young, E. M. T. Jones, *Microwave filters, impedance-matching networks and coupling structures*. Norwood, MA: Artech House, 1980.

[1-49]   D. Budimir, *Generalized filter design by computer optimization*, Boston, London: Artech House, 1998.

[1-50]   I. C. Hunter, *Theory and design of microwave filters*. London: Institution of Electrical Engineers, 2001.

[1-51]   R. J. Cameron, C. M. Kudsia, R. R. Mansour, *Microwave filters for communication systems: fundamentals, design and applications*. Hoboken, N. J.: Wiley-Interscience, 2007.

[1-52]   P. Jarry, J. Beneat, *Advanced design techniques and realizations of microwave and RF filters*. Hoboken, N. J.: Wiley-IEEE Press, 2008.

[1-53]   U. Rosenberg, S. Amari, and J. Bornemann, "Inline TM110-mode filters with high-design flexibility by utilizing bypass couplings of nonresonating TE1001/ modes," *IEEE Trans. Microw. Theory Tech.*, vol. 51, no. 6, pp. 1735–1742, Jun. 2003.

[1-54]   B. Yassini, M. Yu, D. Smith and S. Kellett, "A Ku -Band High-Q Tunable Filter With Stable Tuning Response," *IEEE Transactions on Microwave Theory and Techniques*, vol. 57, no. 12, pp. 2948-2957, Dec. 2009.

[1-55]   S. Bastioli, L. Marcaccioli, and R. Sorrentino, "Waveguide Pseudoelliptic Filters Using Slant and Transverse Rectangular Ridge Resonators," *IEEE Trans. Microw. Theory Tech.*, vol. 56, no. 12, pp. 3129–3136, Dec. 2008.

[1-56]   M. Oldoni, G. Macchiarella, and F. Seyfert, *Synthesis and Modelling Techniques for Microwave Filters and Diplexers: Advances in Analytical Methods with Applications to Design and Tuning*. Saarbrücken: Scholars' Press, 2014.

[1-57]   J. Ossorio, J. Vague, V. E. Boria and M. Guglielmi, "Exploring the Tuning Range of Channel Filters for Satellite Applications Using Electromagnetic-Based Computer Aided Design Tools," *IEEE Transactions on Microwave Theory and Techniques*, vol. PP, no. 99, pp. 1-9.

[1-58]   George Goussetis, "Waveguide bandpass filters with improved performance," Thesis PhD - University of Westminster, 2002.

[1-59]   O. Shelkovnikov, "Novel waveguide filter structures for broadband wireless systems," Thesis PhD - University of Westminster, 2006.

[1-60]   Niranchanan Suntheralingam, "Development of waveguide filters for next generation wireless transceiver front ends," Thesis PhD - University of Westminster, 2009.

[1-61]   O. Glubokov, "Development of waveguide filter structures for wireless and satellite communications," Thesis PhD, University of Westminster, 2011.

2. Waveguides and Waveguide Resonators

Waveguides [1-1], [1-11], [2-1] are wave-guiding structures by the means of material boundaries that have less than two conductors [2-2]. In the original and usual sense in microwave engineering, and in the case concerned here, they are essentially hollow metallic pipes7. This is in contrast with the other type of wave-guiding structures - transmission lines, which have two or more conductors. Waveguides are also sometimes referred to as a type of transmission lines, and the other way round, because they are intended for the same applications and it is not counterintuitive regarding the terms. Nevertheless, that use will be avoided in this work for clarity purpose. In Figure 2.1, cross sections of various types of waveguides and transmission lines are presented. Figure 2.2 shows a picture of a monolithic waveguide section with flat connecting face flanges at its ends. From the electromagnetic point of view, distinctive feature of waveguides is that they, unlike transmission lines, do not support propagation of TEM waves in the longitudinal direction, but only of TE (H) or TM (E) waves. In comparison, TEM is the fundamental mode of ideal coaxial lines and striplines, whereas the basic mode for microstrip lines and coplanar waveguides, which have nonhomogeneous dielectric, is considered to be quasi-TEM (technically, hybrid modes with zero cutoff frequency and low dispersion, for which quasi-static analysis gives good approximation). For TEM waves, total charge per unit length in any of cross sections that are uniform along theoretically infinitely long structure has to be zero in order for energy to be finite. This limits the number of conductors to be not less than two. Waveguides might be counter intuitive for many people used to direct current (DC) and low frequency electrical circuits and 'need for a pair of wires to close a circuit'. From physicists' point of view, a waveguide can be viewed behaving as one-dimensional plasma [2-3].

Small available bandwidths can be a disadvantage of waveguides. At the lower side of the passband, the bandwidth is bounded by a non-zero cutoff frequency, resulting in inherent behaviour of a highpass filter. In comparison, TEM waves propagate from the zero frequency, so transmission lines can be used starting with DC. On the side of higher frequencies, the usability is limited by propagation of higher order modes, just as it is the case with transmission lines, as the desired functionality within the electromagnetic field of overmoded waveguides becomes difficult to control. Unwanted formation of modes is very hard to prevent since they naturally emerge at waveguide discontinuities. There are, however, available techniques that increase bandwidth of a waveguide. Ridged waveguide has cutoff frequency of the fundamental mode reduced more than the cutoff frequency of the first higher order mode. In addition, as the operating frequency decreases, waveguides become less practically usable because of their size. They are rarely found below 5 GHz and at DC are not even theoretically feasible with cross section dimensions surging to infinity. As a rule of thumb, propagation in a rectangular waveguide is possible for waves having the free space wavelength shorter than the double width of the waveguide's broad wall. Even at frequencies of 10 or 20 GHz, where they are widely used, standard metal waveguides are relatively bulky and heavy. Also, in comparison with the microstrip technology, waveguide technology is less available, more difficult to produce and more expensive.

---

7 Waveguides can also be dielectric, meaning that an optical fibre is also a type of waveguide (optical). Interestingly, coplanar waveguides (CPW) are by the mentioned taxonomy type of transmission lines despite their name suggesting different.
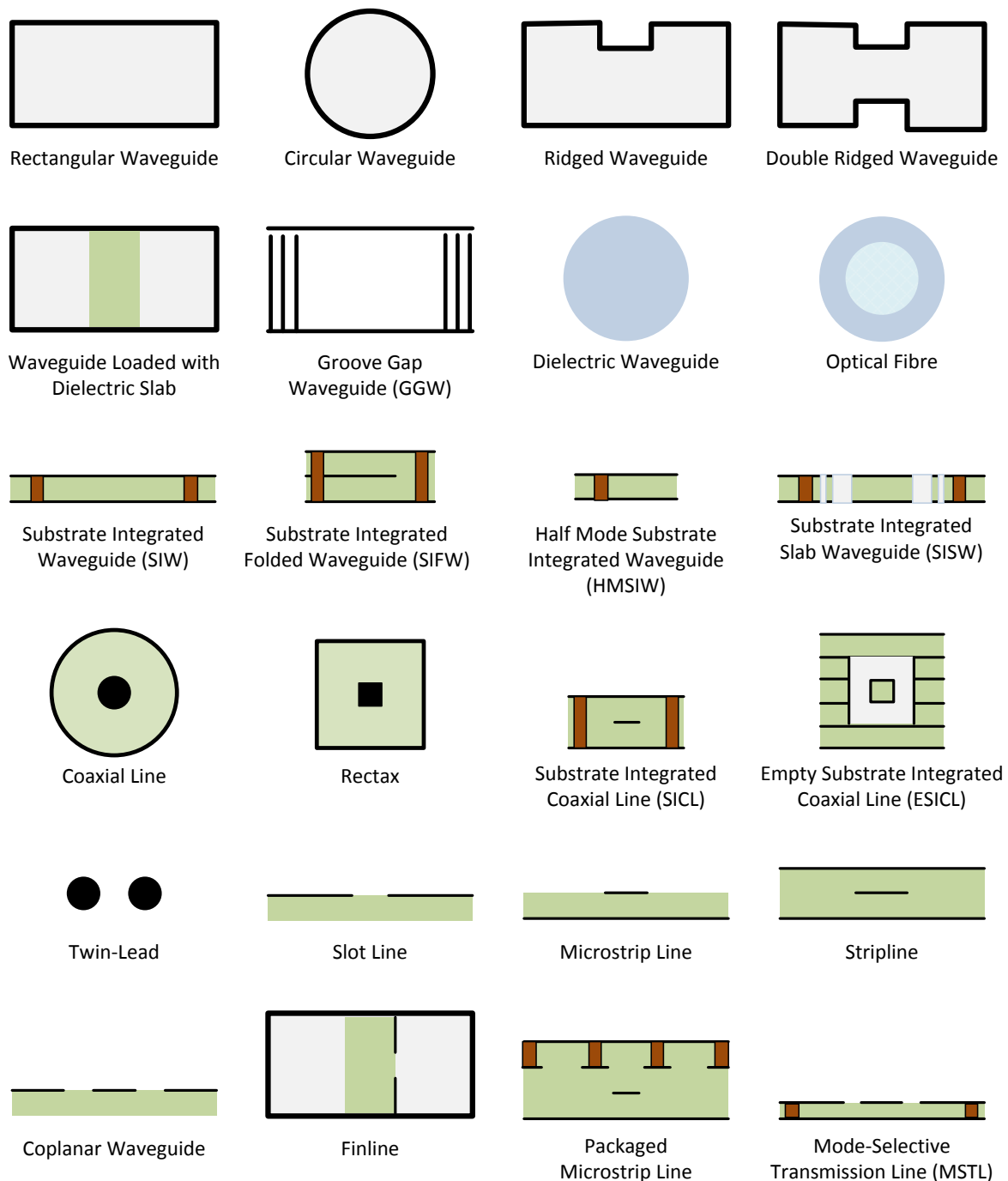
Figure 2.1 Cross-sectional views of wave-guiding structures widely used commercially and in academia, as well as some recently introduced ones.

Figure 2.2 X-band WR-90 straight rectangular waveguide section with square flanges. (Amitec Electronics Ltd.)

Nevertheless, there is a number of applications where previously mentioned properties are not of main concern. Instead, high performance characteristics like low losses and high

power handling capability as well as excellent isolation are paramount. Such are satellite communications, point-to-point microwave links and radar systems, where waveguide structures are typically the first choice. Despite the stress in modern high frequency electronics being generally more on mass producible compact structures like planar components and integrated circuits together with distributed circuit analysis rather than on waveguides and field theory analysis, for aforementioned purposes the advantages of waveguide technology, dominating earlier periods of microwave engineering, still easily outweigh their shortcomings. At a given frequency, waveguides have about 10 times lower loss than coaxial lines. Likewise, coaxial lines have about 10 times lower loss than microstrip lines of the same length. Air dielectric, close to the perfect one, is prevalent in waveguides because they have self-supported structures. Not only that air has very low loss, but it is also readily available and free of cost. To reach higher power levels, even in megawatts, waveguides are pressurized with gasses which increase the peak power level. However, superiority of waveguide characteristics comes to the full extent with further increase in frequency, when millimetre-wave range is reached[8]. Dielectric losses exceed conductor losses at these frequencies, and waveguides become very small in dimensions. Even state of the art MMIC terahertz transceivers for short-range wireless links under development rely on waveguide packaging to reduce losses, although it is seen as a burden for commercialisation [2-4], [2-5].

A limitation of standard waveguides is their rigidness. It is effectively surpassed in flexible waveguides, which can be twistable or non-twistable, made out of helically wound strip or thin wall pressed to form the convolutions. Over the time, there has been a number of other alternative waveguide constructions proposed. Additive manufacturing [2-6] has a particularly good application in waveguide technology, both for fabricating conventional and non-conventional waveguide designs, being suitable for prototyping, weight reduction, having no obstacles with complexity like machining, etc. Another popular approach has been fusion of waveguide and PCB technologies. Laminated waveguides [2-7] are multilayer PCBs in which waveguide sidewalls are built from lined via-holes and edges of metallized planes, so that both vertical and horizontal current flow is supported in them. There has been a whole range of single layer substrate integrated circuits (SICs) offered as reduced cost, mass producible and planar-circuit integrated waveguide alternatives [2-8]. Among them, without any doubt the most used one has been substrate integrated waveguide (SIW) [2-9], having side walls made from cylindrical via fences. From SIW, there have been other derived structures like substrate integrated folded waveguides (SIFWs) [2-10]. Groove gap waveguides (GGWs) [2-11] have been recently proposed promising at millimetre-waves advantage over conventional waveguides built in two parts because they do not require electrical contact between the top and bottom broad walls.

2.1.   Wave Propagation in Waveguides

We start by simplifying Maxwell's equations through applying the conditions that hold for idealised waveguide structures. The space is filled with linear, homogenous and isotropic (LIH) as well as lossless and source-free dielectric medium inside conducting shield. In fact, that is the volume through which the energy is transferred in the form of electromagnetic

---

[8] Although waveguide structures are more appropriate for use at higher frequencies, it is usually more comfortable to do fabrication and testing at lower frequencies. X-band is one of the frequently used frequency bands, and designs done by Wireless Communications Research Group mostly belong to it.

waves, not the metal enclosure itself. Faraday's law and Ampere's law in phasor differential form are[9]:

$$\nabla \times \mathbf{E} = -j\omega\mu\mathbf{H}, \tag{2.1a}$$

$$\nabla \times \mathbf{H} = j\omega\varepsilon\mathbf{E}. \tag{2.1b}$$

In this case, the other two Maxwell's equations are redundant as they can be derived taking divergences of (2.1) (dot products of del operators):

$$\nabla \cdot \mathbf{D} = \varepsilon\nabla \cdot \mathbf{E} = 0, \tag{2.2a}$$

$$\nabla \cdot \mathbf{B} = \mu\nabla \cdot \mathbf{H} = 0. \tag{2.2b}$$

On the other side, by taking curls of (2.1) (vector products of del operators) and subsequently applying curl of the curl vector calculus identity and (2.2), two new frequently used partial differential equations (PDEs) emerge. These are (vector) Helmholtz equations:

$$\nabla^2\mathbf{E} = -k^2\mathbf{E}, \tag{2.3a}$$

$$\nabla^2\mathbf{H} = -k^2\mathbf{H}, \tag{2.3a}$$

where the constant at a chosen frequency

$$k = \omega\sqrt{\mu\varepsilon} \tag{2.4a}$$

is called the wavenumber or propagation constant of the medium.

The following step is to introduce cylindrical geometry, Figure 2.3, with the z-axis representing distance along the cylinder. Assuming wave propagation in the longitudinal direction, vector field functions can be expressed as the product of a function that purely depends on two transverse coordinates and the multiplication factor $e^{\pm\gamma z}$. Here, γ is the propagation constant, negative sign represents the wave propagating in the positive direction and positive sign represents the wave propagating in the negative direction of the z-axis. However, due to symmetry, only positive direction propagation will be further examined. In the configuration with source and load connected to the waveguide ports (the load being placed at $z = 0$), negative sign represents the incident wave - resultant wave travelling in the direction from the source to the load. On the other side, positive sign represents the reflected wave - resultant wave travelling in the direction from the load to the source. When del operator is also separated into the transverse and longitudinal components, $\nabla = \nabla_t - \gamma\mathbf{i}_z$, and squared $\nabla^2 = \nabla_t^2 + \gamma^2$, Helmholtz equations are transformed into:

$$\nabla_t^2\mathbf{E} = -(\gamma^2 + k^2)\mathbf{E}, \tag{2.5a}$$

$$\nabla_t^2\mathbf{H} = -(\gamma^2 + k^2)\mathbf{H}. \tag{2.5b}$$

A new constant, the cutoff wavenumber, can be defined as $k_c = \sqrt{\gamma^2 + k^2}$. The cutoff wavenumber cannot be zero for waveguides since TEM waves do not propagate inside them. We will consider here TE ($E_z = 0, H_z \neq 0$) and TM ($E_z \neq 0, H_z = 0$) waves. Hybrid waves ($E_z \neq 0, H_z \neq 0$) occur in waveguides with nonhomogenous dielectric, such as with inserted dielectric slabs.

---

[9] Standard boldface type vector notation is used and complex variables do not have special designation.
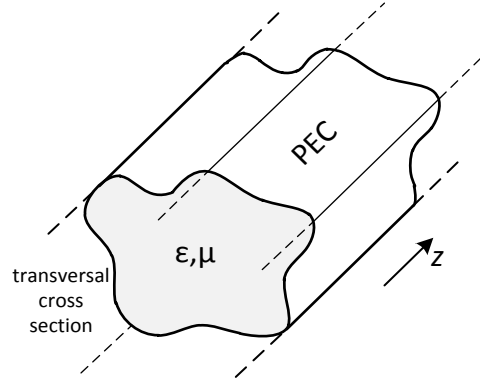
Figure 2.3 Geometry of a general uniform waveguide.

In the TE waves case, the equation (2.5b) gives scalar PDE

$$\nabla_t^2 H_z + k_c^2 H_z = 0. \tag{2.6}$$

Indeed, based on (2.5), same wave equation can be written for transversal electric and magnetic field components as the unknown functions. However, we will not proceed solving all of them, since field components are not mutually independent as it may seem from (2.5), but still linked through Maxwell's equations. Nevertheless, Helmholtz equations were used to isolate one scalar field component, so its general solution can be found solving the PDE.

Now, the metal enclosure of the waveguide is finally being introduced to provide the boundary conditions and determine particular solutions of the differential equation. Field equations in their differential form are restricted to the space with no electromagnetic discontinuities in the medium. Thus, integral formulation of Maxwell's equations is used for deriving boundary conditions to fill in this deficiency in the differential formulation of the equations. Although for each of four integral Maxwell's equations can be derived one boundary condition, just like redundancy of (2.2), only two of them between tangential field components, coming from closed curve line integral equations,

$$\oint_C \mathbf{E}\, dl = -j\omega \int_S \mathbf{B}dS, \tag{2.7a}$$

$$\oint_C \mathbf{H}\, dl = j\omega \int_S \mathbf{D}dS + \int_S \mathbf{J}dS. \tag{2.7b}$$

are sufficient. These cyclic integrals are taken around the contours that run parallel to the boundary on both sides of it and at infinitesimal distance from it.

In the ideal case considered here with metal modelled by perfect electric conductor (PEC, conductivity $\sigma \to \infty$), the resulting boundary condition stating that tangential component of electric field in dielectric next to the boundary is equal to zero is enough to find the particular solutions of the differential equation (2.6) for H_z. If we designate unit normal pointing outward from the conductor surface by **n**, this condition can be expressed as $\mathbf{n} \times \mathbf{E} = 0$. The other independent boundary condition for transverse components, $\mathbf{n} \times \mathbf{H} = \mathbf{J}_s$, can be used to calculate surface current, $\mathbf{J}_s$, distribution at the boundary of the perfect waveguide conductor once the field distribution inside waveguide dielectric is determined. It turns out that (2.6), together with the tangential electric field boundary condition, has a solution only for infinite number of discrete values of the cutoff wavenumber k_c. Apart from being the axial magnetic field component, H_z can be used to calculate the remaining (transverse) field components using the following relations derived from (2.1):

$$\mathbf{E}_t = \frac{j\omega\mu}{k_c^2}\mathbf{i}_z \times \nabla_t H_z, \tag{2.8a}$$

$$\mathbf{H}_t = -\frac{\gamma}{k_c^2}\nabla_t H_z. \tag{2.8b}$$

The transverse field components are orthogonal, mutually related by the expression $E_t = -Z_{TE}\mathbf{i}_z \times \mathbf{H}_t$, where

$$Z_{TE} = \frac{j\omega\mu}{\gamma} \tag{2.9}$$

is the TE wave impedance.

By analogy, PDE for TM waves becomes

$$\nabla_t^2 E_z + k_c^2 E_z = 0, \tag{2.10}$$

which combined with the same tangential boundary condition, $E_{tang} = 0$, yields the solutions for the axial electric field component E_z. Similarly, the transverse field inside the waveguide can be found from E_z by

$$\mathbf{E}_t = -\frac{\gamma}{k_c^2}\nabla_t E_z, \tag{2.11a}$$

$$\mathbf{H}_t = -\frac{j\omega\varepsilon}{k_c^2}\mathbf{i}_z \times \nabla_t E_z. \tag{2.11b}$$

They give the relation $E_t = -Z_{TM}\mathbf{i}_z \times \mathbf{H}_t$, where

$$Z_{TM} = \frac{\gamma}{j\omega\epsilon} \tag{2.12}$$

is the TM wave impedance.

From (2.6) or (2.10) and $E_{tang} = 0$ boundary condition, it follows that the eigenvalue k_c^2 is dependent on the shape of waveguide cross section and type of wave, but not frequency. Also, for closed structures, it is always a real number [10]. Thus, the propagation constant can be expressed using the same form for both TE and TM waves as

$$\gamma = \sqrt{k_c^2 - k^2} = j\sqrt{\omega^2\varepsilon\mu - k_c^2} = j\beta = j\omega\sqrt{\varepsilon\mu}\sqrt{1 - \left(\frac{f_c}{f}\right)^2}, \tag{2.13}$$

where β is called the phase constant and there exists the cutoff frequency

$$f_c = \frac{k_c}{2\pi\sqrt{\varepsilon\mu}} \tag{2.14}$$

at which γ(β) is equal to zero. Below this frequency, γ(jβ) becomes purely real since radicands in (2.10) change signs, and the wave has exponential decay of magnitude that gets steeper with decrease in frequency and constant phase. This means that such a wave does not propagate and it is called evanescent. When a wave is excited as evanescent one because the operating frequency is below the cutoff frequency of that wave type, there is still certain reactive energy stored in it. However, it remains in the near-field, oscillating in time and changing form between electric and magnetic, but without transmission.[11]

---

[10] In [2-12] is described a numerical method for computing cutoff wavenumbers in waveguides of arbitrary cross sections accompanied by several evaluation examples that illustrate the stated properties.

[11] Modes in dielectric waveguides also have cutoff frequencies, albeit, they can be zero for the dominant mode in certain cases. For dielectric waveguides the wave bellow cutoff is no longer guided through total internal reflections.

In realistic situations like when having diaphragms and tuning screws inside waveguide filters, observing at a certain frequency, evanescent modes are generated at these discontinuities so that boundary conditions on them can be satisfied. Similar to the far-field concept applied for antennas, by increasing the distance along the waveguide from the source of evanescent waves, we finally reach the distance at which, with certain accuracy, it can be declared that evanescent modes are negligible and only propagating modes can be taken into account. This distance needs to be estimated both when adding measurement ports on a filter (either in simulation or when testing with a network analyzer) and between discontinuities inside the filter, so that it is known if single-mode coupling approximation is valid or not. Nevertheless, apart from monomode operation, existence of evanescent modes can be deliberately used for highpass filtering with no propagating modes at all, or even realising couplings at electrically shorter distances for filter miniaturization [2-13]. Finally, in real-world applications the evanescent waves do not only store energy because its dissipation is inevitable.

The term $\sqrt{1 - \left(\frac{f_c}{f}\right)^2} = \cos\theta$ repeatedly occurs in a number of important equations related to waveguides. θ can be given physical interpretation of the angle that TEM wave, which continuously re-reflect from the side walls of the waveguide producing resultant field expressed in the form of the analysed TE or TM wave, has to the *z*-axis. For $\theta = 0$, TE/TM wave equations ought to be equivalent with the TEM wave equations, which can be used for error-proofing. On the other side, for $\theta = \pi/2$, TEM waves are not propagating along the waveguide, but bouncing between the side walls instead. This is plausible since it happens at the cutoff frequency.

The guide wavelength, defined as the distance between two nearest equiphase transverse planes inside waveguide, is found using the expression

$$\lambda_g = \frac{2\pi}{\beta} = \frac{\lambda_0}{\sqrt{\varepsilon_r \mu_r}\sqrt{1 - \left(\frac{f_c}{f}\right)^2}}, \tag{2.15}$$

where λ_0 is the wavelength in free-space. Guide wavelength is $1/\cos\theta$ times longer than the wavelength of a plane (TEM) wave in the medium filling the waveguide, $\lambda = 2\pi/k = \lambda_0/\sqrt{\varepsilon_r \mu_r}$. It is meaningful for frequencies above the cutoff, where it always holds $\lambda_g > \lambda$. Guide wavelength has the limit of wavelength in the medium when frequency approaches infinity and infinite limit when frequency approaches the cutoff. This is essential for understanding dimensions of waveguide elements such as waveguide resonators. Interestingly, the phase velocity $c_\varphi = f\lambda_g$ in air-filled waveguides (approximated as vacuum-filled) is $1/\cos\theta$ times higher than the speed of light in vacuum. Nevertheless, this does not contradict special theory of relativity as it does not represent the speed of energy transfer.

Expressing wave impedances of TE and TM waves in terms of the cutoff frequency, (2.9) and (2.12) transform to:

$$Z_{\text{TE}} = \frac{Z_{\text{TEM}}}{\sqrt{1 - \left(\frac{f_c}{f}\right)^2}}, \tag{2.16a}$$

$$Z_{\text{TM}} = Z_{\text{TEM}}\sqrt{1 - \left(\frac{f_c}{f}\right)^2}, \tag{2.16b}$$

where $Z_{\text{TEM}} = \sqrt{\frac{\mu}{\varepsilon}}$ is the intrinsic impedance of the medium, at the same time representing the wave impedance of a TEM wave. It is important to notice here that, unlike Z_{TEM}, both Z_{TE} and Z_{TM} are frequency dependent. This makes wideband impedance transformation and matching more complex to achieve for waveguides than for transmission lines.

Using previously introduced physical quantities, it is possible to relate a fictional equivalent transmission line to a waveguide, or one for each mode if there is more of them in the frequency range of interest. The equivalent transmission lines can be used as standard microwave distributed circuit elements and not only expressed in the way appropriate for physical waveguide measurement, typically using S-parameters. The characteristic impedance of such equivalent transmission line is equal to the wave impedance of analysed wave inside the waveguide and its wavelength is equal to the guide wavelength of the waveguide mode. Also, it is possible to assign equivalent voltages and currents, and make use of lumped circuit concepts.

More details about the presented and upcoming derivations can be found in [1-1]-[1-6]. Here is dominantly taken step-by-step approach to find a particular class of solutions for a problem of interest, tailored for comprehension. On the other side, in [1-15], there is stronger connection with general underlying mathematical theory, which is more appropriate for quick deduction of classes of solutions for larger set of related problems.

In the following material is also specified the 2D coordinate system to best match the geometry in the transverse plane of the analysed structure. For rectangular waveguides, which are the most used ones, the most appropriate is the Cartesian coordinate system (Figure 2.4). For circular waveguides, the polar coordinate system is adequate. (Cylindrical coordinate system becomes its 3D extension.)

2.1.1.   Rectangular Waveguides

With the introduction of Cartesian coordinate system, transverse del and Laplace operators adopt the forms $\nabla_t = \frac{\partial}{\partial x} + \frac{\partial}{\partial y}$ and $\Delta_t = \frac{\partial^2}{\partial x^2} + \frac{\partial^2}{\partial y^2}$. PDE (2.6) can now be rewritten as

$$\frac{\partial^2 H_z}{\partial x^2} + \frac{\partial^2 H_z}{\partial y^2} = -k_c^2 H_z. \tag{2.17}$$

Similarly, (2.8) transform into $E_x = \frac{-j\omega\mu}{k_c^2}\frac{\partial H_z}{\partial y}$, $E_y = \frac{j\omega\mu}{k_c^2}\frac{\partial H_z}{\partial x}$, $H_x = \frac{-\gamma}{k_c^2}\frac{\partial H_z}{\partial x}$, and $H_y = \frac{-\gamma}{k_c^2}\frac{\partial H_z}{\partial y}$. (Vector products can be elegantly expressed by a determinant of a 3 x 3 matrix, in which first row are the vectors of Cartesian axes, followed by the left side expanded in Cartesian coordinates in the second and the right side in the third row. These may not just be vector components, but also del operator Cartesian components in the case of the curl.)
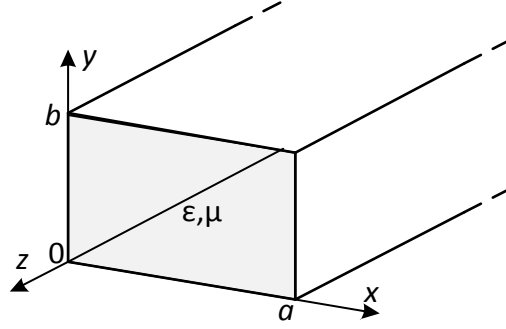
Figure 2.4 Geometry of a uniform rectangular waveguide.

The method of separation of variables is used to solve Helmholtz equations, and after expressing the axial magnetic field component as $H_z = Hx_z(x)\,Hy_z(y)$, (2.17) yields $-\frac{1}{Hx_z}\frac{d^2 Hx_z}{dx^2} - \frac{1}{Hy_z}\frac{d^2 Hy_z}{dy^2} = k_x^2 + k_y^2 = k_c^2$. Not only that general solutions for Hx_z and Hy_z can now be found independently by solving linear ordinary differential equations, but because of symmetry they have exactly the same form. After multiplying them, the general solution for H_z take the form $H_z = [A\sin(k_x x) + B\cos(k_x x)][C\sin(k_y y) + D\cos(k_y y)]$, where A, B, C and D are arbitrary complex constants.

After substituting the general solution of H_z into expressions for transverse electric field components E_x and E_y, the boundary conditions stating that the tangent electric field disappears on $x = 0$ and $y = 0$ waveguide side walls give $A = C = 0$. Axial magnetic field can be further reduced to the form $H_z = H_0 \cos(k_x x)\cos(k_y y)$, including the new constant $H_0 = BD$. The remaining two boundary conditions $E_x = 0\,\big|_{y=b}$ and $E_y = 0\,\big|_{x=a}$ finally give

$$k_x = \frac{m\pi}{a} \text{ and} \tag{2.18a}$$

$$k_y = \frac{n\pi}{b}. \tag{2.18b}$$

Coefficients m and n ($m, n \in N_0$) are called mode numbers. Values of the mode numbers give the name to a waveguide mode - a discrete solution for a wave with unique field distribution that can exist inside the waveguide. An interpretation of mode numbers m and n is that they represent number of half sine or half cosine variations for each of existing field components in the x and y directions respectively. There is no TE mode with both m and n coefficients zero, because that would mean no transverse field components, thus no wave propagation. Each wave mode can be propagating or non-propagating, depending whether its cutoff frequency is below or above the operating frequency, respectively.

Lastly, TE wave longitudinal field component inside a rectangular waveguide are

$$E_z = 0, \tag{2.19a}$$

$$H_z = H_0 \cos\left(\frac{m\pi x}{a}\right)\cos\left(\frac{n\pi y}{b}\right); \tag{2.19b}$$

and the transverse field components are

$$E_x = \frac{j\omega\mu}{k_c^2} k_y H_0 \cos\left(\frac{m\pi x}{a}\right)\sin\left(\frac{n\pi y}{b}\right), \tag{2.20a}$$

$$E_y = \frac{-j\omega\mu}{k_c^2} k_x H_0 \sin\left(\frac{m\pi x}{a}\right)\cos\left(\frac{n\pi y}{b}\right), \tag{2.20b}$$

$$H_x = \frac{j\beta\omega\mu}{k_c^2} k_x H_0 \sin\left(\frac{m\pi x}{a}\right)\cos\left(\frac{n\pi y}{b}\right), \tag{2.20c}$$

$$H_y = \frac{-j\omega\mu}{k_c^2} k_y H_0 \cos\left(\frac{m\pi x}{a}\right) \sin\left(\frac{n\pi y}{b}\right). \tag{2.20d}$$

(All the listed electric and magnetic field components have the same $e^{-j\beta z}$ dependency in the axial direction.)

On the other side, the corresponding equations for TM waves, derived in analogue way from (2.10) and (2.11) are:

$$E_z = E_0 \sin\left(\frac{m\pi x}{a}\right) \sin\left(\frac{n\pi y}{b}\right), \tag{2.21a}$$

$$H_z = 0; \tag{2.21b}$$

for the transverse field components and

$$E_x = \frac{-j\beta}{k_c^2} k_x E_0 \cos\left(\frac{m\pi x}{a}\right) \sin\left(\frac{n\pi y}{b}\right), \tag{2.22a}$$

$$E_y = \frac{-j\beta}{k_c^2} k_y E_0 \sin\left(\frac{m\pi x}{a}\right) \cos\left(\frac{n\pi y}{b}\right), \tag{2.22b}$$

$$H_x = \frac{j\omega\varepsilon}{k_c^2} k_y E_0 \sin\left(\frac{m\pi x}{a}\right) \cos\left(\frac{n\pi y}{b}\right), \tag{2.22c}$$

$$H_y = \frac{-j\omega\varepsilon}{k_c^2} k_x E_0 \cos\left(\frac{m\pi x}{a}\right) \sin\left(\frac{n\pi y}{b}\right). \tag{2.22d}$$

for the longitudinal field components. Since for TM modes $E_z \neq 0$, (2.21a) implies that it is impossible that either k_x or k_y is equal to zero. (For TE modes one of them can be zero.)

After substituting (2.18) back into $k_c = \sqrt{k_x^2 + k_y^2}$, a frequently used expression for the cutoff frequency of both TE$_{mn}$ and TM$_{mn}$ modes emerges from (2.14):

$$f_c = \frac{1}{2\sqrt{\varepsilon\mu}} \sqrt{\left(\frac{m}{a}\right)^2 + \left(\frac{n}{b}\right)^2}. \tag{2.23}$$

Expressions like (2.13), (2.15) and (2.16) can now be evaluated as functions of frequency for any TE or TM rectangular waveguide mode. The mode with the lowest cutoff frequency, considering all TE and TM modes, is also known as the dominant mode and is by far the most important one in waveguide applications. In a rectangular waveguide, TE$_{10}$ is the dominant mode if, without loss of generality, $a > b$.

Because of special importance of the dominant mode, (2.19) and (2.20) simplified for the case of TE$_{10}$ mode ($E_x = H_y = E_z = 0$) are emphasized here:

$$H_z = H_0 \cos\left(\frac{\pi x}{a}\right), \tag{2.24a}$$

$$E_y = -j\omega\mu \frac{a}{\pi} H_0 \sin\left(\frac{\pi x}{a}\right), \tag{2.24b}$$

$$H_x = j\beta \frac{a}{\pi} H_0 \sin\left(\frac{\pi x}{a}\right). \tag{2.24c}$$

Distribution of TE$_{10}$ mode field lines is drafted in Figure 2.5. The TE$_{10}$ cutoff frequency is reduced to:

$$f_c = \frac{1}{2a\sqrt{\varepsilon\mu}}. \tag{2.25}$$

The usable frequency spectrum for TE$_{10}$ single-mode operation does not actually start with the TE$_{10}$ cutoff frequency. Right above $f_{cTE_{10}}$, both attenuation and phase dispersion of modulated waves are high. The latter can be seen from the formula for the group velocity,

$c_g = \left(\frac{d\beta}{d\omega}\right)^{-1} = c\sqrt{1 - \left(\frac{f_c}{f}\right)^2}$, where c is the speed of light in the medium, showing that the group velocity approaches zero as the frequency approaches cutoff. Also, the upper side of the monomode band is as well not used all the way up to the limit of cutoff frequencies of higher order modes, but slightly lower so that their influence can be eliminated.
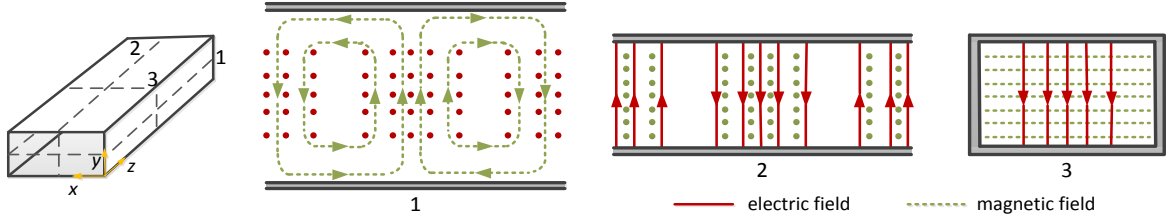
Figure 2.5 Field distribution of TE_{10} mode in rectangular waveguide.

There are several compatible rectangular waveguides standards, notably by RSCS [2-14] (WG designation), EIA [2-15] (WR designation) and IEC [2-16] (R designation). The width to height aspect ratio $a:b$ they have is approximately 2:1. $b = a/2$ is the largest height a waveguide can have still keeping the maximum monomode bandwidth of one octave ($f_{cTE_{20}} = f_{cTE_{01}} = 2f_{cTE_{10}}$). Increasing the waveguide height improves power handling capability and lowers attenuation. The reason why standard waveguides do not have the aspect ratio of exactly 2 is because their sizes are based on extrusions which were available during WWII. Also, the nominal range of waveguide operation is roughly between 1.25 and 1.9 $f_{cTE_{10}}$.

Waveguide flanges are used to interconnect different waveguide sections and components so that they can be bolted together or disassembled. Ordinary cover-type waveguide flanges have flat faces and use contact connection [2-17], [2-18]. At lowest frequencies (WG00 – WG9A rectangular waveguides), because of large waveguide sizes, flanges are typically of rectangular shape, not much larger than waveguides themselves. Also, they use very large number of holes for fixing - ten, or even several times higher for WG00. Above that (WG10 - WG14), circular flanges are used aside with the rectangular ones. At mid-range frequencies (WG15 - WG22), having most commonly used waveguide sizes, including those used in this work, square flanges with four hole fixing (holes positioned in the corners) are the standard, even though rectangular and round may occasionally be found. At millimetre-waves (WG23 - WG32) circular flanges with four hole fixing are regular. In addition, standard millimetre-wave waveguide flanges are doweled, although lower frequency ones can be equipped as well with dowel pins for high precision use. On the other side, there are cover-to-choke connections (one choke flange and one cover flange mated) that do not rely on excellent physical touch, but realizing zero or low impedance at the place where effective radial short circuited stub of choke meets the waveguide wall. In between, at the loci of contact between flanges, these effective transmission lines produce zero or very small input admittances. Nevertheless, cover-to-choke joins are not recommended for broadband waveguide equipment. Furthermore, if a waveguide needs to be pressurized, there is a sealing groove added to accommodate a rubber ring and make the connection airtight. Commonly used rectangular waveguide flange standards are IEC [2-19] (UAR, UBR, UDR, UER, PAR, PBR, PDR, CAR, CBR, RDR designations, where the first letter stands for the flange style: U-plain, P-sealing groove, C-choke/sealing groove; and the second letter stands for flange shape: A-circular, B-square, D,E-larger and smaller rectangular) and MIL-DTL (UG designations). It should be noted that not all of them are mutually compatible.

In Figure 2.6 are pictured brass and aluminium (two in practice frequently used metals for waveguide structure enclosures) housings made at the University of Westminster Faculty of Science and Technology machine shop, designed for experimental testing of waveguide filters with metal inserts. They are split in two blocks divided by the centre E-plane that can be bolted together. Laboratory purpose determined their shapes to be optimized for easy fabrication rather than for economical use of materials.

Constructing waveguide components from two block split by E-plane is frequently used for several reasons. First of all, machining of metal blocks itself is much easier this way. Secondly, assembling parts together can be effectively done, as signal leakage can be controlled by tightening the bolts that keep the parts together, increasing the pressure between flat surfaces. Another important reason is that the cut runs along the current flow of the dominant waveguide mode rather that interrupting it. In other words, opening along the cut acts as a nonradiating slot.
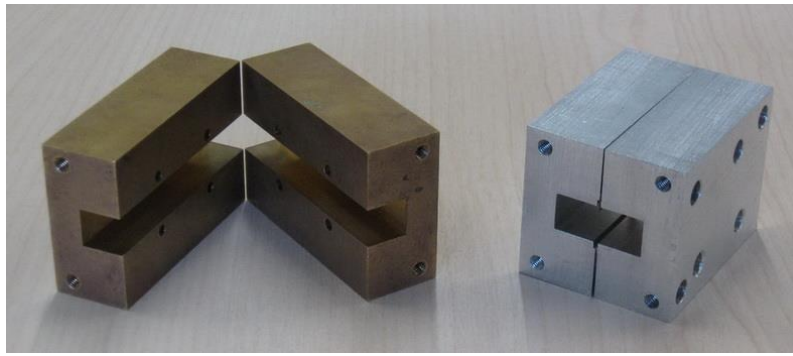
Figure 2.6 Brass (left) and aluminium (right) WG16 waveguide filter housings for laboratory testing at X band. Aluminium is significantly lighter metal and has higher electrical conductivity as well, σ_{Al}= 35.6 MS/m compared to $\sigma_{Br65\%}$= 15.9 MS/m. Connecting faces are compatible with UBR 100 flanges of waveguide-to-coax adaptors.

2.2.   Power Flow and Loss in Waveguides

From the Poynting's theorem, the (active) power flow is calculated as the real part of flux of Poynting vector (directional energy flux density that can readily be calculated from electric and magnetic field components). In waveguides, the flux is calculated through a transverse cross section of the waveguide dielectric,

$$P_t = \frac{1}{2}\text{Re} \int_{S_t} \mathbf{E} \times \mathbf{H}^* d\mathbf{S}, \tag{2.26}$$

where peak values of field components are used like in [1-1], rather than their effective values. For rectangular waveguides, (2.26) takes the form $P_t = \frac{1}{2}\text{Re} \int_{y=0}^{b} \int_{x=0}^{a} (E_x H_y^* - E_y H_x^*) dx dy$. Substituting transverse electric and magnetic field components from (2.20) or (2.22) in it, exact formula for real power flow of a particular TE or TM mode, respectively, can be derived. For the dominant TE_{10} mode in a rectangular waveguide, the real power flow is $P_{tTE_{10}} = \omega\mu \frac{a^3 b}{4\pi^2} |H_0|^2 \text{Re}(\beta)$. $|H_0|$ is the value of H_z maximum magnitude and the term $\text{Re}(\beta)$ shows that there is no active power flow below the cutoff frequency.

The equations that have been derived for lossless waveguides can also be directly extended to describe more realistic waveguide models which include losses in conductors and

dielectrics. Applying perturbation method, the electromagnetic field distribution is still approximated as the one calculated from the simpler lossless case, and the losses are later independently added assuming that their influence on change in the field distribution can be neglected. In this way, much more cumbersome calculation is avoided with low cost in accuracy in usual cases when conductor is close to the ideal conductor and dielectric close to the ideal dielectric.

Taking losses into account, the propagation constant becomes complex. The phase constant can be perturbed by adding real value attenuation constant α into the expression for the propagation constant, yielding

$$\gamma = \alpha + j\beta. \tag{2.27}$$

The attenuation constant $\alpha = \frac{P'_{loss}}{2P_t}$ is directly proportional to the power loss per unit length, $P'_{loss} = -\frac{P_t}{dz}$, where the power flow can be expressed as $P_t = P_t(0)e^{-2\alpha z}$. (Factor 2 comes from power being proportional to the product of electric and magnetic field quantities, which decay with $e^{-\alpha z}$ along the waveguide.) The attenuation constant can be split into two parts − one representing attenuation coming from loss in conductor and the other one representing attenuation coming from loss in dielectric (there is essentially no radiation loss):

$$\alpha = \alpha_c + \alpha_d = \frac{P'_{loss,c}}{2P_t} + \frac{P'_{loss,d}}{2P_t}. \tag{2.28}$$

Starting with the conductor loss, linear power density dissipated in the conductor can be found by integrating real energy flux density penetrating into the conductor around the transverse contour C_c on the inner side of the conductor,

$$P'_{loss,c} = \frac{1}{2}\oint_{C_c} \text{Re}(\mathbf{E} \times \mathbf{H}^*) \cdot (-\mathbf{n})dl = \frac{1}{2}\oint_{C_c} R_s |H_{tang}|^2 dl. \tag{2.29}$$

In this equation, H_{tang} is the tangential component of magnetic field at the waveguide conductor surface and can readily be expressed in terms of calculated magnetic field components H_z and H_t inside the lossless waveguide, and R_s is the surface resistance of the conductor. In this case, the surface resistance can be found as the real part of the wave impedance $Z_{\text{TEM},c} = \sqrt{\frac{\mu_c}{\varepsilon_{e,c}}}$ of the local plane wave penetrating into the conductor and getting entirely absorbed. (Subscript c denotes that medium parameters refer to the conductor. A good conductor in current conduction sense is a poor dielectric in field propagation sense and vice versa.) This is a more general form of the intrinsic wave impedance that involves equivalent complex permittivity, $\varepsilon_e = \varepsilon - j\frac{\sigma}{\omega}$. The term with finite conductivity that results in power dissipated in metal comes from more general form of (2.1b) including free electron current, $\nabla \times \mathbf{H} = j\omega\varepsilon\mathbf{E} + \sigma\mathbf{E} = (j\omega\varepsilon + \sigma)\mathbf{E} = j\omega\varepsilon_e\mathbf{E}$. In a good conductor, $\sigma_c \gg \omega\varepsilon_c$, $\varepsilon_c = \varepsilon_{c,r}\varepsilon_0$ and $\varepsilon_{c,r} = 1$, thus, $\varepsilon_{e,c} = -j\frac{\sigma_c}{\omega}$ and consequently $Z_{\text{TEM},c} = \sqrt{j\frac{\omega\mu_c}{\sigma_c}} = (1+j)\sqrt{\frac{\pi\mu_c f}{\sigma_c}}$. Finally, the surface resistance is

$$R_s = \sqrt{\frac{\pi\mu_c f}{\sigma_c}}. \tag{2.30}$$

(It can be observed that the phase angle between $\mathbf{E}$ and $\mathbf{H}$ vectors in a good conductor is approximately 45°, compared to the 0° angle in a perfect lossless dielectric (2.16). Naturally, arbitrary lossy materials have phase angles of their wave impedances somewhere in between

these two values.) In the lossless case, σ_c is infinite since the conductor is PEC, there is no wave propagation in it whatsoever, and $Z_{\text{TEM},c} = R_s = 0$.

In the used model for losses in the waveguide conductor, we only need to know magnetic field on its surface and its conductivity and permeability. However, it is also of interest to investigate how this local TEM wave penetrating into the conductor propagates perpendicularly to its surface. The propagation constant of this wave can be obtained as

$\gamma_c = j\omega\sqrt{\varepsilon_{e,c}\mu_c} = j\omega\sqrt{\mu_c}\sqrt{\varepsilon_0 \text{-} j\frac{\sigma_c}{\omega}}$, and using $\sigma_c \gg \omega\varepsilon_0$, $\gamma_c \approx j\omega\sqrt{\mu_c}\sqrt{\text{-}j\frac{\sigma_c}{\omega}} = \sqrt{j\omega\mu_c\sigma_c} = \sigma_c Z_{\text{TEM},c} = (1+j)\sqrt{\pi\mu_c f \sigma_c}$. The importance of this result is that it describes the well-known skin effect, that is how the electric current in the conductor is concentrated in its thin surface layer, being rapidly damped to insignificant values by exponential decay with the attenuation constant $\alpha_c = \text{Re}(\gamma_c) = \sqrt{\pi\mu_c f \sigma_c}$. A measure used to quantify this phenomenon is the skin depth, also known as the characteristic depth of penetration, which is the reciprocal of the attenuation constant α_c,

$$\delta_s = \frac{1}{\alpha_c} = \frac{1}{\sqrt{\pi\mu_c f \sigma_c}} = \frac{1}{R_s \sigma_c}. \tag{2.31}$$

It represents the distance from the metal surface at which the field intensity is reduced e times. At the commonly used thickness margin of five skin depths, the field drops to less than 1% of its initial value. Thus, we know what is the minimum thickness of a good conductor we need at a particular microwave frequency for sufficient shielding (prevention of wave being transmitted through the conductor), and can provide diminutive radiation loss that way.

On the other side, regarding calculation of loss in dielectric, Maxwell's equation (2.1b) for a lossy dielectric medium can be generalised as $\nabla \times \mathbf{H} = j\omega(\varepsilon'\text{-}j\varepsilon'')\mathbf{E} + \sigma_d\mathbf{E} = j\omega\varepsilon_{e,d}\mathbf{E}$. (Subscript d denotes that medium parameters refer to the dielectric.) Although it is in the end mathematically formulated in equal way as for good conductor, the in-between step change is made to represent different underlying physical mechanisms in materials. Here, ε'' accounts for bound charge and dipole relaxation phenomena, which give rise to linear-frequency-dependent polarisation loss that dominates at high frequencies. The loss due to the finitely small free charge conduction σ_d is basically frequency independent and dominates at DC and low frequencies. Therefore, equivalent complex permittivity of dielectric is $\varepsilon_{e,d} = \varepsilon_d\text{-}j\frac{\sigma_d}{\omega} = \varepsilon' - j\left(\varepsilon'' + \frac{\sigma_d}{\omega}\right) = \varepsilon'\text{-}j\frac{\sigma_{e,d}}{\omega}$ and its equivalent conductivity is $\sigma_{e,d} = \omega\varepsilon'' + \sigma_d$. In reality, all effects intrinsically act together and give aggregate result that is integrated into dielectric loss tangent $\tan\delta_d = \frac{\varepsilon'' + \sigma_d/\omega}{\varepsilon'}$, a standard measure in dielectric specifications. In the end, power loss per unit length in the dielectric can be obtained as

$$P'_{loss,d} = \int_{St} \sigma_{e,d}|\mathbf{E}|^2 dS. \tag{2.32}$$

Dielectric attenuation constant can directly be found by substituting ε_d with $\varepsilon_{e,d}$ in the expression (2.13) for the propagation constant, $\gamma_d = j\sqrt{\omega^2\varepsilon_{e,d}\mu_0 \text{-} k_c^2} = j\sqrt{\omega^2\varepsilon'\mu_0 \text{-} j\omega\mu_0\sigma_{e,d} \text{-} k_c^2} = j\sqrt{\omega^2\varepsilon'\mu_0 \text{-} k_c^2}\sqrt{1 \text{-} j\frac{\omega\mu_0\sigma_{e,d}}{\omega^2\varepsilon'\mu_0 \text{-} k_c^2}}$. This intuitive result can be verified by using (2.28) with (2.26) and (2.32). Unlike conductor losses, here dissipation occurs in the same volume which is used for propagation of waveguide signal, so by further simplification, it can be shown that there is no dependence from waveguide dimensions other than how they anyway determine the propagation of TE and TM modes by cutoff frequencies. This is in direct connection with Q factor of a cavity coming from dielectric losses depending on nothing else than $\tan\delta_d$.

In a good dielectric $\sigma_{e,d} \ll \omega\varepsilon'$, and by using $\sqrt{1-x} \approx 1-\frac{x}{2}, x \ll 1$ approximation that reduces the function to the first two terms of its Maclaurin series, after transformation $\sqrt{\omega^2\varepsilon'\mu_0 - k_c^2} = \omega\sqrt{\varepsilon'\mu_0}\sqrt{1-\left(\frac{f_c}{f}\right)^2}$, emerges the needed expression for the propagation constant, $\gamma_d \approx \frac{\sigma_{e,d}}{2}\sqrt{\frac{\mu_0}{\varepsilon'}}\frac{1}{\sqrt{1-(f_c/f)^2}} + j\omega\sqrt{\varepsilon'\mu_0}\sqrt{1-\left(\frac{f_c}{f}\right)^2}$. Finally, the attenuation constant is

$$\alpha_d = \text{Re}(\gamma_d) = \frac{\sigma_{e,d}}{2}\sqrt{\frac{\mu_0}{\varepsilon'}}\frac{1}{\sqrt{1-(f_c/f)^2}}. \tag{2.33}$$

Dielectric loss in an air-filled or a gas-filled waveguide is essentially zero. Accordingly, only conductor loss is usually taken into account unless a dielectric-filled waveguide or SIW is considered. Even though in standard applications of all guided wave structures losses in conductors generally dominate over losses in dielectrics, dielectric losses grow more rapidly. As it has been seen in previous equations, dielectric losses are principally proportional to f compared to $\sqrt{f}$ in the case of metals. Therefore, with the frequency rise, they take over in solid materials. That is a reason why waveguides increasingly display advantages over transmission lines like microstrip or coax while approaching millimetre waves.

Likewise, surface roughness is not as big problem in waveguides as in microstrip and other planar lines because conductors are not laminated on dielectric substrates. Nevertheless, at frequencies around 5 GHz deviations from ideally smooth surface introduced during standard fabrication processes start to reduce conductivity because of the skin effect [1-2]. Imperfections comparable to δ_s in size are enough to significantly increase effective surface. As a result, measurements agree less with values of theoretical predictions disregarding surface roughness effect. The loss generated this way rises with frequency and in total can be up to two times higher than the calculated value.

When there are more standard waveguides with overlapping bandwidths from which selection can be made for use at a frequency range of interest, the largest one of them gives the smallest loss as well as the highest power handling capability at the expense of increased size.

2.3.   Waveguide Resonators

Waveguide resonators are nothing else than, ideally, waveguide sections made of PEC and filled with perfect dielectric material, short-circuited on both their ends to form resonant cavities. Unlike transmission line resonators, which are frequently left open-circuited on one or both ends, waveguide resonators are not because open waveguide ends significantly radiate energy. Yet, properties of waveguide (as well as transmission line) resonators are comparable with lumped-element resonant circuit properties, having similar frequency characteristics around the resonant frequency. Hence, LC circuits can be used as their equivalent circuit models. Nevertheless, resonators with distributed elements possess infinite number of discrete resonances, which is not the case with resonators made of inductors and capacitors. In practical applications, however, all higher resonances are usually regarded as spurious, and are initially neglected to simplify the design procedure. (Notable exceptions are when higher order resonances are deliberately used to realize couplings between resonators or in dual- or multi-mode filters.) The unique criterion at the resonant frequency applicable for all resonators is that reactive power in the resonator is zero. The power balance expression for a resonator can be obtained by applying Poynting's theorem to the resonator as the domain. (In

this idealised lossless case, energy stored in EM field of a resonator stays constant without change in time.)

We will use already derived expressions for field inside a waveguide, now taking into account both direct and reflected waves, as well as adding short circuit boundary condition at the beginning and the end of a waveguide section for the total transverse electric field component. For any individual waveguide mode, this reads

$$\mathbf{E}_t = \left[\mathbf{E}_{t0}^+ e^{-j\beta z} + \mathbf{E}_{t0}^- e^{+j\beta z}\right] = 0\,\big|_{z=0,l}, \tag{2.34}$$

where subscript 0 denotes field components at $z = 0$ plane, superscripts $+$ and $-$ denote incident and reflected waves, respectively, and l is the length of the waveguide resonator. Thus, the boundary conditions yield $\mathbf{E}_{t0}^+ = \mathbf{E}_{t0}^-$ and $E_t(l) = -E_{t0}^+ 2j \sin(\beta l) = 0$. This leads to the important conclusion that the length of a waveguide resonator at the resonant frequency of selected type of wave is a natural number multiple of its half-guide wavelength, that is $\beta l = p\pi$, $p = 1,2,3, ...$ (Trivial solution, $E_{t0}^+ = 0$, and non- propagating waves, $\beta \le 0$, are not of interest.) Since the universal expression for the phase constant of all wave types is $\beta = \sqrt{\omega^2 \varepsilon \mu - k_c^2}$, the general formula for the resonant frequency of a resonator is

$$f_r = \frac{1}{2\pi\sqrt{\varepsilon\mu}} \sqrt{k_c^2 + \left(\frac{p\pi}{l}\right)^2}. \tag{2.35}$$

If the problem of finding all EM field components inside a waveguide resonator is completed, it can be seen that entire electric field is in phase. Likewise, all the total magnetic field components are in phase as well. The difference from the 2D waveguide case in which only transverse components have the same phase, is that here a standing wave is formed in the axial direction as well. Furthermore, electric and magnetic field components are in quadrature phase relationship, which verifies the periodic transformation of energy between electric and magnetic ones.

Although fields in resonators are for simplicity and universality reasons calculated without couplings to external circuitry, they are indeed necessary in order to apply waveguide resonators in microwave structures. The presented results are valid for both resonances as input impedance minima and antiresonances as input impedance maxima. Like quarter-wave and half-wave microstrip resonators are basic building blocks of most microstrip filters, half-wave waveguide resonators are basic building blocks of many important waveguide filters.

2.3.1. Rectangular Waveguide Cavities

As a special case of the analysis in the previous section, rectangular waveguide cavities can be viewed as rectangular waveguides short-circuited at both their ends. By using the expressions (2.19)-(2.22) for both incident and reflected waves and applying the PEC boundary conditions at the end walls, full field distribution for idealised lossless rectangular waveguide cavities can be determined. (It is also possible to directly solve (2.3) in combination with PEC boundary conditions from all sides.) After replacing the cutoff wavenumber k_c in (2.35) with the mode numbers of a rectangular waveguide using (2.18), the formula for the resonant frequencies of TE$_{mnp}$ and TM$_{mnp}$ modes analogue to (2.23) emerges:

$$f_r = \frac{1}{2\sqrt{\varepsilon\mu}} \sqrt{\left(\frac{m}{a}\right)^2 + \left(\frac{n}{b}\right)^2 + \left(\frac{p}{l}\right)^2}. \tag{2.36}$$

It should be noted that in the case of rectangular waveguide resonators, having the shape of a rectangular cuboid, there is no fundamental difference between the longitudinal and

transversal directions. In practise, however, usually the natural choice for the length is the longest dimension. Therefore, assuming without loss of generality that $b < a < l$, the dominant resonant mode is the TE_{101} mode (Figure 2.7). Being the mode with the lowest resonant frequency, it corresponds to the TE_{10} dominant rectangular waveguide mode. Besides, as there are no TM modes with the mode numbers $m = 0$ or $n = 0$, neither m or n can be zero for TM modes in rectangular waveguide cavities. Only $l = 0$ is possible, so the dominant TM mode is TM_{110}. One peculiarity about waveguide cavities is that depending on declarative choice of axial direction, physically same resonant modes not only have reshuffled indices, but even change the type between TE and TM. (E.g. the dominant TE_{101} mode coincides with the dominant TM mode, TM_{110}, if the new axial direction becomes what used to be the direction along the waveguide height as its shortest dimension.)
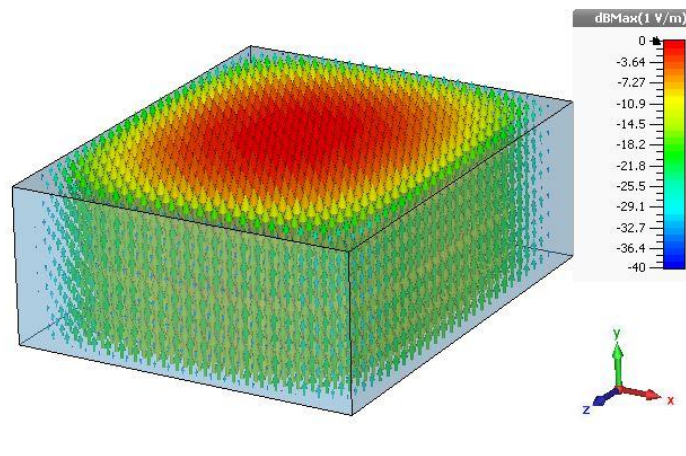
Figure 2.7 Rectangular waveguide cavity with displayed electric field distribution at the resonant frequency of the dominant TE_{101} mode.

In Figure 2.8 is given a mode chart of a rectangular waveguide resonator. It is frequently used in practical designs as a good graphical overview of resonant frequencies belonging to various modes, especially to predict spurious performance of a filter when selecting its resonators. By following vertical grid lines from the bottom to the top (each one of them represents a physical resonator of certain normalized dimensions), the resonant modes can be found in the order as they appear with the increase in frequency. Similarly, by following horizontal grid lines from the left to the right (each one of them represents a certain normalized frequency), the resonant modes can be found as they appear with the increase of waveguide cross section dimensions with a fixed aspect ratio.
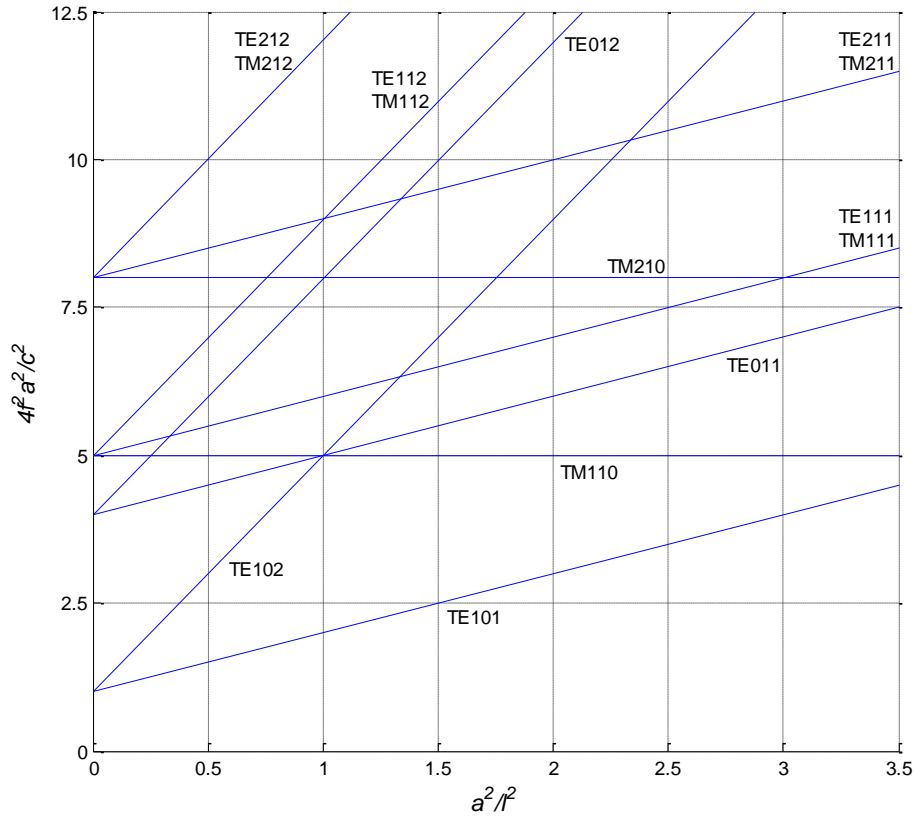
Figure 2.8 Mode chart for a rectangular waveguide resonator with *b=2a* vertical to horizontal side ratio.

2.4. Loss in Waveguide Resonators

Standard way of calculating waveguide resonator loss, just like for waveguides themselves, is once again by using the perturbation method. In the case of resonators, however, it is usually expressed by the quality or *Q* factor. (This dimensionless parameter is not just used for waveguide, transmission line of lumped circuit resonators, but also for optical, acoustical and mechanical ones.) A universal definition of *Q* factor, applicable to any kind of resonant systems, is

$$Q = \omega \frac{W_{tot}}{P_{loss}}, \tag{2.37}$$

where W_{tot} is the average energy stored in the system and P_{loss} is the energy loss per second in it. For a waveguide resonator, W_{tot} can be found by integrating electric or magnetic energy density in the volume of the resonator. More precisely, $W_{tot} = W_{e,\max} = W_{m,\max}$, where $W_{e,\max} = \int_V \varepsilon|\mathbf{E}|^2 dV$ is the maximum energy stored in the electric field and $W_{m,\max} = \int_V \mu|\mathbf{H}|^2 dV$ is the maximum energy stored in the magnetic field. On the other side, P_{loss} can be found by calculating the conductor and dielectric losses according to the procedures outlined in the chapter 2.2, applied to a waveguide resonator geometry. The higher the *Q* factor is, the less lossy (damped) the resonator is.

In relation to what has been said about comparison of losses in different types of wave-guiding structures, it should not come as surprise that waveguide resonators have higher *Q* factors than coaxial resonators, even more than microstrip and other planar resonators, and

further more than lumped element ones, of course, at the expense of larger volume. Very big Q factors, at the order of thousands, can also be achieved by inserting dielectric resonators into waveguide cavities, since very low loss dielectric materials are now available for this purpose.

The type of Q factor that has been considered so far is the so-called unloaded Q factor. It represents an intrinsic characteristic of a resonator itself. However, since in practical applications a resonator has to be coupled to external circuitry, a different Q factor which represents the entire structure of a loaded resonator is introduced. It is known as the loaded Q factor, denoted Q_L, and is connected with the unloaded Q trough $\frac{1}{Q_L} = \frac{1}{Q} + \frac{1}{Q_e}$. Here, Q_e is the Q factor of the external circuitry loaded onto the resonator, also known as the external Q factor. As it might be expected, the loaded Q factor can't have any value higher than the unloaded Q factor. It should be noted that Q_L is inversely proportional to the fractional bandwidth of the resonator's frequency response.

References

[2-1]   J. Uher, J. Bornemann, and U. Rosenberg, *Waveguide Components for Antenna Feed Systems: Theory and CAD*. Boston: Artech House Publishers, 1993.

[2-2]   Institute of Electrical and Electronics Engineers Content Provider, *IEEE 100: the authoritative dictionary of IEEE standards terms*, Seventh Edition, IEEE Press, 2000.

[2-3]   R. Marques, J. Martel, F. Mesa, and F. Medina, "Left-handed-media simulation and transmission of EM waves in subwavelength split ring resonator-loaded metallic waveguides," *Phys. Rev. Lett.*, vol. 89, no. 18, pp. 183901–183904, Oct. 2002.

[2-4]   I. Kallfass, "300 GHz Fixed Wireless Links," Millimetre-Wave Technologies for 5G Mobile Networks and Short-Range Communications Workshop (WF03), *46th European Microwave Conference (EuMC 2016)*, London, 2016.

[2-5]   Project TERAPAN, Available: www.terapan.de

[2-6]   B. Zhang, Y. X. Guo, H. Zirath and Y. P. Zhang, "Investigation on 3-D-Printing Technologies for Millimeter- Wave and Terahertz Applications," *Proceedings of the IEEE*, vol. 105, no. 4, pp. 723-736, April 2017.

[2-7]   H. Uchimura, T. Takenoshita and M. Fujii, "Development of a "laminated waveguide"," *IEEE Transactions on Microwave Theory and Techniques*, vol. 46, no. 12, pp. 2438-2443, Dec 1998.

[2-8]   Ke Wu, D. Deslandes and Y. Cassivi, "The substrate integrated circuits - a new concept for high-frequency electronics and optoelectronics," *6th International Conference on Telecommunications in Modern Satellite, Cable and Broadcasting Service, 2003. TELSIKS 2003.*, 2003, pp. P-III-P-X vol.1.

[2-9]   F. Xu and K. Wu, "Guided-wave and leakage characteristics of substrate integrated waveguide," *IEEE Trans. Microw. Theory Tech.*, vol. 53, no. 1, pp. 66–73, Jan. 2005.

[2-10]   N. Grigoropoulos, B. Sanz-Izquierdo and P. R. Young, "Substrate integrated folded waveguides (SIFW) and filters," *IEEE Microwave and Wireless Components Letters*, vol. 15, no. 12, pp. 829-831, Dec. 2005.

[2-11]   A. Berenguer, V. Fusco, D. E. Zelenchuk, D. Sánchez-Escuderos, M. Baquero-Escudero and V. E. Boria-Esbert, "Propagation Characteristics of Groove Gap Waveguide Below and Above Cutoff," *IEEE Transactions on Microwave Theory and Techniques*, vol. 64, no. 1, pp. 27-36, Jan. 2016.

[2-12]   M. Swaminathan, E. Arvas, T. P. Sarkar, A. R. Djordjevic, "Computation of cutoff wavenumbers of TE and TM modes in waveguides of arbitrary cross sections using a surface integral formulation," *IEEE Trans. Microwave Theory Tech.*, vol. 38, no. 2, Feb. 1990.

[2-13]   V. Tornielli di Crestvolant and F. De Paolis, "Dimensional Synthesis of Evanescent-Mode Ridge Waveguide Bandpass Filters," *IEEE Transactions on Microwave Theory and Techniques*, vol. PP, no. 99, pp. 1-8.

[2-14]   MOD UK DEF-5351, "Specification for Tubing, Waveguide"; *Standard of the Ministry of Defence of the United Kingdom*, June 1959, incorporating Amendments Nos. 1 (1960) to 6 (1974).

[2-15]   EIA RS-261-B, "Rectangular Waveguides (WR3 to WR2300)", *Standard of the Electronic Industries Association of the United States of America*, May 1979.

[2-16]   IEC 60153-2:2016, "Hollow metallic waveguides - Part 2: Relevant specifications for ordinary rectangular waveguides", *Standard of the International Electrotechnical Commission*, May 2016.

[2-17]   Waveguide and Flange Data, Available: www.flann.com

[2-18]   Technical Information TD-00077, Available: www.spinner-group.com

[2-19]   IEC 60154-2:2016, "Flanges for waveguides - Part 2: Relevant specifications for flanges for ordinary rectangular waveguides", *Standard of the International Electrotechnical Commission*, July 2016.

3. Filter Networks

Full-wave electromagnetic analysis built on Maxwell's equations gives complete background theory for all the problems of interest for us[12]. Nevertheless, for practical purposes of comprehending problems and making new designs, the higher level of abstraction of electric circuits has been developed to reduce complexity of the models at the cost of reduced accuracy. How the laws that apply to electrical networks connecting circuit quantities (having integral relationship with the field quantities) can be derived from the Maxwell's equations can be found in the chapter 1 of [1-15].

The concept of idealised electrical elements assumes deliberately removing all nonessential properties of real electrical components to suit mathematical operations. In LLFPB (Lumped, Linear, Finite, Passive and Bilateral) networks, which analog non-active low-frequency filter circuits belong to, resistors, capacitors, inductors and transformers are used. If we analyse these networks using mesh or nodal analysis, we can directly see that system functions belong to the group of rational functions [1-28], chapter 2. Obviously, the lumped condition has to be eventually removed for microwave circuits, nevertheless, most of the concepts still apply, at least approximately.

In figure 3.1, electrical network is presented from the system theory standpoint in the realm of Laplace transform. A transfer function, *H(s)*, of a LLFPB network is the quotient of some output function of the complex frequency and some input function of the complex frequency, giving a rational function
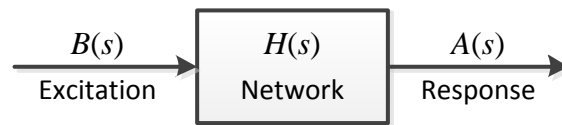
Figure 3.1 Block diagram of an electrical network showing relationship between the three key terms: the network, the excitation and the response.

$$H(s) = \frac{a_n s^n + a_{n-1} s^{n-1} + \cdots + a_1 s + a_0}{b_m s^m + b_{m-1} s^{m-1} + \cdots + b_1 s + b_0}. \tag{3.1}$$

We only specified the domain of the excitation and the response, so there is large freedom of their choices (they can be at the same or different ports, they can represent the same or different physical quantities, etc.). However, their order in the quotient, which one is the dividend and which one is the divisor, is strict. This is because there is an essential difference between the zeros of the denominator, representing fundamental natural frequencies of the entire electrical circuit, and the zeros of the numerator, representing frequencies at which there is no signal transfer between the two of selected network ports.

From this generalized system view, it is also useful to define network analysis as finding the response function when the excitation and the network functions are known. Network

---

[12] Classical electrodynamics can explain all of known electromagnetic phenomena (not exactly, but with excellent accuracy) down to the scale of quantum ones, which are encompassed as well by the quantum electrodynamics (QED). This makes electromagnetic force the best studied of all the fundamental physical interactions and QED the most complete physical theory, which Richard Feynman called the jewel of physics. Maxwell's equations actually motivated Einstein's development of the special theory of relativity, meaning implicit compatibility, and need for preceding theories (Newtonian mechanics) to be corrected.

analysis has a unique solution. Conversely, network synthesis is finding the network function when the excitation and response functions are known. Network synthesis may not have a solution at all, and if it exists, it is not unique. It turns out from the study of the realizability theory that not all transfer functions can be implemented in real time through real circuit elements. The fundamental restrictions are causality and stability [1-30], chapter 10. They are easier formulated in the time domain, but we are interested in their frequency domain outcomes.

Causality

Even though causality is implied by stability knowing that LLFPB networks already have transfer functions restricted to the rational functions, the causality requirements are highlighted in order to have clearer picture of the essential design restrictions. A system is causal if the response is independent of future excitations, that is if the input signal $B(t) = 0$, $t < t_0$, then the output signal $A(t) = 0$, $t < t_0$. In other words, the impulse response of the network must satisfy $h(t) = 0$, $t < 0$. Regarding the frequency domain, the Paley-Wiener criterion states that a necessary and sufficient condition for a system to be causal is

$$\int_{-\infty}^{\infty} \frac{|\log|H(j\omega)||}{1+\omega^2} d\omega < \infty, \tag{3.2}$$

where $|H(j\omega)|$ is the amplitude function of the system. Preconditions are that the impulse response of the system must have Fourier transform and that $|H(j\omega)|^2$ is integrable. Corollaries of the Paley-Wiener criterion are that amplitude function $|H(j\omega)|$ cannot be zero over a finite frequency band (only discrete points) and that it cannot fall off to zero faster than exponentially.

Stability

Here we assume bounded-input, bounded-output (BIBO) stability, which in the time domain means that if at any time t for the input signal amplitude it holds $|B(t)| < C_1$, then the output signal amplitude satisfies $|A(t)| < C_2$, where C_1 and C_2 are real and positive finite constants. For the impulse response a stable system means that it has to be absolutely integrable, $\int_{-\infty}^{\infty} |h(t)| dt < \infty$.

Moving to the frequency domain, stability conditions for the transfer function are as follows:

1) $H(s)$ does not have poles in the (strictly) right-half of the complex plane.

2) $H(s)$ does not have multiple poles on the imaginary axis.

3) The degree of $H(s)$ numerator, n, cannot exceed $H(s)$ denominator, m, by more than one, $n - m \leq 1$.

(Conditions 2) and 3) are actually not independent, as 3) can be derived from 2) at the infinity point, which also belongs to the imaginary axis.) Condition 1) is intuitive as stable networks cannot have infinite response if the excitation is a unilateral damped sinusoid. Further to the distinction between the numerator and denominator of the transfer function, we can again see that stability is only influenced by the zeroes of the denominator polynomial (i.e. natural modes of vibration) and that there are no restrictions regarding the zeros of the numerator polynomial.

Although it is not feasible to realize them in reality, ideal elements like capacitors and inductors are crucial for theoretical analysis. Hence they are not removed from consideration, even though their impulse responses are not absolutely integrable, but just bounded for all t. Such networks are referred to as marginally stable. This enables having individual singularities on the very imaginary axis.

The denominator of the system function, described purely in terms of its zeros to be located in the left half of the complex frequency plane with only simple zeros permitted on the $j\omega$ axis, is a Hurwitz polynomial $E(s)$, which can defined by:

1) $(\forall s \in \mathbb{R})\ E(s) \in \mathbb{R}$ (This statement is equivalent to all polynomial coefficients being real.) and

2) $(\forall s_i, E(s_i) = 0)\ \text{Re}(s_i) \leq 0$.

Hurwitz polynomials have several other important properties:

Grouped into three types or roots (real, imaginary with conjugate pairs and complex with conjugate pairs, the latter two always existing together according to the complex conjugate root theorem since $E(s)$ is a polynomial with real coefficients), Hurwitz polynomials can be factored as $E(s) = \prod_i (s + \gamma_i) \cdot \prod_i (s^2 + \omega_i{}^2) \cdot \prod_i ((s + \alpha_i)^2 + \beta_i{}^2)$, where $\gamma_i, \omega_i, \alpha_i, \beta_i \in \mathbb{R}$ and $\gamma_i, \alpha_i > 0$. Because all the coefficients in factors of $E(s)$ are positive, it comes that all coefficients of a Hurwitz polynomial $E(s)$ are also positive.

Factors $(s^2 + \omega_i{}^2)$ formed by purely imaginary zeros create even polynomials and when additionally being multiplied by s (zero at the origin), odd polynomials. Factors $(s + \gamma_i)$ and $((s + \alpha_i)^2 + \beta_i{}^2)$ create polynomials with no terms missing between the one with the highest degree and zero degree. Thus, $(\forall i \in \{1,2,\dots,N\}, N = \deg(E(s)))\ s_i \neq 0$ if $E(s)$ is neither even nor odd polynomial.

In addition, if a Hurwitz polynomial $E(s)$ is split into the even polynomial $e(s)$ and the odd polynomial $o(s)$ parts, both $e(s)$ and $o(s)$ have only purely imaginary zeros. When the function $\Psi(s) = \frac{o(s)}{e(s)} = \frac{E(s) + E(-s)}{E(s) - E(-s)} = \frac{E(s)/E(-s) + 1}{E(s)/E(-s) - 1}$ is formed, it belongs to the positive real (PR) class of functions. Positive real function, $PR(s)$, of great importance in synthesis of electrical networks, is defined by the conditions:

1) $(\forall s \in \mathbb{R})\ PR(s) \in \mathbb{R}$,

2) $(\forall s \in \mathbb{C}, \text{Re}\ s \geq 0)\ \text{Re}\ PR(s) \geq 0$.

To prove PR characteristics, it can first be shown that $\left| \frac{E(s)}{E(-s)} \right| \geq 1$ [1-28], sec. 4.2. Hence, when $\Psi(s)$ is represented in the form of continuous fractions, all of its coefficients have to be positive. This is used for testing if a given polynomial is a Hurwitz one without the need to find the roots of the polynomial.

As a special case of universal transfer function, classical synthesis procedures use input (driving-point) immittance function to develop the network extracting one element at a time from it and updating the immittance function form to represent the remainder of the network. Every network can be represented in this way while closing other ports with their nominal impedances. (One-port networks per se are actually not of greatest practical interest.) In

addition, the input reflection coefficient can be directly found from the input and source immittances. Input immittance functions have characteristics of PR functions. After extraction of any element from the preceding input immittance, the remaining immittance is still a PR function. It should be also noted that for the input immittance there is symmetry between the numerator and denominator polynomials, since reciprocal value of input impedance is input admittance, which have completely dual properties. Hence, the PR rational functions have symmetric properties with respect to their numerators and denominators.

In addition to (real or equivalent) transmission lines being used in microwave filter networks, resulting in infinite number of poles and zeros appearing in their transfer functions, immitance inverter elements are usually found instead of transformers. There is one more element used, called frequency-invariant reactance (FIR), which in fact cannot be practically realized, but serves its purpose in lowpass prototype filter circuits so that after transformations into passband or stopband filters they can also have asymmetric responses with respect to the centres of their passbands/stopbands [1-51], sec. 3.10. The use of FIR elements changes the character of input immittance from positive real to only positive function, since transfer functions now can have complex coefficients.

There are many types of parameters used to describe electrical networks with one or more ports. Although they have no influence whatsoever on fundamental characteristics of networks, like with different languages, network properties and interconnections are expressed in different ways and with different levels of difficulty within different types of parameters. For example, impedance (Z), admittance (Y), hybrid (h) and inverse hybrid (g) parameters are naturally used for 2-port lumped element networks connected in series, parallel, series-parallel and parallel-series respectively [1-29]. ABCD-parameter are the most suitable ones when it comes to cascading 2-port networks, since the resulting ABCD matrix can be acquired only by multiplying matrices of individual networks in that chain. This makes ABCD-parameter frequently used to describe filter networks. Scattering (S) and transfer (T) parameters, on the other hand, are more commonly seen used to characterize distributed element circuits. Direct conversions between all the aforementioned network parameters are possible.

3.1.   S-parameters

S-parameters [3-1] are unitless and give relationships between input and output signals based on powers, meaning that they come more natural at high frequencies than parameters based on currents and voltages, difficult of impossible to physically define and measure. More precisely, the basic matrix equation of S-parameters for an *N*-port network takes the form $[b]_{N,1} = [s]_{N,N} \cdot [a]_{N,1}$, with indices of S-parameters being in to-from port order. The incident power waves, a_i, and the reflected power waves, b_i, satisfy relations $P_{in,i} = |a_i|^2$ and $P_{out,i} = |b_i|^2$ for the input and output powers at the port i. Microwave filter networks are reciprocal and because of relatively small losses are modelled as lossless during synthesis, so it is of interest to see how are these properties represented by the S-parameters.

Reciprocity

Directly from the reciprocity definition, for each pair of network ports, $s_{ij} = s_{ji}$. In other words, the scattering parameter matrix is symmetrical with respect to the main diagonal.

Lossless networks

If a network is lossless, it means that when power enters a port, the total power exiting all the ports will equal it. For instance, if there is no input at port 2 ($a_2 = 0$), then, $b_1 = s_{11}a_1$, $b_2 = s_{21}a_1$ and $|b_1|^2 + |b_2|^2 = |a_1|^2$. This can be reduced to the expression involving only S-parameters when the first two equations are substituted into the third one and a_1 cancelled. Using the same logic, this can be generalised into a matrix equation of the summation form

$$\sum_{k=1}^{N} s_{ki} \cdot s_{kj}^* = \delta_{ij}, \tag{3.3}$$

where $\delta_{ij} = \begin{cases} 1, & i = j \\ 0, & i \neq j \end{cases}$ is a Kronecker delta symbol. In other words, the scalar products of columns with conjugates of themselves are unity (vectors are of length one), whereas scalar products of columns with conjugates of different matrix columns are zero (vectors are orthogonal). In expanded form for a 2-port network, (3.3) gives

$$s_{11}s_{11}^* + s_{21}s_{21}^* = 1,$$

$$s_{12}s_{12}^* + s_{22}s_{22}^* = 1,$$

$$s_{11}s_{12}^* + s_{21}s_{22}^* = 0.$$

Another interesting result in connection with lossless 2-port networks is that the reflection S-parameters need to satisfy $|s_{11}| = |s_{22}|$ even when the network is not symmetrical, although their arguments do not need to be equal, but to satisfy $\theta_{21} - \frac{\theta_{11}+\theta_{22}}{2} = \frac{\pi}{2}(2k + 1)$, k being integer, equality [1-51], sec. 6.1.

For 2-port lossless passive linear filter networks that are primarily of interest here, we can write $s_{11} = \frac{F(s)}{E(s)}$ and $s_{21} = \frac{P(s)}{E(s)}$, which are related by $|s_{11}(s)|^2 + |s_{21}(s)|^2 = \frac{|F(s)|^2+|P(s)|^2}{|E(s)|^2} = 1$. $F(s)$, $P(s)$ and $E(s)$[13] are so-called characteristic polynomials and are of particular importance [1-51], sec. 3.2. It is practical to see $F(s)$, which real frequency zeros are called reflection zeros or transmission poles (TPs), and $P(s)$, which real frequency zeros are called transmission zeros (TZs) or reflection poles as the starting polynomials that carry entire essential information with them, and $E(s)$ as a derived polynomial, which is important in giving the response shape for the filter parameters we can measure. Polynomial $F(s)$ has real coefficients and its zeros lie on the imaginary axis in conjugate pairs, with multiple roots restricted to the origin. Polynomial $P(s)$ has real coefficients as well, with its zeros not only in conjugate pairs on the imaginary axis, but also in pairs on the real axis or as complex quads in the complex frequency plane. Consequently, $F(s)$ is a pure even or pure odd polynomial, whereas $P(s)$ can be only pure even polynomial. Characteristic polynomial $E(s)$ is obviously a Hurwitz polynomial as it is denominator of transfer functions.

---

[13] Not knowing the reason for the original selection of the letters representing the characteristic polynomials, words First, Plural and Every were found as suitable mnemonics.

Considering that filter networks are typically optimized so that from the power available from the source, $P_1 = P_{\max}$, the power delivered to the load, P_2, is maximised, then the transmission (transducer) function $H(s) = \frac{E(s)}{P(s)}$ satisfies the equalities:

$$|H(s)|^2_{s=j\omega} = \frac{P_{\max}}{P_2} = 1 + |K(s)|^2_{s=j\omega} = \frac{1}{|s_{21}(s)|^2_{s=j\omega}} = \frac{1}{1-|s_{11}(s)|^2_{s=j\omega}}, \qquad (3.4)$$

on one side having natural physical interpretation through powers of interest and bounded values by $P_{\max} = \frac{E_g^2}{4R_1} \geq P_2$, and on the other side being directly linked with the S-parameters. Here, $K(s) = \frac{F(s)}{P(s)}$ is a characteristic rational function for which are typically used well-known approximation functions like Butterworth, Chebyshev, elliptic, Bessel, etc. $K(s)$ contains both 'information' polynomials $F(s)$ and $P(s)$, so we have complete description of the filter's key response parameters in explicit form in only one function, however, it represents mathematical construction rather than a measurable quantity.

One very handy characteristic of filter networks is that different types of them, namely lowpass filter (LPF), highpass filter (HPF), bandpass filter (BPF) and bandstop filter (BSF), all share common fundamental characteristics and can be easily mathematically transformed from one into another. As the common model is most often used the lowpass prototype − a lowpass filter with dimensionless normalized parameters.

3.2.   Approximations

Typical filter design starts with approximating ideal filter frequency response in such a way that the specification is fulfilled. For this purpose, we use approximation functions [3-2] - mathematical functions which are responses of filter networks realisable using ideal circuit elements. Approximation of a filter function can be guided by countless error criteria, such as forcing the curve to pass through fixed points [1-28], sec. 1.1, or the method of least squares. Nevertheless, the approximation theory is well developed and there is limited number of solutions used in most cases. Thus, in most real-world problems, approximation theory is basically reduced to just following well-known rules of selected approximation function in order to calculate the filter response. For example, for Butterworth and Chebyshev filter functions, the shapes of the lowpass prototype passband amplitudes are instantly known together with their bound values. The former has maximally flat passband at the origin, $F(s) = s^N$, and the latter equiripple passband, $F(s) = \cos\left(N\arccos(s/j)\right)$. It is also known that the stopbands have monotonic increase in rejection. (Both approximations have maximally flat stopbands, having TZs only at the infinity, $P(s) = 1$, for which reason they are called all-pole approximations.) What is left is to find is the filter order to satisfy required attenuation minimum, which can also be analytically calculated, but often in practice it is easier to solve the problem iteratively increasing the filter order. In addition, these two filter functions are the only ones with closed-form expressions for g element values [1-48], ch. 4, that enable direct synthesis of filter networks.

Furthermore, there are synthesis methods of generalised Chebyshev filter functions. Important class of them are responses with prescribed finite TZs and equiripple in the passband [1-51], sec. 6.3. Unlike elliptic rational functions, which, symmetrically to the

passband, define the stopband with minimum insertion loss from the stopband cutoff frequency, when this filter functions are used, the stopband is defined by exact position of TZ frequencies. It is shown that the characteristic function in their case is in the form

$$K(\omega) = \cosh \left[\sum_{i=1}^{N} \text{arccosh} \left(\frac{\omega - 1/\omega_i}{1 - \omega/\omega_i} \right) \right], \tag{3.5}$$

where ω_i are the angular frequencies of all the transmission zeros, including those in the infinity, hence their total number is equal to the filter order N. The function in the argument $x_i(\omega) = \frac{\omega - 1/\omega_i}{1 - \omega/\omega_i}$ is found through satisfying the conditions $x_i(\omega) = \begin{cases} \pm\infty, & \omega = \omega_i \\ \pm 1, & \omega = \pm 1 \end{cases}$ and $(\forall \omega \in [-1,1])$ $-1 \leq x_i(\omega) \leq 1$. Expression (3.5) is sufficient for plotting the filter response, however, to be able to continue with the procedure of filter element synthesis, we need to find its equivalent as a rational function. After several transformations, (3.5) is taken to the form

$$K(\omega) = \frac{1}{2} \left[\frac{\prod_{i=1}^{N}(c_i + d_i) + \prod_{i=1}^{N}(c_i - d_i)}{\prod_{i=1}^{N}(1 - \omega/\omega_i)} \right], \tag{3.6}$$

where $c_i = \omega - 1/\omega_i$ and $d_i = \omega' \sqrt{1 - 1/\omega_i^2}$, $\omega' = \sqrt{\omega^2 - 1}$.

In [1-51], sec. 6.3, recursive technique is used to determine $F(\omega)$ polynomial, i.e. the numerator of (3.6). Here, a conceptually clearer approach is used to directly select only the terms from the numerator that don't cancel each other. It can be noticed that the numerator in (3.6) is composed only of terms that have all different indexes, from 1 to N, either of c_i or d_i, and that all of them have even number of d_i factors. Hence, each of these terms can be represented by a binary number, with each c_i being 0 and each d_i being 1 at the location of the i-th bit. The number of bits is then equal to the filter order and sum of all ones in the binary number is an even number. For example, the term $d_1 c_2 d_3 c_4$ can be represented as 1010. Thus, any such binary number can be used as a mask applied to the $d_1 d_2 \ldots d_N$ vector and the negation of that binary number as a mask applied to $c_1 c_2 \ldots c_N$ vector to choose factors in each term of the sum that forms $F(\omega)$. In addition, since it is known that each term can contain just even order of ω', all such intermediate polynomials can be calculated in advance and multiplied when needed. In Appendix B is given a MATLAB script that finds $F(\omega)$ using the outlined procedure.

Finally, computer-aided optimization techniques can come as close as necessary, if the filter order is increased enough, to any other response for which analytical techniques do not exist [1-51], ch. 4. For typical conditions like maximum passband and minimum stopband insertion loss, optimization is also needed in the general case to find appropriate pole and zero positions. This can be extended to the general case of multi-band filters [3-4], although for special symmetrical cases it is not necessary [1-51], sec. 6.5.

When poles and zeros have fixed positions, the only other adjustment that can be made to the filter response is along the y-axis through ε and ε_R coefficient, where the former is used for transmission response and the latter for rejection response. Regarding ripple factors for both conventional and generalized Chebyshev responses, since the characteristic functions are constrained by $|K(j\omega)| \leq 1$ in the normalized passband $-1 \leq \omega \leq 1$, from $s_{11}(j\omega) = \frac{\varepsilon^2 |K(j\omega)|^2}{1 + \varepsilon^2 |K(j\omega)|^2}$ it follows that the minimum return loss in the passband is $RL = -10 \log \left(\frac{\varepsilon^2}{1 + \varepsilon^2} \right) =$

$10 \log \left(1 + \frac{1}{\varepsilon^2}\right)$. Hence, the ripple factor can be calculated from the permitted passband return loss by the equation $\varepsilon = \dfrac{1}{\sqrt{10^{\frac{RL}{10}}-1}}$.

This determines the return loss RL, which is typically at least 20 dB, for which $\varepsilon = 0.1005$, in the entire normalized passband [-1,1], having exactly $s_{11}(\pm 1) = -RL$ on the slopes in transitions between the passband and the stopbands. For unit ripple factor ($\varepsilon = 1$), $RL = -s_{11}(\pm 1) = 3$ dB. That is, the [-1,1] passband is half-power. (This can easily be verified by plugging the value for ε in the previous expression for RL.)

In other situations, ε is differently defined, such as by $F(s)$ and $P(s)$ both having unit leading coefficients [1-51], equation (3.26). This changes the mentioned notions about the ripple factor values typical for Chebyshev responses coming from Chebyshev polynomial values. In addition, there is a tradeoff between improving the minimum return loss in the passband and minimum insertion loss in the stopband. Both are desirable, but increasing one reduces the other.

3.3. Frequency and Element Transformations of Scaled Filter Networks

Transformation of normalized lowpass prototype filter response into scaled lowpass one comprises of only linear frequency scaling. In the related element transformations, impedance scaling with the factor related to network port impedances is additionally present [3-3], sec. 3.3.

Of main concern for us is transformation of lowpass prototype filter to bandpass filter, characterized by the frequency transformation

$$\Omega = \frac{1}{FBW}\left(\frac{\omega}{\omega_0} - \frac{\omega_0}{\omega}\right) = \frac{1}{f_2 - f_1}\left(f - \frac{f_1 f_2}{f}\right), \tag{3.7}$$

where Ω is the normalized frequency of lowpass prototype ($\Omega_C = 1$), ω is the unnormalized angular frequency, $\omega_0 = \sqrt{\omega_1 \omega_2}$ is the bandcentre angular frequency, f is the unnormalized linear frequency, f_1 and f_2 are the lower and upper passband edge frequencies, and $FBW = \frac{f_2 - f_1}{f_0}$ is the fractional bandwidth.

Although it may seem that this transformation can be achieved only by translation and uniform scaling, realisable systems need to have symmetrical response between the negative and positive real frequencies (have axial symmetry with respect to the real axis), so the bandpass filter response graphically has to resemble the spectrum of a modulated signal. Hence, the relation between the real frequency and the filter prototype frequency is given by a quadratic equation, namely $f^2 - \Delta f \, \Omega \, f - f_0^2 = 0$, where $\Delta f = f_2 - f_1$ and $f_0 = \sqrt{f_1 f_2}$. Representative frequency points from this equation are listed in Table 3.1.

Table 3.1 Mapping of the critical frequencies between the bandpass and lowpass prototype filters connected by the equation (3.5).

Real freq. f<0	$-f_2$	$-f_1$	$-f_0$	$\rightarrow -\infty$	$\rightarrow -0$
Real freq. f>0	f_1	f_2	f_0	$\rightarrow +\infty$	$\rightarrow +0$
Prot. freq. Ω	-1	1	0	$\rightarrow \mp\infty$	$\rightarrow \pm\infty$

It is interesting to notice that both the zero and the infinity frequency points in the bandpass response are mapped from the frequency infinity point in the lowpass prototype. Let us take the example of a series LC circuit, which can also be a part of a lowpass filter producing a TZ. As it has infinite impedances at 0 and $+\infty$ frequencies and only one zero impedance at the resonant frequency, it may seem that the number of poles and zeros are not the same. However, this rule is not violated. There are indeed two of each in total, as $\pm\infty$ are the same point in infinity, like it is graphically represented on the Smith chart, and $-f_0$ resonant frequency also has to be included in the count of zero impedances.

Since the function that associates f to Ω is not one-to-one (injective), there is not inverse function in the strict mathematical sense of a well-defined function having exactly one output for each input. Hence, $f^+ = \sqrt{\left(\frac{\Delta f}{2}\right)^2 \Omega^2 + f_0^2} + \frac{\Delta f}{2}\Omega$ is the function that maps the lowpass prototype frequencies to the positive real frequencies, and $f^- = -\sqrt{\left(\frac{\Delta f}{2}\right)^2 \Omega^2 + f_0^2} + \frac{\Delta f}{2}\Omega$ is the function that maps the lowpass prototype frequencies to the negative real frequencies. It can be easily noticed that the expression for f^+ is always positive and expression for f^- always negative because there is relation between the addend under the square root and the second one is $\sqrt{\left(\frac{\Delta f}{2}\right)^2 \Omega^2 + f_0^2} > \sqrt{\left(\frac{\Delta f}{2}\right)^2 \Omega^2} = \left|\frac{\Delta f}{2}\Omega\right|$.

The LPF to BPF mapping can be used in more general cases, like with asymmetric responses. However, $f_0 = \sqrt{f_1 f_2}$ may not hold any more and variables may change their meaning. For example, if just the lowpass passband centre needs to be shifted to a particular frequency and TZ position is important, Ω_c (normalized cutoff frequency) becomes the TZ baseband frequency. On the other side, if Ω_1 and Ω_2 are generalised edges of the prototype passband which need to be transformed into f_1 and f_2, mapping is determined by the ratio $\frac{\Omega_1}{\Omega_2} = \frac{f_1 - \frac{f_0^2}{f_1}}{f_2 - \frac{f_0^2}{f_2}} = \frac{f_2}{f_1}\frac{f_1^2 - f_0^2}{f_2^2 - f_0^2}$, since scaling relative to the centre point represented by geometric mean needs to be preserved. Expanding this further,

$$\Omega_1 f_1 (f_2^2 - f_0^2) = \Omega_2 f_2 (f_1^2 - f_0^2),$$

$$f_0^2 (\Omega_2 f_2 - \Omega_1 f_1) = f_1 f_2 (\Omega_2 f_1 - \Omega_1 f_2), \text{ and}$$

$$f_0^2 = f_1 f_2 \frac{\Omega_2 f_1 - \Omega_1 f_2}{\Omega_2 f_2 - \Omega_1 f_1}. \tag{3.8}$$

It can be verified that in the special case when $\Omega_1 = -\Omega_2$ the equation (3.6) is reduced to $f_0^2 = f_1 f_2$.

BPF element transformations map prototype LPF inductors to series LC resonant circuits and prototype LPF capacitors to parallel LC resonant circuits.

Regarding other types of transformations, highpass filter transformations are analogue to lowpass ones, with inverse frequency transformation and individual circuit element

immittances, as well as duality of using L/C elements. Likewise, stopband filter transformations are analogue to bandpass ones, with inverse frequency transformation and circuit element immittances, as well as duality of using series/parallel LC resonators.

References

[3-1]   K. Kurokawa, "Power Waves and the Scattering Matrix," *IEEE Transactions on Microwave Theory and Techniques*, vol. 13, no. 2, pp. 194-202, Mar 1965.

[3-2]   R. W. Daniels, *Approximation methods for electronic filter design*, New York: McGraw-Hill, 1974.

[3-3]   J.-S. Hong and M. J. Lancaster, *Microstrip Filters for RF/Microwave Applications*, John Wiley & Sons. Inc. New York, 2001

[3-4]   S. Bila, R. J. Cameron, P. Lenoir, V. Lunot and F. Seyfert, "Chebyshev Synthesis for Multi-Band Microwave Filters," *2006 IEEE MTT-S International Microwave Symposium Digest*, San Francisco, CA, 2006.

4. Compact E-plane Waveguide Bandpass Filters

In [4-1], Konishi and Uenakada proposed the use of metal E-plane inserts for implementation of direct-coupled waveguide filters [1-33], which marked the beginning of the E-plane filter technology. E-plane technology has benefits of being inexpensive and having mass producible capabilities. Such an idealised lossless all-pole 5th order E-plane filter is presented in Figure 4.1, with the dimensions described in the Table 4.1. WR19 EIA standard rectangular waveguide housing is used, whereas the thickness of the E-plane metal insert is 0.1 mm. Typical property that metallic septa which are closer to the filter centre are wider, meaning reduced coupling, is noticeable.
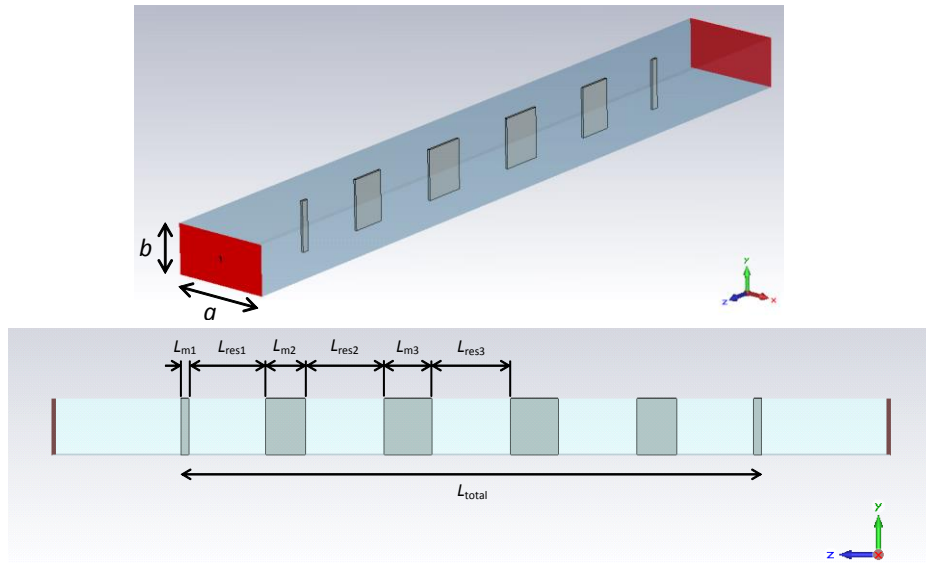
Figure 4.1 Layout of the designed V band E-plane filter.

Table 4.1 Dimensions of the designed V band E-plane filter

Dimension	L_{m1}	L_{m2}	L_{m3}	L_{res1}	L_{res2}	L_{res3}	a	b	L_{total}
Length [mm]	0.340	1.718	2.058	3.309	3.392	3.393	4.776	2.388	25.027

This filter was designed and optimized to satisfy the specifications outlined in the Table **4.2** for future Huawei 5G mobile base stations working in millimeter frequency range. The simulated S-parameter Chebyshev responses graph is displayed in Figure 4.2, showing fulfilment on the given constraints.

Table 4.2 Future 5G mobile base station filter specification

Frequency Band	Passband	Lower Stopband	Upper Stopband
Upper – Lower Limit	45.5 GHz – 47.0 GHz	37 GHz – 43.5 GHz	50.4 GHz – 52.6 GHz
Insertion Loss, L_I	< 1.8÷2 dB	> 40 dB	> 40 dB
Return Loss, L_R	> 18 dB	-	-
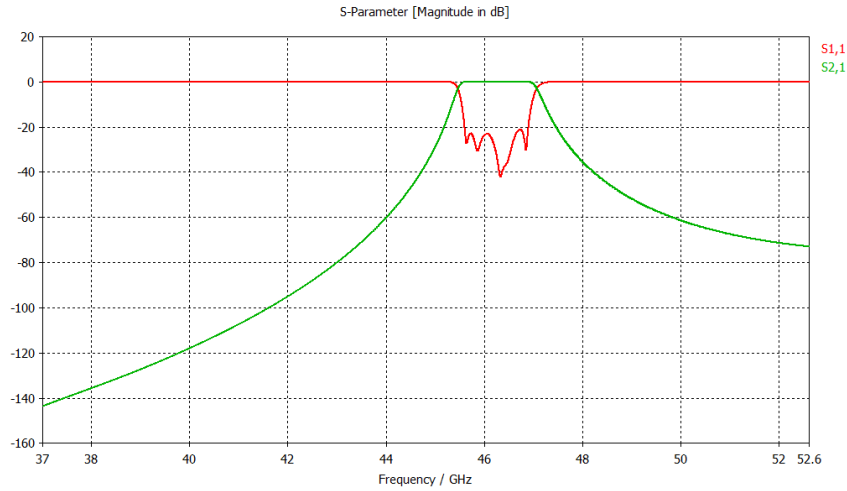
Figure 4.2 S-parameter responses of the E-plane filter in Figure 4.1.

Although conventional E-plane waveguide filters are robust and have well developed design processes, such as given in [1-49], hence well suited for industrial applications, new demands exceed their performances. Accordingly, the dimension of the filter in Figure 4.1 are too large to satisfy available space limitations for the referenced base station project. Thus, waveguide filter miniaturization has clear applicative drive in the present time.

4.1 Ultra-Compact Pseudo-Elliptic Inline Waveguide Bandpass Filters Using Bypass Coupling

This ultra-compact waveguide bandpass filter [P-10], [P-3] implemented inside straight rectangular waveguide section exhibits pseudo-elliptic response. The transmission zero created in the upper stopband to form rapid roll-off is produced through a bypass coupling between the source and load through a higher order mode. The filter utilizes E-plane waveguide technology, and filter insert patterns can be milled out of metall sheets by a circuit board plotter. However, this filter realisation is constructed not from a single E-plane insert like [4-1], but from two of them. This also implies a slight adaptation of the filter housing.

4.1.1. Singlet

In Figure 4.3 is shown a singlet of the proposed ultra-compact bandpass filter with bypass coupling, and the housing, which will be reused for a higher older filter has separation between the two inserts of 3 mm. The singlet fin is 6.7 mm long and 1.4 mm wide, whereas the ground septum is 15 mm wide. Its simulated unloaded Q factor is 1673, calculated from the s21 parameter of symmetric 2-port network. In Figure 4.4 are presented coupling diagram and matrix, as well as their responses compared to full-wave simulated frequency responses for such a singlet with distance between the inserts of 2 mm.

42
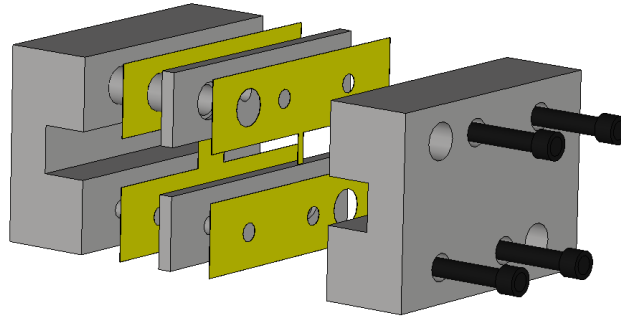
Figure 4.3 Assembling waveguide bandpass filter with bypass coupling composed of two metal sheets. The presented inserts form a singlet.

	1	2	3	4
1	0	1.017	1.678	0
2	1.017	0.073	0.672	1.017
3	1.678	0	-135.1	1.678
4	0	1.017	1.678	0

a)   b)   c)
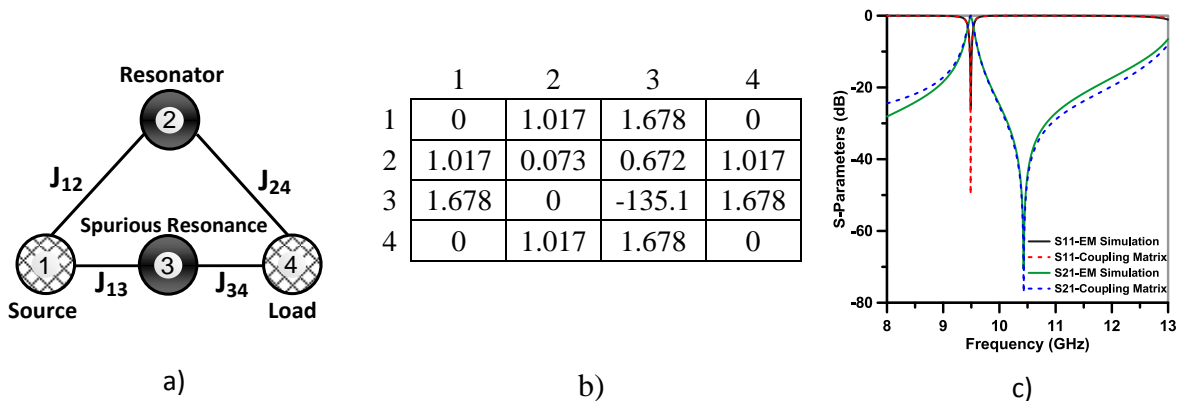
Figure 4.4 a) Coupling diagram of a waveguide singlet, b) its coupling matrix and c) simulated S-parameter responses.

4.1.2. 3rd Order Filter

Layouts of 3rd order filter inserts are presented in Figure 4.5. The wide septum and the suspended metallic fins within a waveguide resemble the ground plane and the signal lines respectively of compact side coupled shielded microstrip quarter‑wave resonators. An advantage of this configuration is that it allows short circuiting of the resonators' signal lines on one side, thus enabling the resonators to be self‑suspended. This inherently prevents the need of a dielectric substrate to support the resonator and further losses can be avoided. Likewise, metallization is made out of copper sheets rather than copper cladding around a laminate, which has lower surface roughness, thus produces lower losses in the conductor.

The resonators are separated by metal septa inserted coplanar with fins. They contribute towards reducing unwanted cross coupling between the resonators, and at the same time the resonators can be moved closer, shrinking the filter size.

43
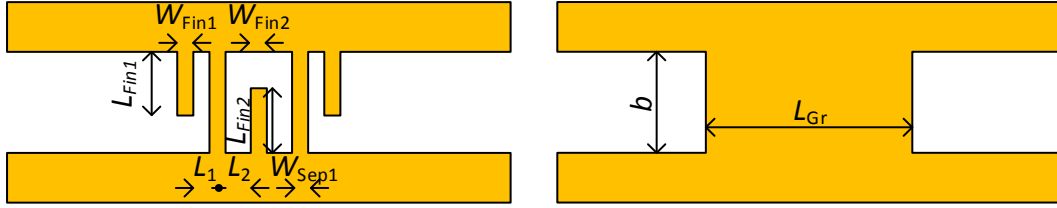
Figure 4.5 3rd order filter insert layouts.

The transmission zero is formed due to appearance of two signal paths (the dominant through the resonators formed between the fins and the septum whereas the other is mainly between the fins and the adjacent sidewall). The filter resonant frequency is lower than the cutoff frequency of the waveguide sections containing the fins, which basically means that this filter essentially operates as an evanescent mode waveguide filter. The coupling matrix (Figure 4.6) shows the three resonators being tuned to the same frequency, and the only non-zero value on the main diagonal is detuned spurious resonance. Crosscouplings C_{S2}, C_{13} and C_{2L} are much lower than the mainline couplings, and are consider just for the sake of response accuracy. Thus, the passband response characteristics of the filter can be well understood by direct coupled filter model.

	S	1	2	3	SP	L
S	0	0.888	0.024	0	0.145	0
1	0.888	0	0.672	0.042	0	0
2	0.024	0.672	0	0.672	0	0.024
3	0	0.042	0.672	0	0	0.888
SP	0.145	0	0	0	-14.4	0.145
L	0	0	0.024	0.888	0.145	0
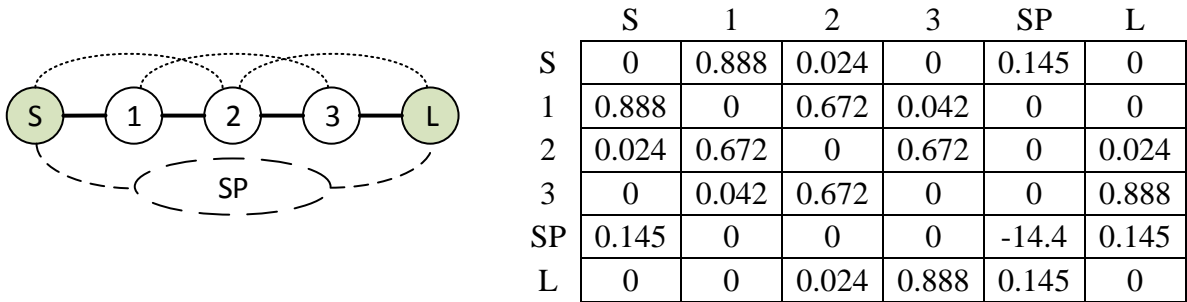
Figure 4.6 Coupling diagram and coupling matrix of the designed 3rd order ultra-compact pseudo-elliptic inline waveguide bandpass filters using bypass coupling

A 3rd order filter using bypass coupling, designed at the centre frequency of 9.4 GHz with a 5.3% fractional bandwidth, Table 4.3, has been fabricated and tested to validate the simulated results, Figure 4.7 The proposed structure's size is 38% smaller than one of a 3rd order E‑plane extracted pole filter with comparable response.

Table 4.3 Dimensions on the fabricated 3rd order ultra-compact bypass coupled filter

Parameter	W_{SEPT}	$W_{SEP1,2}$	$W_{FIN1,2,3}$	$L_{FIN1,3}$	L_{FIN2}
Length [mm]	20.5	1.6	1.6	6.4	6.5
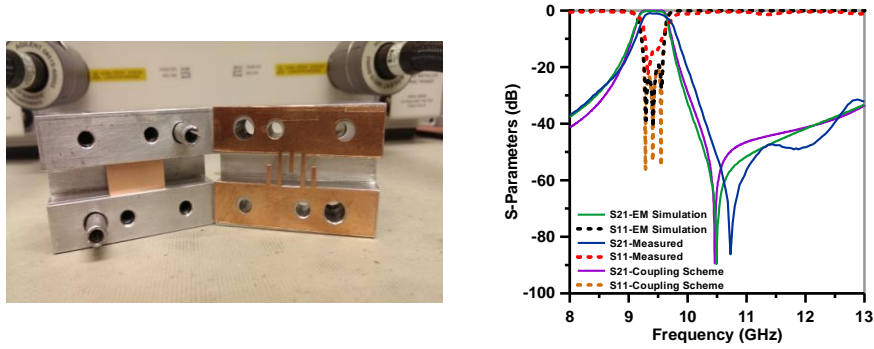
Figure 4.7 Fabricated 3rd order filter and its measured frequency responses compared to electromagnetically simulated and ideal responses of the coupling matrix

4.1.3. Wideband 3rd Order Filter

This design is appropriate not only for narrowband, but also for wideband filters. In Table 4.4 are given dimensions of an ultra-compact filter that correspond to the layouts in Figure 4.5 having accurately 12% 3dB fractional bandwidth. The distance between the two metal inserts in this filter is increased to 7 mm, while still keeping the inserts having equal offsets from the central E-plane. Together with narrower septa and fins, like microstrip line characteristics depend on the ratio w/h, it increases the couplings that is needed for wider passband. In addition, less noticeable effect in the same direction is done by decrease of distance between the fins of the resonator. This is similar to control of bandwidth in interdigital filters, between narrowband/moderate and wideband [1-48] sec. 10.06 and 10.07, where topology of the ultra-compact pseudo-elliptic inline waveguide bandpass filters using bypass coupling matches interdigital filter topology with open first and last lines. In either case, what bounds the bandwidth is exactly how small physically these dimensions can be reliably manufactured. What is different for the presented waveguide filters are the coupling of the first resonator to the source and the last resonator to the load. They are made stronger by decreasing the length of the ground septum, which makes the end fins closer to the unperturbed waveguide and sections of narrow waveguide having the evanescent modes shorter.

Making filter wideband also included proportional shift of the TZ to a higher frequency. Otherwise, ripple in the passband is increased by the vicinity of the TZ. TZ position can be controlled by. Simulated S-parameters of this filter are presented in Figure 4.8.

The coupling matrix is very similar to the coupling matrix of the fabricated filter, and it was actually further optimized from it using Coupling Matrix Optimizer MATLAB App. A reason for it is that to get frequency response, the coupling matrix is scaled by actual centre frequency and bandwidth. In this case, these are $f_0 = 9.60$ GHz and $BW = 1.15$ GHz, respectively.

Table 4.4 Dimensions on the wideband 3rd order ultra compact bypass coupled filter

Parameter	W_{SEPT}	$W_{SEP1,2}$	$W_{FIN1,2,3}$	$L_{FIN1,3}$	L_{FIN2}
Length [mm]	11.1	0.7	0.5	6.5	7.0

	1	2	3	4	5	6
1	0	0.956	0.032	0	0.534	0
2	0.956	0	0.759	0.042	0	0
3	0.032	0.759	0	0.759	0	0.032
4	0	0.042	0.759	0	0	0.956
5	0.534	0	0	0	-14.8	0.226
6	0	0	0.032	0.956	0.226	0
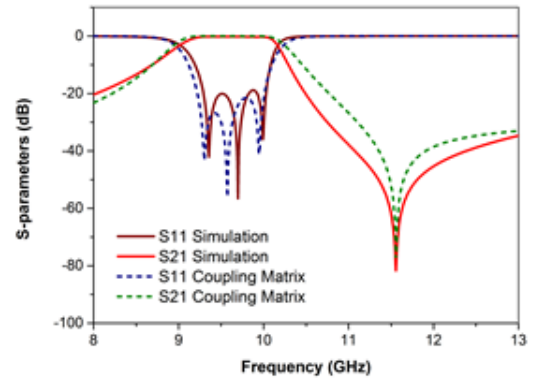
Figure 4.8 Coupling matrix of the wideband ultra compact bypass coupled filter and the corresponding S-parameters compared to the full-wave simulation response

4.1.4. Design flexibility

The presented filters have an upside that they can also obtain a desired filter response in a variety of ways. In Table 4.5 are listed three of such filters, and in Figure 4.9 are displayed their simulated S-parameters.

Table 4.5 Comparison of dimensions between three different 3rd order filters producing the same response. The dimensions which are constant are D=3.0 and W_{Fin1}=W_{Fin2}=W_{Sep1}=1.6. All the dimensions are in millimetres

Filters by fins	L_{Fin1}	L_{Fin2}	L_{Gr}	L_1	L_2
Shorter inner	6.4	6.5	20.7	1.1	3.9
Equal	6.4	6.4	20.4	1.4	3.4
Longer inner	6.5	6.4	20.2	1.7	3.0
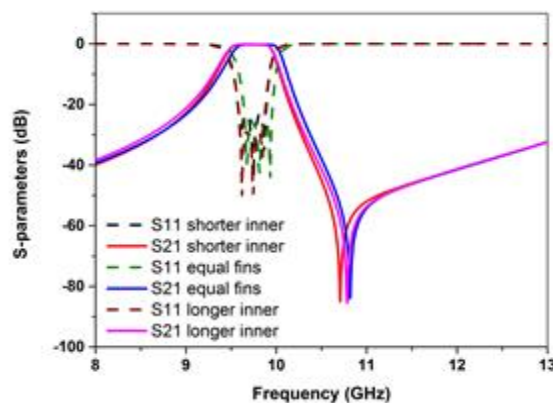
Figure 4.9 S-parameters of filters with the same insert shape, but different dimensions.

The first apparent conclusion is that the fin lengths are the most sensitive dimensions of all in Table 4.5, as changing them in steps of 0.1 mm requires several times larger change of other parameters. Furthermore, the filter gets shorter when inner fin becomes shorter and outer longer.

4.1.5. Sensitivity analysis

In Figures 4.10 and 4.11 are given S-parameters of the equal fin filter from the section 4.1.4. together with new responses obtained when changes of different filter dimensions are present. This is done in order to investigate fabrication tolerances. All of the parameters a, b, L_{Gr}, L_1, L_2, W_{Sep1}, D, L_{Fin1}, L_{Fin2}, W_{Fin1} and W_{Fin2} have been changed by ±0.1 mm, one at the time. This is because the entire design had been made with 0.1 mm resolution, expecting fabrication accuracy within that range. Additionally tests have been with metallization thickness of $+0.1$ mm, as well as the longitudinal misalignment of the two inserts.
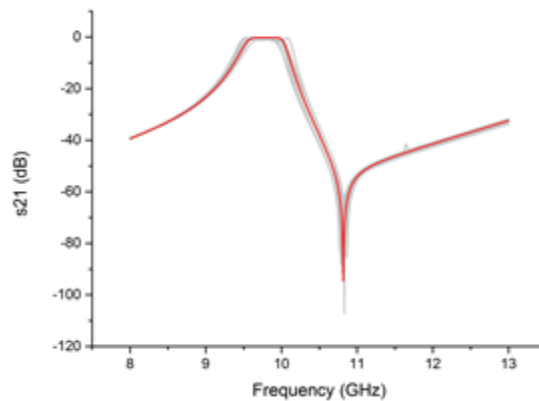
Figure 4.10 Filter transmission responses depending on the dimension variations.
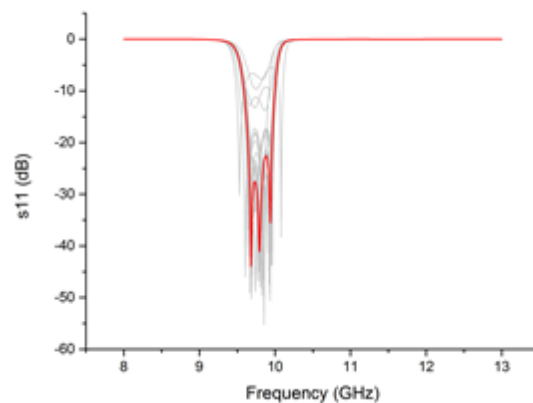
Figure 4.11 Filter reflection responses depending on the dimension variations.

This experiment has confirmed that the fin lengths are the only dimensions which have produced significantly different responses on their own, and the only serious concern regarding sensitivity. Apart from them, if metal strip thickness is increased, it results in visible shift of the design frequency.

4.1.6. Mechanical tuning

As real life filters inevitably possess certain imperfections, filter tuning is implemented in most applications to correct these differences and satisfy the specifications. It is a more economical approach compared to using extremely accurate fabrication process. In

47

Figure 4.12 is given the model of the same 3rd order filter with equal fins. At first, it was detuned by altering the most sensitive dimensions. Then, tuning elements were introduced to restore the filter response. Relevant dimensions are given in Table 4.6.

The tuning screws opposite the fins in longitudinal direction mainly affect resonant frequencies of the resonators they are part. On the other side, the tuning screws at the edges of the large grounded septum and between it and the narrow septa that separate fins, mainly affect input/output and interresonator couplings, respectively. However, the edge ones are more effective in the tuning process. All the tuning screws which are used here have radiuses of 0.8 mm.

In order to control the position of TZ, this design requires the ground septum to be slid between the two narrow walls. This assumes a compromise regarding fabrication in the E-plane technology. Otherwise, additional moveable septum can be used between the insert with signal lines and the nearer narrow wall.
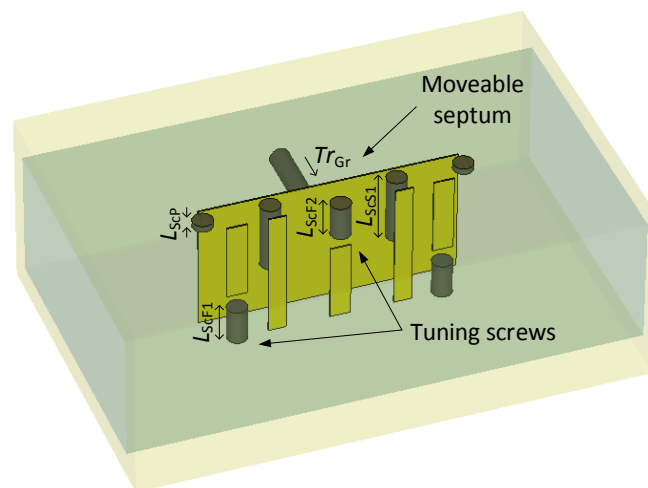
Figure 4.12 3rd order filter with elements added for mechanical tuning (dark).

Table 4.6 Dimension of the original filter elements that are changed, values of these changes, and dimensions of the tuning elements used for correcting.

Filter Parameter	L_{Fin1}	L_{Fin2}	W_{Sep1}	L_{Gr}	
Size [mm]	6.4	6.4	1.6	20.4	
Change [mm]	-0.2	-0.2	-0.2	-0.2	
Tuning Parameter	L_{ScF1}	L_{ScF2}	L_{ScS1}	L_{ScP}	Tr_{Gr}
Size [mm]	2.80	2.73	5.30	0.50	0.50

In Figure 4.13 are plotted all three pairs of responses representing different tuning stages of the structure in Figure 4.12. It is interesting to notice that the capacitances produced by the tuning screws opposite the fins move upper spurious passband further away in a way similar to the combline filters.
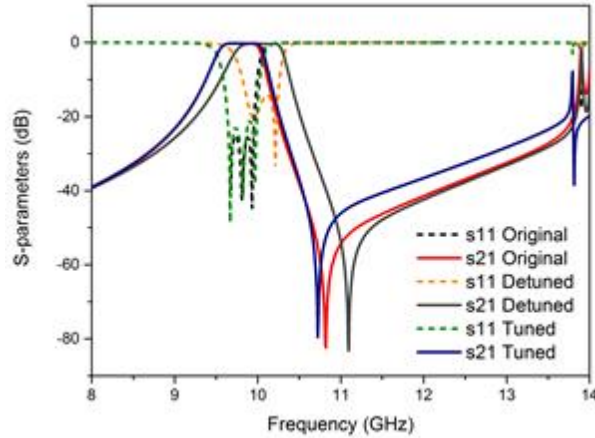
Figure 4.13 Undisturbed filter response compared to the responses after dimensions are changed and tuning is performed to compensate for them.

4.1.7. A 5th Order Filter Sample

In Figure 4.14 is given a longitudinal cross section of a 5th order filter which preserved the same topology filter of the 3rd order filter, with its dimensions given in Table 4.7. (Parameters in Table 4.7 are analogue to those in Figure 4.3.)
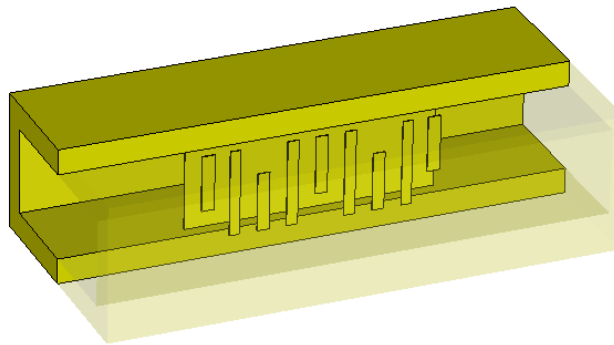
Figure 4.14 3D view of a 5rd order ultra compact pseudo-elliptic inline waveguide bandpass filter using inductive bypass coupling.

In Figure 4.15 are given the frequency responses similar to those in Figure 4.7. The centre frequency is 9.45 GHz and the upper stopband transmission zero at 10.41 GHz Apart from increased selectivity, fractional bandwidth is also increased to 6.5 %, whereas simulated insertion loss at the centre frequency is around 0.4 dB. A conclusion can be made that increasing the order improves filter compactness per resonator.

Table 4.7 Dimension of the designed 5rd order filter.

Parameter	L_{Gr}	L_1	L_2	L_3	L_4	W_{Sep1}	W_{Sep2}
Size [mm]	29.5	1.8	2.2	2.3	2.3	1.1	0.9
Parameter	D	L_{Fin1}	L_{Fin2}	L_{Fin3}	W_{Fin1}	W_{Fin2}	W_{Fin3}
Size [mm]	3.0	6.6	6.9	6.9	1.6	1.0	0.9
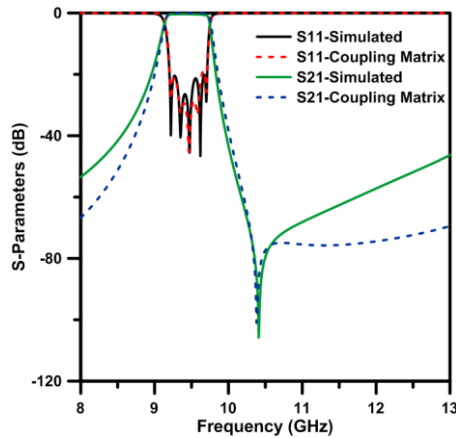
Figure 4.15 Frequency responces of the 5th order ultra compact bypass coupled filter.

4.2   E-plane Resonators for Compact Inline Waveguide Filters

Apart from directly coupled waveguide filters [4-1], E-plane waveguide technology is very suitable for implementation of ridged waveguide resonators and quasi-lowpass corrugated-waveguide filters [4-2]. In [4-3], the size of the conventional E-plane resonator was reduced and transmission zero introduced through the addition of metal S-shaped lines on dielectric slab. Finally, in [4-4] extracted pole sections using fins have been introduced. Further miniaturization was achieved by use of several fins [4-5], and multiplexers based on this filter structure have been designed [P-8]. In this section, compact E-plain resonators with fins are explored in more details regarding their fundamental characteristics, resonant frequencies and quality factors, as well as for their power handling capability as one of the chief characteristics of resilience of these microwave components in real life applications.

4.2.1   Resonator Structure

A 3D model of an E-plane inline symmetric resonator with a fin coupled on both sides to form an EPS section is shown in Figure 4.16 a), whereas its equivalent circuit diagram is depicted in Figure 4.16 b). That is, the straight waveguide sections can be represented by equivalent transmission lines having the same characteristic impedance as the waveguide wave impedance, the central fin by a parallel connected series LC circuit, and the enclosing septa as immitance inverters added with short negative length waveguide sections that are absorbed to reduce the resonator size. (Parasitic couplings between septa and fin are not taken into account.)
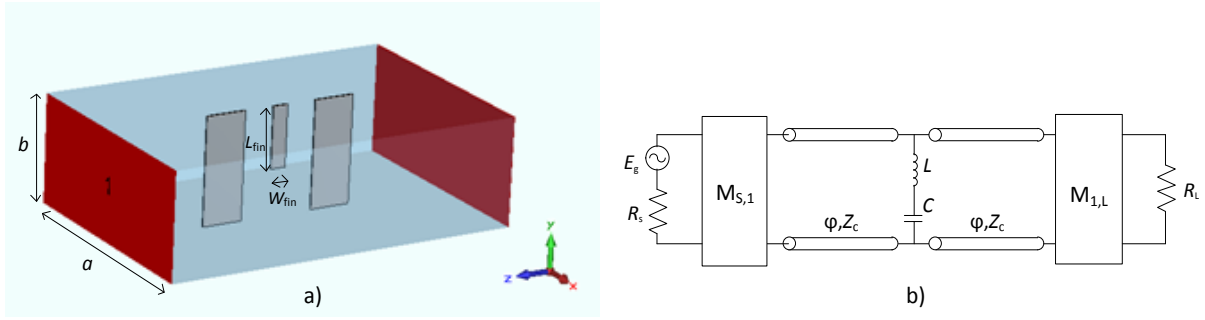
Figure 4.16 a) 3D model of the proposed E-plane inline resonator and b) its equivalent circuit

The dominant mode is based on TE_{101} rectangular cavity mode, Figure 4.17. It can be observed by half sine oscillatory field patterns in x and z directions. In horizontal plane, electric field fades on all side walls, while around the centre, where it is the strongest, it surrounds the fin and is much more constricted than it is for the resonator without a fin.
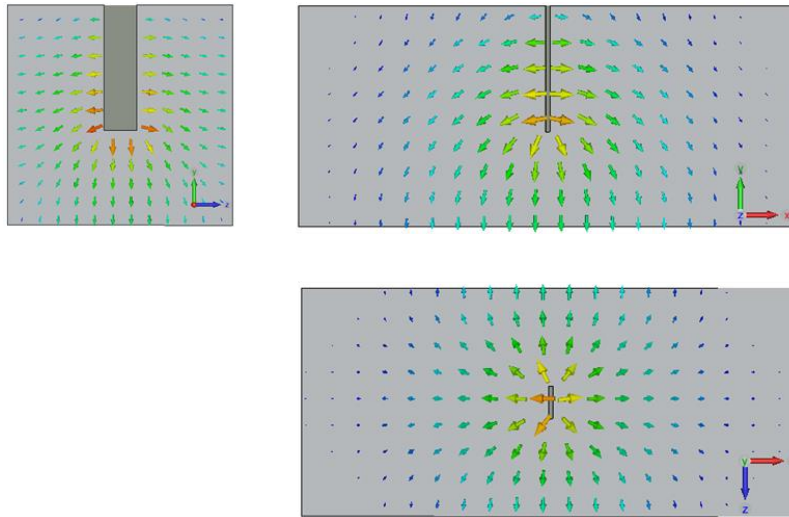
Figure 4.17 Electric field distribution of the dominant modified TE_{101} mode. The field is meandered by the fin and is the strongest around its tip

Effectively, the fin meanders the electric and magnetic fields inside the cavity. Fin can be represented as a continuous transformation of the top waveguide wall.

4.2.2 Resonances

To start with matching the physical dimension with the frequency response, firstly, the fin length will be extracted from the TZ position. Transmission zeros are inherent property of the transmission functions of a network between two of its ports. They tell at which (complex) frequencies the ports are decoupled. For that reason, it does not matter which impedances terminate those two ports. If the transfer function relation for that pair of ports is inspected through different network parameters (Z,Y,S), it will have exactly the same transfer function numerator zeros if possible cancellation effects are not taken into the account. In other words, there is always a cut of the signal path at the TZ frequency. This directly implies that we can extract EPS section zeros with inverters removed, that is, by just keeping the fin inside a waveguide, provided that coupling between the fin and the septa can be neglected.

The fin length turns out to be just slightly larger than the quarter of a wavelength. This can be explained by the fact that the fin lays in a cross section plane and not along the waveguide. And by image theory applied on waveguide walls, the fin transforms into 2D array of half-wavelength dipoles in open space. Hence, at the cutoff frequency, the fin length is roughly equal to the waveguide height. Metal insert thickness is supposed to be small ($< 2\%$ a), but larger than the skin depth, so that perturbation method applies. Under these conditions it can be taken that it does not influence the transmission zero frequency.

With the rise of frequency, in the zone where higher order modes start to appear, there is a visible shift in the fin length. When its length is about $3\lambda/4$, secondary radiation from the fin is mostly transferred to higher modes with first index odd (odd number of half-sine oscillations along the wider cross section rectangle side due to the position of the fin in the centre which fixes field maximum in that position). That is to say TE_{11}, TM_{11}, $TE_{30},\ldots$ in the order they appear, so TZ effect in the dominant mode diminishes Figure 4.18. Since for historical reasons the wider rectangle side (a) is a bit more than double length of the shorter one (b), these spurious modes are further shifted to higher frequencies, i.e. more than twice the cutoff frequency of the dominant mode. E.g. for X band WR-90, cutoff frequencies of TE_{11} and TM_{11} modes are 16.16 GHz.
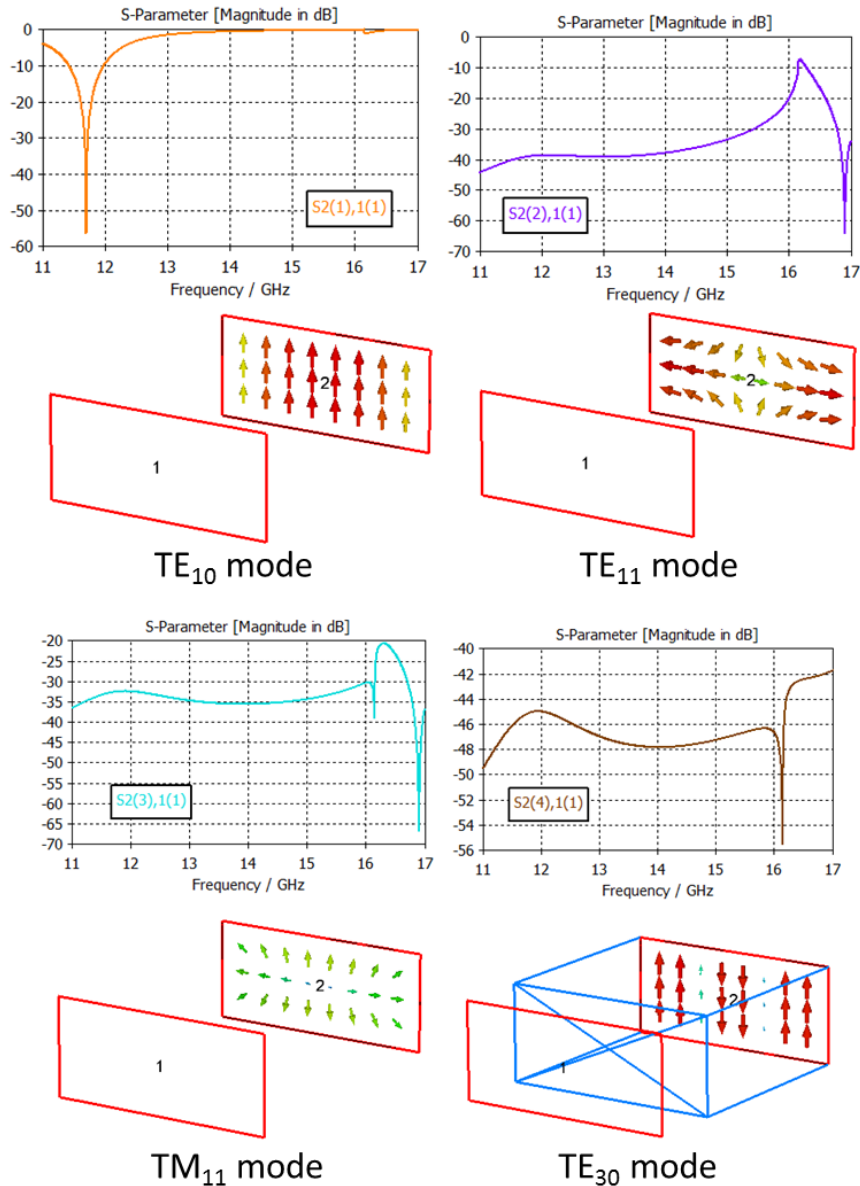
Figure 4.18 When fin length reaches about 3λ/4, its secondary radiation from is mostly transferred to higher order waveguide modes with odd first index.

Pole resonant frequency in an unloaded resonator can be calculated starting with the ubiquitous expression for the TE_{101} mode resonance in the rectangular waveguide cavity, modifying it through division with a nonlinear function larger or equal than one, which depends on L_{fin} and has relatively modest steepness for small values of L_{fin}, but increases afterwards. Nevertheless, of interest are only those larger values of L_{fin}, for which this function can be linearized.

Examined structure is the rectangular cavity with completely closed ports – limit case of septa becoming infinitely wide – with a fin inside it. CST Eigenmode solver detects only frequencies that correspond to transmission poles, because these are the natural frequencies of the complete electric circuit.

There may be a confusion arising by the asymmetric properties of TPs and TZs. If a reflexion parameter is taken as an example, there is indeed symmetry between the numerator

and the denominator, since two different reflection parameters like z_1 and y_1 are just reciprocal one to another. But this is only an exception which does not violate the more universal property of not having symmetry between the numerator and the denominator. It is important to stress that the mathematical function through which natural frequencies (complex in general case) can be observed is a transfer function, which in strictly the response function over the source function in the Laplace domain. This is to emphasize that although in both numerator and denominator of a rational transfer function there is a polynomial, no symmetry in the general case exists between them – the fundamental characteristic of a circuit lays in the zeros of the denominator, not the numerator.

4.2.3   Higher Order Modes

In [4-4], higher order modes are used as well and put together to form dual-mode resonator. In fact, these are not degenerate modes, but of different nature and not mutually symmetric, though are set to have similar resonant frequencies. The first mode in the transmission pole pair is almost unaltered TE_{102} mode due to the fact that the fin is positioned where the field has its minimum. This also means that changing fin length, while having large effect on the neighbouring transmission pole and transmission zero, has negligible effect on the transmission pole resulting from this cavity resonance. Second one is modification of TE_{103} mode, similar to the dominant mode for having odd number of amplitude maxima along the resonator, however, with a different field pattern in the volume around the fin from TE_{102} mode. This can be viewed by comparison of the field distributions for these two modes in Figure 4.19. For all the mentioned modes so far it can be checked that varying a and d alters the resonant frequencies, whereas changing b has only minuscular indirect effect over the fin. Although their practical significances are questionable, different properties of two modes allow various different responses such as transmission pole-zero-pole sequence. In other words, although the TZ produced by the central fin cannot be at a frequency below the one of the TP formed by the dominant TE_{101} mode resonance, it can be both below and above the frequencies of either TE_{102} or TE_{103} TPs.
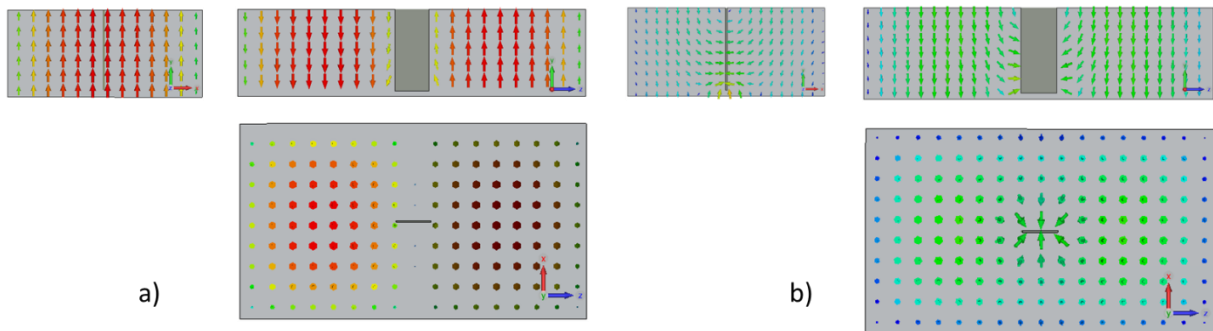
Figure 4.19 Electric field lines in *x*, *y* and *z* cross section for a) modified TE_{102} mode and b) modified TE_{103} mode.

4.2.4   Q factor

Comparison of (unloaded) Q factors for different cavity resonators at f = 10 GHz is given in Table 4.8.

Table 4.8 Comparison of unloaded Q factors for various resonant cavities.

Cavity type (mode)	Model	Calculation method	Q value	Volume V[mm^3]	Q/V [mm^{-3}]
Rectangular waveguide cavity (TE$_{101}$ mode) [4-7], Sec. 6.3		$Q_u = \frac{(kad)^3 b Z_0}{2\pi^2 R_s} \frac{1}{(2a^3 b + 2bd^3 + a^3 d + ad^3)}$ $V = a \cdot b \cdot d$	6075.9	4611.1	1.32
Circular waveguide cavity (TE$_{111}$ mode) [4-7], Sec. 6.4		$Q_u = \frac{(ka)^3 Z_0 ad}{4(x'_{11})^2 R_s} \frac{1 - \frac{1}{(x'_{11})^2}}{\left\{ \frac{ad}{2}\left[1 + \left(\frac{\beta_{11}a}{(x'_{11})^2}\right)^2\right] + \left(\frac{\beta_{11}a^2}{x'_{11}}\right)^2 \left(1 - \frac{1}{(x'_{11})^2}\right) \right\}}$ $V = \pi \cdot a^2 \cdot d$	8897	9710	0.92
Circular waveguide cavity (TE$_{011}$ mode) [4-8]		$Q_u = \frac{(ka)^3 Z_0 ad}{4(x'_{01})^2 R_s} \frac{1}{\left\{ \frac{ad}{2} + \left(\frac{\beta_{01}a^2}{x'_{01}}\right)^2 \right\}}$ $V = \pi \cdot a^2 \cdot d$	20807	40 957	0.51
Rectangular waveguide cavity (TM$_{120}$/TM$_{210}$ degenerate modes) [4-9]		$Q_u = \frac{(ka)^3 d\, Z_0}{10\pi^2 R_s} \frac{1}{(2d+a)}$ $V = a^2 \cdot d$	4170	5055.5	0.82
Rectangular SIW cavity (TE$_{101}$ mode)		Q_u: CST Eigenmode solver + Loss and Q calculator $V = a_{SIW}^2 \cdot h$	612.6	341.3	1.8
Rectangular SIW dual mode cavity (TE$_{102}$/TE$_{201}$ degenerate modes)		Q_u: CST Eigenmode solver + Loss and Q calculator $V = a_{SIW}^2 \cdot h$	627.8	844.1	0.74
Rectangular waveguide cavity with E-plane fin (dominant TE$_{101}$ mode)		Q_u: CST Eigenmode solver + Loss and Q calculator $V \approx a \cdot b \cdot d$	1) 4097.6 2) 2110.6	1) 2420.1 2) 808.3	1) 1.69 2) 2.61
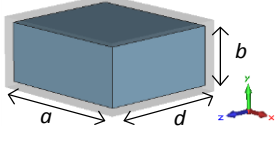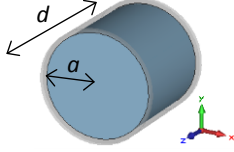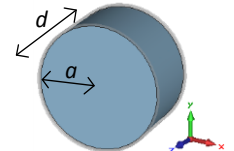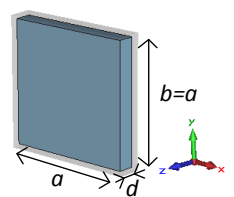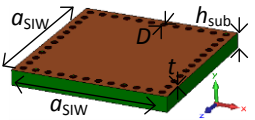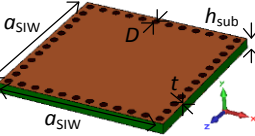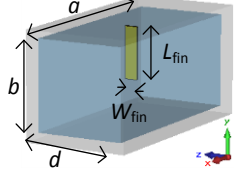
Rectangular waveguide cavity with E-plane fin (second TE$_{101}$ and TE$_{102}$ modes)		Q_u: CST Eigenmode solver + Loss and Q calculator $V \approx a \cdot b \cdot d$	1) H$_{101}$ 5410.6 2) H$_{102}$ 6759.7	1) H$_{101}$ 9058 2) H$_{102}$ 9452.9	1) H$_{101}$ 0.6 2) H$_{102}$ 0.72
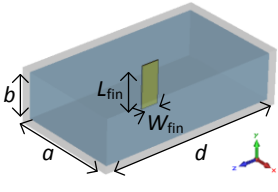
Here, universally, $\varepsilon_0 = 8.85$ x 10^{-12} $\frac{F}{m}$ and $\mu_0 = 4\pi$ x 10^{-7} $\frac{H}{m}$ are vacuum permittivity and vacuum permeability constants respectively, $Z_0 = \sqrt{\frac{\mu_0}{\varepsilon_0}} = 376.73$ Ω is impedance of free space, $k = \omega\sqrt{\varepsilon_0\mu_0}$ is angular wavenumber and $R_s = \sqrt{\frac{\omega\mu_0}{2\sigma}}$ is surface resistance.

Regarding material properties, it is assumed that metal waveguide housings are made of aluminium, $\sigma_{Al} = 3.5$ x 10^7 $\frac{S}{m}$, $R_s = 33.6$ mΩ, and metallic inserts of annealed copper, $\sigma_{Cu} = 5.8$ x 10^7 $\frac{S}{m}$. In SIW design, hsub = 1.575 mm thick low loss Rogers RT/duroid 5880 high frequency laminate is used having relative permittivity $\varepsilon_r = 2.2$ and tan$\delta = 0.0009$ dielectric characteristics. Copper cladding has $t = 17.5$ µm thickness with $R_q = 1.8$ µm RMS surface roughness on the dielectric side for electrodeposited copper to result in effective conductivity of $\sigma_{Cu,clad} = 2.5$ x 10^7 $\frac{S}{m}$.

As the rectangular waveguide is used the standard X band WR 90 having cross section dimensions $a = 22.86$ mm and $b = 10.16$ mm to accommodate the dominant TE$_{101}$ mode resonant cavity, being guided by its inline applications such as in directly coupled waveguide filters. From $k_{101} = \sqrt{\left(\frac{\pi}{a}\right)^2 + \left(\frac{\pi}{d}\right)^2} = k$ is calculated the rectangular waveguide cavity length $d = \dfrac{1}{\sqrt{\frac{4f^2}{c_0^2} - \frac{1}{a^2}}} = 19.85$ mm.

Use of degenerate TM$_{120}$ and TM$_{210}$ modes was proposed in [4-6] for the sake of having design flexibilities in terms of the number and position of transmission zeros, response bandwidth as well as of the cavity length. The latter is because of having the last mode index referring to the longitudinal direction zero. Actually, this also applies to standard TE$_{101}$ modes and the height of the cavity, which is typically not altered due to the constant height to width ratio of the standard rectangular waveguides. Nevertheless, they are sometimes used having the equal width and height so as to accommodate degenerate TE$_{101}$ and TE$_{011}$ modes. The rectangular waveguide cavity accommodating TM$_{120}$ and TM$_{210}$ modes is set to have dimensions exactly like in [4-6] where resonant frequency is already 10 GHz (since the resonant frequency is independent of d, for equal sides a and b, $f = \frac{\sqrt{5}c_0}{2a}$), hence $a = b = 33.52$ mm and $d = 4.5$ mm. When calculated $Q_u = 4170$ is scaled by the factor $\sqrt{\frac{\sigma_{Ag}}{\sigma_{Al}}}$, which corresponds to using silver plating instead of pure aluminium, the resulting Qu is 5505.1, which is close to the value 5550 given in the paper.

As the circular waveguide is used X band WC 80 waveguide having inner radius of $a = 10.122$ mm to accommodate the dominant TE$_{111}$ mode resonant cavity, being guided by its inline applications. From $k_{npq} = \sqrt{\left(\frac{x'_{np}}{a}\right)^2 + \left(\frac{q\pi}{d}\right)^2} = k$, $x'_{11} = 1.841$, is calculated the

circular waveguide cavity length, $d = \dfrac{\pi}{\sqrt{k^2 - \left(\frac{x'_{11}}{a}\right)^2}} = 30.17$ mm.. In addition,

$\beta_{\text{TEnp}} = \sqrt{k^2 - \left(\frac{x'_{np}}{a}\right)^2}$. There is actually a pair of orthogonal degenerate TE_{111} modes, and this Q_u is applicable for either of them as well as in the case both of them are simultaneously excited when the resonator is used in the dual-mode regime. This latter is obvious by the principles of superposition and symmetry, if the coupling between the two modes does not exist.

In contrast, the overmoded (6th mode, not counting degenerate ones) cavity accommodating TE_{011} mode is scaled to have proportions like the average cavity in [4-7], $\dfrac{d}{a} = 1.108$. Having $x'_{01} = 3.832$, $a = 22.75$ mm and $d = 25.20$ mm is calculated. Comparison of the quality factors of the two presented circular waveguide cavities supports what is pointed out in [4-8], p.292, and graphically depicted in Figure. 6.10, that Q_u for TE_{011} mode is significantly higher than the ones for the lower order TE_{111}, TM_{010}, or TM_{111} modes.

First SIW cavity analysed here is the dominant TE_{101} mode rectangular one. More precisely, the base is of square shape to maximize the Q factor, having no more restriction of adhering to standardized waveguide dimensions or maximizing power handling capability this way due to inherent low-profile limitation that predetermines breakdown characteristics. The SIW cavity design starts with idealisation of all its walls being ideally flat PEC surfaces, as for a conventional rectangular waveguide resonator. Such a resonator has the base edge length of $a = \dfrac{c_0}{\sqrt{2}\sqrt{\varepsilon_r}f} = 14.29$ mm. Now considering more precise model of SIW with metalized vias, firstly, via diameters and distances between sequential via centres were chosen to be as to satisfy the conditions $D \le \lambda_g/5$ and $s \le 2D$ [4-9]. Therefore, $D = 0.7$ mm and the number of via-holes along one side wall including corner vias shared with adjacent side walls is 12. Having the calculated length of a as the desired effective length, the exact design-oriented length between via centre of opposite side walls was further by optimization found to be $a_{\text{SIW}} = 14.72$ mm.

Eigenmode solver is used for calculation of the cavity resonant modes and their field distribution in the lossless case, whereas in post processing Loss and Q calculation is applied, meaning that the Q factor in CST is also calculated by the perturbation method.

For SIW resonator, Q is composed of Q factor due to conductor losses, $Q_c = 1365.3$, and Q factor due to dielectric losses, $Q_d = 1111.1$, $Q = \left(\dfrac{1}{Q_c} + \dfrac{1}{Q_d}\right)^{-1}$.

TE_{102} and TE_{201} mode pair is the most common one for SIW dual mode cavities, dictated by the substrate height being much smaller than the other two dimensions [4-10]. In fact, TM_{120} and TM_{210} modes already described are the same as TE_{102}/TE_{201} modes provided a rotation swapping axes and transforming what is the height of cavity for TE modes (substrate thickness for SIW) to the length of cavity for TM mode. Thus, the formula for unloaded Q factor of TM_{120}/TM_{210} modes in Table 1 was derived by readily given formula for TE_{102} mode [4-8], (6.46) using the mappings: $a_{TM} \rightarrow d_{TE}$, $b_{TM} \rightarrow a_{TE}$, $d_{TM} \rightarrow b_{TE}$. Furthermore, a TM_{120}/TM_{210} mode

waveguide filter structure with cascaded cavities can be linked to a multilayer SIW one. Certainly, differences remain in terms of air dielectric, solid metal walls and source and load feed implemented using waveguides rather than planar transmission lines.

Taking this into account, for degenerate TE_{102}/TE_{201} modes in a square base cavity, it holds $a = \frac{\sqrt{5}c_0}{2\sqrt{\varepsilon_r}f} = 22.60$ mm. Moving to the model of SIW with via-holess, via diameters are $D = 1.1$ mm and the number of vias along one side wall including corner vias shared with adjoining side walls is 12. The final base side is by simulation found to be $a_{SIW} = 23.27$ mm.

For SIW dual-mode resonator, Q factor due to conductor losses is $Q_c = 1443.2$, and Q factor due to dielectric losses is $Q_d = 1111.1$. It can be observed that Q_d is exactly the same as in the case of TE101 as it only depends on dielectric loss tangent (more precisely, it is its inverse) and not on the cavity dimensions [4-8].

Finally, a rectangular WR 90 waveguide cavity with an E-plane fin is investigated. The metal insert on which the fin is etched is 0.2 mm thick.

The fin length and width are 1) Lfin = 5.8 mm and Wfin = 1.5 mm; 2) Lfin = 6.8 mm and Wfin = 1 mm respectively for the dominant TE_{101} mode. Although the eigenmode solver finds purely resonant frequencies that turn into transmission poles when the cavity is coupled, the fin dimension are selected so as the transmission zero of EPS is located at around 1) fz = 11.5 GHz and 2) fz = 10.25 GHz. The cavity dimensions itself are $a = 22.86$ mm, $b = 10.16$ mm and 1) $d = 10.42$ mm. or 2) $d = 3.48$ mm..

For higher order modes, second TE_{101} and TE_{102}, fin dimensions are Lfin = 9.5 mm and Wfin = 4.0 mm, so that there is good level of coupling between the two poles of the dual-mode cavity and that the frequency of transmission zero in the lower stopband is about fz = 8.8 GHz. For the second TE_{101} mode, the WR-90 waveguide housing cavity is $d = 39.0$ mm long and for TE_{102} mode it is $d = 40.7$ mm long.

4.2.3 Power Handling Capability

Electrical breakdown is an undesirable physical phenomenon regarding microwave filter design in which dielectric conductivity rapidly increases after high enough (breakdown) voltage is applied on it. It leads to signal distortion and in more severe cases to permanent damage of microwave components. Although breakdown mechanisms, different in solid, liquid and gaseous materials, are well-studied, an accurate breakdown occurrence is intrinsically very hard to be predicted.

High power consideration is naturally of importance for waveguide filters due to their distinctive high power system applications, either terrestrial or space, especially when they are located after a power amplifier (PA), e.g. in a communication satellite output multiplexer (OMUX). Additional reason for waveguide filters to be susceptible to ionization breakdown is that they have high Q resonators and are typically narrowband (for wideband filters, Q factor is less critical, so more compact technologies are usually preferred), meaning large voltage

magnification [4-12]. Also, microwave filters, especially waveguide ones, are required to work reliably, often in very harsh condition, so it is crucial to investigate their limitations and possible improvements to overcome them. In Tables 4.9 and 4.10 typical power levels of high power transmitters according to [4-13] are presented. Sharp edges of conductive surfaces and decrease in distance between them, which are both present while using fins in waveguides, are well-known causes of local increase of electric field strength and subsequent sooner reach of breakdown field.

Table 4.9 High-Power Requirements for Terrestrial Systems as in Table 20.1 of [1-51]

System type	Typical Power Requirements (W)
Personal Communications Service (PCS)	0.1-1
Cellular-handheld	0.6
Mobile unit	4
Cell sites	60
Line of sight (LOS)	1-10
Cable television (CATV)	100

Table 4.10 High-Power Requirements for Typical Satellite Systems as in Table 20.2 of [1-51]

Satellite System (GHz)	Transponder Bandwidths (MHz)	Typical Power Requirements (per Transponder)	
		Uplink – Earth Station (W)	Downlink – Satellite (W)
1.5	10s of KHz Uplink 0.5-5 MHz Downlink	1-10	150-220
6/4	36, 54, 72	500-3000	10-100
14/11	27, 54, 72	500-3000	20-200
30/20	36, 72, 112	100-600	5-80

For air and other gases, unless the pressure is very low, breakdown occurs partially as corona discharge or as full corona breakdown arcing. The breakdown ignition happens as avalanche-like

increase of free electron density through collision ionization of neutral gas molecules by free electrons with high kinetic energy built up from microwave field, transforming isolating gas into conducting plasma. Pre-quantum model based on classical kinetic theory of gases, describing particles and their collisions like billiard balls, is used. Process is described in terms of the nature of the gas, collision frequency (mean free path), diffusion and attachment. In a region without sources of free electrons, electron density equation reads:

$$\frac{\partial n}{\partial t} = \nabla(D\nabla n) + (v_i - v_a)n,$$

where n stands for electron density, D for diffusion coefficient, v_i for ionization frequency and v_a for attachment frequency, paired with the boundary condition n = 0 on the conducting walls [4-14].

The dependence of ionization frequency on the electric field amplitude is much stronger than those of attachment frequency and diffusion coefficient, which are primarily dependent on pressure. Conditional to problem geometry, this differential equation is solved in various exact or approximate ways. It is assumed that electric field distribution had been determined prior to solving the continuity equation for electron density. The breakdown threshold is reached when sum of electron losses in diffusion and attachment are balanced by ionization, i.e. $\frac{\partial n}{\partial t} = 0$. More complex models can include electron energy equation describing electron temperature evolution, density equation of surface metal atoms, heat diffusion of the gas medium equation [4-15], etc.

As a result, breakdown field (voltage) versus pressure for different gases and on different frequencies are described by Paschen's curves, Figure 20.3-5 [4-13]. Pashen's law was first empirically obtained and published in 1889 [4-16].

Since the field strength for air is 22.8 KV/cm RMS or 32 KV/cm peak, the proposed EPS can withstand 142.6 W peak power at the resonant frequency of 10 GHz for the dimensions Lfin=5.8 mm and L=7.3 mm. The field has its maximum near corners of the bottom tip of the fin. Also, it is about an order of magnitude higher for the transmission pole that for the transmission zero. (In CST Microwave Studio, standard E-field view gives peak electric field value, here obtained 2.68 x 105 V/m or 2.68 KV/cm for normalized peak port power of 1 W.)

A study [4-17] showed that for right angle conductor edges in air on 10 GHz under normal conditions, the critical field determining breakdown strength is localized very near the corner tip having electric field singularity around it ("edge-localized breakdown").

In addition, ionization and breakdown were simulated in CST MWS using a non-linear Drude model for cold plasma, parameterised through a macro depending on primary gas (N), its pressure, temperature and degree of ionization. Cold plasma approximation adopts that ions, having much bigger masses than electrons, are stationary when the working frequency is higher than the ion plasma frequency (2 rad/s). Below the threshold plasma maintain frequency (1 rad/s), the gas (air) behaves like an ordinary one.

These have been described under 'normal' conditions: room temperature of 298 K, sea level pressure of 760 Torr, 10-60 % humidity and perfect matching. Derating factors are imperfect

impedance matching, altitude, moisture, temperature, dirt. Their influence is graphically presented in [4-13]. Decrease due to mismatch is directly proportional to SWR value. From the 1 Atm pressure at the sea level, on higher altitudes the power handling capability drops with the fall of pressure until it reaches the bottom of Pashen's curve, where the gas collision frequency is equal to the RF frequency (e.g. about 10 Torr at 10 GHz for air). Afterwards, the breakdown field starts to rise and eventually multipaction takes over as the dominant breakdown mechanism.

Under very low pressure condition that are typical for space applications in which devices are not hermetically enclosed, where corona discharge effect requires much higher field strength, to prominence comes multipaction effect [4-18]. When pressure is this low, mean free path cannot be considered much smaller than distances between conducting surfaces. Multipaction breakdown is based on secondary electron emission (SEE) as a result of free electrons accelerated by RF field hitting conducting walls, causing avalanche effect sustained through resonance of SEE with the electric field. It is a more global mechanism compared to ionization breakdown, depending on voltage as path integral of electric field rather than peak electric field at a point, hence more predictable. Two well-known secondary electron yield models are Vaughan's [4-19], popular in RF & microwave industry, and more recent Furman's [4-20], popular with plasma physicists. Vaughan's model has fewer parameters to set not specifying emission process, faster to compute, but less accurate, considering only direct secondary electrons.

Safety margins used by industry are typically in the range of 0-6 dB, though this is to a large extent determined by economic interests [4-12].

4.3   Compact Inline E-plane Waveguide Resonators and Bandpass Filters with I-shaped Resonant Insets

Difference from the previous E-plane filters in this case of newly introduced filters is the dielectric substrate has been maximally utilized to support balanced topology. Centrally positioned floating I-shaped inset acts as a half-wavelength resonator to form a TZ antiresonance. The inset is simple enough to enable quick initial design, but has sufficient degrees of freedom for fine tuning to particular requirements. Another improvement is that high level of inset symmetry allows significant reduction of simulation time.

Loading a waveguide with a dielectric slab is like adding central capacitance with ridges. It lowers the cutoff frequency of the dominant mode, but not significantly affecting the next higher one. It effectively increases the bandwidth. Importantly, the power handling capacity is bigger when having higher dielectric strength material filling the space with the strongest field [4-26]. Compared to all-metal inserts, PCB manufacturing is generally more accessible and it removes response sensitivity to metal bending. Since waveguide filter housings are reusable and other waveguide components are standardized modules, the proposed filters have edge in ease of fabrication even over SIW and microstrip filters for neither needing vias nor soldering coaxial connectors.

4.3.1 Proposed Resonators

Configuration of an E-plane waveguide resonator with an I-shaped inset coupled on both sides to form an extracted pole section (EPS) is given in Figure 4.20 a), while the equivalent circuit is in Figure 4.20 b).
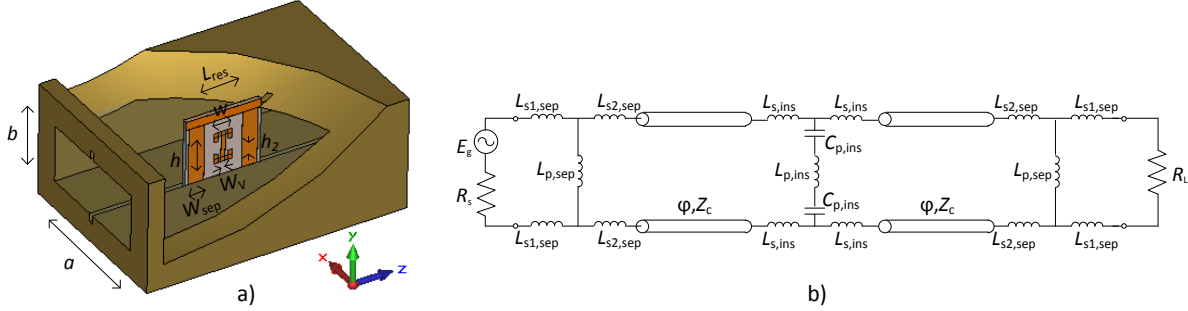
Figure 4.20 a) 3D model of the proposed E-plane resonator with I-shaped inset and b) its equivalent circuit.

The resonator structure has central x- and z-planes of symmetry. Central y-plane is just slightly violated in this implementation due to asymmetric position of the dielectric substrate. These properties are transposed into balanced symmetrical equivalent circuit.

For each resonator discontinuity inside the waveguide, its equivalent 2-port network is extracted from de-embedded center frequency Z-parameters of only that discontinuity independently full wave simulated in the waveguide. Equations $Xs1 = \text{Im}(z11 - z12)$, $Xs2 = \text{Im}(z22 - z12)$ and $Xp = \text{Im}(z12)$ are applied to find Xs1 and Xs2 as serial reactances at ports 1 and 2 respectively and Xp as the parallel reactance of the equivalent T-network. This network is further transfigured into one of equivalent networks in Figure. 1b in a straightforward manner, with *Ls,ins* and *Cs,ins* satisfying the relation $f_z = 1/2\pi\sqrt{L_{s,ins}C_{s,ins}}$, where f_z is the frequency of the TZ produced by an independent I-shaped inset.

The physical length of I-shaped inset is shorter than half a wavelength. This is because of the top and bottom capacitive loadings. Therefore, the TZ position can be regulated by the inset height as well as by the sizes of the loadings. The width of the line representing the loading has been fixed for all the presented designs to 0.8 mm. Smaller width has been excluded to avoid problems with sensitivity. This is similar to the effect accomplished with adding capacitive loadings to a dipole antenna. Applying image theory on waveguide walls, the I-shaped insets are transformed into 2D array of dipoles in their transverse z-planes.

The resonant frequency can be controlled by changing the length of the waveguide resonator. (It is assumed that the waveguide profile is known.) The resonator bandwidth depends on the amount of coupling between source and load. A more narrowband response can be achieved through wider septa forming immitance inverters. Other way is by a wider I-shaped inset.

Sample structures have been designed at X band. Standard WR 90, (a x b) = (22.86 mm x 10.16 mm), brass rectangular waveguide (σBr = 15.9 MS/m) with useful frequency

band between 8.2 and 12.4 GHz is used. In the top and bottom broad walls along one side of the central E-plane are carved 1.5 mm deep and 0.8 mm wide grooves to accommodate a dielectric slab with etched metallization pattern. The housing is split in longitudinal direction in two halves. In this way, the slab can easily be put into the groove in one half and the other half can afterwards be placed onto the first one and screwed.

The slab is made out of hsub = 0.79 mm thick low loss (tanδ = 0.0009 at 10 GHz) Rogers RT/duroid 5880 high frequency laminate with relative permittivity εr = 2.2 [4-27]. ED copper cladding is t = 17 μm thick with Rq = 1.8 μm RMS surface roughness on the dielectric side to result in effective conductivity of σCu,clad = 15.4 MS/m.

Propagation characteristics in the waveguide sections between the septa and the insets that are loaded with off-centered dielectric substrate can be found following the procedure outlined in [4-28]. In circuit simulation, they are modeled by standard TE10 mode sections with the waveguide width increased by 2.73 mm to match the phase constant and characteristic impedance of the actual distorted mode.

The PCB has been fabricated using LPKF ProtoMat C60 [4-29] circuit board plotter (Figure 4.21). Nevertheless, Rogers RT/duroid 5880 glass microfiber reinforced PTFE composite threaded structure is not particularly suitable for milling, which has somewhat negatively affected the measured responses.
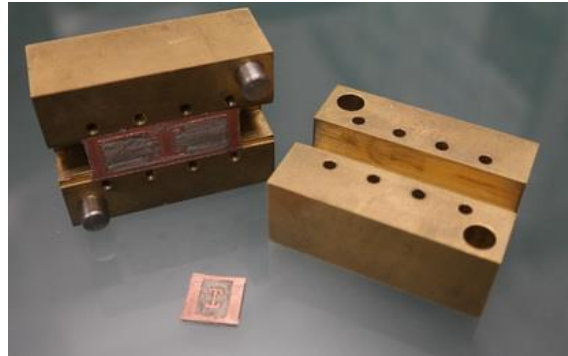
Figure 4.21 Photograph of the two fabricated resonator inserts with the brass waveguide housing.

A. *Dominant Mode Resonator*

The dominant mode in the resonator is TE101. This can be verified by investigating standing wave patterns within field distribution and by the resonant frequency shifts while changing various resonator dimensions. The electromagnetic field is, expectedly, strongest in the resonator center region, around the inset. Aside from finding the TZ location, the I-shaped inset size affects the transmission pole (TP) location as well because it meanders the EM field inside the resonant cavity. What is more, the surge in its size more rapidly lowers the resonant frequency than adding of cavity length does, helping to considerably contract the resonator size.

In Figure is displayed simulated response from CST Microwave Studio [CST] of a dominant TE101 mode resonator with physical lengths and values of equivalent circuit lumped elements in

the Table 4.11, corresponding to the dimensions in Figure 4.22. It can be established that miniaturization of 35% has been achieved in comparison with the conventional E-plane filter. Between the septum and the inset, the energy is mostly transferred by TEn0 modes, n = 1, 3, 5, …, where each higher modes has about 10 dB lower level. With no additional coupling between discontinuities modeled, TZ frequency is about 6% higher than its actual value, whereas TP frequency is only about 1.5% under 10 GHz. The response of the fabricated dominant mode resonator was measured using Agilent E8361A PNA Network Analyzer, and is also shown in Figure 4.22.
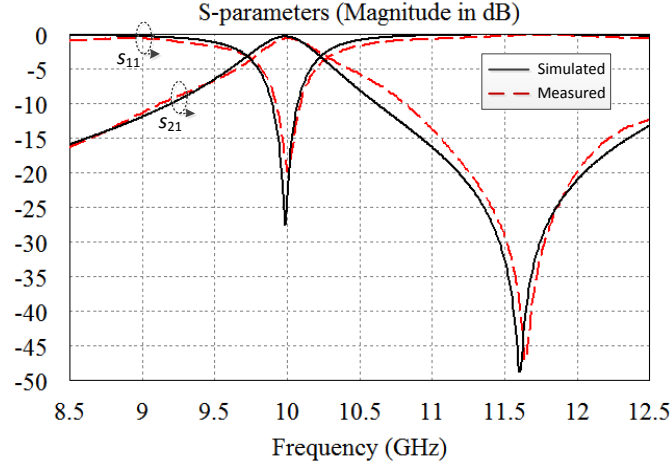
Figure 4.22 Simulated and measured transmission and reflection S- parameters of the dominant mode resonator.

Table 4.11: Dimensions of the EPS With the Dominant Mode Resonance and Equivalent Circuit Lumped Element Values

Dimension	L_{res}	W_{sep}	W_V	h	h_2	w
Length [mm]	7.0	2.9	0.8	5.6	1.7	3.4
Element	$L_{s1,sep}$	$L_{s2,sep}$	$L_{p,sep}$	$L_{s,ins}$	$L_{p,ins}$	$C_{p,ins}$
Value [nH/µF]	2.24	1.29	3.39	2.13	8.51	$3.9e^{-8}$

Using eigenmode solver in CST Microwave Studio, unloaded Q factor was calculated to be 1873. I-shape inset dimensions were kept constant while completely closing the resonator couplings. The new resonator length was set to be 12.1 mm, so that the resonant frequency of the dominant mode is 10 GHz sharply. Qu is calculated using perturbation method, with components Q factor due to conductor (surface) losses Qc = 6517 and Q factor due to dielectric (volume) losses Qd = 2628, in total $\frac{1}{Q_u} = \frac{1}{Q_c} + \frac{1}{Q_d}$.

B. *Higher Order Dual Mode Resonator*

First two higher order modes are TE_{102} and TE_{103}. Since the field distribution of TE_{103} mode has maximum in the center of the cavity, whereas TE_{102} has its minimum there, the I-shaped inset considerably more affects the TE_{103} mode than the TE_{102} mode. Hence, the distance between the two TPs can be adjusted using the inset. The simulated and measured responses of the resonator with these two modes are given in Figure 4.23. Dimensions and circuit element values are listed in the Table 4.12, referring to the dimensions described in Figure 4.. In this case with no additional coupling between discontinuities modeled, TZ frequency is about 15% below its real value. At the same time, TP frequency has much smaller shift, of around 3% to the lower side.
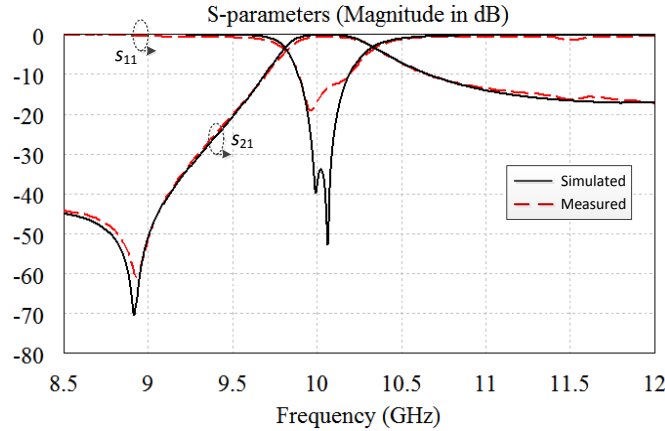
Figure 4.23 Simulated and measured transmission and reflection S-parameters of the higher order dual mode resonator.

Table 4.12 Dimensions of the EPS With the Higher Mode Resonances and Equivalent Circuit Lumped Element Values

Dimension	L_{res}	W_{sep}	W_V	h	h_2	w
Length [mm]	30.4	2.9	4.2	8.8	2.4	8.6
Element	$L_{s1,sep}$	$L_{s2,sep}$	$L_{p,sep}$	$L_{s,ins}$	$L_{p,ins}$	$C_{p,ins}$
Value [nH/μF]	2.24	1.29	3.39	5.86	7.79	$8.1e^{-8}$

For TE103 mode, Qu = 2610 with Qc = 5330 and Qd = 5114 (Lres = 35.1 mm). In the case of TE102 mode, Qu = 2821 with Qc = 4586 and Qd = 7327 (Lres = 37.6 mm)

4.3.2   Filters With I-Shaped Resonant Insets

By cascading a section of dominant mode resonator and a section of dual mode cavity with higher order modes, a 3rd order E-plane filter with I-shaped insets is created. In Figure 4.24 is shown the layout of the filter insert, and in Table 4.13 dimension for such a filter having the passband centered at 11 GHz.

66
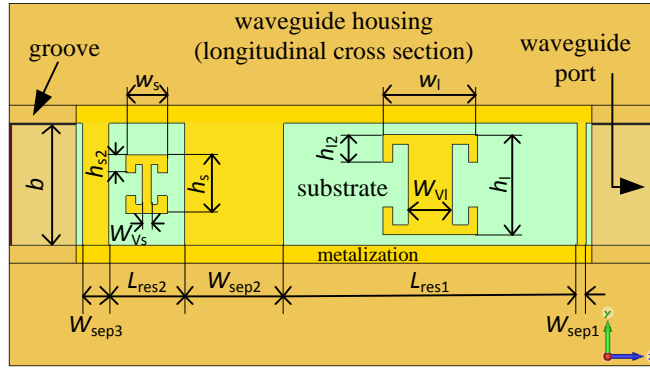
Figure 4.24 Longitudinal cross section of a 3rd order filter.

Table 4.13 Dimensions of the 3rd Order Filter

Dimension	Length [mm]	Dimension	Length [mm]
L_{res1}	24.4	h_l	8.3
L_{res2}	6.3	h_{l2}	2.3
W_{sep1}	0.7	w_l	7.9
W_{sep2}	8.2	h_s	4.9
W_{sep3}	2.2	h_{s2}	1.5
W_{Vl}	3.7	w_s	3.4
W_{Vs}	0.8		

In Figure 4.25 are given S-parameter responses of the 3rd order filter with generalized Chebyshev response, simulated in CST Microwave Studio. The difference between the two reflection parameters is minimal even though the structure is not symmetric, so s22 parameter is not presented for clarity.
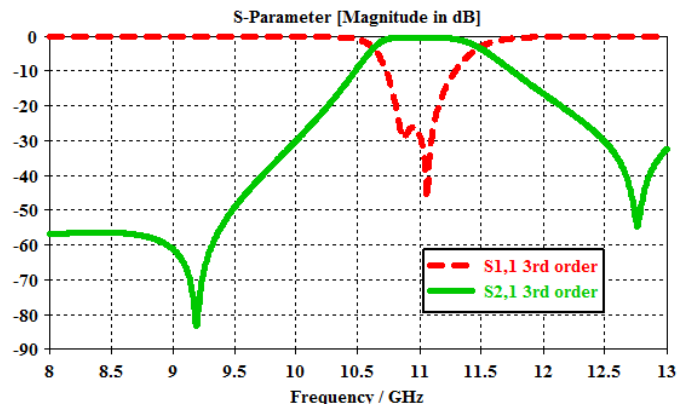
Figure 4.25 Transmission and reflection S-parameters of the 3rd order filter.

Simulation results show that reflection loss is better than 20 dB in the frequency range between 10.808 GHz and 11.154 GHz. In the same band insertion loss is less than 0.4 dB. The 3db bandwidth is between 10.625 GHz and 11.482 GHz. This effect of having noticeably different center frequencies while using two different criteria for the passband is due to much steeper roll-off in the lower passband than in the upper one. Differences in passband to stopband transition steepness comes from the waveguide behaving as a high-pass filter. (In addition, it has spurious passbands at higher frequencies where the filter discontinuities cease to reflect higher order waveguide modes). In conclusion, for having more symmetric response, it is needed to introduce higher number of transmission zeros in the upper stopband.

References

[4-1]   Y. Konishi and K. Uenakada, "The Design of a Bandpass Filter with Inductive Strip - Planar Circuit Mounted in Waveguide," *IEEE Trans. Microw. Theory Tech.*, vol. 22, no. 10, pp. 869–873, Oct. 1974.

[4-2]   G. Goussetis and D. Budimir, "Novel periodically loaded E-plane filters," *IEEE Microwave Wireless Components Lett.*, vol. 13, no. 6, pp. 193–195, Jun. 2003.

[4-3]   S. Niranchanan, A. Shelkovnikov, and D. Budimir, "Novel millimetre wave metawaveguide resonators and filters," *2007. European Microwave Conference*, 2007, pp. 913–916.

[4-4]   O. Glubokov and D. Budimir, "Extraction of Generalized Coupling Coefficients for Inline Extracted Pole Filters With Nonresonating Nodes," *IEEE Trans. Microw. Theory Tech.*, vol. 59, no. 12, pp. 3023–3029, Dec. 2011.

[4-5]   N. Mohottige, O. Glubokov, and D. Budimir, "Ultra Compact Inline E-Plane Waveguide Extracted Pole Bandpass Filters," IEEE Microw. Wirel. Compon. Lett., vol. 23, no. 8, pp. 409–411, Aug. 2013.

[4-6]   S. Bastioli, C. Tomassoni, and R. Sorrentino, "A New Class of Waveguide Dual-Mode Filters Using TM and Nonresonating Modes," *IEEE Trans. Microw. Theory Tech.*, vol. 58, no. 12, pp. 3909–3917, Dec. 2010.

[4-7]   A. Morini, M. Baldelli, G. Venanzoni, M. Farina, N. Sidiropoulos, P. Angeletti, P. M. Iglesias, and C. Ernst, "Modeling and design of microwave filters employing overmoded empty cylindrical resonators," *Microwave Conference (EuMC), 2015 European*, 2015, pp. 971–974.

[4-8]   David M. Pozar, *Microwave engineering*, 3rd ed. / International ed. New York ; Chichester: Wiley, 2004.

[4-9]   F. Xu and K. Wu, "Guided-wave and leakage characteristics of substrate integrated waveguide," IEEE Trans. Microw. Theory Tech., vol. 53, no. 1, pp. 66–73, Jan. 2005.

[4-10] D. Deslandes and K. Wu, "Substrate integrated waveguide dual-mode filters for broadband wireless systems," *Radio and Wireless Conference*, 2003. RAWCON '03. Proceedings, 2003, pp. 385–388.

[4-11] D. Deslandes and K. Wu, "Design Consideration and Performance Analysis of Substrate Integrated Waveguide Components," *2002. 32nd European Microwave Conference*, 2002, pp. 1–4.

[4-12] M. Yu, "Power-handling capability for RF filters," *IEEE Microw. Mag.*, vol. 8, no. 5, pp. 88–97, Oct. 2007.

[4-13] Richard J. Cameron, Raafat R Mansour, and Chandra M Kudsia, Microwave Filters for Communication Systems: Fundamentals, Design and Applications. Wiley-Interscience, 2007.

[4-14] D. Anderson, U. Jordon, M. Lisak, T. Olsson, and M. Ahlander, "Microwave breakdown in resonators and filters," *IEEE Trans. Microw. Theory Tech.*, vol. 47, no. 12, pp. 2547–2556, Dec. 1999.

[4-15] K. Frigui, D. Baillargeat, S. Verdeyme, S. Bila, A. Catherinot, J. Puech, and D. Pacaud, "Microwave Breakdown in Waveguide Filters Theoretical and Experimental Investigations," *IEEE Trans. Microw. Theory Tech.*, vol. 56, no. 12, pp. 3072–3078, Dec. 2008.

[4-16] F. Paschen, "Ueber die zum Funkenübergang in Luft, Wasserstoff und Kohlensäure bei verschiedenen Drucken erforderliche Potentialdifferenz (On the potential difference required for spark initiation in air, hydrogen, and carbon dioxide at different pressures)," Annalen der Physik, vol. 273, no. 5, pp. 69–75, 1889.

[4-17] T. Olsson, U. Jordan, D. S. Dorozhkina, V. Semenov, D. Anderson, M. Lisak, J. Puech, I. Nefedov, and I. Shereshevskii, "Microwave Breakdown in RF Devices Containing Sharp Corners," *Microwave Symposium Digest*, 2006. IEEE MTT-S International, 2006, pp. 1233–1236.

[4-18] Vaughan, "Multipactor", *IEEE Transactions on Electron Devices*, Vol. 35, No. 7, July 1988,pp. 1172-1180

[4-19] J. R. M. Vaughan, "A new formula for secondary emission yield," *IEEE Trans. Electron Devices*, vol. 36, no. 9, pp. 1963–1967, Sep. 1989.

[4-20] Furman and Pivi, "Probabilistic model for the simulation of secondary electron emission",Physical Review Special Topics – Accelerators and Beams, Vol. 5, (no. 124404), pp. 124404-1through 124404-18, 2002

[4-21] Volume 1-27, *MIT Radiation Laboratory Series*, McGraw-Hill, New York, 1947.

[4-22] A. E. Atia, A. E. Williams, "Narrow-Bandpass Waveguide Filters," *IEEE Trans. Microw. Theory Tech.*, vol.20, no.4, pp.258-265, Apr 1972.

[4-23] G. Macchiarella and S. Tamiazzo, "Design of "Masthead" Combiners," *2015 European Microwave Conference*, 2015, pp. 686–689.

[4-24] C. Dehos, J. L. González, A. D. Domenico, D. Kténas, and L. Dussopt, "Millimeter-wave access and backhauling: the solution to the exponential data traffic increase in 5G mobile communications systems?," *IEEE Commun. Mag.*, vol. 52, no. 9, pp. 88–95, Sep. 2014.

[4-25] S. Niranchanan, A. Shelkovnikov, and D. Budimir, "Novel millimetre wave metawaveguide resonators and filters," *2007 European Microwave Conference*, 2007, pp. 913–916.

[4-26] W. P. Ayres, P. H. Vartanian, and A. L. Helgesson, "Propagation in Dielectric Slab Loaded Rectangular Waveguide," *IRE Trans. Microw. Theory Tech.*, vol. 6, no. 2, pp. 215–222, Apr. 1958.

[4-27] https://www.rogerscorp.com/

[4-28] N. Eberhardt, "Propagation in the Off Center E-Plane Dielectrically Loaded Waveguide," *IEEE Trans. Microw. Theory Tech.*, vol. 15, no. 5, pp. 282–289, May 1967.

[4-29] http://www.lpkf.com/

5. Compact E-plane dual band filters and diplexers

In scenarios when different users, transmitters and receivers need to be accommodated simultaneously within the same system over common transmission medium (scarce and costly resource), multiplexing methods are used. Signals from different sources are combined into one (multiplexed) signal on the communication channel. Spectral efficiency helped by multiplexing is especially significant for wireless communications because of limited nature of the frequency spectrum, which is shared with many other systems. Examples are time-division, code-division, polarization-division, orbital angular momentum-division and space-division multiplexing. Related multiple access methods are used if various users have direct access to the multiplexed signal.

A special case of particular importance for application of filters is frequency-division multiplexing (FDM), in which the available bandwidth is further separated into contiguous frequency bands by use of channel filters. As it has already been mentioned, analog low-frequency filters for POTS multiplexers made revolution in early electronics. Application of FDM is well-known in television and radio systems (including broadcast and cable distributions) and multiplexers composed of waveguide filters are standardly used in satellite communications, where those carried in satellite payloads are of critical design and fabrication requirements because of high cost penalties regarding excess of size, weight and reliability constraints. In the satellite transponders, between uplinking and downlinking through common antennas, channel groups are demultiplexed to allow separate routing and processing followed by power amplification. Most commonly used configurations of these multiplexers are hybrid-coupled, circulator-coupled, directional filter, and manifold-coupled [1-51], [5-1]. In analogue way, frequency-division multiple access (FDMA) is typical for ground users of satellite system services.

On the other side, receivers/transmitters in modern telecommunications often use multiple contiguous and non-contiguous frequency bands in order to increase capabilities of single devices. For example, current smartphones can support connectivity to cellular networks in different bands, in different countries, within different systems belonging to different generations (e.g. 850/900/1800/1900 MHz quad band phones for global access to 2G, 3G and 4G systems). In addition, they use both 2.4 GHz and 5 GHz ISM bands for 802.11 a/b/g/n/ac Wi-Fi standards and Bluetooth, being able to connect to personal and local area wireless networks as well, can receive signals from satellite navigation systems, and some even traditional FM radio signals. This drives the need for developing multiband RF components, including filters. Although multiband filtering can be realized by connecting the required number on single band filters in parallel, significant size reduction can be made if the filtering is performed within shared resonators of a multiband filter.

In this chapter, the focus is on 2nd order structures. Firstly, these are dual band filters, and they are followed by diplexers [P-8], both being in E-plane waveguide technology. Microwave diplexers are mostly used as duplexers. They enable full-duplex communication by connecting receiver and transmitter to a common antenna through frequency-division duplex (FDD) [5-2].

Such an essential application of microwave diplexers is in base stations of mobile telephony systems, known for highly demanding specifications. One application of dual band filters is to produce compact diplexers, and this can be generalized to multi band filters and multiplexers.

5.1   E-plane dual band waveguide resonators

Three types of resonant cavities, in each of them two resonances being used in two separate bands, are introduced in this section (Figure 5.1). One produces just a TP in each of the two passbands, whereas the other two in addition have a pair of TZs between the two passbands and a pair of TZs in both the upper and lower stopbands respectively. This makes cascades of such resonators capable of having steep skirt in any transient band. In addition, the response can be made either symmetrical or asymmetrical for any of these resonators[14].

All the TPs are utilized through TE_{10n} modes. Each resonant cavity uses a pair of consecutive TE_{10n} modes, where n is increased by 1 when moving to the next type of resonator, resulting in the use of modes from TE_{101} up to TE_{104}. Since one of the modes in any resonator type has odd order in longitudinal direction and the other one even, the differences in EM field distributions are used for independent control of each mode to form its own passband.

All three dual band resonators can be realized in E-plane technology. Another common feature, also seen in the case of single band resonators, is that inserts form resonators (thus TPs) with a pair of septa that enclose fins, whose widths control couplings. Likewise, the lengths of fins dominantly determine TZ frequencies. With these two degrees of freedom, fins can achieve frequency dependable and passband independent control of i/o and interresonator couplings. As the mode numbers increase by 1 between the resonators, the number of waveguide discontinuities composed of metal fins in the resonators also increases by 1. Thus, the number of waveguide discontinuities in the resonators is in the range between 2 and 4. A newly introduced degree of freedom to have different offsets of pairs of fins from the centre transverse plane helps control the separation between the two passbands.
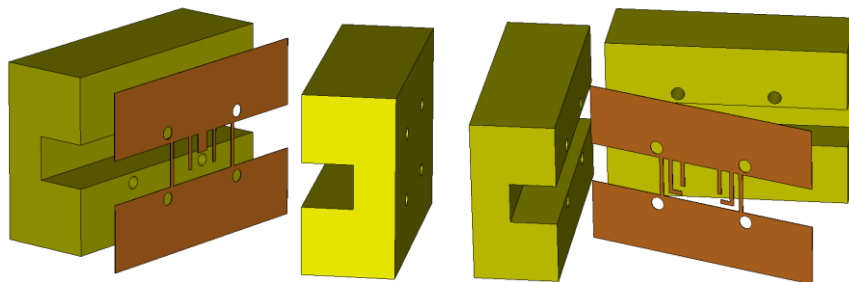
Figure 5.1 3D models of two dual band resonators with metal E-plane inserts: PZZP (left) and ZZPPZZ (right).

---

[14] Responses of the resonators are inherently asymmetrical, however, the positions of their poles and zeros make it possible to achieve good approximations of symmetrical responses if needed.

For independent control of two TPs of a dual band resonator, displacing only one fin in the longitudinal direction is sufficient (Figure 5.2). Nevertheless, a problem which is encountered that way concerns reflection losses at these TP frequencies. Let us first take a look at the impedance matching at the TP frequency in the simplest case of a half-wavelength waveguide resonator. Both of its ports are terminated by the nominal TE_{10} wave impedance Z_0 (calculated at the TP frequency), which is purely real for a lossless medium (2.9), and also used as the normalization constant. Visualised by the impedance Smith chart (Figure 5.3a), the load impedance is in its centre. Then, it is shifted to the left along real Γ and normalized impedance axis towards $\Gamma = -1$ (zero impedance) point after looking to it through impedance (K) inverter, $z_1 = K^2/Z_0^2$ and $K<Z_0$[15]. Phase length of $\pi/2$ inside the resonator rotates this point for 360° clockwise in the Smith chart back to the same point, $z_2 = z_1$, and another impedance inverter puts the point back to the centre of the circle, $z_{in} = z_L$. Thus, the perfect impedance matching is obvious in this ideal case.

a)

WR90 waveguide

$W_{fin}=W_{sep}=1$

All dimensions are in mm

b)

c)
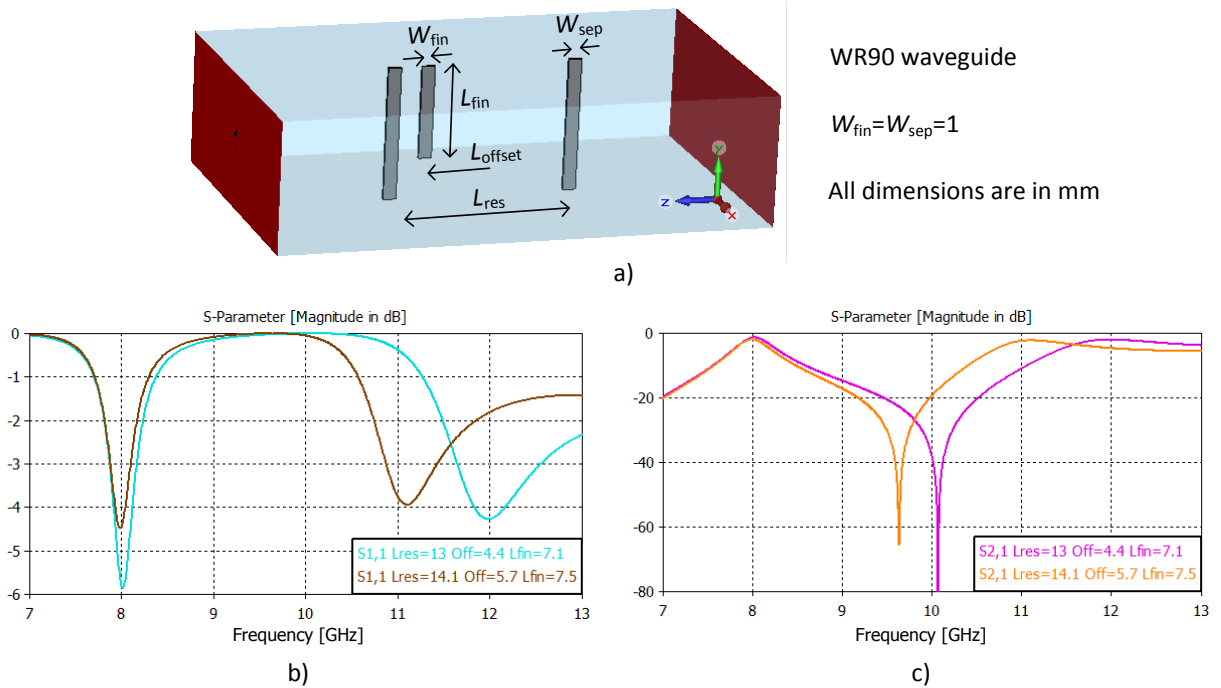
Figure 5.2 Control of frequency separation between TE_{101} and TE_{102} resonances by longitudinally offsetting only one fin inside E-plane waveguide resonator: a) Perspective of the resonator with labelled dimensions, b) reflection responses, and c) transmission responses. Problem with low reflection loss in the passbands is evident.

When a metal fin is added at the centre of the resonator, pure rotation for 360° clockwise does not happen anymore, but instead a central section of that rotation is substituted by adding shunt susceptance (Figure 5.3b). Because of the need for adding a shunt element, in this case it is more convenient to work with admittances, and y_1 is found as point symmetrical to z_1 from Figure 5.3a)

---

[15] The shunt reactance of a discontinuity that acts as an inverter can go from infinitely large one, when the waveguide is undisturbed, to the zero one, when the waveguide is short-circuited.

72

with respect to the chart centre. Alternatively, admittance (J) inverter is used directly instead of impedance inverter to find y_1 on the real axis in $0<\Gamma<1$ interval. This can also be verified by representing metal septum by negative shunt susceptance, followed by rotation in anticlockwise direction. In fact, the point reached after adding susceptance of the septum only is more representative regarding constraints of matching through waveguide length and fin in physical resonator, since anticlockwise rotation is purely fictional action performed only to accommodate the theoretical concept of an immittance inverter.

Back to the effect of the fin, it can also be noticed here that its susceptance needs to be positive. This explains why resonators with fins in Sec. 4.2.1 must have TZ in the upper stopband for the dominant mode resonance. However, when the fin is offset (Figure 5.3c), susceptance is not added symmetrically with respect to the real Γ axis, so y_4 is not collocated with y_1, and thus does not come back to the centre of the circle after the source inverter. Although there can be different ways to compensate for that effect, bearing in mind that two passbands need to be matched and that there is frequency dependence of elements, the easiest way to do the matching was to use longitudinally symmetrical resonators. It should be noted that return loss problem cannot be rectified by having two asymmetrical resonators in chain making symmetrical compound structure. Although used model is excellent for getting insight into the working principles of E-plane resonators, it should not be forgotten that a number of effects, prominently coupling of waveguide discontinuities through higher order modes, have been neglected, so that obtained element values may not be best representatives of the real physical dimensions.

Just like the TZ produced by a single fin cannot be at a frequency lower than the TP of TE_{101} resonance, the TZs produced by a pair of longitudinally symmetrical fins cannot be at a frequency lower than the TP of TE_{102} resonance.
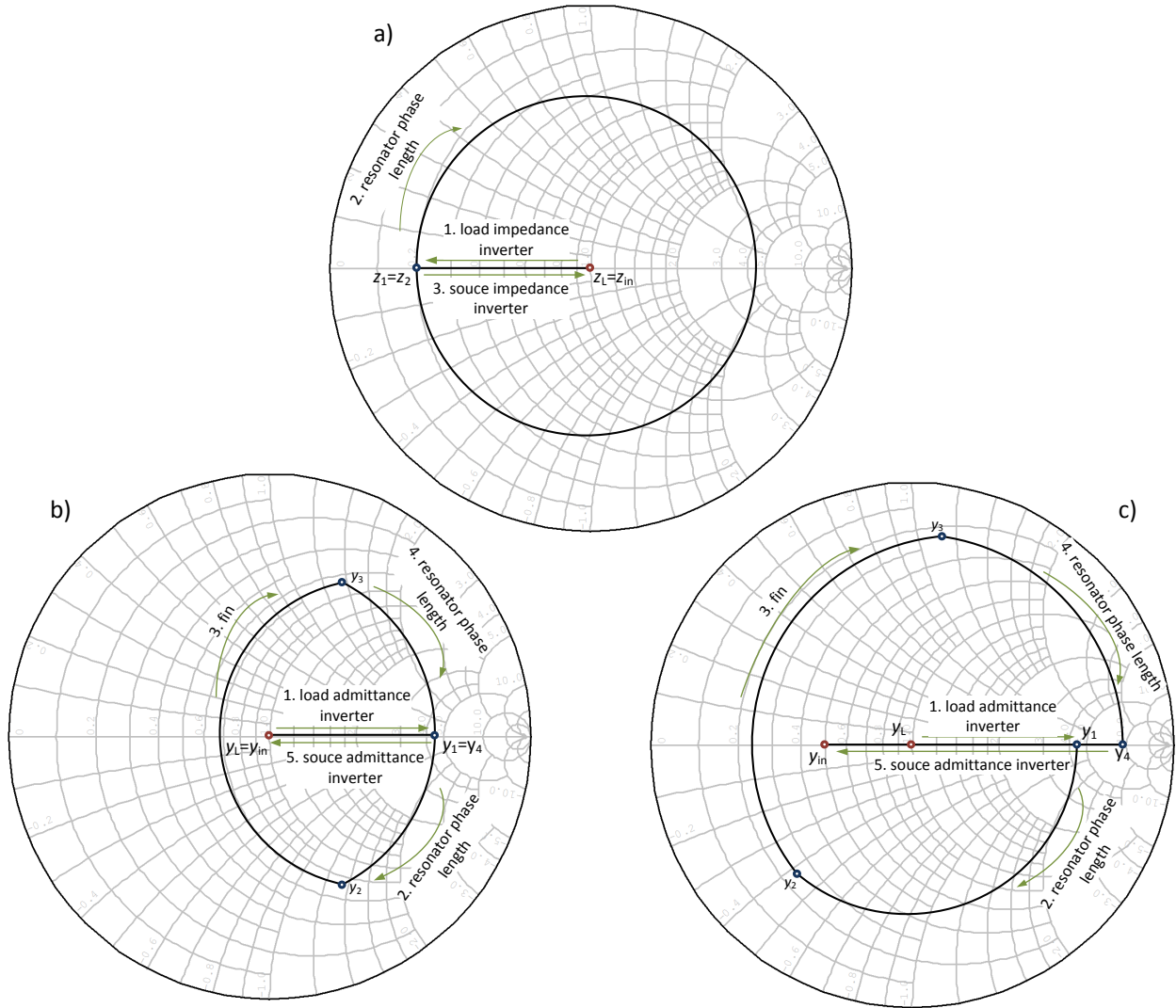
Figure 5.3 Impedance matching at the resonant frequency looking into E-plane resonator from the side of the source for: a) conventional half-wave resonator, b) resonator with centrally positioned fin, and c) resonator with fin offset from the central plane of symmetry in the longitudinal direction.

5.1.1 PP Resonator

PP resonator has been chiefly designed to produce one TP in either passband. Nevertheless, a pair of TZs still exists in the upper stopband and can be used to improve selectivity in this part of the response, although here we keep it far enough that the response can be viewed as symmetrical. There is only one pair of waveguide discontinuities consisting of metal fins inside the resonator, symmetrically positioned with respect to the centre transverse plane. The lengths of fins are proportional to the wavelengths of TZs, and making them wider results in having more wideband effect of TZs. However, since fins are relatively short because of high frequencies of

TZs, they are doubled by having them symmetrically positioned with respect to the centre H-plane as well (Figure 5.4).

a)

b)
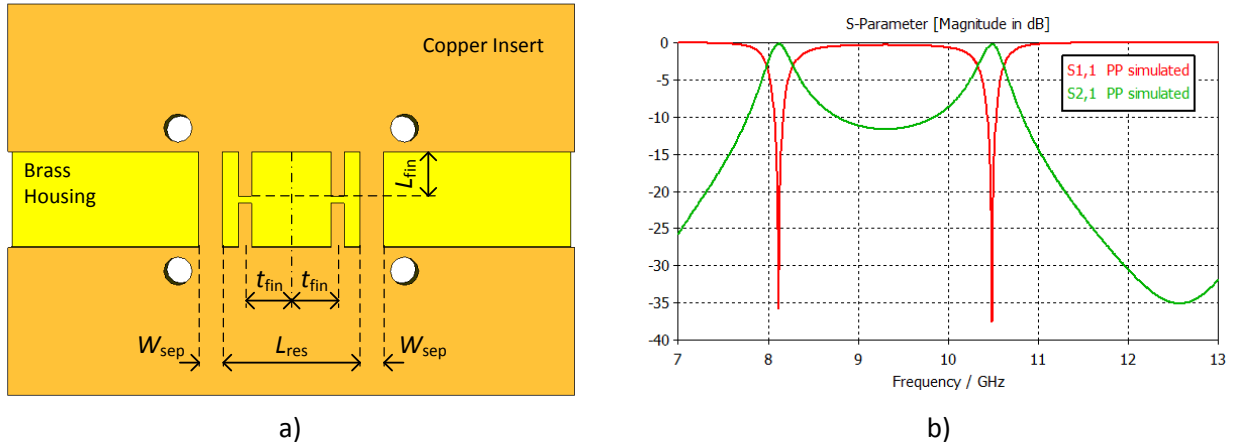
Figure 5.4 a) Resonator with labelled dimensions, and b) its simulated S-parameters.

The lower passband TP of a PP resonators is formed by the dominant TE_{101} mode. On the other side, the upper passband TP is formed by TE_{102} mode. The frequency shift between the two passbands in decreased when the ratio of the distance between the pair of discontinuities and the distance between the discontinuities and septa is increased.

We can see this from Figure 5.5 and Table 5.1, where the upper TP frequency is swiped between 1 GHz and 4 GHz from the lower TP. Another conclusion is that the resonator can realise wide range of separations between TPs, being especially effective at high separation values as the entire useful waveguide bandwidth can be covered without reaching the physical limit.
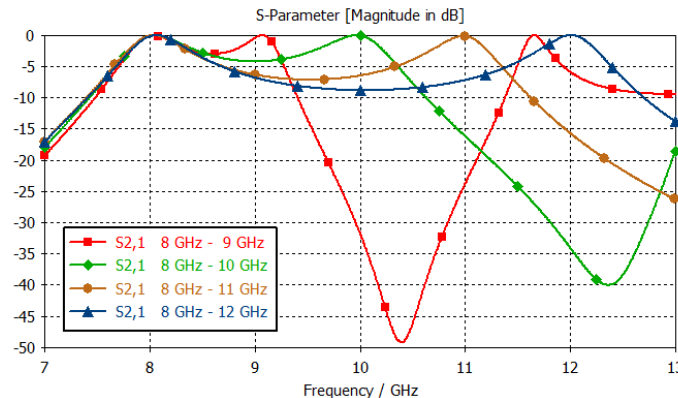
Figure 5.5 Span between 1 GHz and 4 GHz of the frequency shift that can be produced between the two resonant frequencies of PP resonator.

75

Table 5.1 Dimensions (in millimetres) of PP resonators with the lower passband at 8 GHz and variable upper passband.

Stopband width	L_{res}	t_{fin}	L_{fin}	W_{fin}	W_{fin2}
8 GHz – 9 GHz	16.0	7.1	5.0+0.8	1.5	0.8
8 GHz – 10 GHz	16.0	6.4	4.8+0.0	1.7	-
8 GHz - 11 GHz	14.0	4.2	4.5+0.0	1.4	-
8 GHz - 12 GHz	13.6	3	4.4+0.0	1.2	-

5.1.2 PZZP Resonator

In the case of PZZP resonators (Figure 5.6), the pair of offset fins yields a pair of TZs in between the two passbands. Even though it is not the principal role of the central fin, it also produces a TZ in the upper stopband not much higher from the ZZPPZZ resonator upper stopband TZs, hence aiding to the sharp skirt as well.

a)   b)
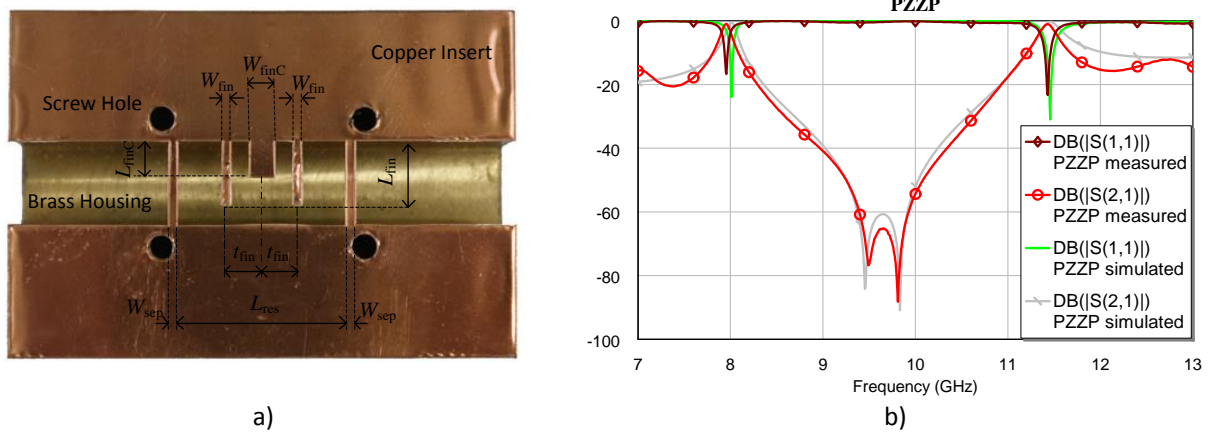
Figure 5.6 a) Fabricated PZZP resonator with labelled dimensions, and b) its simulated and measured S-parameters.

The fundamental role of the central fin can be better understood knowing that in PZZP resonator the lower passband TP is formed by TE_{102} mode, whereas the upper passband TP is formed by TE_{103} mode. Hence, this fin length almost exclusively alters the upper TE_{103} mode, whereas the lower TP produced by TE_{102} mode is effectively controlled by the distance of the surrounding pair of fins from the centre cross section plane.

In Figure 5.7 is shown changing of the upper TP frequency between 1 GHz and 4 GHz from the lower TP fixed at 8 GHz, and from Table 5.2 it can be seen how it has been utilized following the mentioned rules of TP control. Again, like ZZPPZZ resonators, PZZP resonators can achieve wide range of separations between TPs, to the maximum one able to cover entire useful waveguide bandwidth.

The measured unloaded Q factors, extracted from 2-port model are 732 and 542, respectively, for the lower and higher frequency resonances.
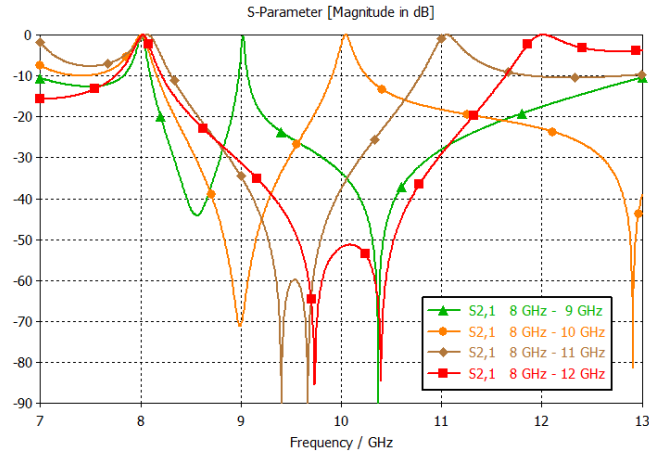
Figure 5.7 Span between 1 GHz and 4 GHz of the frequency shift that can be produced between the two resonant frequencies of PZZP resonator.

Table 5.2 Dimensions (in millimetres) of PZZP resonators with the lower passband at 8 GHz and variable upper passband.

Stopband width	L_{res}	t_{fin}	W_{finC}	L_{fin}	L_{finC}
8 GHz – 9 GHz	10.0	3.5	4.0	8.6	7.0
8 GHz – 10 GHz	14.0	5.0	4.0	8.2	5.3
8 GHz - 11 GHz	18.0	6.5	4.0	7.8	2.7
8 GHz - 12 GHz	23.0	5.3	4.0	7.5	0.0

5.1.3   ZZPPZZ Resonator

This resonator can produce two TZs in both the lower and upper stopbands. The structure is composed of two pairs of fins symmetrically positioned with respect to the centre transverse plane, and placed inside conventional resonator realized in E-plane technology (Figure 5.8). The outer pair of fins is longer and yields lower stopband TZs, whereas the inner pair is used to form higher stopband TZs.
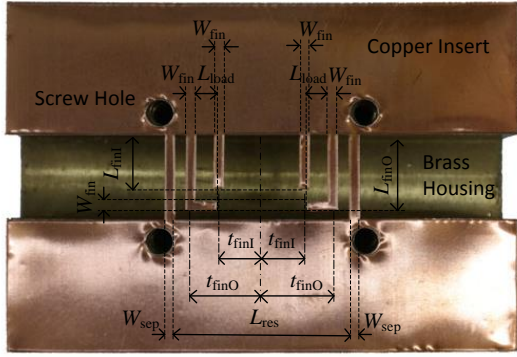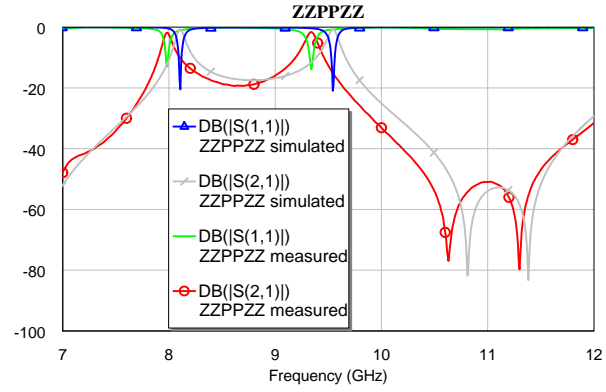
Figure 5.8 a) Fabricated ZZPPZZ resonator with labelled dimensions, and b) its simulated and measured S-parameters.

These resonators bear similarities with conventional resonator realized in E-plane technology, where the distance between the septa determines the resonant frequency and the widths of septa determine the coupling with adjacent resonators or source/load. Here, the resonator length is reduced by the use of the fins, and although it controls the span in which both the lower and upper passbands are positioned, further adjustments are made through fin positions. Likewise, apart from septa widths, couplings can be controlled by fin widths.

In ZZPPZZ resonators, the lower passband TP is formed by TE_{103} mode, whereas the upper passband TP is formed by TE_{104} mode. This explains why the higher offset of outer fins from the resonator centre dominantly shifts both TPs downwards in spectrum whereas the lower offset of inner fins from the resonator centre dominantly increases band between the two TPs.

This can be verified from Figure 5.9 and Table 5.3, where swiping the upper TP frequency between 1 GHz and 4 GHz from the lower TP is demonstrated. Also, we can draw a conclusion that these resonators are capable of realising wide range of separations between TPs, and especially high maximum separation value, which is able to cover complete useful waveguide bandwidth.

The measured unloaded Q factors, extracted from 2-port model, are 624 and 553, respectively, for the lower and higher frequency resonances.
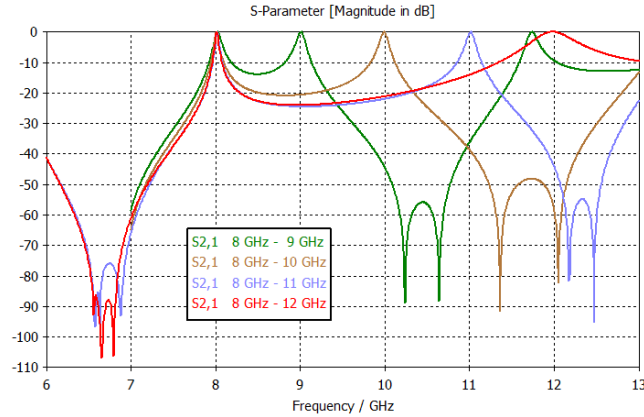
**Figure 5.9** Span between 1 GHz and 4 GHz of the frequency shift that can be produced between the two resonant frequencies of ZZPPZZ resonator.

Table 5.3 Dimensions (in millimetres) of ZZPPZZ resonators with the lower passband at 8 GHz and variable upper passband.

Stopband width	L_{res}	t_{finO}	t_{finI}	L_{finO}	L_{finI}
8 GHz – 9 GHz	21.4	8.7	6.5	8.7 +2.5	7.0
8 GHz – 10 GHz	22.0	9.0	4.0	8.8 +2.5	6.2
8 GHz - 11 GHz	23.4	9.3	2.2	8.8 +2.5	5.8
8 GHz - 12 GHz	26.4	11.2	1.8	9.0+2.5	5.0

5.1.4 E-plane Dual Band Filters

The proposed resonators, of same or mixed types, can be cascaded to form dual band filters of higher order with customized stopband characteristics. It should be noted that resonators of different types require different septa widths to realise same coupling coefficients. The filters have been designed for 0.254 mm thick Rogers 5880 substrate with rolled copper cladding.
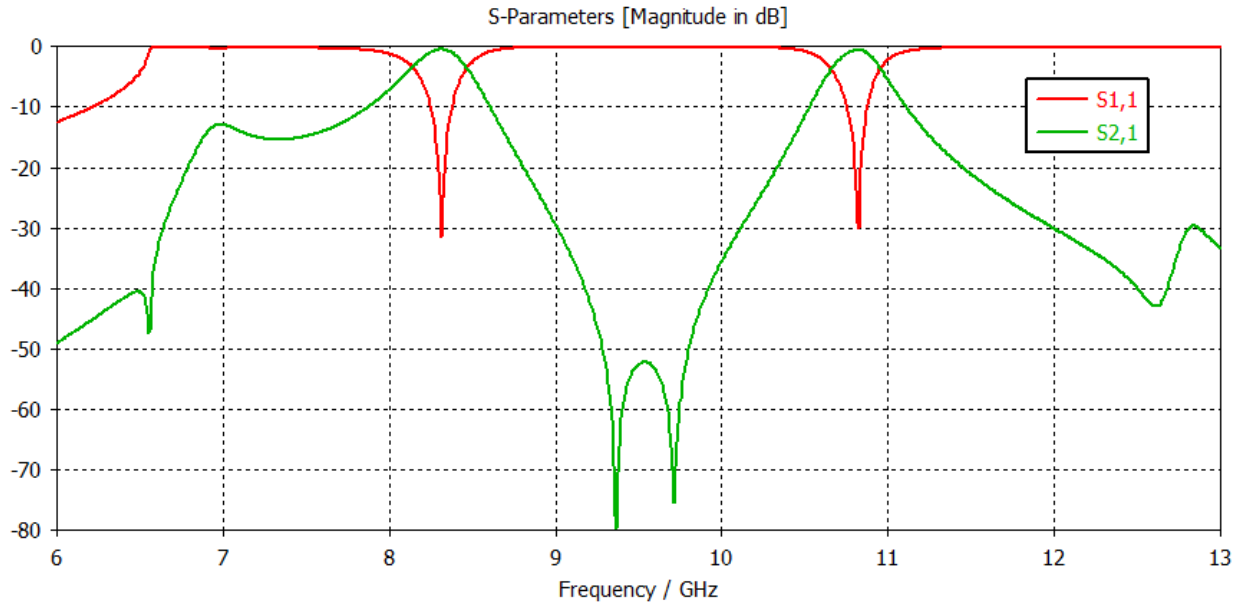
Figure 5.10 Simulated responses of PPZZPP filter.
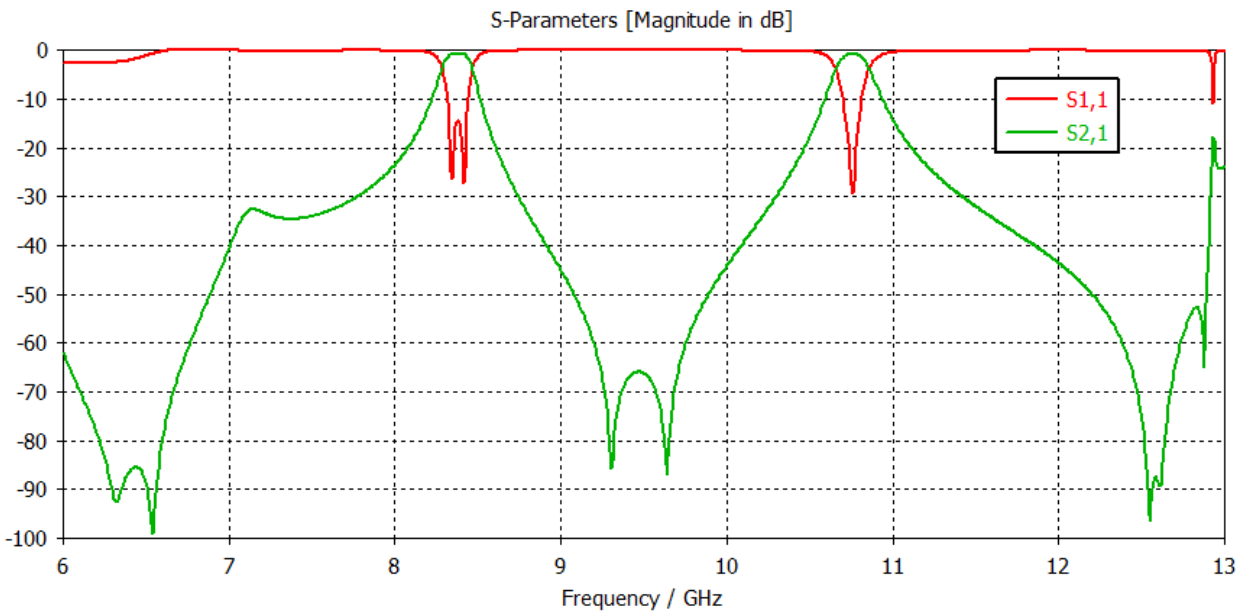
Figure 5.11 Simulated responses of ZZPPZZPPZZ filter.

5.2   Ultra Compact E-plane Diplexers

These ultra compact diplexers employ ultra compact E-plane design [4-5] for receiver and transmitter filters, which are in turn interconnected through a waveguide T-junction (Figure 5.12). The unit cells of the channel filters are doublets that can be viewed as dual mode

80

resonators from section 4.2.3 added with a fin per each of two cavities separated with the central fin, like the resonator in section 4.2.1. Consequently, the doublets produce one TZ in the lower stopband, and two TZs in the upper stopband for sharp skirts in filter response. Furthermore, the size of such a doublet is about 65% reduced in comparison with the size of related 2nd order all-pole E-plane filter.
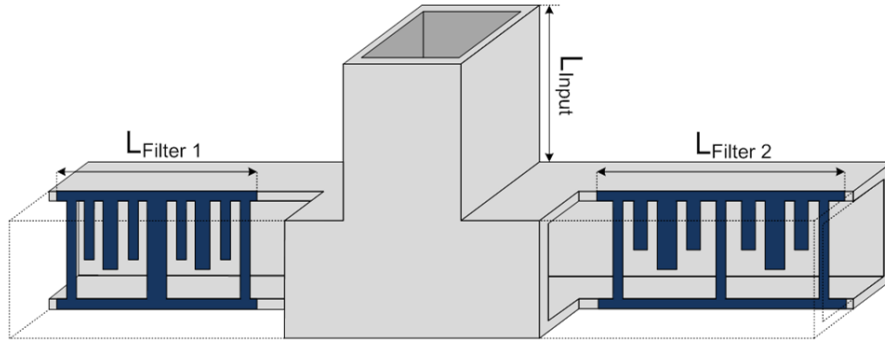
Figure 5.12 Layout of a waveguide diplexer using 4th order ultra compact E-plane channel filters.

Channel filters in the proposed E-plane diplexers are of 4th order, with the centre frequencies of 10.32 GHz and 10.60 GHz, made by cascading pairs of doublets. Their dimensions are listed in Table 5.4, where the length variables of a filter insert are labelled in Figure 5.13.

Table 5.4 Diplexer dimensions [mm].

Channel 1 Filter				Channel 2 Filter			
parameter	value	parameter	value	parameter	value	parameter	value
L_{sept1}	1.0	L_1	8.13	L_{sept1}	1.0	L_1	13.3
L_{sept2}	4.6	L_2	8.13	L_{sept2}	9.0	L_2	13.3
L_{sept3}	1.0	H_{res1}	6.52	L_{sept3}	1.0	H_{res1}	5.9
W_{res1}	1.0	H_{res2}	7.60	W_{res1}	1.0	H_{res2}	7.1
W_{res2}	2.0	H_{res3}	6.52	W_{res2}	1.1	H_{res3}	5.9
W_{res3}	1.1	H_{res4}	6.52	W_{res3}	1.0	H_{res4}	5.9
W_{res4}	1.1	H_{res5}	7.60	W_{res4}	1.0	H_{res5}	7.1
W_{res5}	2.0	H_{res6}	6.52	W_{res5}	1.1	H_{res6}	5.9
W_{res6}	1.0	*Total length*	22.86	W_{res6}	1.0	*Total length*	37.6
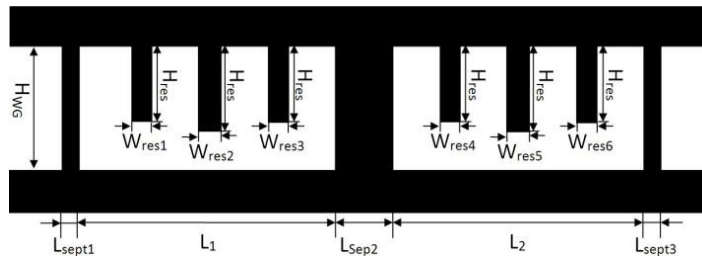
Figure 5.13 E-plane insert of a 4th order ultra compact waveguide channel filter.

In Figure 5.14 are given transmission responses between the common port (port 1) and channel 1 and channel 2 ports, as well as reflection responses of these two channel ports. It can

be seen that the inner rejection level is not less than 60 dB. In addition, the cross over attenuation is around 35 dB.
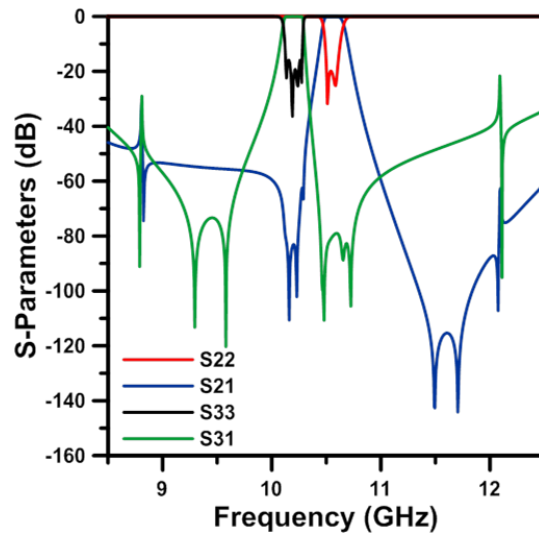
Figure 5.14 Simulated S-parameter responses of the proposed ultra compact diplexer.

References

[5-1]   R. I. Cameron and M. Yu, "Design of manifold-coupled multiplexers," *IEEE Microwave Magazine*, vol. 8, no. 5, pp. 46-59, Oct. 2007.
[5-2]   G. Macchiarella and S. Tamiazzo, "Design of "masthead" combiners," *2015 European Microwave Conference (EuMC)*, Paris, 2015, pp. 686-689.

6. Additive and Hybrid Manufactured Cavity Filters

Being tailored for fabricating high complexity and lightweight 3D structures, surging additive manufacturing technologies have outstanding potential for application in waveguide technology. 3D printing is not used here only for the purpose of rapid prototyping of the filters, but design for additive manufacturing (DFAM) paradigm is followed.

6.1. Low-Cost Hybrid Manufactured Waveguide Bandpass Filters with 3D Printed Insert Dielectric

Fabrication technology is an important area of improvement for waveguide filters. We are witnessing the years of great expansion of additive manufacturing and so far filters implemented as both conventional waveguide structures [6-1], [6-2] as well as SIW structures [6-3] have been made by 3D printing of polymers and their subsequent metallization. Nevertheless, they suffer from problems with the plastic-metal interface, no matter if the plastic is located on the outer or inner side of the metal walls. Main issues are with large scale surface roughness of the polymer caused by its layered fabrication, and the metallization process itself, either using electrochemical deposition, or covering with metal tape. Here, 3D printing is chiefly utilized to create holders for complex object positioning and subtractive technologies are still used to fabricate critical metal parts so as to maintain high performances.

Classical direct-coupled waveguide filters have shunt inductive discontinuities realized as diaphragms, posts or circular irises [1-48]. E-plane waveguide filters [4-1] were later introduce as alternative for cost effective mass production. Downsides of using E-plane inductive strips are worse upper stopband and increased filter length, which is particularly pronounced for narrower bandwidths.

The aim of the proposed hybrid manufactured filters is to add fabrication benefits of E-plane discontinuities to transverse discontinuities, which have size and performance advantages. They are very suitable for prototyping, as it takes less than 2 hours for an entire 3rd order filter insert to be fabricated using currently affordable desktop machines and materials. Furthermore, no demanding process such as metal plating is necessary, hence mostly automated procedure can be repeated as many times as needed to obtain good experimental results. Unlike conventional realisations, the one being described here can be used with monolithic waveguide sections, not only simplifying production, but also being able to completely eliminate signal leakage.

6.1.1 Rectangular Ring Discontinuities

Standard inductive diaphragms (FIG. 8.06-1,2 in [1-48]) rely on electrical connection between the conductors of the diaphragm and the housing. The response is very sensitive to the gaps that can appear next to the top and bottom H-plane side walls, introducing series capacitances in the shunt discontinuity networks inversely proportional to the gap height. During our initial

experimental attempts, good metal contact with the housing could not be achieved when using independent filter insert composed solely from 3D printed polymer and cut copper diaphragms, repeatedly obtaining responses without a distinctive resonance.

In order to stabilize the response, two side of symmetrical diaphragm are first connected by top and bottom sections to form a rectangular iris. Now, when the rectangular iris is detached from the waveguide side walls, it emerges as a connected rectangular ring discontinuity (Figure 6.1) with significantly larger gap capacitances due to longer outer H-plane ring edges. In the frequency range of interest, the newly formed rectangular ring can be approximated by a series inductor. This inductance is mainly increased by enlarging the ring hole area and reducing ring metal surface to produce higher magnetic flux.

Thus, around the passband, the rectangular ring can be represented by a series LC network, whose antiresonant frequency in the lower stopband can be pushed up to increase roll-off either by decreasing gap capacitance or ring inductance. At the same time, this shunt network needs to have selected negative susceptance in the passband to control the couplings of waveguide resonators.
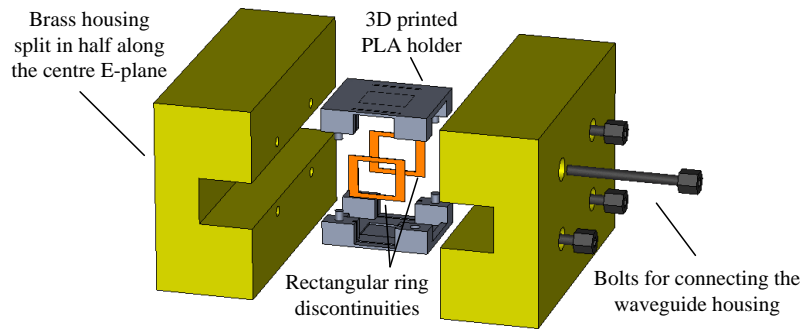
Figure 6.1 Proposed waveguide resonator: metal rings milled from a copper sheet are enclosed within a 3D printed thermoplastic holder to form an insert that can be put inside a brass waveguide housing.

6.1.2 Resonator

A cavity resonator is formed by positioning two rectangular rings in transverse waveguide planes so that the dominant quasi TE_{10} mode sees 180° phase difference between them at the transmission pole (TP) frequency. The resonator which exploded view drawing is given in Figure 6.1 is inside WR 90 waveguide housing with inner ring dimensions of 6 mm x 6 mm, horizontal ring thickness of 2.4 mm, vertical ring thickness of 1.4 mm, and the distance between the two rectangular rings of 14.7 mm.

Insert holders have the main task to keep the distance between the rings, at the same time tightly positioning them within their cross sections. Holders have been fabricated by fused deposition modelling (FDM) method with Ultimaker 2+ Extended 3D printer and 0.4 mm nozzle for extruding heated PLA filament. It was chosen that the melted PLA is deposited in 0.05 mm thick H-plane layers (vertical resolution). In addition, the shell thickness was set to 0.4 mm and the top and bottom layer thicknesses to 0.2 mm, whereas the enclosed volume was selected to be 40% filled with PLA. Lower fill densities experimentally proved to have less spurious effects.

Since PLA material properties are not optimized for EM applications, the holder was shaped to be inclined towards low passband dielectric losses in the tradeoff with the size. Thus, it provides support along all the principal waveguide axes, but is hollow in the central parts of ring and cavity resonators, where the strongest EM field is localized. Before an insert is ready for use, it is often needed to remove PLA residues in several locations, the hardest ones being spots in inner corners.

The rings have been cut out of 0.1 mm thick copper foil with the ProtoMat C60 milling unit. Influence of ring bending can be reduced by using thicker copper sheet as well as by taking care of 3D printing imperfections. For that reason, slits holding rectangular rings were set for printing slightly wider than the copper thickness with the aim to prevent the hot PLA bonding over them.

In Figure 6.2 are shown simulated and measured resonator S-parameters. The dominant resonant mode TP is at $f_0 = 11.13$ GHz, with the bandwidth $\Delta f_{3dB} = 157$ MHz. The transmission zeros (TZs) are essentially at the same frequency of around 8.7 GHz as the two synchronously tuned rectangular rings are mutually loosely coupled, having the coupling coefficient $k_R = 0.0021$. The full wave EM analysis was performed using CST Studio Suite [CST]. Dielectric modelling was simplified and simulation time reduces by using effective medium approximation [6-3] for PLA characteristics instead of applying exact inner geometry specified to the 3D printer in the G-code file, which is by itself prone to fabrication irregularities.
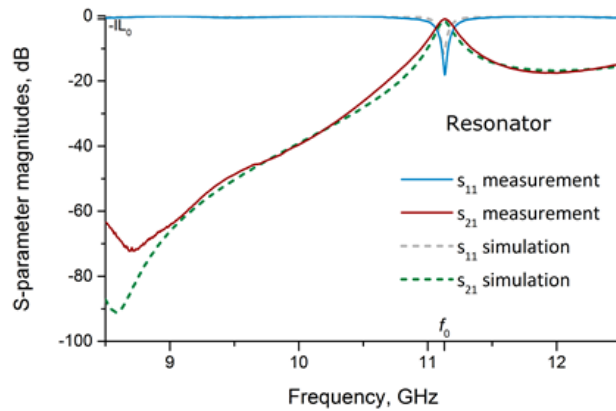
Figure 6.2 X band resonator simulated and measured frequency responses.

The coupling coefficient between the rings was calculated by directly exciting one of the rings with a discrete source, keeping the closest waveguide port matched with the wave impedance, and having in one case PEC and in the other PMC wall between the two rings. CST Eigenmode Solver, which is the preferable tool for extracting a coupling coefficient, could not be used because it requires the structure being completely enclosed within PEC, which was violated by the existence of the matched waveguide port. So as to least disturb the natural modes of operation and natural frequency of the ring, weak coupling to the resonator is typically used [3-3], [1-51]. In order not to additionally disturb the setup, any probes were avoided, and a 0.1 mm gap was made in the centre of the bottom H-plane ring section to place the discrete port. Relatively good matching with its 10 Ω impedance was obtained, chosen to minimize the frequency shift like with weak coupling. Finally, equation $k_R = \frac{f_e^2 - f_m^2}{f_e^2 + f_m^2}$ for two synchronously tuned resonators [3-3],

sec. 8.2, was applied, where $f_m = 8.752$ GHz is the resonant frequency with PMC at the symmetry plane, and $f_e = 8.770$ GHz is the resonant frequency with PEC at the symmetry plane ($f_e > f_m$).

Unloaded quality factor of the resonator obtained from the transmission S-parameter measurement of symmetrical network is $Q_u = \frac{f_0}{\Delta f_{3dB}}/(1 - 10^{-IL_0/20}) = 624$.

Application of commercial desktop FDM printers is not limited to X band structures. In Figure 6.3 is shown an insert for hybrid manufactured resonator with ring discontinuities designed at 28.5 GHz centre frequency and printed with Ultimaker 2+ Extended 3D printer using 0.25 mm nozzle [P-2]. For the sake of sturdiness, the insert now looks more like a solid block, nevertheless, it is still hollow in the centre.
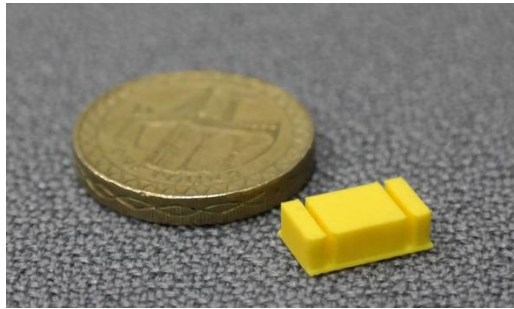
Figure 6.3 Printer insert dielectric for WR 28 waveguide made using Ultimaker 2+ Extended 3D printer.

6.1.3   Higher Order Filters

In order to test the proposed filter structure, a 3rd order unit has been designed. Its fabricated insert, now containing 4 rings, is displayed in Figure 6.4 together with the assembled filter after testing with the Agilent Technologies E8361A PNA Network Analyzer.
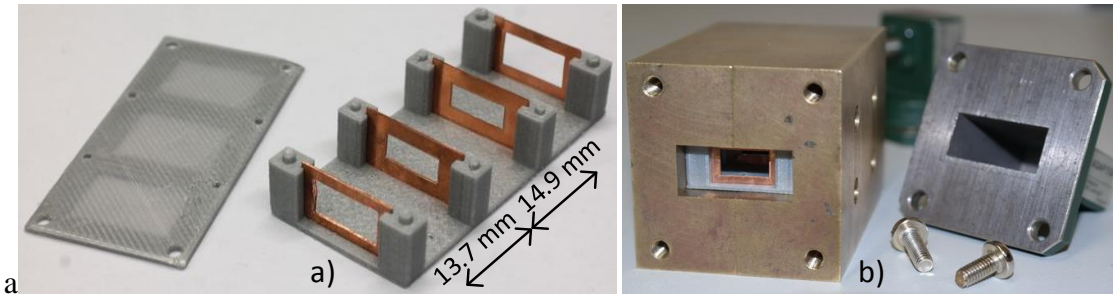
Figure 6.4 Photographs of a) 3rd order filter insert with asymmetrical holder and b) complete filter with removed waveguide to coaxial adapters. Grained texture of the bottom part of this sample is due to low infill percentage.

In the resonator case, the thermoplastic holder was built from two equal parts (Figure 6.1) that can interlock with each other along the centre H-plane through pins and holes, similar to Lego bricks. This is very useful in terms of need to design just one half of the holder, while the

interlocking also deals with the issue of misalignment. Nevertheless, another interlocking H-plane near waveguide sidewall was gradually adopted for higher order filters (Figure 6.4*a*) to allow for easier connecting of the two PLA parts together that does not require additional care about ring alignments.

The dimensions of the fabricated filter are presented in Table 6.1 and the corresponding layouts are in Figure 6.5, where inner waveguide dimensions are $a = 22.86$ mm and $b = 10.16$ mm. The top and bottom dielectric layer thicknesses are $T_B = 1$ mm. Fill density of 15% was used in this case.

Table 6.5 Designed 3rd order filter dimensions in millimetres

Filter element	Dimension				
	a_r	b_r	W_{ar}	W_{br}	W_P
Inner ring	8.6	3.8	3.6	2.8	4.1
Outer ring	10.0	5.4	2.2	2.0	4.8
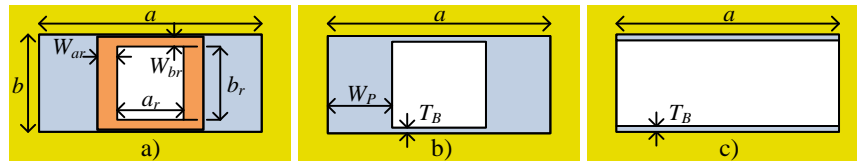
Figure 6.5 Filter transversal cross sections: a) ring plane, b) plane of dielectric that holds the ring in place along the longitudinal direction, and c) waveguide sections containing top and bottom dielectric slabs as parts of the insert.

In Figure 6.6 are given the results of this measurement, compared to the simulation responses. A very good overlapping of the two has been achieved when small undercutting of 0.1 mm on each edge of the rings made by the circuit board plotter had been taken into account.
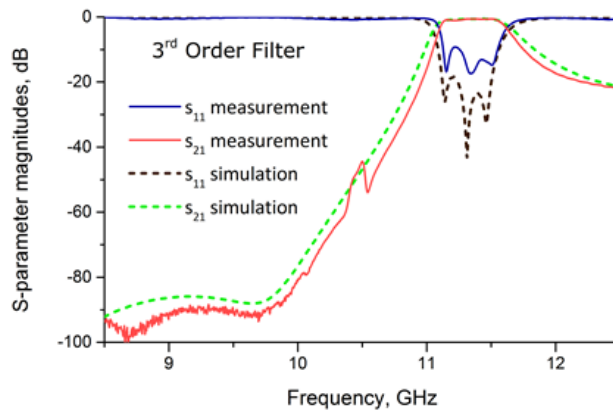
Figure 6.6 Simulated and measured S-parameters of the designed and fabricated 3rd order bandpass filter with 3D printed insert dielectric.

The filter has 4.6% 3 dB fractional bandwidth. Measured insertion loss at the centre passband frequency of $f_0 = 11.36$ GHz is about 0.6 dB. and it is not higher than 1 dB between 11.15 and 11.55 GHz. The first upper spurious TP is at 1.39 x f_0, which is 20% larger difference than in the case of a corresponding E-plane filter. The locations of the two pairs of finite TZs are 8.65 GHz, produced by outer rings, and 9.7 GHz, produced by inner rings.

In Figure 6.7 are plotted together s_{21} responses of the 3rd order filters with rectangular ring and other common waveguide filter discontinuities. In the lower stopband, the proposed filter has steepest transition from the passband to the stopband with the help of two pairs of transmission zeros. Although that is compensated in the upper stopband with the least steep transition, the first spurious passband is still further away than for the E-plane filter. Moreover, the presented filter is 34.3% shorter than the E-plane counterpart.
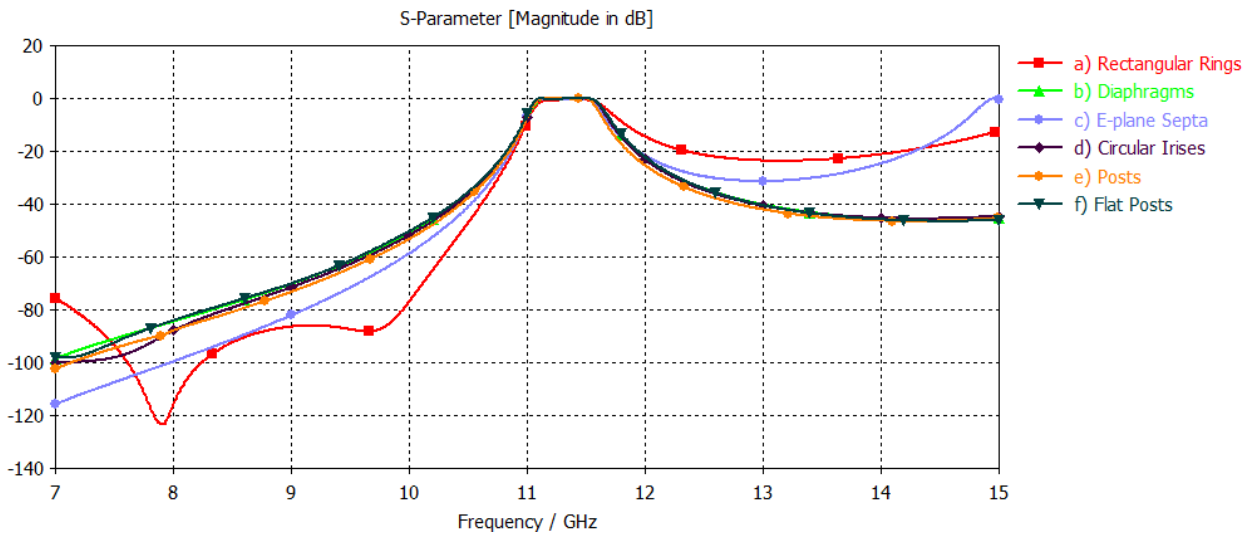
Figure 6.7 Comparison of the transmission S-parameters belonging to 3rd order direct-coupled filters with different types of discontinuities to realize impedance inverters.

Hybrid manufactured waveguide bandpass filters with rectangular rings can, in fact, feature both inductive and capacitive couplings. In Figure 6.8 is shown such a filter together with its frequency responses. It produces 3 TZ in the lower stopband and 2 TZ in the upper stopband. Rectangular rings that produce capacitive couplings are of smaller sizes than those which produce inductive couplings.
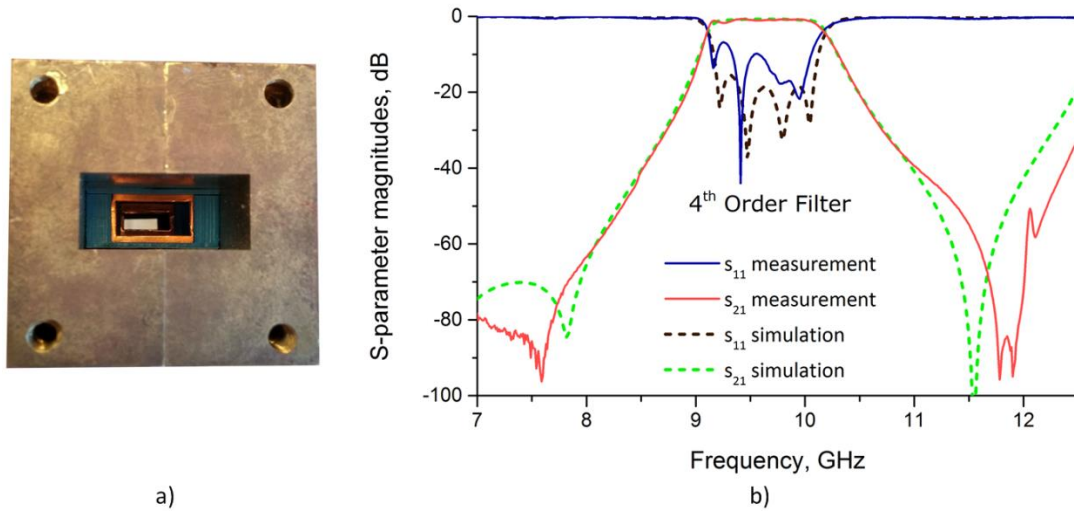
Figure 6.8 a) One-point perspective along fabricated 4th order bandpass filter with 3D printed insert dielectric inside its waveguide housing, and b) simulated and measured S-parameters of this structure.

6.2. Low-Profile High Q Integrated 3D Printed Cavity Filters

3D printing has been used for fabrication of high Q lightweight resonators which are otherwise very difficult to produce, such as minimum loss spherical ones [6-4] or others with more complex geometries that take into consideration spurious free band [6-5]. On the other side, waveguide cavity problems with cost, bulkiness and integration with planar technologies have given rise to SIW technology [6-6]. Nevertheless, SIW filters have noticeably higher losses than conventional waveguide filters and are harder to manufacture than microstrip filters due to numerous vias. There have been attempts to address these issues with approaches like [6-7], which, however, introduce more complex fabrication, but still do not reach the full potential of loss reduction.

Like planar filters, the proposed filters have constrained height, are lightweight, can be quickly and cheaply fabricated and can be integrated with other planar components by mounting on the same substrate. Nevertheless, by the means of additive manufacturing, performances are enhanced in terms of ease of fabrication, reduced insertion loss due to optimized resonator shapes, and the ability to control tradeoff between high resonator Q factors and the upper stopband performance.

6.2.1. High Q Low-Profile Resonators

The proposed resonator is axially symmetric. It can be generated by revolving a half-disk connected to the axis of symmetry by a disk diameter wide strip (Figure 6.9). Described solid has the lowest surface area to volume ratio (minimum isoperimetric quotient) in the volume

constrained by two parallel planes, degenerating to a ball when the distance between the planes is large enough.

This can be shown using the classical isoperimetric problem, which solution is a ball (disk in 2D). Firstly, since the resonator limits are only in vertical direction, it is clear that the body has axial symmetry, reducing the problem to 2D one. If the optimal shape is split by two vertical dashed lines like in Figure 6.9 a), and the two outer parts are glued together (the lines have to cross each other because of axial symmetry), both parts have maximum isoperimetric quotients in their respective regions under the same bounds. (E.g. this can be tested against rectangle/cylinder and ellipsoid/ellipse shapes).

The resonator can be easily modelled by adding concentric and equally axially oriented torus and cylinder. The height of the cylinder (H) is twice the minor radius of the torus ($r = H/2$), and the radius of the cylinder is equal to the major radius of the torus (R). One more way of modelling the resonator is by blending edges of a cylinder with the radius $R + r$ and height $2r$. In that case, the radius of blending is r. Initially, circles in CST Microwave Studio [CST] were approximated by polygons with 64 edges. In later simulations, 2nd order curved elements were used in meshing of the resonators with curved surfaces.

a)   b)
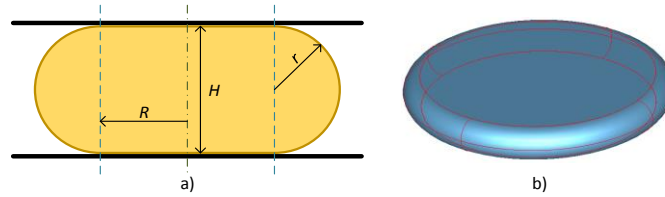
Figure 6.9 Proposed resonator: a) cross section in the shape of elongated circle and b) 3D shape.

Since $R \gg H$, the dominant mode in the resonator is quasi TM_{010}[16] (the lowest mode in cylindrical resonator with such R and H dimensions, Figure 6.10), having the longitudinal direction along the resonator height. (It corresponds to TE_{101} mode of rectangular cavity in which longitudinal direction is horizontal.) As H is increased, this mode transforms into TM_{011}[17] mode of spherical cavity (radius is longitudinal, but z is aligned with the height). In addition, the first two higher order degenerate modes, quasi $TM_{110,}$ also have good separation from other modes and can be used in filter design. (This can be well observed from the right hand side of cylindrical cavity mode chart. For $H<R$, the second resonance is at 1.59 times higher frequency than the first one.) The tradeoff between the lower losses and better separation from the spurious modes can be adjusted through the resonator height.

a)   b)   c)
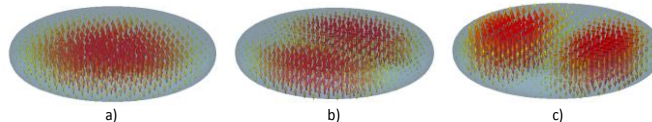
Figure 6.10 Resonant electric field: TM_{010} mode, a), and degenerate TM_{110} modes, b) and c).

---

16 The indices are used in the order (ϕ,ρ,z).
17 The indices are used in the order (ϕ,θ,ρ).

The quality factor of TM_{010} and TM_{110} modes calculated by CST eigenmode solver for the ideal case of perfectly smooth surface silver plated walls ($\sigma = 63$ MS/m) in $H = 4$ mm high resonators at 10 GHz are 4988 ($H/R = 0.336$, R=11.9) and 5450 ($H/R = 0.214$, R=18.7), respectively. However, if the walls are sprayed with Solemi copper conductive paint ($\sigma = 0.4$ MS/m), theoretical unloaded Q is 504. When TM_{110} are resonant at 10 GHz in ideal cavity, TM_{010} NRN resonates at 6.29 GHz.

6.2.2. Filter Design

To illustrated application of the proposed low-profile high Q TM_{010} and TM_{110} resonators, a fourth order filter with one transmission zero in each stopbands has been designed. The result of normalized baseband polynomial synthesis of generalized Chebyshev response is:

$$\varepsilon K(s) = \varepsilon \frac{F(s)}{P(s)} = 13.12 \frac{(s+0.91)(s+0.30)(s-0.47)(s-0.94)}{(s+8.48)(s-2.06)}. \tag{6.1}$$

The non-realizable asymmetric lowpass S-parameter responses derived from the characteristic function in (6.1) are plotted in Figure 6.11.
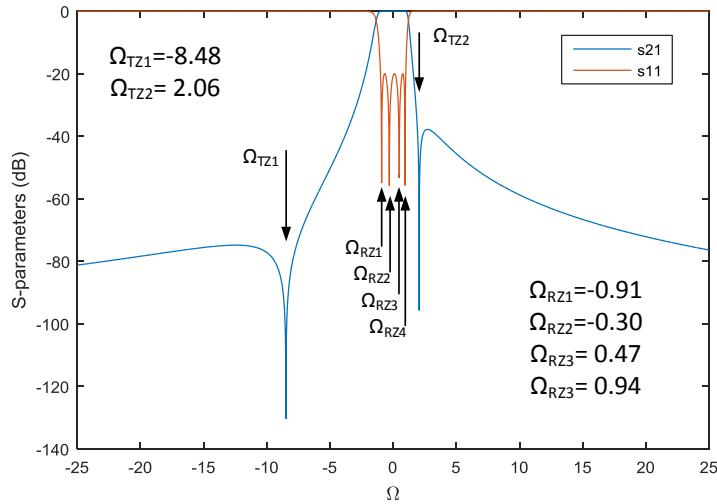
Figure 6.11 Lowpass prototype response with labeled normalized frequency values of transmission and reflection zeros.

The layout of the bandpass filter can be seen in Figure 6.12 a). TM_{010} modes are resonant in the passband in the two cavities adjacent to the filter ports, whereas TM_{110} modes are resonant in the passband in the large central cavity. In the coupling diagram, the former refer to the green nodes 1 and 4, whereas the latter refer to the blue nodes 2 and 3. Important for the filter response is also the non-resonating node (NRN), which is basically realized by another resonance outside the passband collocated inside the large cavity. The form of the coupling matrix given in Table 6.2 was instrumental for finding the values of the couplings through optimization, since it defines which coupling values are mutually equal, which have opposite signs, and which are zeros.

91

a)   b)
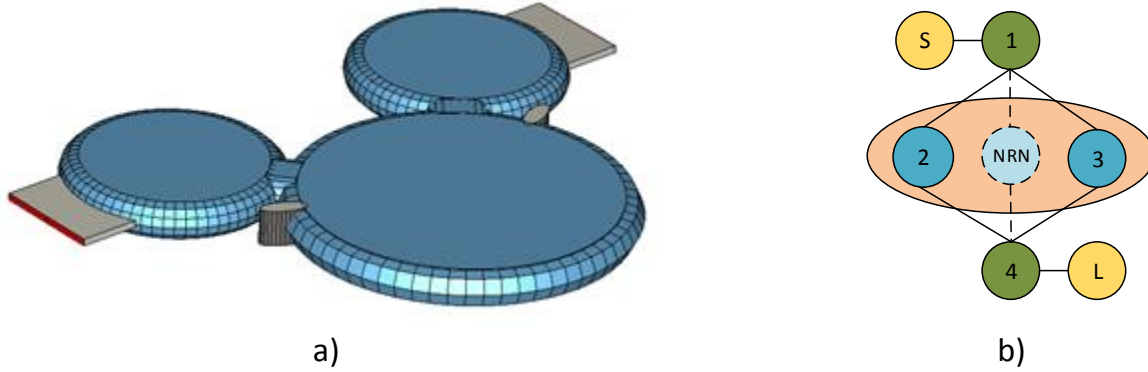
Figure 6.12 a) 3D model and b) coupling diagram of a 4th order low-profile high Q integrated cavity filter for 3D printing.

Table 6.2 Coupling matrix referring to the coupling diagram in Figure 6.12: $M_{S1} = 1.08$, $M_{12} = 0.76$, $M_{1NRN} = 1.06$, $M_{13} = 0.60$, $M_2 = 0.60$, $M_{NRN} = 44.00$, $M_3 = -0.87$

	S	1	2	NRN	3	4	L
S	0	M_{S1}	0	0	0	0	0
1	M_{S1}	0	M_{12}	M_{1NRN}	M_{13}	0	0
2	0	M_{12}	M_2	0	0	M_{12}	0
NRN	0	M_{1NRN}	0	M_{NRN}	0	M_{1NRN}	0
3	0	M_{13}	0	0	M_3	$-M_{13}$	0
4	0	0	M_{12}	M_{1NRN}	$-M_{13}$	0	M_{S1}
L	0	0	0	0	0	M_{S1}	0

Finally, the filter was realized according to the coupling matrix values. Its frequency responses are given in Figure 6.13. The center frequency is $f_0 = 10$ GHz, lower passband limit is at $f_{L3dB} = 9.88$ GHz, and upper passband limit is at $f_{U3dB} = 10.13$ GHz. Also, lower TZ is at $f_{TZL} = 9$ GHz, and upper TZ is at $f_{TZU} = 10.265$ GHz.
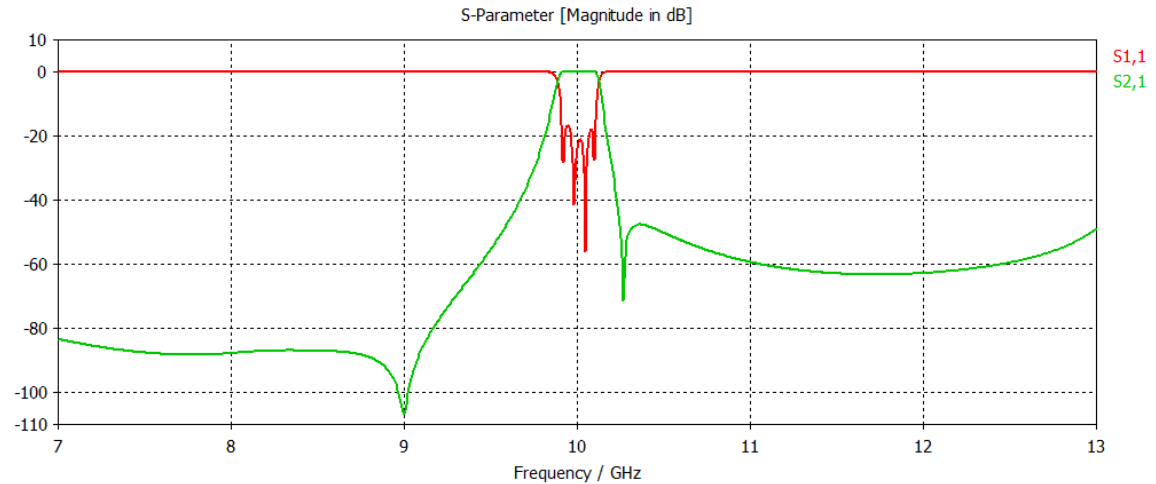
Figure 6.13 S-parameters of the filter in Figure 6.12, simulated by F solver of CST Studio Suite.

References

[6-1]   Saucourt, J., et al.: 'Design of 3D printed plastic modular filters', *46th European Microwave Conference (EuMC)*, London, UK, October 2016, pp. 369-372

[6-2]   Guo, C., Shang, X., Lancaster, M. J., Xu, J.: 'A 3-D Printed Lightweight X-Band Waveguide Filter Based on Spherical Resonators', *IEEE Microwave and Wireless Components Letters*, vol. 25, no. 7, pp. 442-444, July 2015

[6-3]   Tomassoni, C., Bahr, R., Tentzeris, M., Bozzi, M., Perregrini, L.: '3D printed substrate integrated waveguide filters with locally controlled dielectric permittivity', *46th European Microwave Conference (EuMC)*, London, UK, October 2016, pp. 253-256

[6-4]   Guo, X. Shang, M. J. Lancaster and J. Xu, "A 3-D Printed Lightweight X-Band Waveguide Filter Based on Spherical Resonators," *IEEE Microwave and Wireless Components Letters*, vol. 25, no. 7, pp. 442-444, July 2015.

[6-5]   P. Booth and E. V. Lluch, "Enhancing the Performance of Waveguide Filters Using Additive Manufacturing," *Proceedings of the IEEE*, vol. 105, no. 4, pp. 613-619, April 2017.

[6-6]   X. P. Chen, K. Wu and D. Drolet, "Substrate Integrated Waveguide Filter With Improved Stopband Performance for Satellite Ground Terminal," *IEEE Transactions on Microwave Theory and Techniques*, vol. 57, no. 3, pp. 674-683, March 2009.

[6-7]   Belenguer, M. D. Fernandez, J. A. Ballesteros, H. Esteban and V. E. Boria, "Experimental study in Ku-band of the propagation inside Empty Substrate Integrated Waveguides," *46th European Microwave Conference (EuMC 2016)*, London, 2016, pp. 639-642.

7. Substrate Integrated Waveguide Circuits

This sample structure in Figure 7.1 shows implementation of 4th order direct-coupled cavity filter in the substrate integrated waveguide (SIW) technology. In fact, it was designed according to the same specification of V band base station filter as the direct-coupled E-plane filter in chapter 4. In Table 7.1 and Figure 7.2 can be found all the details about the dimension of the filter as well as the materials used. It is clear that the height of the filter has been drastically reduced compared to the standard waveguide implementation, from 2.388 mm to 0.381 mm just for the inner side, not even including that metal waveguides have much thicker walls and the size of waveguide flanges. Expectedly, this comes at the cost of increased losses (Figure 7.3) and reduced power handling capacity.
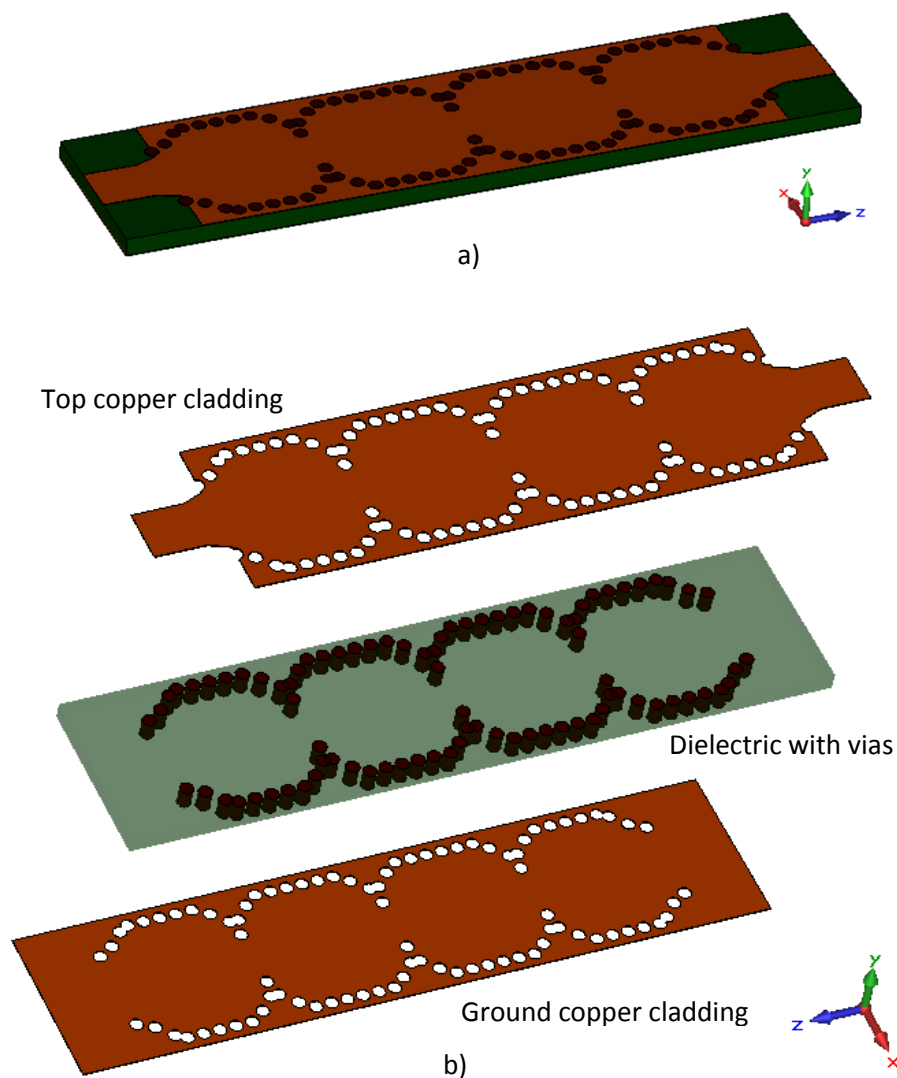
Figure 7.1 a) Isometric and b) exploded views of a V band direct-coupled filter in SIW technology with resonators in the shape of generalized cylinder over a squircle.

Furthermore, SIW structures can have increased complexity of geometry in one horizontal layer practically at no additional cost. Thus, the resonators are slightly rounded, which increases their Q factors, since a cylinder has the highest Q of all 2D defined cavity resonators.

Table 7.1 SIW laminate characteristics

Substrate		Copper cladding		Vias	
Rogers RT/duroid 5880 high frequency laminate		electrodeposited copper		Via (outer) diameter	$D = 0.3$ mm
Dielectric constant	$\varepsilon_r = 2.2$	Metallization thickness	$H_{met} = 17$ μm	Via pitch	variable, but $\leq 2D$
Loss tangent	$\tan\delta = 0.0009$ (value specified at $f = 10$ GHz)	RMS surface roughness	$R_q = 1.8$ μm		
Substrate thickness	$H_{sub} = 0.381$ mm	Inside effective conductivity of copper	$\sigma_{Cu,clad} = 15.43$ MS/m		
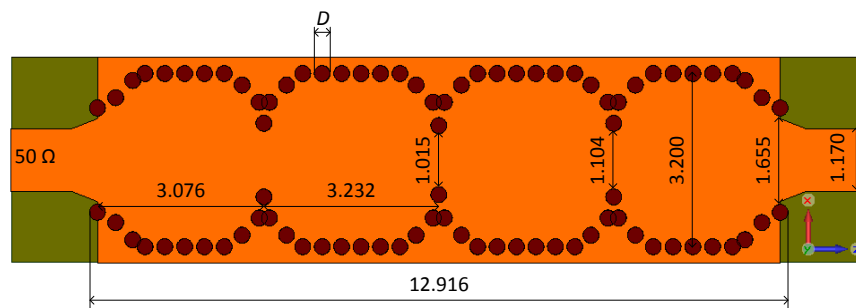
Figure 7.2 Layout of the V band direct-coupled SIW filter with dimensions in millimetres.
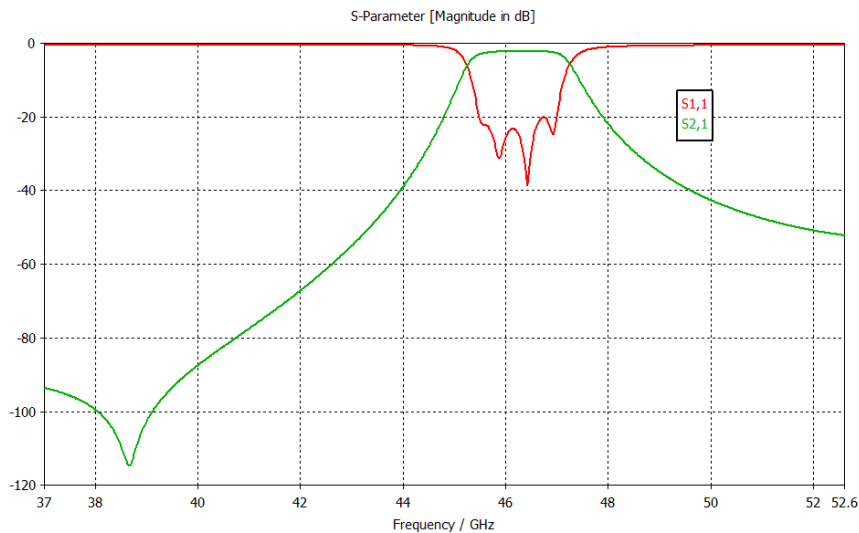
Figure 7.3 S-parameter of the 4th order SIW filter network from Figure 7.1.

95

Nevertheless, SIW filters have also over time undertaken significant improvements regarding miniaturization and utilizing more complex filtering functions. In the following section is introduced one such design.

7.1   Substrate Integrated Waveguide Filters Using Dual-Mode Cavities With Diagonal Slot Line Perturbations

Substrate integrated waveguide technology represents a compromising solution between the waveguide and microstrip technologies. With its structure forms, working principles and design procedures it closely resembles the former, whereas practical implementation is like in the latter. Characteristic feature are side walls made out of arrays of via-holes.

This tradeoff is advantageous because waveguide technology has essential high-performance benefits of low-losses, high power handling capability and excellent electromagnetic shielding. However, the conventional waveguide technology lacks compactness, easy and inexpensive fabrication procedures as well as simple transition to planar transmission lines, which are available with printed circuit board designs and much desired in modern electronic systems. The first SIW was introduced in [7-1] as a feed waveguide, and its full integration with a microstrip line on the same substrate, using tapered line transition, in [7-2]. SIW designs are particularly well targeted to be integrated in highly packed millimeter-wave circuits requiring high Q factors for massive communication applications [7-3].

Inside resonators of dual-mode filters can exist pairs of degenerate modes instead of just singe ones, halving the number of physical resonators required for a filter of a certain order. Proposals of space saving dual-mode bandpass filters in different technologies have been milestones in the history of microwave filters. The idea of cavities excited with more than one mode can actually be traced back to the very early development of microwave filters [7-4]. Practical dual-mode waveguide filters with elliptic responses and linear phases were realized many years later becoming the satellite industry standard [7-5]. Similarly, among the most important developments within dielectric resonator filters were inline dual-mode devices [7-6]. Further on, in the area of planar filters, it was commencement of dual-mode patch and ring filters reported in [7-7], which are also well suited for implementation using high temperature superconductors.

A well-known approach for obtaining folded dual-mode SIW cavities is placing a pair of posts (vias) along a diagonal of a square shape cavity with port lines connected to adjacent cavity walls, as concisely reviewed in [7-8]. Apart from two poles in the passband, this configuration is able to create additional two finite TZs distributed on both sides of the passband as a result of source-load bypass coupling. In the same paper, it is explained how to control intracavity coupling between degenerate modes changing the distance between posts, as well as how to change locations of TZs by shifting the positions of the ports. In addition, an alternative way of now non-degenerate mode coupling with a rectangular shape cavity is proposed in [7-8]. Another way to excite degenerate modes for passband signal transmission that has been reported is by using a pair of slots [7-9]. There are rectangular shaped inline variations, with ports at opposite sides of a cavity: frequently used ones, without additional perturbation elements, but with just

single transmission zeros [7-10]; with etched coplanar waveguide section [7-11]; or a slot with less selective Chebyshev response [7-12]. Also, different cavity shapes have been used for dual-mode designs, like circular and elliptic [7-13] and hexagonal [7-14].

7.1.1 Dual-mode Resonant Cavities

Analysis and Design

Figure 7.4 depicts the proposed SIW dual-mode resonator. In the first approximation, let us assume that the cavity side walls are also made of solid metal, i.e. we have a low-profile dielectric-filled waveguide resonator. Since the substrate thickness is much smaller than the other two dimensions, the electric and magnetic field over this coordinate are virtually constant at the frequencies of interest. In other words, if assigned coordinate system is like in Figure. 7.4 and the *z*-axis represents longitudinal direction, the second index in the dominant mode and in all the modes close to it in frequency is zero. Moreover, this means that only TE modes exist, as TM modes cannot have either of the first two indices zero. Now, the choice of modes we can use is reduced to be between TE$_{m0n}$ (*m*, *n* $\in$ N) modes, with the resonant frequency of a mode given by

$$f_r = \frac{c}{2a_{RWG}}\sqrt{m^2 + n^2}, \tag{7.1}$$

where a_{RWG} are lengths of the longer sides of the rectangular cavity and c is the speed of light in the substrate dielectric medium. With the solution space reduced in this way, the choice of TE$_{102}$ and TE$_{201}$ degenerate modes (nodes 1 and 2 in the Figure 7.5) as active ones becomes natural. It is also practical to start modelling and simulation with this kind of simplified dielectric-loaded waveguide structure and to transform it to exact model only after reaching dimensions that are close to the final ones. This is more time efficient, especially because full-wave simulation of SIW structures is in general computationally demanding.
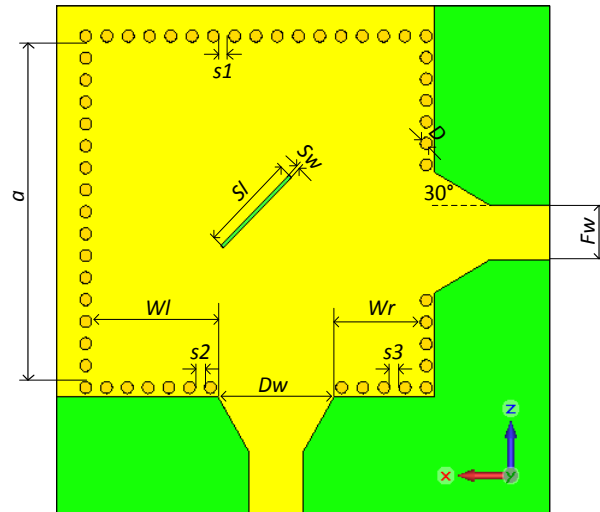
Figure 7.4 Top view of the proposed dual-mode cavity.
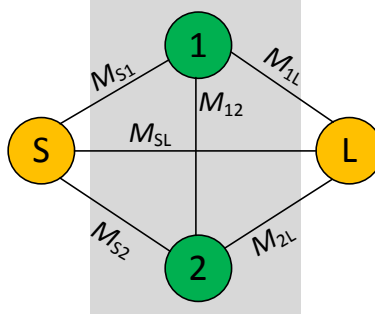
Figure 7.5 Coupling schematic of the SIW dual-mode cavity.

A new type of coupling between the TE_{102} and TE_{201} modes made by a diagonal slot on the top cladded surface is introduced. The slot creates disturbance in the surface currents, forcing them to flow parallel to the slot. Consequently, the field inside the cavity is formed satisfying new boundary conditions that lead to an adequate mode mixture. This discontinuity is well tailored for PCB designs. It is easy for precise fabrication, which can be preceded by accurate design since the response is not very sensitive to small changes in slot dimensions. In addition, there is ability for manual fine tuning of the physical model. Also, it is suitable for miniaturized designs, as slots are well known for property of shrinking size by meandering currents. In these senses, slot has clear edge over using vias [7-8]. Moreover, it is also simpler for utilization and coupling control than the fellow slot design in [7-9].

The structures is designed for Taconic TLX fiberglass reinforced substrate of 1.575 mm thickness and relative permittivity $\varepsilon_r = 2.55$. Its copper cladding is 18 μm thick with surface roughness of $R_{MS} = 0.3$ μm on untreated side.

Inclusion of vias into calculation brings in several constrains. First of all, cavity horizontal dimensions need correction described in [7-15] by:

$$a_{RWG} = a_{SIW} \text{-} 1.08 \frac{D^2}{s} + 0.1 \frac{D^2}{a_{SIW}}, \tag{7.2}$$

where a_{SIW} is the width of a SIW structure, D is the via diameter and s is the shift between vias. Further on, taking into account how current lines are distributed within TE_{mkn} ($k{\neq}0$) and TM modes, it is apparent that slots formed between vias become the radiating ones. Hence, at higher frequencies at which these modes appear, there are high radiation losses.

To prevent energy leakage around the passband, sufficient conditions are [7-16]:

$$s \leq 2D \text{ and } D \leq \lambda_g/5, \tag{7.3}$$

with λ_g being guided wavelength. Also, smaller via diameters mean smaller total dimensions of a SIW structure. Nevertheless, s and D are preferred to be kept at larger values in order to have less vias to simplify fabrication as well as to make structure less sensitive to tolerances in fabrication, so a trade-off has to be found. Here, the choices are $D = 1$ mm, which satisfies (7.3) by a large margin, and s_i are around 0.8 mm so as a natural number of vias forms side walls of desired lengths.

Regarding parametric analysis, the longer the slot is, the stronger the intra-cavity coupling is, and vice versa. Like with comparable topologies, here both TZs can also be shifted to lower frequencies when ports are moved towards each other. Similar effect, but less pronounced, can be made by moving the slot along the diagonal between ports. However, for the sake of simplicity, the slot is kept at the centre position. The widths of the cavity openings for the feed lines can be used to control the bandwidth – the wider the openings along with tapered lines are, the wider is the bandwidth is when internal coupling is adjusted to stay constant, and vice versa. At the same time, the cavity size is reduced for the same centre frequency.

Results

The dual-mode resonator has been designed at the centre frequency of 7 GHz and with 3 dB fractional bandwidth of about 450 MHz. TZs are positioned at 6.33 GHz in the lower stopband and at 7.73 GHz in the upper stopband. In Table 7.2 are given the extracted coupling matrix coefficients. As expected by the geometry of the structure and the field distribution of the pair of modes responsible for the signal transmission in the passband, the coupling with source or load is prominent for just a single mode within the cavity. Likewise, it could have been expected that the coupling between two degenerate modes is by far the strongest one.

Table 7.2 Coupling matrix related to the schematic in Figure 7.5 calculated using Guided Wave Technology's Coupling Matrix Synthesis (CMS) online tool.

M	S	1	2	L
S	0	1.132	0	-0.351
1	1.132	-0.143	1.896	-0.068
2	0	1.896	0.086	0.964
L	-0.351	-0.068	0.964	0

The frequency responses (Figure 7.6) were simulated using CST Microwave Studio full-wave simulator and its frequency domain solver. The remaining dimension from Figure 7.4 are: $a = 27.8$ mm, $Wl = 10.55$ mm, $Wr = 7.15$ mm, $Dw = 10.1$ mm, $s1 = 0.8$ mm, $s2 = 0.76$ mm, $s3 = 0.79$ mm, $Sl = 8.2$ mm, $Sw = 0.3$ mm. Finally, widths of 50 Ω feed lines are $Fw = 4.5$ mm. To enhance simulation speed, vias, which are of cylindrical shape with circular bases, were modelled having octagonal bases. This is because polygonal bases are more compatible with simulator's mash than circular ones. Furthermore, on the upper side of the structure were used open boundaries in order to avoid artificial strong transmission along the top waveguide formed when PEC boundaries are used on that side.
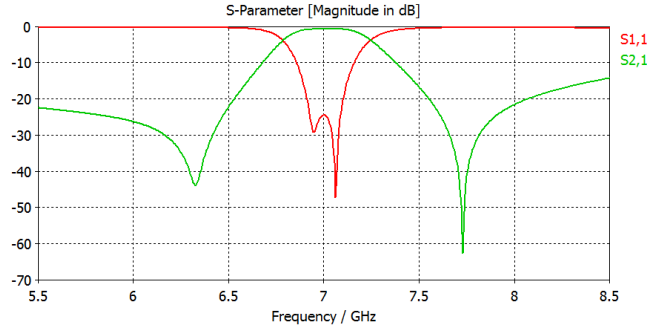
Figure. 7.6 Simulated S-parameters of the dual-mode resonant cavity with symmetric transmission zeros.

Even with quite high margins taken for conductor and dispersive dielectric losses compared to the values calculated according to the substrate specification, the insertion loss in the passband is about 0.7 dB. The lower stopband, as expected, has better attenuation in the spectrum regions farther from the passband since the first lower mode (TE_{101}) is at the theoretically maximum distance for a rectangular shaped cavity, with about 1.58 times lower centre frequency.

All-pole dual-mode variation

Similar to switching a pair of posts to the opposite diagonal to form all-pole dual-mode resonator in the resonator given in [7-8], when reversing the direction of the slot etched on the top surface (Figure 7.7), there are no more TZs in the stopbands around the main passband (Figure 7.8).
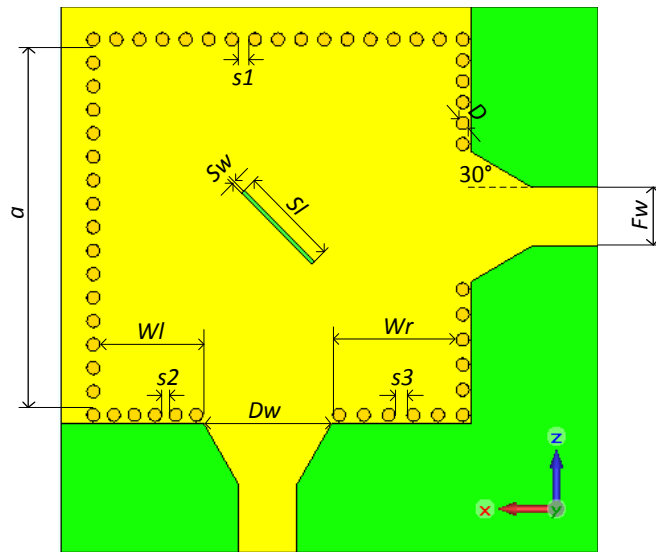
Figure. 7.7 Top view of allpole dual-mode cavity.

The new dimensions are: a = 27.7 mm, Wl = 8 mm, Wr = 9.6 mm, Dw = 9.88 mm, $s1$ = 0.79 mm, $s2$ = 0.6 mm, $s3$ = 0.92 mm, Sl = 7.7 mm, Sw = 0.3 mm and Fw = 4.5 mm.

100
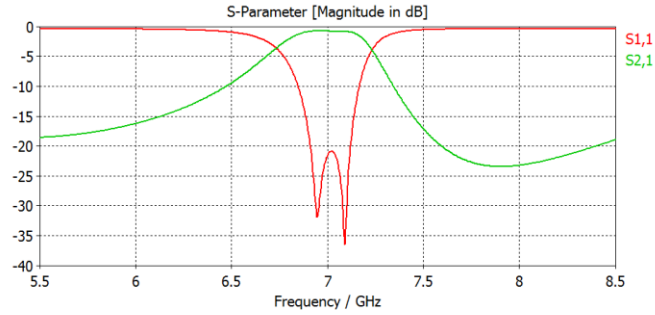
Figure 7.8 Simulated S-parameters of the dual-mode resonator with transmission zero free response.

The insertion loss at the same center frequency as for the resonator with elliptic function response is again slightly more than 0.7 dB.

7.1.2 Dual-mode 4th order filter

Individual dual-mode resonators can be combined into filters with even steeper skirt. They can form versatile structures in the sense of shapes, sizes and port locations as well as. In Figure 7.9 is presented such a 4th order folded filter, made out of two inductively coupled modified resonators as described in Figure 7.4 Its ports are co-located on the same edge. Moreover this filter uses long outer edge to implement cavity walls by fully metallized surfaces instead of vias used in standard SIW designs. Its simulation results are presented in Figure 7.10.
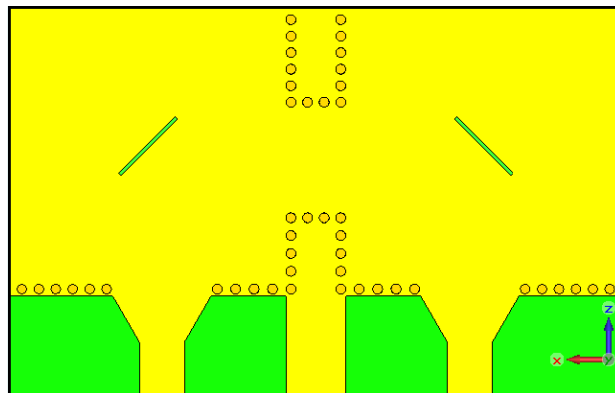
Figure 7.9 Top view of two cascaded folded dual-mode cavities.
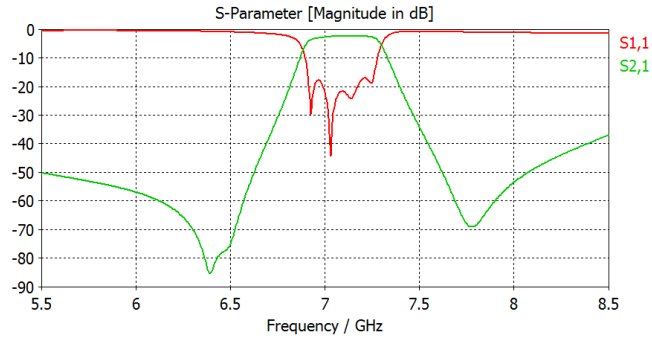
Figure 7.10 Simulated S-parameters of the 4th order filter.

The selectivity of the presented 4th order filter is excellent with a pair of TZs on either side of the passband. Nevertheless, insertion loss has risen to about 2 dB and upper stopband needs certain corrections in order to produce better attenuation in wider frequency range. The simulation also showed effects of unwanted coupling between two parallel feed lines and their isolation was needed to improve performances.

7.2   Stepped-bend Substrate Integrated Waveguide to Rectangular Waveguide Transition

Waveguide components such as high Q filters, couplers or horn antennas are often inevitable in high performance applications like satellite systems. Nevertheless, fusion of conventional metal waveguides with planar technologies is a well-known bottleneck. Even when it comes to commonly used waveguide to coaxial adapters, standard high precision ones are relatively difficult to fabricate and expensive. Furthermore, even manufacturers that are waveguide components specialists usually do not have in their standard range of products many transitions that may be needed in practice, such as to a circular or single-ridged waveguide, or to a rectangular waveguide with non-standard dimensions [7-17].

On the other side, one of the main advantages of SIW is its same-substrate integration with different planar transmission lines, most commonly microstrip [7-2], [7-18]-[7-20] and coplanar waveguide (CPW) [7-21], [7-22]. In addition, transition from a planar line to coaxial interface is neither a challenge with readily available coaxial connectors that can be soldered on a PCB. So far less exploited property is that a SIW can be as well very effectively coupled with a standard waveguide. Thus, SIW can be an excellent interconcting element between waveguide and various transmission lines and a universal link between different technological implementations. One of well-tailored applications of SIW based transitions and the main incentive in this case is rapid low cost laboratory testing, knowing the fact that the number of different conventional coaxial to waveguide adapters in microwave laboratories is usually very limited.

The proposed transition [P-6] has the right angle shape so it can be easily surface mounted onto a waveguide flange like the most published designs so far [7-23], [7-24][18]. This new approach avoids both sensitivity of inline designs [7-25], as well of those with the resonant slots [7-23], [7-24]. It also deploys stepped transition region offering good transmission characteristics similar to the alternative design [7-26]. However, unlike in [7-26], the steps are utilized through several PCB layers rather than by milling bulk aluminum, which significantly simplifies the fabrication process. Furthermore, although [7-27] transition offers a large bandwidth through the use of a ridge, it includes inconvenient rectangular waveguide (RWG) alterations. Here, proposed stepped-bend SIW to RWG transition assumes not changing the waveguide itself, but purely SIW implemented ridge.

7.2.1 Structure Design

Initial model of the 2-layer PCB transition with SIW sections represented by equivalent thin dielectric-loaded RWG is shown in Figure 7.11. The visible volume is filled with dielectrics (SIW substrate and RWG air), and all the outer boundaries apart from two faces acting as ports are considered by the solver as PEC.
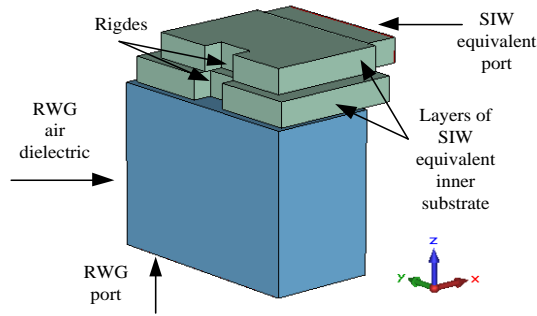
Figure 7.11 3D model of the idealised stepped-bend SIW to RWG transition viewing its dielectric interior.

A sample stepped-E-bend transition has been designed at K band. It connects to a standard WR 51, $(a \times b) = (12.954 \text{ mm} \times 6.477 \text{ mm})$, rigid rectangular waveguide made of aluminium, $\sigma_{Al} = 35.6 \text{ MS/m}$, with useful frequency band between 15 GHz and 22 GHz. The high frequency laminate is 1.575 mm thick Rogers RT/duroid 5880 having relative permittivity ε_r=2.2 and loss tangent $\tan \delta = 0.0009$ dielectric characteristics. Electrodeposited copper cladding is 17.5 µm thick with surface roughness of $R_q = 1.8 \text{ µm}$ on the dielectric side, resulting in effective conductivity of $\sigma_{Cu, \text{Surf}} = 15.4 \text{ MS/m}$.

---

[18] In fact, the initial idea for the right hand connection was inspired by the conventional coaxial to waveguide adapter, and the coupling was intended to be realized by a slot in the ground plane of SIW. After finding that the use of slot had already been proposed in [7-24], the simulation results were replicated for this kind of transition with elongated rectangular slot displaced to one side of SIW rather than being along the central E-plane, essentially represents a magnetic dipole when Babinet's principle is applied. Also, different slot shapes like of a dipole with loads and elliptic one which aligns with the field distribution in circular waveguide have been successfully tested.

Via diameters, chosen to be $D = 0.6$ mm, are well under the threshold for prevention of signal leakage of $\lambda_g/5 = 2$ mm at the upper limit of 22 GHz. On the other side, the via pitch is kept up to the limit of $2D$, or only slightly below it. The structure has reflection symmetry with respect to the centre y-plane. (The tangential magnetic component at this centre E-plane is zero, so a perfect magnetic wall can be placed there and simulation run within only one half of the space.) This plane is used as the cutting plane in Figure 7.12, depicting geometry of the full structure.
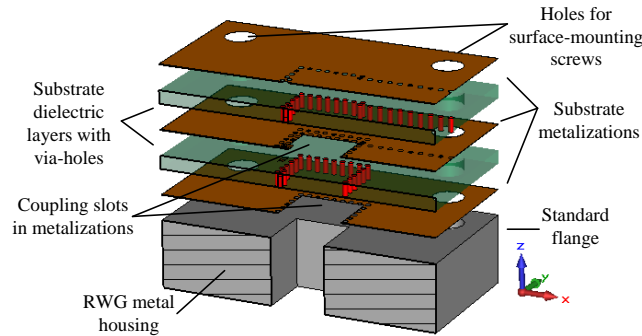
Figure 7.12 Layered 3D model of the proposed surface-mounted transition seen from longitudinal cross section along the plane of symmetry.

The feed SIW line has been designed as to have the effective width of $a/\sqrt{\varepsilon_r}$, matching the single mode frequency span of the fixed RWG. Adjusting the lengths of the ridges formed by vias on the stretched bend side, the distance between the two transmission poles can be controlled, directly determining how wideband the transition is.

7.2.2   Results

In Figure 7.13 are shown horizontal cross sections of the upper and lower SIW layers, respectively. The view is oriented into the bottom sides. All dimensions are given in millimetres.
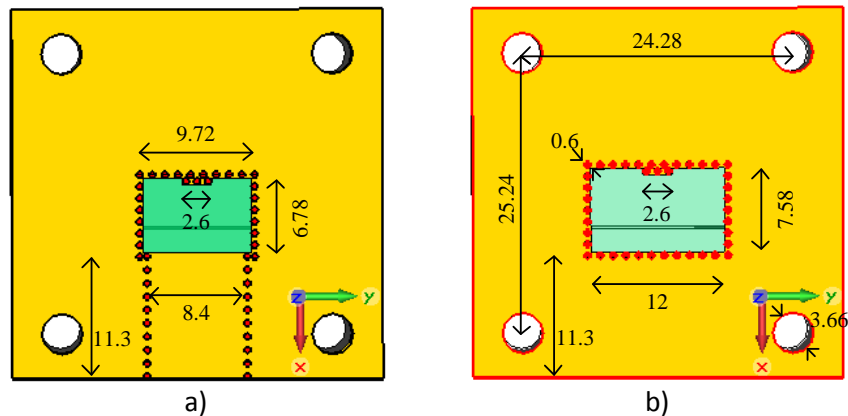
Figure 7.13 a) Top and b) Bottom SIW layer with bottom side slot.

In Figure 7.11 are presented S-parameters of the transition as a 2-port microwave network, calculated in CST Microwave Studio [CST].
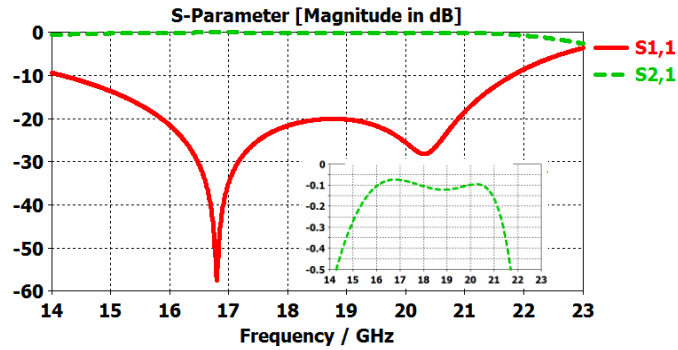
Figure 7.14 Simulated reflection and transmission frequency characteristics of the transition.

The return loss is above 20 dB in the range between 15.86 GHz and 20.89 GHz (27.4 % fractional bandwidth), whereas the insertion loss is lower than 0.2 dB in the range between 15.31 GHz and 21.15 GHz (32 % fractional bandwidth), both spanning through almost entire useful frequency band between 15 GHz and 22 GHz.

7.3 A Fully Planar Substrate Integrated Probe-Based Wideband Orthomode Transducer

Orthomode transducers (OMTs) are microwave components used for separating/exciting two signals inside metal waveguides transferred by a pair or orthogonally polarized dominant degenerate modes. They are widely found in applications like wireless communications and radiometry, especially in radio astronomy receivers. Waveguide OMT implementations use 4-way junctions [7-28]-[7-31] (2 output branches), 5-way Bøifot junctions [7-32]-[7-35] (3 output branches) and 6way turnstile junctions [7-36]-[7-43] (4 output branches). (In fact, turnstile junction precedes Bøifot one, being described within MIT Radiation Laboratory book series [7-44].) However, although bringing quality in terms of low losses and power handling capacity, these all-waveguide components are naturally large, heavy and expensive solutions, and this problem gets worse as the wideband isolation and polarization purity are improved by adding more side branches coming out of the main dual-polarized waveguide, thus increasing the level of symmetry. (This way, waveguide OMTs also become less suitable for higher frequency applications, especially if designs include septa and tuning pins, since in millimeter and terahertz bands tolerances become much more stringent.) Coaxial (probe) transducers like [7-45] are less bulky, but still relatively complex and expensive solutions. They can also spread over a long section of the main waveguide such in [7-46], even though this can be used to increase the bandwidth using finlines or ridges [7-47]. OMTs in [7-48], [7-49] are planar inside the waveguide, but still have vast external circuitry for combining/dividing signals. Moreover, [7-49] has several orthogonal PCB elements. Fully planar OMTs like [7-50] [7-51] and [7-52] are relatively narrowband. Although simple, [7-50] does not have full symmetry and microstrip circuits increase losses. [7-52] is very compact, but its integration with the radiating elements limits flexibility, especially for higher performances.

The motivation for development of a new OMT came from need to provide feeding for dual band waveguide filters using orthogonal polarizations to separate signals in different frequency bands and have them independently processed. A number of different structures was tested at the beginning, however, whether they had centrally positioned slots with rotational symmetry, SIWs directly connected to the waveguide side walls or probes, all these early attempts were futile because they used just one pair of feed lines, and the lack of symmetry resulted in strong coupling between the two port supposed to be mutually isolated.

The proposed OMT is entirely planar, including line transitions and power combining microwave circuits. It is implemented through shielded substrate integrated waveguides and rectangular coaxial lines, hence practically eliminating radiation losses and spurious couplings. Apart from manufacturing advantages, a PCB OMT design allows direct integration with other planar circuit components. There is a "full symmetry" inside the main waveguide - 4 planes of symmetry, having an identical probe coming out of each of 4 waveguide side walls. Thus, the inherent symmetry of the square shape of the waveguide is preserved and isolation and cross-polarization minimized. Other waveguide shapes with at least four planes of symmetry, most notably the circular one, can directly replace the square one and minimal parameter changes are required to optimize the performance. Another essential attribute of the OMT is its fractional bandwidth wider than 44%, which required wideband design of each of its elements.

7.3.1. OMT Structure

The OMT is implemented inside a two-layered PCB inserted transversally into metal square waveguide having common physical port with two orthogonal polarizations at one end and short termination at the other. As the PCB substrate is chosen 0.81 mm thick ceramic based Rogers RO4003C for its favourable fabrication properties. A layout of the OMT is given in Figure 7.15.
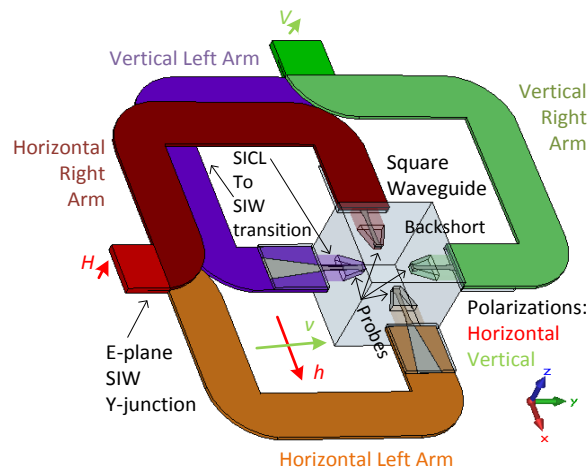
Figure 7.15 Layout of the proposed substrate integrated probe-based wideband orthomode transducer.

The footprint of the OMT can in fact be reduced in size if the substrate integrated lines are positioned tighter with the main metal waveguide inner walls. However, these areas are left for

bolts to go through and connect together the stacked structure, providing good contact between the conductive surfaces of PCB layers and waveguide sections. Another reason is to reduce the number of corner bends of the lines and diminish reflections.

The presented design is also scalable. For example, it can be made more compact by using three probes and shorter SICL to SIW transition tapers at the cost of worse isolation, polarization purity as well as smaller bandwidth. On the opposite side, it can be made very wideband by using ridged square waveguide.

Non-standard square waveguide and flange are based on standard WR 90 rectangular waveguide and standard square UBR 84 flange for WR 112 rectangular waveguide. Nevertheless, there exist International Electrotechnical Commission (IEC) standards for hollow metallic square-shaped waveguides [7-53], as well as for their flanges [7-54].

As it is more often used in such a way, the OMT will be, without loss of generality, referred to from the receiver perspective.

Probes

The coupling between the side lines and the main waveguide supporting propagation of orthogonally polarized modes is made through balanced substrate integrated coaxial electric probes (Figure 7.16). They have good wideband characteristics even with electrically thin substrate, which is a considerable problem if a turnstile waveguide junction is tried to be implemented in this way.19.

Since the width of a substrate integrated coaxial line (SICL) outer conductor has negligible effect on the dominant TEM mode, and directly determines the first upper waveguide mode [7-55], it was chosen to be $a_{SICL} = 5.2$ mm so that the TE_{10} cut off frequency is significantly above the X band. With the substrate height fixed by the PCB laminate thickness, the flat inner conductor width was selected to be $W_{COND} = 1.0$ mm in order to have characteristic impedance around 50 Ω and relatively easy fabrication regarding tolerance. In turn, W_{COND} has miniscule effect on TE_{10} mode (slightly lowering its cutoff frequency as it gets wider).

The probes have been optimized having wider inner conductor ends to improve overall matching and with ground plane stubs parallel to the inner conductors, having the roll of improving the matching at the higher frequency side of the passband. Optimization process could be made almost four times faster by using two symmetry planes – PMC along the center E-plane of the square waveguide and PEC along its H-plane relative to the polarization of the selected input TE10 mode. Since the SICL probe on the opposite side of the measured output port is actually not used in such simulation because of the PEC plane, the transmission between the square waveguide port and the SICL port is optimized with the goal of 0 dB, rather than -3 dB.

---

[19] From antenna perspective, using probes is analogue to using wire (monopole) antennas, using slots [7-51] is analogue to using slot antennas, using junctions like turnstile for each branch is analogue to using horn antennas, whereas approach [7-50] is analogue to using microstrip patch antennas.

Furthermore, the square waveguide is terminated with a quarter-wave short circuit stub on top of the cross section containing probes, with its exact length also being an optimization variable.
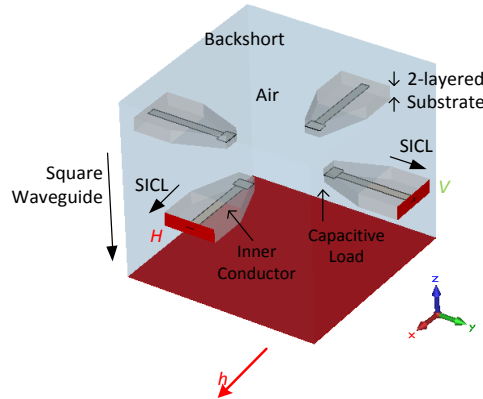
Figure 7.16 Input short circuited square waveguide with inserted loaded SICL probes.

Dielectric inside the main waveguide follows the shapes of the planar metal probes, both to give mechanical support and provide smoother transition between the SICLs and the hollow square metal waveguide interfaces. Removal of the rest of the substrate inside the waveguide reduces dielectric losses.

SICL to SIW transition

Apart from realizing SICLs, the second substrate layer is needed because intersection of arms belonging to different polarizations within the same layer (Vertical Left Arm and Horizontal Right Arm in Figure 7.15) has to be avoided. Substrate integrated waveguide (SIW) was selected to be used in the arms crossing over region as a shielded and low loss single layer guided wave structure. Thus, there was a need for developing a wideband inline SICL to SIW transition (Figure 7.17).
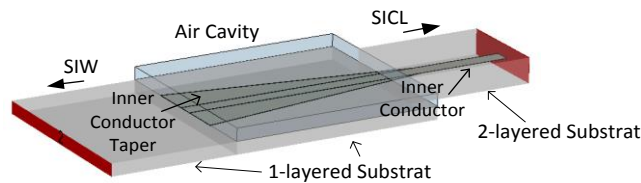
Figure 7.17 Wideband double layer SICL to single layer SIW transition.

The central piece of the transition is linearly tapered metallization between the two PCB layers, starting as the narrow inner SICL conductor and spreading to the full width of SIW broad wall. The transition medium is piece-wise homogeneous. Only the bottom layer is laminate, whereas the upper one is air. This way, the signal is guided through only one substrate layer, without strong reflection coming from the other layer. There is resemblance with the microstrip taper, both in the way how it is connected to SICL and SIW as well as inhomogeneous dielectric. However, unlike microstrip taper, this SICL to SIW transition is shielded at all four sides.

Phase difference management

The proposed design makes possible to route both arms of one polarization through the same layer or have them in different layers. This is controlled by selecting the layer in which SIW is coupled through the transition from SICL. Interesting aspect is that if same polarization equal length SIWs are in unchanged layer, the signals in arms have opposite phases (180° phase difference), whereas if these SIWs are in different layers, signals are in phase (0° phase difference).

Different power dividers and directional couplers have different inherent phase shifts between their output ports (0°, 90° or 180°). If phase correction needs to be made, a suitable way is using the self-compensating phase shifter [7-56]. Taking only SIW delay line leaves the phase shift almost linearly increasing with the frequency. The self-compensating phase shifter adds opposite phase characteristic of equal-length unequal-width SIW phaser with declining trend of phase shift relative to the frequency. This minimizes the frequency dependence of the total phase shift.

Power dividers and directional coupler

Using symmetrical 3-port power dividers has advantage in exactly equal split of power between the output ports and same phases at any frequency as the result of the symmetry between the output ports and central position of the input port, but disadvantage in terms of matching ports since lossless reciprocal 3-port networks cannot be matched on all 3 ports. Moreover, neither two ports can be matched, because that would leave the third port completely mismatched [1-1]. In addition, isolation between two output ports is weak.

4-port hybrid (3 dB) directional couplers have advantage in terms of port matching and isolation. What is more, all hybrid couplers have matched ports, and all 4-port matched networks are hybrid couplers [7-57]. Symmetrical couplers with perfectly matched and isolated ports have 90°phase shift between their output ports. Also, symmetrical hybrid couplers have equal magnitudes of their reflection and isolation characteristics. However, power distribution is actually never equal between the through and coupled ports of a hybrid coupler in wider band. Likewise, phase difference between these two ports is also frequency dependent.

Rat race (hybrid ring) coupler, although having interesting and useful properties of 0° and 180° phase shifts between its output ports being antisymmetrical coupler, has not been tested because it has unpractical geometry for the developed OMT design, and has been regarded outdated for its narrowband characteristics for a long time. Even its planar (microstrip) version has not been very successfully implemented regarding bandwidth in OMTs [7-50].

The first structure that was experimented with was single layer SIW H-plane T-junction power divider using inductive post (via) inside the junction for port matching (Figure 7.18) [7-58] [7-59]. Although reflection loss at the input port better than 15 dB could be accomplished in entire band, using two different arms to create 180° phase difference using self-compensating phase shifter adds phase and magnitude difference fluctuation between them. The biggest problem is that complete OMT structure has response which in unsuitable for use being filled with spikes (Figure 7.19).
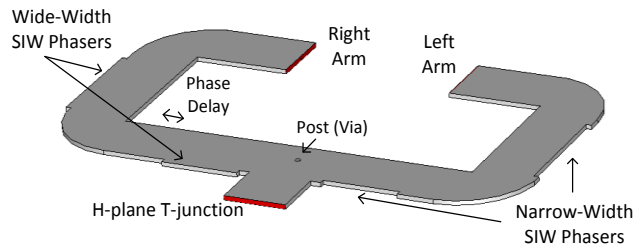
Figure 7.18 Power dividing network based on H-plane SIW T-junction, with additional 180° phase difference in two arms provided by self-compensating phase shifter.
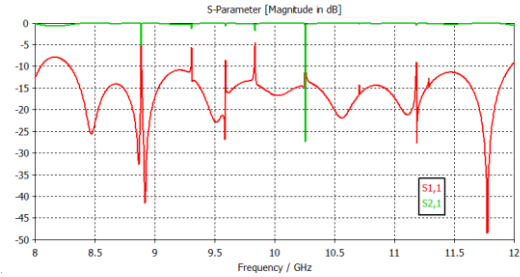
Figure 7.19 Glitches in the response of OMT using H-plane SIW T-junction from Figure 7.18.

Similar bandwidth problem exists with single layer SIW H-plane Y-junction power dividers (Figure 7.20), both straight and having angles >0° and <180° between the two output branches. It is not possible to both move up the TE_{30} cut off frequency above 12 GHz and have good matching in the entire $8 - 12$ GHz band with only TE_{10} as the propagating mode in the junction.
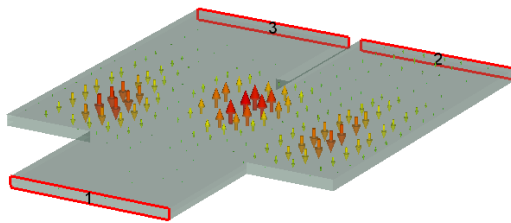
Figure 7.20 Electric field distribution around the TE_{30} cutoff frequency in a straight H-plane SIW Y-junction.

Riblet short-slot hybrid [7-60]-[7-62] is a narrow-wall coupler essentially similar to H-plane Y-junction, having the isolated port symmetrical to the input port instead of just one central input port (Figure 7.21). Now, the interplay between the even TE_{10} mode and the odd TE_{20} mode in the central part along the slot results in constructive interference at the coupled and destructive interference at the isolated port [7-63]. Phase difference needed from self-compensating phase shifter is here halved to 90°. Although its pro is compact size, this hybrid coupler is also not capable of utilizing full 4 GHz bandwidth due to undesired appearance of TE_{30} mode propagation (Figure 7.22). Testing different shapes of the central junction area did not bring any significant improvements.
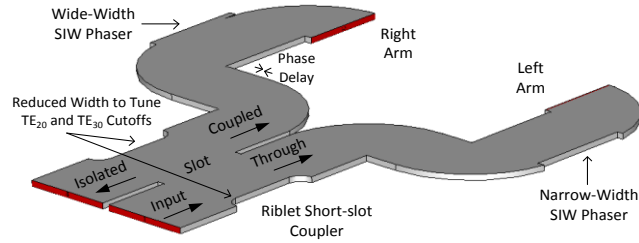
Figure 7.21 Power dividing network based on Riblet short-slot hybrid quadrature directional coupler, with additional 90° phase difference in two arms provided by self-compensating phase shifter.
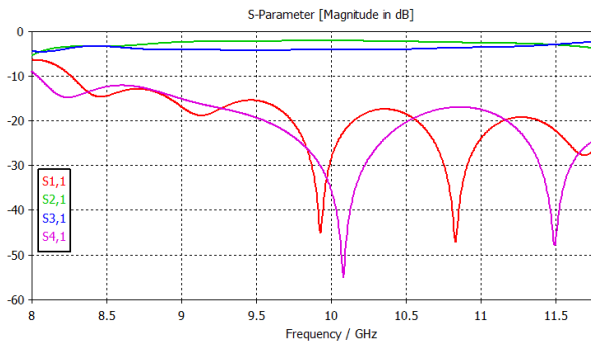
Figure 7.22 Amplitude reflection and transmission responses on through, coupled and isolated ports of the structure in Figure 7.21, when input port is excited.
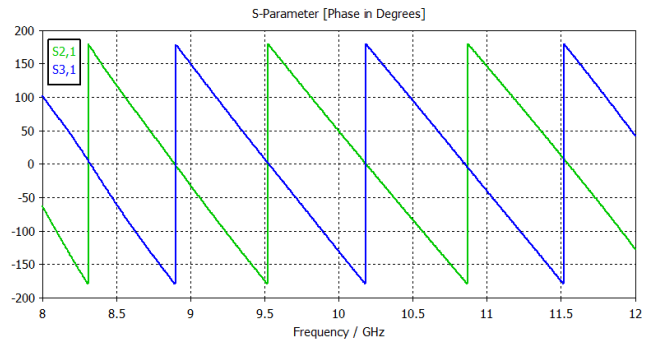
Figure 7.23 Through and coupled port output signals with 180±7° phase difference when input port of the structure in Figure 7.21 is excited.

The bandwidth issue in a single layer could, expectedly, be resolved by scalable Transvar directional coupler design [7-64], [7-65], switching from continuous to multiaperture coupling. Nevertheless, its size (length) is very large. Being even more massive and complex, branch-guide directional couplers [7-66] have been excluded without testing.

Nevertheless, broad-wall variation of multihole coupler (Figure 7.24) turned out to be smaller (shorter), and Bethe's small-hole coupling theory [7-67] shows that broad-wall couplers have inherently better wideband properties than narrow-wall couplers. The design with two longitudinal rows of equidistant circular holes set apart symmetrically in transverse direction was used [7-68] [7-69], with the increased number of rows reducing the sizes of individual holes so they do not overlap when strong coupling is needed. If the same designation of probes and input/isolated coupler ports is kept like in single layer cases, the phase difference between the two arms is -90°, which can be utilized by swapping input with isolated ports rather than swapping phase shifters between the arms. This directional coupler finally provided very good overall wideband OMT response.

Transverse Pair of
Round Coupling Holes

7ᵗʰ Order Multihole
Broad-wall Coupler
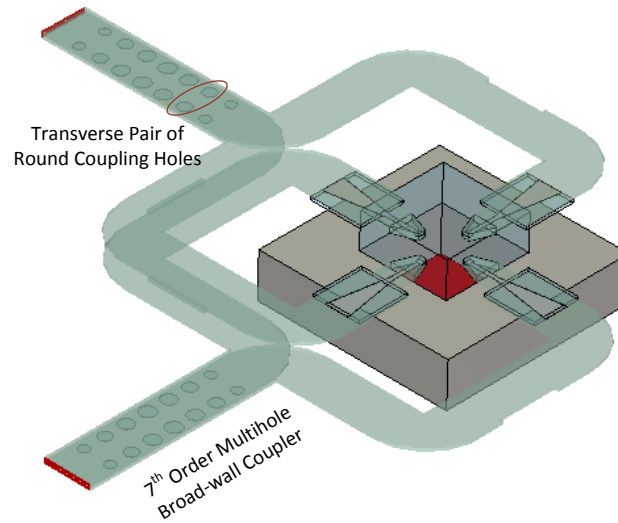
Figure 7.24 Substrate integrated probe-based OMT using broad-wall directional coupler with two rows of round coupling holes.
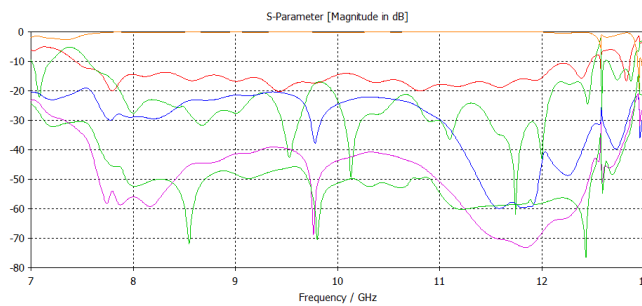
Figure 7.25 S-parameters of the OMT given in Figure 7.24.

Finally, even better results were obtained using E-plane straight Y-junction (Figure 7.15). (It is used in most turnstile and Bøifot junction waveguide OMT implementations.) Essentially, two SIW layers separated by metalized broad wall are turned into a single SIW of double substrate thickness by removing metallization of this sandwiched broad wall. There are no remaining problems with equal power or phase delivery because complete arms in each polarization, from the square waveguide to the power divider, can be transformed one into another by composition of two plane symmetries. However, the output SIW is two layered, so if further signal needs to be in a single layer, at least one additional transition is needed. Of course, for direct measurement, coaxial connectors can be directly put on two layered planar transmission line.

7.3.2 Results

SIWs and SICLs were designed with the following constraints regarding vias: $d < \lambda_\mathrm{g}/5$ and $p < 2d$, where d is the via diameter, p is the via pitch (distance between adjacent vias), and λ_g is the guided wavelength. The diameter for all the OMT vias was selected to be $d = 0.6$ mm, and the via pitch to be flexible in order to have the first and the last via of a wall at particular

112

locations. However, the number of vias in a wall was determined so as to have the distance between the consecutive vias around 0.4 mm.

In Figure 7.26 are given the layouts of the OMT PCB layers, and the numerical values of their dimensions are presented in Table 7.3. In addition, the length of the square waveguide backshort is $L_{SWGs} = 6.7$ mm. Except for the tuning stubs, the top and bottom substrate layer are mutually symmetrical with respect to the diagonal as the axis of symmetry. (Consequently, the central metal layer has the diagonal as its own axis of symmetry.)
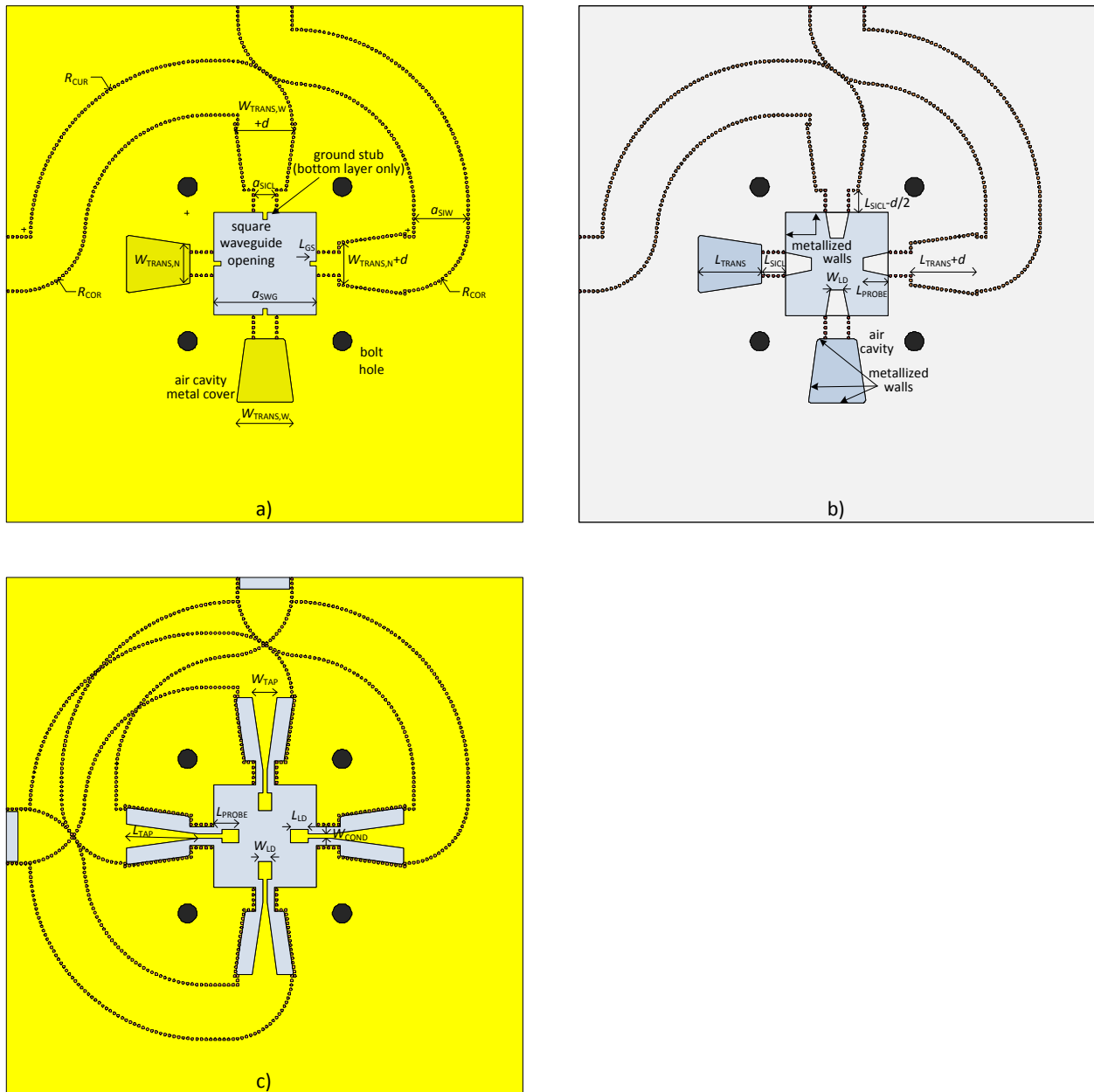
Figure 7.26 PCB layouts of the wideband planar substrate integrated OMT: a) top/bottom metallization, b) top/bottom substrate and c) central metallization layer.

113

Table 7.3 OMT dimensions in millimeters

a_{SWG}	22.9		L_{PROBE}	5.7
a_{SIW}	12.1		L_{LD}	3.9
a_{SICL}	5.2		W_{LD}	2.9
L_{SICL}	5.3		W_{COND}	1.0
L_{TRANS}	14.1		L_{TAP}	16.0
$W_{\text{TRANS, N}}$	8.7		W_{TAP}	5.5
$W_{\text{TRANS, W}}$	12.8		R_{COR}	14.1
L_{GS}	1.5		R_{CUR}	33.8

Since the structures with long via fences are computationally intensive, this OMT has practical advantage coming from the shielded nature that its operation can be simulated relatively accurately piece by piece, and the total response can be found as the response of the microwave circuit having the aforementioned parts as its components.

Figure 7.27 gives the S-parameters of the OMT calculated in CST Microwave Studio [CST], accurately modelled with line walls made out of vias, lossy RO4003C dielectric and lossy copper metallization that takes the surface roughness into account. The insertion loss does not exceed 1.2 dB in the frequency band between 8.07 and 12.53 GHz. In the same band, return loss is better than 19 dB. If narrow spikes attributed to numerical errors are disregarded, cross-polarization discrimination is higher than 65 dB and inter-port isolation higher than 62 dB within this span.
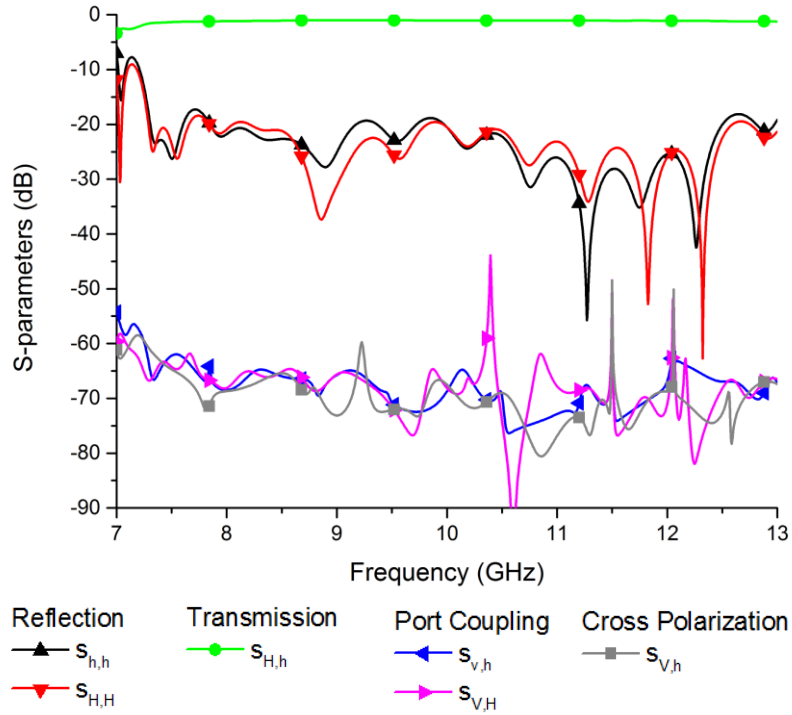
Figure 7.27 Return loss (RL), insertion loss (IL), inter-port isolation (IPI) and cross-polarization discrimination (XPD) characteristics of the proposed OMT.

The OMTs have been fabricated in modified design with no plated routing, but with all the metal walls realized by via fences. Also, because of limited facilities of the PCB fabricator, Supreme Circuits in Delhi, 2-layered PCBs of OMTs were fabricated as two independent 1-layered PCBs. Rectangular waveguide sections were machined from 1 cm thick aluminium board and entire structure was assembled and measured in back-to-back configuration at the Indian Institute of Technology Delhi (Figure 7.28). Bolts completely penetrate the structure, hold PCB layers together instead of using adhesives, and help the alignment. Their number was increased to 8 in order to have more even distribution of pressure. Wider cylindrical holes are used to have heads of bolts inside the backshort and leave the surface flat, as well as to decrease the weight of the backshort. Nuts are used instead of threading the aluminium, so that higher torque can be applied with the wrench, as well as because they are made of stronger material (steel).
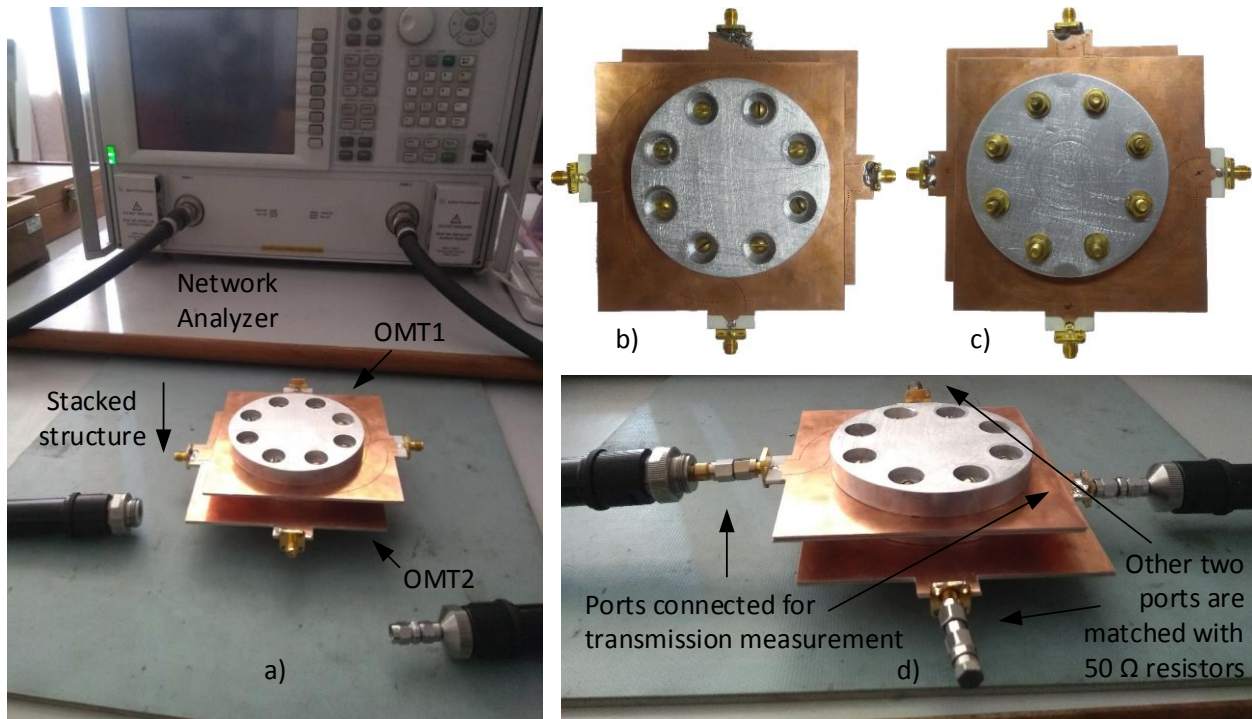
Figure 7.28 Back-to-back measurement of a pair of OMTs: a) setup, b) top view of OMTs, c) bottom view of OMTs, and d) $s_{h2,h1}$ measurement.

Results of the measurement are shown in Figure 7.29. Expected reasons for discrepancies between simulated and measured frequency responses include manual machining of aluminium block, marking and drilling holes in them with relatively low accuracy, as well as inherent problem with misalignment between the layers of a stacked structure.
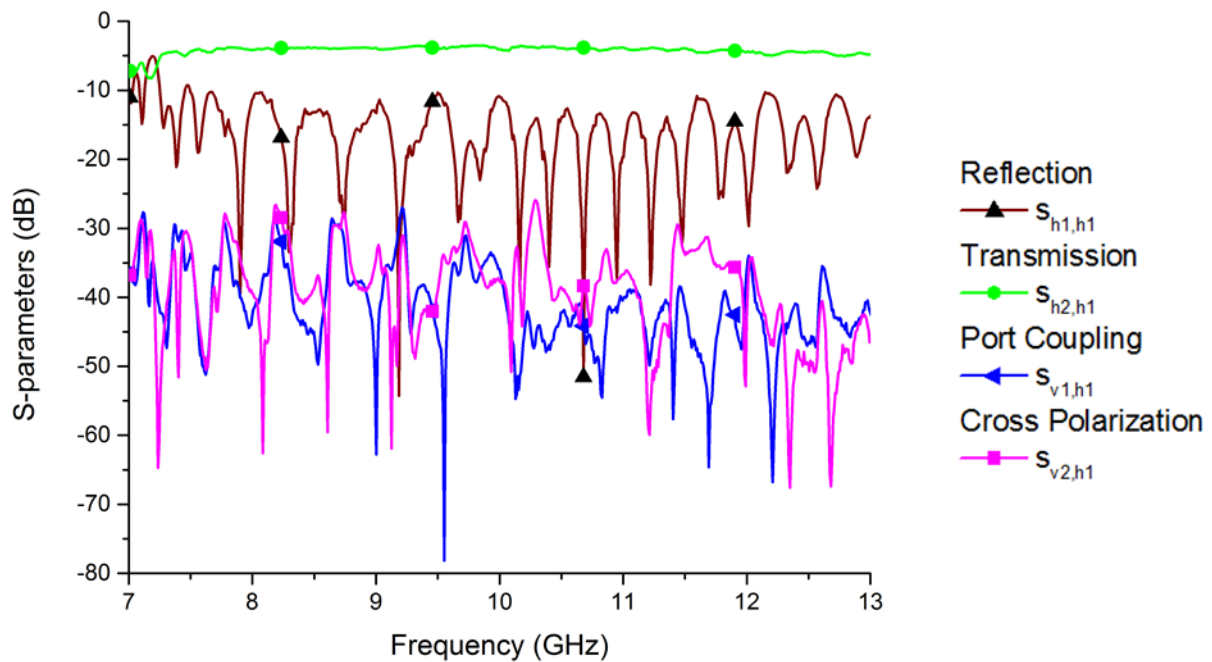
Figure 7.29 Measured return loss (RL), insertion loss (IL), inter-port isolation (IPI) and cross-polarization discrimination (XPD) of a pair of fabricated OMTs in back-to-back configuration.

References

[7-1]   J. Hirokawa and M. Ando, "Single-layer feed waveguide consisting of posts for plane TEM wave excitation in parallel plates," *IEEE Trans. Antennas Propag.*, vol. 46, no. 5, pp. 625–630, May 1998.

[7-2]   D. Deslandes and K. Wu, "Integrated microstrip and rectangular waveguide in planar form," *IEEE Microw. Wirel. Compon. Lett.*, vol. 11, no. 2, pp. 68–70, Feb. 2001.

[7-3]   K. Wu and T. Djerafi, "SIW Techniques for MHz-to-THz Packaging and Interconnects Technology," Chip Packaging and System in Package Workshop, *11th European Microwave Integrated Circuits Conference (EuMIC 2016)*, London, UK, 3-7 October 2016.

[7-4]   G. L. Ragan, *Microwave Transmission Circuits*. McGraw-Hill Book Company, 1948.

[7-5]   A. Atia and A. Williams, "Narrow-Bandpass Waveguide Filters," *IEEE Trans. Microw. Theory Tech.*, vol. 20, no. 4, pp. 258–265, Apr. 1972.

[7-6]   S. J. Fiedziuszko, "Dual-Mode Dielectric Resonator Loaded Cavity Filters," *IEEE Trans. Microw. Theory Tech.*, vol. 30, no. 9, pp. 1311–1316, Sep. 1982.

[7-7]   J. . Curtis and S. J. Fiedziuszko, "Miniature dual mode microstrip filters," *Microwave Symposium Digest, 1991., IEEE MTT-S International*, 1991, pp. 443–446 vol.2.

[7-8]   C.-C. Chuang, H.-H. Lin, and C.-L. Wang, "Design of dual-mode SIW cavity filters," *TENCON 2007 - 2007 IEEE Region 10 Conference*, 2007, pp. 1–4.

[7-9]   R. Q. Li, X. H. Tang, and F. Xiao, "Substrate integrated waveguide dual-mode filter using slot lines perturbation," *Electron. Lett.*, vol. 46, no. 12, pp. 845–846, Jun. 2010.

[7-10] D. Deslandes and K. Wu, "Substrate integrated waveguide dual-mode filters for broadband wireless systems," *Radio and Wireless Conference, 2003. RAWCON '03. Proceedings*, 2003, pp. 385–388.

[7-11] W. Shen, X.-W. Sun, W.-Y. Yin, J.-F. Mao, and Q.-F. Wei, "A Novel Single-Cavity Dual Mode Substrate Integrated Waveguide Filter With Non-Resonating Node," *IEEE Microw. Wirel. Compon. Lett.*, vol. 19, no. 6, pp. 368–370, Jun. 2009.

[7-12] X. Zhan, Z. Tang, Y. Wu, and B. Zhang, "Substrate Integrated Waveguide Dual-Mode, Dual-Band Filter.," *Microw. J.*, vol. 57, no. 3, 2014.

[7-13] H.-J. Tang, W. Hong, J.-X. Chen, G. Q. Luo, and K. Wu, "Development of Millimeter-Wave Planar Diplexers Based on Complementary Characters of Dual-Mode Substrate Integrated Waveguide Filters With Circular and Elliptic Cavities," *IEEE Trans. Microw. Theory Tech.*, vol. 55, no. 4, pp. 776–782, Apr. 2007.

[7-14] P. Chongder, K. V. Srivastava, and A. Biswas, "Realisation of controllable transmission zeros by perturbation technique for designing dual-mode filter using substrate integrated hexagonal cavity," *IET Microw. Antennas Propag.*, vol. 8, no. 6, pp. 451–457, Apr. 2014.

[7-15] F. Xu and K. Wu, "Guided-wave and leakage characteristics of substrate integrated waveguide," *IEEE Trans. Microw. Theory Tech.*, vol. 53, no. 1, pp. 66–73, Jan. 2005.

[7-16] D. Deslandes and K. Wu, "Design Consideration and Performance Analysis of Substrate Integrated Waveguide Components," *32nd European Microwave Conference (EuMC 2002)*, Milan, Italy, 2002, pp. 1–4.

[7-17] Waveguide to Coax Adaptors, Flann Microwave Ltd., Available: www. flann.com/products/ adapters/

[7-18] D. Deslandes, "Design equations for tapered microstrip-to-Substrate Integrated Waveguide transitions," *2010 IEEE MTT-S International Microwave Symposium*, Anaheim, CA, 2010, pp. 704-707.

[7-19] Hee Nam, Tae-Soon Yun, Ki-Byoung Kim, Ki-Cheol Yoon and Jong-Chul Lee, "Ku-band transition between microstrip and substrate integrated waveguide (SIW)," *2005 Asia-Pacific Microwave Conference Proceedings*, 2005, pp. 4

[7-20] Z. Kordiboroujeni and J. Bornemann, "New Wideband Transition From Microstrip Line to Substrate Integrated Waveguide," *IEEE Transactions on Microwave Theory and Techniques*, vol. 62, no. 12, pp. 2983-2989, Dec. 2014.

[7-21] D. Deslandes and Ke Wu, "Integrated transition of coplanar to rectangular waveguides," *2001 IEEE MTT-S International Microwave Sympsoium Digest (Cat. No.01CH37157)*, Phoenix, AZ, USA, 2001, pp. 619-622 vol.2.

[7-22] F. Taringou and J. Bornemann, "New substrate-integrated to coplanar waveguide transition," *2011 41st European Microwave Conference*, Manchester, 2011, pp. 428-431.

[7-23] L. Li, X. P. Chen, R. Khazaka, and K. Wu, "A transition from substrate integrated waveguide (SIW) to rectangular waveguide," *2009 Asia Pacific Microwave Conference (APMC)*, Singapore, 2009, pp. 2605–2608.

[7-24] R. Głogowski, J.-F. Zürcher, C. Peixeiro, and J. R. Mosig, "Broadband Ka-band rectangular waveguide to substrate integrated waveguide transition," *Electron. Lett.*, vol. 49, no. 9, pp. 602–604, Apr. 2013.

[7-25] J. Li, G. Wen, and F. Xiao, "Broadband transition between rectangular waveguide and substrate integrated waveguide," *Electron. Lett.*, vol. 46, no. 3, pp. 223–224, Feb. 2010.

[7-26] J. L. Cano, A. Mediavilla, and A. R. Perez, "Full-Band Air-Filled Waveguide-to-Substrate Integrated Waveguide (SIW) Direct Transition," *IEEE Microw. Wirel. Compon. Lett.*, vol. 25, no. 2, pp. 79–81, Feb. 2015.

[7-27] J. Dong, Z. Yang, H. Peng, and T. Yang, "Full Ka-band right-angle transition from substrate integrated waveguide to air-filled rectangular waveguide," *Electron. Lett.*, vol. 51, no. 22, pp. 1796–1798, 2015

[7-28]   J. M. Rebollar, J. Esteban, and J. D. Frutos, "A dual frequency OMT in the Ku band for TT amp;C applications," *IEEE Antennas and Propagation Society International Symposium*. 1998 Digest. Antennas: Gateways to the Global Network. Held in conjunction with: USNC/URSI National Radio Science Meeting (Cat. No.98CH36, 1998, vol. 4, pp. 2258–2261 vol.4.

[7-29]   T. J. Reck and G. Chattopadhyay, "A 600 GHz Asymmetrical Orthogonal Mode Transducer," *IEEE Microw. Wirel. Compon. Lett.*, vol. 23, no. 11, pp. 569–571, Nov. 2013.

[7-30]   C. A. Leal-Sevillano, Y. Tian, M. J. Lancaster, J. A. Ruiz-Cruz, J. R. Montejo-Garai, and J. M. Rebollar, "A Micromachined Dual-Band Orthomode Transducer," *IEEE Trans. Microw. Theory Tech.*, vol. 62, no. 1, pp. 55–63, Jan. 2014.

[7-31]   X. Shang, P. Klasmann, and M. J. Lancaster, "A compact Ka-band waveguide orthomode transducer fabricated by 3-D printing," *2016 46th European Microwave Conference (EuMC)*, 2016, pp. 365–368.

[7-32]   A. M. Boifot, E. Lier, and T. Schaug-Pettersen, "Simple and broadband orthomode transducer (antenna feed)," *Antennas Propag. IEE Proc. H - Microw.*, vol. 137, no. 6, pp. 396–400, Dec. 1990.

[7-33]   G. Narayanan and N. Erickson, "Full-waveguide band orthomode transducer for the 3 mm and 1 mm bands," *Proceedings of the 14th International Symposium on Space Terahertz Technology*, 2003, pp. 508–512.

[7-34]   D. Yong, T. Zongxi, Z. Biao, and B. Lifen, "A broad band orthomode transducer," 2010 International Symposium on Intelligent Signal Processing and Communication Systems, 2010, pp. 1–3.

[7-35]   C. A. Leal-Sevillano, T. J. Reck, G. Chattopadhyay, J. A. Ruiz-Cruz, J. R. Montejo-Garai, and J. M. Rebollar, "Development of a Wideband Compact Orthomode Transducer for the 180-270 GHz Band," *IEEE Trans. Terahertz Sci. Technol.*, vol. 4, no. 5, pp. 634–636, Sep. 2014.

[7-36]   Y. Aramaki, N. Yoneda, M. Miyazaki, and T. Horie, "Ultra-thin broadband OMT with turnstile junction," *IEEE MTT-S International Microwave Symposium Digest*, 2003, 2003, vol. 1, pp. 47–50 vol.1.

[7-37]   A. Navarrini and R. L. Plambeck, "A turnstile junction waveguide orthomode transducer," *IEEE Trans. Microw. Theory Tech.*, vol. 54, no. 1, pp. 272–277, Jan. 2006.

[7-38]   G. Pisano et al., "A Broadband WR10 Turnstile Junction Orthomode Transducer," *IEEE Microw. Wirel. Compon. Lett.*, vol. 17, no. 4, pp. 286–288, Apr. 2007.

[7-39]   A. Tribak, J. L. Cano, A. Mediavilla, and M. Boussouis, "Octave Bandwidth Compact Turnstile-Based Orthomode Transducer," *IEEE Microw. Wirel. Compon. Lett.*, vol. 20, no. 10, pp. 539–541, Oct. 2010.

[7-40]   S. Srikanth and M. Solatka, "A compact full waveguide band turnstile junction orthomode transducer," *2011 XXXth URSI General Assembly and Scientific Symposium*, 2011, pp. 1–4.

[7-41]   J. R. Montejo-Garai, J. A. Ruiz-Cruz, C. A. Leal-Sevillano, and J. M. Rebollar, "Modelling of dual-polarisation diplexers based on enhanced multiport turnstile junctions," *Antennas Propag. IET Microw.*, vol. 7, no. 7, pp. 485–492, May 2013.

[7-42]   D. Dousset, S. Claude, and K. Wu, "A Compact High-Performance Orthomode Transducer for the Atacama Large Millimeter Array (ALMA) Band 1 (31-45 GHz)," *IEEE Access*, vol. 1, pp. 480–487, 2013.

[7-43]   A. Bhutani et al., "3D metal printed Ku/Ka Band modified turnstile junction Orthomode Transducer," *2016 Asia-Pacific Microwave Conference (APMC)*, New Delhi, 2016, pp. 1–4.

[7-44]   M. A. Meyer and H. B. Goldberg, "Applications of the Turnstile Junction," *IRE Trans. Microw. Theory Tech.*, vol. 3, no. 6, pp. 40–45, Dec. 1955.

[7-45]   G. Engargiola and A. Navarrini, "K-band orthomode transducer with waveguide ports and balanced coaxial probes," *IEEE Trans. Microw. Theory Tech.*, vol. 53, no. 5, pp. 1792–1801, May 2005.

[7-46] M. A. Moharram, A. Mahmoud, and A. A. Kishk, "A Simple Coaxial to Circular Waveguide OMT for Low-Power Dual-Polarized Antenna Applications," *IEEE Trans. Microw. Theory Tech*., vol. PP, no. 99, pp. 1–7, 2017.

[7-47] S. J. Skinner and G. L. James, "Wide-band orthomode transducers," *IEEE Trans. Microw. Theory Tech*., vol. 39, no. 2, pp. 294–300, Feb. 1991.

[7-48] P. K. Grimes, O. G. King, G. Yassin, and M. E. Jones, "Compact broadband planar orthomode transducer," *Electron. Lett*., vol. 43, no. 21, pp. 1146–1147, Oct. 2007.

[7-49] Y. Tao and Z. Shen, "Design of broadband planar orthomode transducers using substrate integrated waveguide," *2008 Asia-Pacific Microwave Conference*, Macau, 2008, pp. 1–4.

[7-50] R. W. Jackson, "A planar orthomode transducer," *IEEE Microw. Wirel. Compon. Lett*., vol. 11, no. 12, pp. 483–485, Dec. 2001.

[7-51] M. K. Mandal, K. Wu, and D. Deslandes, "A compact planar orthomode transducer," *2011 IEEE MTT-S International Microwave Symposium*, 2011, pp. 1–4.

[7-52] M. Esquius-Morote, M. Mattes, and J. R. Mosig, "Orthomode Transducer and Dual-Polarized Horn Antenna in Substrate Integrated Technology," *IEEE Trans. Antennas Propag*., vol. 62, no. 10, pp. 4935–4944, Oct. 2014.

[7-53] Hollow metallic waveguides - Part 7: Relevant specifications for square waveguides, IEC Standard 60153-7:1972. Available: https://webstore.iec.ch/

[7-54] Flanges for Waveguides Part 7: Relevant specifications for flanges for square waveguides, IEC Standard 60154-7:1974. Available: https://webstore.iec.ch/

[7-55] F. Gatti, M. Bozzi, L. Perregrini, K. Wu, and R. G. Bosisio, "A Novel Substrate Integrated Coaxial Line (SICL) for Wide-Band Applications," *2006 European Microwave Conference*, Manchester, 2006, pp. 1614–1617.

[7-56] Y. J. Cheng, W. Hong, and K. Wu, "Broadband Self-Compensating Phase Shifter Combining Delay Line and Equal-Length Unequal-Width Phaser," *IEEE Trans. Microw. Theory Tech*., vol. 58, no. 1, pp. 203–210, Jan. 2010.

[7-57] R. Levy, "Directional couplers" Advances in Microwaves, New York:Academic Press, vol. 1, pp. 155-161, 1966.

[7-58] J. Hirokawa, K. Sakurai, M. Ando, and N. Goto, "An analysis of a waveguide T junction with an inductive post," *IEEE Trans. Microw. Theory Tech*., vol. 39, no. 3, pp. 563–566, Mar. 1991.

[7-59] S. Germain, D. Deslandes, and K. Wu, "Development of substrate integrated waveguide power dividers," *CCECE 2003 - Canadian Conference on Electrical and Computer Engineering*. Toward a Caring and Humane Technology (Cat. No.03CH37436), 2003, vol. 3, pp. 1921–1924 vol.3.

[7-60] M. Surdin, "Directive couplers in wave guides," *J. Inst. Electr. Eng. - Part IIIA Radiolocation*, vol. 93, no. 4, pp. 725–736, 1946.

[7-61] H. J. Riblet, "The Short-Slot Hybrid Junction," Proc. IRE, vol. 40, no. 2, pp. 180–184, Feb. 1952.

[7-62] S. S. Sabri, B. H. Ahmad, and A. R. Othman, "Design and fabrication of X-band Substrate Integrated Waveguide directional coupler," *2013 IEEE Symposium on Wireless Technology Applications (ISWTA)*, 2013, pp. 264–268.

[7-63] U. Rosenberg and K. Beis, "Improved Narrow-Wall Short Slot Coupler Design Exhibiting Significant Increased Bandwidth and Low Cost Production," *2001 31st European Microwave Conference*, London, 2001, pp. 1–4.

[7-64] K. Tomiyasu and S. B. Cohn, "The Transvar Directional Coupler," *Proc. IRE*, vol. 41, no. 7, pp. 922–926, Jul. 1953.

[7-65] R. Srivastava, S. Mukherjee, and A. Biswas, "Design of broadband planar substrate integrated waveguide (SIW) transvar coupler," *2015 IEEE International Symposium on Antennas and Propagation USNC/URSI National Radio Science Meeting*, 2015, pp. 1402–1403.

[7-66] R. Levy and L. F. Lind, "Synthesis of Symmetrical Branch-Guide Directional Couplers," *IEEE Trans. Microw. Theory Tech*., vol. 16, no. 2, pp. 80–89, Feb. 1968.

[7-67] H. A. Bethe, "Theory of Diffraction by Small Holes," *Phys. Rev*., vol. 66, p. 163, Jan. 1944.

[7-68] E. F. Barnett and J. K: Hunton, "A Precision Directional Coupler Using Multi-Hole Coupling," *Hewlett-Packard J.*, vol. 3, Mar.-Apr. 1952.

[7-69] V. A. Labay and J. Bornemann, "E-plane directional couplers in substrate-integrated waveguide technology," *2008 Asia-Pacific Microwave Conference*, Macau, 2008, pp. 1–3.

8. Conclusion

Starting with E-plane filters, major improvements achieved with ultra compact pseudo-elliptic inline waveguide bandpass filters that use bypass coupling are in compactness, although fabrication is also still simpler than for machined waveguide filters. We have put these filters against further challenges occurring in real environments, and they showed well balanced characteristics. They are able to satisfy wide range of passband bandwidths (demonstrated 5.3%-12.0% range of fractional bandwidths for 3rd order filter, though these are not the most extreme values), have versatile ways to obtain the same network response, are not very sensitive, have mechanical tuning possibility and are suitable for making higher order filter units (successfully simulated response of 5th order filter).

Regarding use of filters with I-shaped resonant insets, they are a new type of compact E-plane waveguide filters with inline geometry and quasi-elliptic response. Such resonators designed at 10 GHz have Q factors of 1873, 2610 and 2821 for the three lowest modes, respectively. The resonators have been experimentally tested. Also, equivalent circuits aimed for synthesis have been developed and their accuracy inspected. By producing transmission zeros at either 11.6 GHz or 8.85 GHz, possibility to introducing steep transition by a transmission zero in either upper or lower stopband has been demonstrated. Additionally, a 3rd order filter using all three lowest cavity modes was modeled at 11 GHz center frequency. Its total length is 41.8 mm, which is 23% shorter than its conventional all-pole E-plane equal.

Furthermore, novel waveguide bandpass filters optimized for low-cost hybrid additive/subtractive manufacturing have been presented in this letter. The flexibility of 3D printing is suitable for realization of contactless discontinuity geometries like the rectangular ring ones. A resonator of 11.13 GHz centre frequency fabricated with 40 % fill density was experimentally evaluated to have Q factor > 620. In addition, a third order filter with two pairs of transmission zeros in the lower stopband has been designed, being 34.3% shorter than its E-plane counterpart. Its minimum measured insertion loss in the passband when printed with 15 % infill was 0.6 dB. Even more, a 4th order filter with multiple transmission zeros both in the upper and lower stopband was also demonstrated by building a prototype. A very good matching of simulation and measurement results has been obtained.

Still staying with 3D printing, a high Q alternative for substrate integrated waveguide filters aimed for 5G mm-wave wireless technologies has been developed utilized 3D printing for fabrication of otherwise complex geometries. Resonator Q factors are up to 5000 for TM_{010} mode and up to 5500 for TM_{110} modes. Designing a sample 4th order filter, two transmission zeros of were asymmetrically located on different sides of the passband, where the negative coupling was utilized through a dual mode cavity.

As the probably most significant result, a novel, wholly planar orthomode transducer in mixed SIW/SICL technology has been presented. The square waveguide carrying two orthogonal polarizations is fed by four SICL probes of the OMT. Tapered center conductor sections in nonhomogeneous dielectrics are used for inline transitions between SICLs and single layer SIWs. Finally, each pair of signals belonging to the same polarization and travelling through two branches of SIW is combined in an E-plane straight Y-junction.

Excellent wideband, high isolation and polarization purity performances have been achieved wider than in standard WR 90 X band rectangular waveguide recommended frequency range.

8.1. Contributions of the Thesis

The main contributions of the thesis are new and original designs of passive microwave components, most numerous being filters, that have performance or fabrication improvements in certain segments in comparison with previously known designs:

- **A Fully Planar Substrate Integrated (SI) Probe-Based Wideband Orthomode Transducer (OMT)**
  combining excellent isolation, polarization purity and especially wideband characteristics with a low profile design;
- **Stepped-bend Substrate Integrated Waveguide (SIW) to Rectangular Waveguide (RWG) Transition**
  having 27.4 % fractional bandwidth for an easy to design structure entirely implemented inside two PCB layers, without need for any external matching elements;
- **Substrate Integrated Waveguide (SIW) Filters Using Dual-Mode Cavities With Diagonal Slot Line Perturbations**
  where using diagonal slots as elements for intracavity field perturbation has advantages of not being overly sensitive, accurate fabrication, tuning and miniaturization;
- **Low-Profile High Q Integrated 3D Printed Cavity Filters**
  use resonators with the lowest surface area to volume ratio to maximize their Q factors when their heights are confined, and are tailored for additive manufacturing;
- **Low-Cost Hybrid Manufactured Waveguide Bandpass Filters with 3D Printed Insert Dielectric**
  combine additive manufacturing of dielectric parts with subtractive manufacturing of metal parts to get the best of both worlds, also using rectangular ring resonator as waveguide discontinuities appropriate for implementation of this design;
- **E-plane dual band waveguide resonators**
  extend use of fins between septa of E-plane filters for independent control of two passbands by being offset in longitudinal direction, relying on different field distributions of even and odd resonances, realizing compact filters with steep skirts and entire geometry utilizing the filter function in a single plane;
- **Compact Inline E-plane Waveguide Resonators and Bandpass Filters with I-shaped Resonant Insets**
  are able to realize all the filter functions like E-plane modules using fins, but in balanced design that does not require electrical contact between resonant insets and waveguide housing.

In addition, there have been contributions regarding explaining working principles of E-plane filters such as which higher order modes contribute to filter responses, their eigenmode responses, and passband matching using Smith diagram. Furthermore, suitability of E-plane filter for many uses such as in diplexers, high order filters, tunability and their sensitivity have been investigated for the first time.

8.2. Future Work

The process which is already under way is fabrication of the stepped-bend substrate integrated waveguide to rectangular waveguide transition, as well as of planar substrate integrated probe-based wideband orthomode transducer. Their experimental verifications, together with further explanations about working principles, parameter analysis, scalability testing and applications to different hollow waveguides should wrap up the topic. It would also be interesting to investigate some other attempted ways of coupling planar orthomode transducers to waveguides through slots, but with corrected problems regarding asymmetrical feeds that were producing unwanted couplings between signals with orthogonal polarizations.

Regarding dual band filters, cross-coupled E-plane resonators and filters with back-to-back geometry are also candidates for this application. If this proves to work, there can be possibility for combining them with extracted pole E-plane dual band filters into dual band filters of mixed topologies. Furthermore, diplexers made from compact E-plane filters would benefit from developing a synthesis procedure. Also, non of these filters and diplexers has yet been prototyped using 3D printing.

Although there has been quite few applications for which compact E-plane filters have been tested, a good future step could be designing them at lower frequencies and seeing how they compare with coaxial filters, which are standard in base station applications.

Another topic of interest is to simulate and practically test behaviours of the used low-cost and compact structures under harsh working conditions like high temperatures causing mechanical deformations and breakdown levels at high power inputs.

Appendix A: Fabrication of waveguide filters and related microwave components

This chapter is dedicated to the process of transforming structure models with functionality verified by electromagnetic simulation into fabricated prototypes. Each section describes a different fabrication method, individually very broad and polyvalent subjects, from a niche perspective of application in microwave engineering. Furthermore, hands on aspects like particular steps taken in preparing files for machine input and practical tips for machine settings and control are given.

A.1 Fabrication of filter inserts using LPKF ProtoMat C60 mill/drill unit in WCRG laboratory

A.1.1 From CAD to machine input

Program CircuitCAM 5.0 by LPKF [A-1] (combined Computer Aided Design (CAD) and Computer Aided Manufacturing (CAM) software for data processing [A-2]) is used to prepare a layout to be exported in format suitable for the plotter to perform fabrication. It is useful to point out straight away that, although ideally in PCB fabrication we would like a seamless automated and standardized transition from the drawing board to the plotter, in reality it is still far from that. There are several intermediate steps to be taken and attention is required in order not to lose required properties along this transition.

Even though a layout drawing can be directly created in CircuitCAM, it is easier to have Gerber [A-3] files[20] of individual layers exported from the 3D model of the structure in CST or other EM simulation program. The layer which is exported from CST is the one laying in the z-plane, or what is usually more comfortable, the one laying in the w-plane when local working coordinate system (WCS) is activated. In the Gerber file export dialog box inside CST, units and decimal places before and after the decimal point of a number can be set. For instance, stands for units in millimetres, 3 digits in the integer part and 4 digits in the fractional part. This translates to %MOMM*% and %FSLAX34Y34*% commands in the output Gerber file, respectively, where leading zero is omitted and coordinates are absolute. When E-plane waveguide filters are modelled and simulated in CST Microwave Studio, the waveguide housing should be deselected/removed when exporting (extended) Gerber file of the insert. In CircuitCAM, GerberX (RS-274X) file of the insert conductor is imported into the TopLayer. Although it has not been used, it is
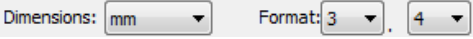
---

[20] Gerber is a relatively old ASCII file format, originally created for vector photoplotter drivers in 1980, widely criticised for its downsides. There have been numerous attempts to have it replaced with other allegedly improved file formats, most notably with ODB++ [A-4] by Mentor Graphics, now a subsidiary of Siemens. Nevertheless, it has remained the dominantly used format with currently more than 90% share in PCB fabrication and being universally supported. There is an ongoing heated debate questioning whether the future lies in further Gerber improvement, arguing that with its simplicity, readability and high volume of use it is easier for it to be debugged, or a format of different foundation [A-5]. The photoplotting origin is also the reason why the basic element for drawing (2D shape that is stroked or flashed) is, confusingly, called aperture, referring to the opening through which the light shines and exposes images on lithographic film.

possible to have PCB designed on both sides, and the alignment is accomplished by drilling holes through the substrate before turning it round. In this case, another GerberX file is imported into the BottomLayer for MillingBottom operations. (Use of older Standard Gerber or RS-274-D file format, having multiple output files, is strongly discouraged - officially revoked and no longer valid - by Ucamco, who claim that it does not have a single advantage over the newer versions.)

For all-metal inserts, Insulate Top Layer command is used after having selected the Top Layer areas to be left covered with copper, and stores the insulation line in the InsulateTop_Std Layer. It corresponds to electrically isolating conductor tracks and pads of a standard low frequency PCB by milling isolation channels around them. The active layer is the TopLayer from the first drop-down list in the CircuitCAM interface, and the plotter uses End Mill (RF) 0.15 mm (6 mil) from LpkfMillingTools, which should be selected from the other two drop-down lists. This limits the minimum gap width to be 0.3 mm. On the other side, LPKF ProtoMat C60 resolution (smallest step of the mill/drill head) is better than 0.01 mm. Nevertheless, this is significantly better than the actual fabrication process precision due to many imperfections such as how the metal foil differs from the perfectly flat one.

For PCB inserts, Rubout Top Layer command is additionally applied, opening Rubout Top Layer for drawing the outline of the area to be rubbed out. Alternative and more elegant way is to import GerberX file of the PCB profile into the RuboutTop Layer. This difference exists because copper sheet inserts only need to be cut along the edges, whereas on printed circuit board inserts all extra copper cladding needs to be removed from the substrate surface. After pressing Insulate Top Layer command for the second time, the rubout area of residual copper is covered with milling path and stored in the InsulateTop_Big Layer.

Although End Mill (RF) 0.15 mm (6 mil) can be used for all milling production phases, other similar surface machining carbide tools available are bigger diameter cylindrical non-RF End Mills as well as conical Micro and Universal Cutters [A-6]. RF End Mill has advantage when forming insulation tight around copper areas, however, it is more expensive and less durable solution. For rubbing out larger copper areas it is inferior option, being also slower, whereas not being able to utilize any advantages in terms of precision, apart from no need for changing the tool.

Unlike thin metal inserts, which are milled out of their copper sheet through insulation of the top layer with an end mill tool, PCB inserts are milled out through contour routing[21].

Contour Routing dialog box is opened by pressing , where Outside is selected and CuttingOutside is the Destination Layer. As the source is selected layer/current selection in which boundary contour has been drown in CircuitCAM, or, more comfortably, Gerber file with the outline/filled surface of the entire structure cross section (i.e. the profile) imported.

Layers are stacked one on top of the other (higher ones covering lower ones when viewed together) and designated by different colours and fill-in patterns. Top to bottom order, colour, as well as visibility and selectability can be changed from Layers window (View>Layers…).

---

[21] Another situation in which contour routing (inside option) is used is for drilling holes larger than 2.4 mm. This is performed automatically by 2.0 mm routing cutter, instead of direct use of large diameter drill tools.

A.1.2   Circuit board plotter control

Driver program BoardMaster 5.0 (machine control software) [A-7] is used for operating the physical machine – ProtoMat C60 circuit board plotter [A-8] to fabricate a prototype. Prior to its use, the design should be exported from CircuitCAM by selecting File>Export>LPKF> LPKFCircuitBoardPlotter. A .cam file is generated, but also LPKF binary file with .LMD extension (LpkfMillDrill format) containing data needed to drive the plotter. File>Import>LMD/LPR… option is used to import the production data inside BoardMaster. However, if BoardMaster is open while LMD file is being exported from CircuitCAM, it is automatically imported into BoardMaster.

In the left-hand side section of the BoardMaster function bar (Figure A.1.) from the top drop-down list can be selected the appropriate active tool element inserted into the ProtoMat C60 shaft of the high-speed spindle to perform the fabrication process. As it is already known, for cutting out metal insert of an E-plane filter from a metal sheet or insulating (we can say complete rubbing for simplicity's sake) the metal surface of a PCB we use End Mill (RF) 0.15 mm (6 mil) tool, as given in the Figure A.1. After having selected the appropriate production phase from the lower drop-down list as well, all the activities with chosen tool within the selected phase can automatically be performed corresponding to the previous assignments in CircuitCAM. For example, End Mill (RF) 0.15 mm (6 mil) and Milling Top pair (Figure A.1.) is selected both for complete all-metal insert processing and for top layer PCB insert copper insulation and rubbing at the same time. Contour Router 2.0 mm [79 mil] and CuttingOutside pair is selected for cutting out PCB inserts from their laminate boards.

Figure A.2. Left section of the BoardMaster Function Bar for selecting current production phase and active tool.

Next, the central part of the function bar (Figure A.2.) is used to navigate the mill/drill head of the machine represented by the crosshair cursor over the board. As in reality, the board is static and both the head and the layout positions can be moved inside the BoardMaster working area.
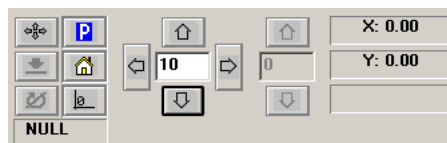
Figure A.2. Central section of the BoardMaster Function Bar with functions for manual control of the mill/drill head.

Initially (parking or pause position), the machine head (cursor) is in the top right corner. When button is pressed, wherever on the board is clicked with the mouse left key, the head moves to that location. Discrete steps along the main axes can be made by using the arrow keys, inserting in the centre text entry box the step length in millimetres.

In order for project layout (single imported LMD file such as one waveguide filter insert) translation by mouse dragging to take effect, it needs to be preceded by pressing button (location in Figure A.3.). More numerically accurate and complete transformations, including rotation, can be made from the window that can be opened on the right mouse click on the layout.
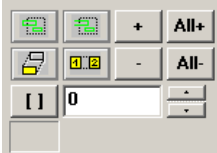
Figure A.3. Right section of the BoardMaster Function Bar with functions for changing the layout position and data selection.

In general, before production phase of fabrication job is started (button is pressed for that action), all data need to be marked by pressing All+. However, if fabrication is done step by step, in a certain order, button is pressed to do rectangular area selection with the mouse, and then + is pressed to add the selected data to the marking.

When the mouse cursor is hovered over any of the tools, in the status bar in the bottom left corner is given the explanation of the actions of that tool. For example, it can be found out that the previously used command only selects lines that are entirely encompassed within the selection area, whereas the similarly looking command also selects the lines that are crossed by the selection area, and can alternatively be used when it is handy.

Before setting out the fabrication process, it is important to verify that the working tool position is upwards (not directly on the board) before it is moved, in order not to damage the board and the tool itself. Also, the knob on the spindle that opens and closes the collet with the tool must be in the top position. Otherwise, the spindle is blocked from rotating, and the tool is statically pushed through the board.

Figure A.4. ProtoMat C60 mill/drill head with high-speed spindle having end mill tool in its shaft.

Fabrication process can be improved if the order of segment milling is chosen manually, rather than being left for BoardMaster to execute it automatically. Here is given an example of such a procedure (Figure A.5.), where individual lines are enumerated in the order of plotter cutting the metal sheet along them. The most critical is milling of thin fins. If their edges are cut consecutively, very often, while changing direction, milling tool bends the fin. This is aggravated by the fact that cut parts tend to distort and pop out from the metal sheet layer. After segment 7 is milled, it is useful to remove the central cut out metal segment in order to prevent the machine head pulling it and damaging the insert.
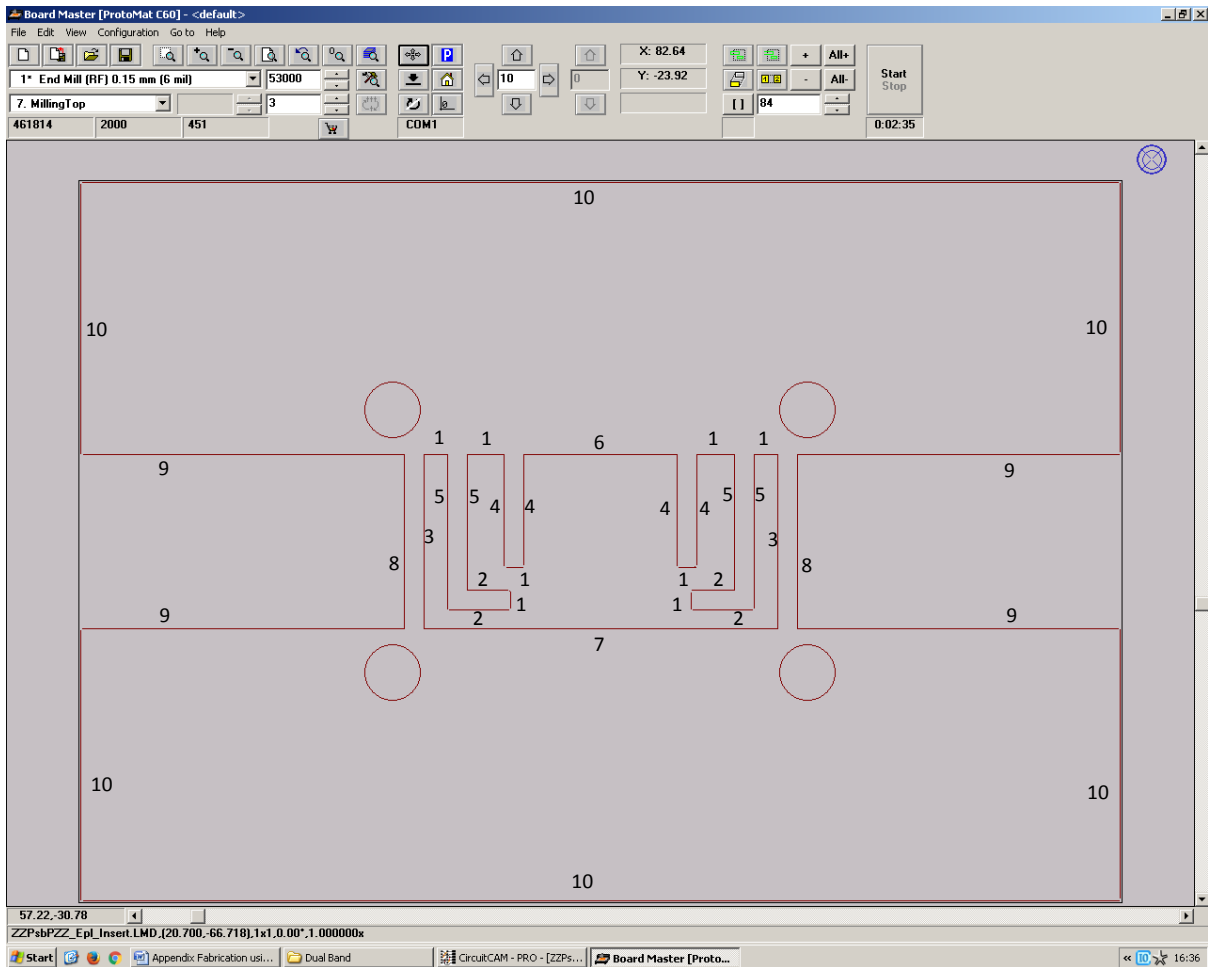
Figure A.5. Layout of dual band resonator insert inside BoardMaster with its line sections numerated in the order for milling.

Selection of substrate can vastly affect how difficult PCB fabrication is. For LPKF milling plotters, it is very suitable to use ceramic based substrates like RO4000 series from Rogers Corp [A-9], having similar processing like FR-4. RO4003C laminate, used here, is considered a good choice up to 20 GHz, whereas for higher frequencies there is LoPro option [A-10], having lower surface roughness. This series of substrates is by far the most used one, outnumbering all others together. Nevertheless, RT/duroid 5880 [A-11] is often seen in research papers for its smallest losses, as authors typically want to showcase best performance. However, this glass microfiber reinforced polytetrafluoroethylene composite (PTFE - Teflon based dielectric) does not work well with milling tools. Its threaded structure results in copper cladding not being fully removed. Interestingly, although crude and lengthy process of manual rubbing was used for resonators with I-shaped insets to remove the residual copper, obtained results were very good.

File>Save As… option lets saving the complete job as a .job file, so next time the prototype can be prepared in its entirety for fabrication from BoardMaster through File>Open… and selecting the same .job file.

Current LPKF ProtoMat machines [A-12] have become smaller, faster and more precise over time. Successors of C60 (E series) have improved vertical adjustment of tools (now having distance rings) in the collet of the spindle, and, as comparable new devices, are even

significantly cheaper than C60 originally was. Higher class LPKF machines (S series) are enclosed and have automatic tool change. Even higher range products (D series) use laser, but come as well at much higher cost. The precision, speed and production capabilities are noticeably better with higher product class.

A.2   Sending files for professional external PCB manufacturing

When Gerber files are sent to a PCB manufacturer for fabrication, layers can be exported one by one from CST Microwave Studio and then added to a common zip archive. Even if designs are exported from electronic design automation (EDA) software packages specialised for PCBs such as Altium Designer, Cadence OrCAD or Autodesk Eagle in one go, still the output contains multiple Gerber files. This characteristic of Gerber files has been criticised, and formats like ODB++ are readily exported as archive files [A-5]. When the structure is complex enough (e.g. double layered OMT with vias compared to a single layered E-plane resonator insert), it is important to include a ReadMe file in the archive, so that it is maximally clear to the CAM engineer what we aim to do.

The essence of the discussed process is that CAD output is PCB manufacturer's CAM input (their equivalent of CircuitCAM), not machine input (their equivalent of BoardMaster). One of the reasons for it is that PCB fabricators typically do panelization, i.e. fabricating different prototypes from the same production panel. Main tips regarding sending files for professional PCB manufacturing are summed up in [A-13]. In addition, large PCB manufacturers give their own recommendations [A-14].

Common Altium (Protel) filename extensions can help CAM engineer identify layers. For E-plane PCB inserts, three layers have been used: Top (.gtl), KeepOut (.gko) and Bottom (.gbl), where the Gerber extensions are noted within the brackets. Nevertheless, Ucamco advises to always use .gbr file extension for all the Gerbers, meaning that the aforementioned files would have .gtl.gbr, .gko.gbr and .gbl.gbr endings. Furthermore, there is Gerber Standard File Naming (GSFN) convention, with the most universal way of explaining the file function within the file name [A-13].

Gerber X2 revision, introduced in the autumn of 2013 and compatible with Gerber X1, supports attributes. Among the rest, it is the answer to the Gerber format criticism that it had not contained the information about how the layers had been stacked up. In Table A.1. is given a sample comparative use of GSFN and Gerber X2 file function attributes.

Table A.1. Example of GSFN Gerber file names and .FileFunction file attributes used for substrate integrated orthomode transducer.

Gerber Standard File Name	.FileFunction file attribute
Copper$Top.gbr	%TF.FileFunction,Copper,L1,Top*%
Copper$Inner.gbr	%TF.FileFunction,Copper,L2,Inr*%
Copper$Bottom.gbr	%TF.FileFunction,Copper,L3,Bot*%
PlatedTopDrill.gbr	%TF.FileFunction,Plated,1,2,Blind,Drill*%
Plated$Bottom$Drill.gbr	%TF.FileFunction,Plated,2,3,Blind,Drill*%
NonPlatedTopRoute.gbr	%TF.FileFunction,NonPlated,1,2,Blind,Route*%
NonPlated$Bottom$Route.gbr	%TF.FileFunction,NonPlated,2,3,Blind,Route*%
Plated$Through$Drill.gbr	%TF.FileFunction,Plated,1,3,PTH,Drill*%
NonPlated$Through$Route.gbr	%TF.FileFunction,NonPlated,1,3,NPTH,Route*%
Outline.gbr	%TF.FileFunction,Profile,NP*%

For the Profile, Outline or Keepout Layer, giving the essential information to the fabricator regarding the extent of the PCB, it is best to have it exported as simple planar inner solid region from CST Microwave Studio. It is easiest to do it from a dielectric layer that is not perforated. Alternatively, it can be defined just by the zero size boundary closed contour, even if it is not filled (G36/G37 commands not included), assuming that the structure is on the inside. If the contour is not zero size (finite size aperture in Gerber language), the centre line of the stroke is taken as the boundary. Although technically it is not needed as the same coordinate system should be used, fabricator may prefer to have outline in all the layers in order to align them in the case of an offset problem [A-14]. Related to this issue, layers should never be mirrored. Each one of them ought to be viewed from the top.

If vias are included into the design, for which exemplars are SIW structures, or any other drilling/routing jobs are required, Excellon format NC (numerical control) files are typically used and many fabricators prefer them [A-14]. More precisely, there are other file formats very similar to Excellon, like IPC-NC-349 or Sieb & Meyer, which are all G-code variations that mutually differ only in minor details. Excellon files store data for driving CNC drilling or routing machines to make round holes or other apertures of different shapes and sizes in the PCB, hence can be used directly for the machining process. Tool list (sizes) and other machine parameters like speeds can but do not need to be embedded. Metallization (if needed) is independently specified to the manufacturer. Nevertheless, as the CAD to CAM transfer is the topic here, image description files, in particular Gerber ones, can be used without problem, just as it is anyway usually done with the outline routing. Moreover, Gerbers are even more appropriate for this task for the reasons like better registration of drill files and copper layers and better resolution. In this work, Gerbers were used to store via and non-plated routing data mostly for simplicity since they are anyway used for transferring information regarding fabrication of metal layers. Although Gerbers standardly keep via information as inner diameters after plating, which is meaningful for through-hole technology, in SIW and related microwave applications, the outer (drill hole, Excellon information) diameters are the ones that matter because vias are used to guide signal

propagation between them. The only constraint for the minimum via plate thickness is that signal does not leak.

There are several different via types in multilayer PCBs. Plated through holes connect top and bottom copper layers, and are naturally the only via type for single-layer boards. PCB with two or more layers can have vias that come to the surface on only one side of the board and are called blind vias. Starting with three layers, there can be vias that connect two inner copper layers, which are called buried vias. In addition to these taxonomy terms, there are several different ways of closing and protecting vias according to IPC-4761, namely tenting, plugging and filling [A-15]. In tenting, vias are only surface covered with dry film. Plugging implies deeper sealing with a non-conductive material which partially enters the via. Finally, filling extends to complete loading with a non-conductive paste. Each of them has several variations such as being used on just one end or both ends of a via. Filled vias can also be capped – overplated on both sides after filling. In fact, via filling itself can be conductive epoxy (DuPont CB100 and Tatsuto AE3030 are widely used) instead of non-conductive one, however, this implementation is more expensive and has larger mismatch with the thermal expansion of the surrounding substrate material [A-16].

If standard chemical processing of etching the residual copper using alkaline solution is used, both Teflon and ceramic based substrates show clean fabrication results. Nevertheless, ceramic based substrate still have better mechanical properties, which for instance mean easier drilling and routing.

So far, only rigid substrates have been discussed, but flexible substrates, as the foundation of flexible circuits and flexible electronics [A-17], have growing importance. Flexible circuits have already had numerous significant applications ranging from beginnings with thin single-crystallline silicon solar cell arrays to improve power-to-mass ratio on satellites, over connectors, electronics in smart cards, to booming technologies in displays like TFT and OLED. The substrate flexibility is closely related to its thickness – everything thin is flexible, and for most materials, stiffness increases proportionally to the cube of thickness. Typical thicknesses of flexible films are in the range from 13 µm to 125 µm. Even the thinnest conventional substrates can be considered as flexible, e.g. 125 µm thick nearly pure PTFE Rogers Corp RT/duroid 5880, which is particularly suitable for high frequency application being low loss [A-18], though it lacks mechanical properties of standard flexible circuit materials. Fundamental difference between dielectric materials designed for flexible circuits compared to the rigid ones is that they are generally manufactured without glass reinforcement, on large rolls of coated film, instead of resin impregnation into a glass cloth [A-19].

In microwave engineering, among most widely used flexible substrates are Kapton, LCP, PEN, PET and paper [A-20]. Kapton (polyimide) is the most prevalent flexible electronics material in general. It is known for temperature stability, excellent flexible-mechanical characteristics, and its relative permittivity and loss tangent were extracted from the measurement between 5 and 40 GHz to be around 3.2 and 0.002 respectively. LCP (liquid crystal polymer) is noted for good millimetre-wave performance, having low water absorption and relative permittivity of 3.16 and loss tangent of 0.0049 nearly steady from 30 to 110 GHz in [A-21]. Likewise, it has been commercially used for a long time. PEN (polyethylene naphthalate), although considered as improvement of PET with better water absorption characteristics, is still more lossy than LCP (e.g. has $\tan \delta = 0.0035$ compared to 0.0024 of

LCD at 1 GHz), and is less often used in high frequency applications [A-22]. PET (polyethylene teraphthalate) is omnipresent thermoplastic polymer encountered in objects such as clothes or food and liquid containers, with obvious strongest side in low cost. In [A-23] it was found that PET has stable $\varepsilon_r = 2.85$ and $\tan \delta = 0.009$ up to 20 GHz. Papers come with even lower cost and are, importantly, degradable and recyclable, though having high surface roughness and high losses. Same DC to 20 GHz measurement found Teslin paper to have $\varepsilon_r = 2.23$ and $\tan \delta = 0.046$, whereas E4D paper had $\varepsilon_r = 2.54$ and $\tan \delta = 0.05$.

Flexible substrates like Rogers Ultralam 3000 LCP [A-24] or DuPont Pyralux Kapton [A-25] can be purchased readily metallized on one side or both sides and processed with conventional PCB photolithography and chemical etching. Unlike rigid substrates, flexible ones are more often covered with rolled than electro-deposited (ED) copper foils, being more appropriate for dynamic applications due to its smooth surface, though having disadvantages in weaker bonding and adhesion [A-26]. Attention should also be paid to which flexible circuit adhesives are used, since traditional acrylic and epoxy ones are high-loss [A-27].

A.3   Fabrication of waveguide cavities using CNC machining

Computer numerical control (CNC) machining [A-28] is dominantly automated modern implementation of classical subtractive manufacturing processes like milling, drilling, routing and sawing. In contrast with CNC machining using LPKF ProtoMat plotters, here is mostly considered machining of bulk metal. For example, the E-plane split waveguide housings that have been used to accommodate filter inserts, had been manual machined using such manufacturing processes (Figure A.6.). CNC machining can also use non-lathe based operations like electrical discharge or laser machining.
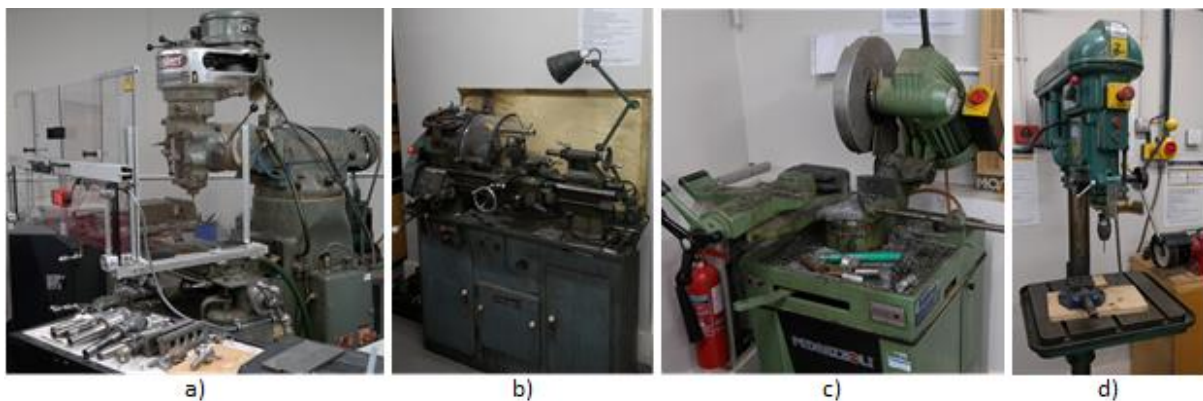
Figure A.6. University of Westminster FST workshop manually operated machine tools: a) milling machine, b) metal lathe, c) cut-off saw, and d) drill press.

Most CNC machine shops facilitate machining with vertical machining centre (VMC), which means vertically oriented main spindle and is more affordable variant. On the other side, horizontal machining centre (HMC) CNC machines can have larger capacities. Common CNC machine tolerances are around 0.5 mm [A-29]. Nevertheless, micrometre precision sufficient for extremely stringent terahertz applications is also achievable [A-30]. However,

special micromachining[22] technologies [A-31], [A-32] like Deep Reactive Ion Etching (DRIE) [A-33] or SU-8 photolithography [A-34] are more suitable for mass production at such high frequencies. Since silicon as material is the core of microfabrication processes, additional, very fine metal plating is required.

In Figure A.7. is shown a CNC machine on display in London's Science Museum. FANUC company pioneered broad engineering use of CNC outside defence industry.

Figure A.7. Colchester 200L Lathe and FANUC control system, part of permanent exhibition in the Science Museum, London.

A.4   3D printing

Additive manufacturing (AM) [A-35], [A-36], also known as 3D printing[23], refers to manufacturing processes in which objects are built layer by layer directly in their required forms, where in each layer material forms a solid shape by one of available techniques under computer control. Even though developed in early 1980s for rapid prototyping (RP), we are presently witnessing heydays of additive manufacturing, which has been even described as starting the third industrial revolution. Unlike machining, AM could not have been implemented before computer technology matured enough. It can be compared with millennia old human practice of constructing buildings layer by layer from stone blocks or bricks.

Although it may appear that additive manufacturing has overwhelming advantages compared to traditional subtractive manufacturing processes, they have rather different upsides and are likely to be applied in different scenarios. 3D printing indeed has edge in producing less waste or objects of greater shape and inner construction complexity. Unlike standard processes in which complexity, if feasible at all, comes with increased cost, in AM not just that the cost is not increased, but it is reduced provided that less build material is

---

[22] Integrated circuit (IC) fabrication is the oldest and most famous application of microfabrication processes, with CMOS still being the most voluminously microfabricated device without close competition.

[23] In fact, terms 3D printing (3DP, coined by MIT researchers) and stereolithography (SL or SLA, coined by 3D Systems) started as referring to two competing technologies of AM, both implying extension of well-established 2D technologies into the third spatial dimension. However, the former has been adopted as the most popular synonym for AM, and not only for binder jetting, whereas the latter has kept the meaning of a particular technology. Before being replaced by the more accurate formal term 'additive manufacturing', now also recognized by ASTM International [A-37], rapid prototyping was used as the most general name of the technology, but has since then reduced to only one of its applications.

spent. Also, fabrication is in general simpler and can be done in less stages. Nevertheless, AM lacks speed and low cost per unit in mass production of elements such as screws or mechanical durability and single part size in elements such as plane wings. For instance, metal springs are in essence antithesis of additive manufacturing. One, possibly overlooked, concerns about AM is repeatability. Still, 3D printing is mostly used for prototyping, and it is yet expected to take its share in product manufacturing industry – direct digital manufacturing (DDM). Anticipated performance enhancements when using AM of RF and microwave passive components are in mass, geometry, interface simplification and reliability [A-38]. On the positive side, engineers using AM can rethink constant use of right angles in designs. In general, sturdiness and safety can benefit from blended edges. In microwave applications, losses can be reduced and power handling capability increased in this way.

Even though it promises direct link between an idea shaped into its 3D model using a CAD tool and the final prototype, additive manufacturing has not yet reached the stage where a designer can completely focus on the designing process and not consider fabrication itself. E.g. screw holes are better build if they are vertical than if they are horizontal. Likewise, with metal printing, care should be taken about how metal powder residue can be eventually removed when fabrication is completed. One of the first questions users come across is the threshold for overhangs without support. The rule of thumb is the angle of 45°. However, AM methods that build structures from powder beds have inherent support, so this does not apply to them.

In fact, many fabrication processes based on additive manufacturing actually contain subtractive corrective stages as well. At very least, almost always certain clean-up of bits of excess build material or removal of support structure is needed. In microwave engineering fabrication, surface smoothing and metal plating post-processing stages are of particular interest.

STL (STereoLithography) file format, which describes only the triangulated surface of an object in either binary or ASCII code, has risen as de facto standard for exporting geometry of CAD models to the 3D printer software. Its origin is in the early days of 3D printing by stereolithography as the first commercial AM process, and is today the best supported file format for this purpose, available and used in CST Microwave Studio. Nevertheless, new formats like 3MF [A-39] are trying to address interoperability limitations of STF files, promising to send full-fidelity 3D models to a variety of services and printers.

In the 3D printer software (CAM), the structure needs to be sliced – turned into a series of 2D geometries to be printed one at a time, representing all the cross sections along the z-coordinate after setting the layer resolution. Interestingly, the STL files do not even contain the units in which are the original model dimensions. There is a number of other settings related to how the actual printing should go such as infill percentage, thicknesses of outer walls (shell, perimeter), bottom and top layers, etc. that can be customized before the model is exported in a numerical control (NC) format used by the machine. For all the 3D printing done here, Ultimaker Cura software [A-40] available under LGPLv3 license has been used with G-code output files. Interesting option available in Cura is 'Load Profile from GCode', which allows recovery of the print settings used for particular output file.

Officially, there are 7 categories of additive manufacturing recognized by the American Society for Testing and Materials [A-37]:

- Vat Photopolymerisation

  Material form: photopolymer liquid resin in a vat
  Process activity: curing (solidifying resin through light-activated polymerization) by selectively delivering laser or projected light energy
- Material Extrusion

  Material form: mostly filaments, but can be liquid, pellets, granules, powder, paste
  Process activity: depositing highly viscous material extruded through nozzle by pressure
- Material Jetting

  Material form: ink, such as waxy polymer or acrylic photopolymer
  Process activity: jetting droplets of ink
- Binder Jetting

  Material form: powder bed
  Process activity: printing liquid bonding agent (binder) to join the powder
- Powder Bed Fusion

  Material form: container filled with powder
  Process activity: powder is melted and its particles fused by scanning laser or electron beam as the energy source
- Directed Energy Deposition

  Material form: predominantly metal powder or wire
  Process activity: energy, typically from laser or electron beam, provided simultaneously with material deposition to fuse it by melting, in contrast with having pre-laid material and comparable with extrusion
- Sheet Lamination

  Material form: sheets, originally and most popularly paper
  Process activity: entire layer of material deposited at a time, needed cutting just along the outline as well as additional bonding between the stacked layers

To find common sides between the 7 listed categories, it is good to use Pham's 2-dimensional classification method [A-41]. One dimension describes the state of raw material before part formation, and the other technique how the layers are constructed. Comparing figures of merit is mostly relevant within the same technology, as there are other hidden factors that influence the quality of the final product. For instance, SLA technology, although older, typically obtains finer details and smoother surfaces than FDM even at the same resolution due to effects like bonding between layers, their misalignment, applied force during printing, etc. It is interesting to note that photoresists used in photolithography PCB fabrication and other processes involving etching like microfabrication are nothing else than single layers of SL with different tolerance requirements.

In AM of conductive parts for microwave applications, the process can be separated between printing stage and plating stage. In this section is only considered the former, whereas the latter is covered in the following section, although if 3D printing is readily made with metal, the second step is not necessary. The major issue characteristic for this type of manufacturing is with surface roughness caused by layered fabrication. Even though it has specific geometry, like with any other form of surface roughness, the conductor's boundary surface is enlarged and loss with it. In addition, materials in powder form are also prone to resulting in grained finish and increased surface roughness [A-42]. Certainly, other problems like mechanical and thermal characteristics of the material or precision of the fabrication process remain as well.

On the other side, when non-conductive elements are 3D printed, dielectric loss tangent of the material starts being significant. Unique for AM, in particular FDM, is the possibility of using fill density <100% (infill, the percentage of volume filled with printing material). As the infill gets lower, up to 0%, and Cura has text entry box to directly set its value, more of so called bridging with the top layers between the outer walls is needed. By reducing the infill factor, dielectric can be made less lossy at the expense of increased structure size. There are different infill patterns available: grid, lines, triangles, etc. In order to significantly simplify simulation of objects with reduced infill, equivalent complex permittivity is used instead of exact geometry of the print structure [A-43]. It can be calculated from effective medium theory Bruggeman's model or measured.

A.4.1 Polymers (plastic materials)

As a matter of fact, the idea of using air-filled metallized low-cost and lightweight polymer waveguide filters and other related components is not exclusively linked with 3D printing and use of injection moulding technology for that purpose precedes the modern expansion of additive manufacturing [A-44]. (Resin casting could be considered as more cost effective alternative for smaller-scale production.) However, plastics have really become much more viable solution with added benefits of 3D printing, especially its availability with no tooling upfront costs. Since polymers have been vastly used as dielectric materials in electrical engineering over years of its existence, there is a substantial technical literature data on their complex permittivity relative to the frequency and temperature [A-45].

Fused Deposition Modeling (FDM)[24], belonging to the material extrusion category of processes, is the most widely used 3D printing technology, dominating the consumer model mass market. Its prevalence coming from affordability and ease of fabrication has granted it to be how we usually visualise a present day 3D printer (Figure A.8.). FDM is ideal for RP in the product design stage, not just having less expensive printers compared to the competing SLA technology, but also the material for it is cheaper and can be reused more times, as well as the initial post-processing stages of cleaning and support removal are significantly easier than for SLA. FDM uses thermoplastic filaments coiled on spools in two standard diameters of 1.75 and 2.85 mm. Thermoplastic filament is pushed into the heating chamber in the print head by the tractor wheel arrangement (feeder), heated up to melt and deposited in layers by the nozzle, using the pressure produced by the feeder for extrusion. This can be compared with glue gun operation. On the build plate, the material turns again into solid while bonding occurs.

---

[24] Fused Filament Fabrication (FFF) is another name of this technology, and Plastic Jet Printing (PJP) term is seldom used as well.

Figure A.8. 3D printing service bureau in a street of Amsterdam.

Most frequently used thermoplastics are ABS (acrylonitrile butadiene styrene) with its different versions (i, plus, M-, etc.), and PLA (polylactic acid) bioplastic, made from renewable resources like corn starch or sugarcane and biodegradable. ABS has slightly better mechanical (stronger, more flexible and durable) and thermal properties than PLA, at the cost of more difficult fabrication. FDM printed ABS materials have relative permittivity approximately between 2.10 and 2.83, and loss tangent approximately between 0.003 and 0.021 in the frequency range between 1 MHz and 60 GHz [A-46], [A-47], [A-48]. Frequency trends agree with standard physical models of polarization mechanisms in dielectrics, notably variants of Debye relaxation equation, and Kramers-Kronig relations imposed by causality, having the real part of permittivity after initial rise dominantly monotonously decreasing after 100 MHz with a modest slope and imaginary part relatively constant with narrow peak at about 10 GHz. Environmentally friendly PLA has very stable relative permittivity and loss tangent of 2.7 – 2.8 and 0.009 - 0.015 respectively in the wide range between 0 and 60 GHz [A-49], [A-50]. What has not been considered so far is that the very process of layered fabrication results in dependence of the complex permittivity on how the electric field is decomposed into the sum of component orthogonal to these surfaces and the one parallel with them. In [A-49], this anisotropy for PLA at mm-wave frequencies was measured to be nearly 7%.

Some other thermoplastics used in FDM filaments include nylon (it is more typical for SLS), PC (polycarbonate) and PP (polypropylene). Extensive comparative broadband characterisation of 3D printing materials for FDM can be found in [A-46]. Complex permittivity is of concern when printed material is inside the EM field (such as substrate, filling, or like in hybrid manufactured waveguide filters presented here), and in that case, FDM materials even have the edge over SLA materials being in general less lossy. Although SLA has superior surface finish after printing, important for plating, there are post-processing steps that can improve the results for FDM. For example, ABS dissolves in acetone, which can be used for smoothing the object surface, making it glossy without visible layer lines.

It should be noted that these are all standard (commodity) and engineering thermoplastics, which adds to their lower cost, but they do not utilized complete material potential of high-performance thermoplastics. Interesting blend of materials is addition of graphite to an FDM polymer, like Proto-pasta composite PLA [A-51]. Although this conductive PLA has too high resistivity for direct use in microwave components (it is anisotropic, between 0.30 and 1.15 $\Omega{\cdot}$m, with higher resistivity in the z direction against the layers), it allows easier

electroplating process. Considering the microwave applications of FDM materials as dielectrics rather that support for metallization, very promising high dielectric permittivity and low loss ceramic-thermoplastic composites for FDM have been recently reported. In [A-52], BaTiO$_3$/ABS polymer composites have been characterized with weight loading of BaTiO3 ceramic varying from 10 to 70% to reach relative permittivity of 8.72, made by dispersing BaTiO$_3$ microparticles in the extrusion processable ABS dissolved in acetone. Composites in [A-48] have Zeonex RS420 COP (cyclo-olefin polymer) as the thermoplastic matrix with loss tangent not exceeding 0.0009 up to 17 GHz, which is not only lower than for ABS, PLA, PC or PP, but being almost at the level of PTFE (Teflon) [A-53]. After being loaded with different ceramic filler particles sintered at temperatures surpassing 1100°C, of which TiO$_2$ has the lowest losses, tan δ of the ceramic-thermoplastic composite materials were measured going as low as 0.0012.

University of Westminster Faculty of Science and Technology (FST) currently has several 3D printers (Figure A.9), and all of them are FDM. Every 3D print in this work has been made using Ultimaker 2+ Extended [A-54] professional desktop printer and Ultimaker or RS Pro PLA filaments. For FDM technology, it has high maximum resolutions, the vertical being 20 μm (z direction, thinnest layer), and horizontal being 0.25 mm (x and y directions, smallest nozzle diameter). Accompanying accuracies are 5 μm in vertical direction and 12.5 μm in horizontal directions. Nevertheless, maximum resolutions in the horizontal and vertical directions cannot be reaches simultaneously as the maximum vertical resolution with 0.25 mm nozzle is 60 μm, and the nozzle with 0.40 mm diameter is the smallest one that can do printing with 20 μm vertical resolution. Obviously, there is tradeoff between building speed and precision, and the fastest printing is possible with 0.80 mm diameter nozzle, which can print layers up to 600 μm thick. The G-code files with complete instructions of model fabrication exported from Cura are transferred to the Ultimaker printer on SD card.

Another printer located at the faculty's campus is low cost XYZprinting da Vinci 1.0A. It has enclosed design, which gives it better temperature stability, but it lacks good enough resolution for intended microwave applications. Although both printers can be used with either PLA or ABS, XYZ is being used with ABS only and Ultimaker with PLA only. This is for the reason of preserving the higher quality printer by using it with the material favourable for printing, and also because enclosure is much more important for ABS than PLA printing. ABS uses higher printing temperature (210-250°C compared to 180-230°C) and higher print bed temperature (80-110°C compared to 20-60°C) and is more prone to warping and cracking. Nonetheless, PLA has disadvantage in being more susceptible to clogging the nozzle.

More recent purchase is dual extrusion Ultimaker 3 Extended. The main difference compared to the previous generation is that it uses additional dissolvable support rather than the same material one, which is difficult to remove and clean without trace. Hence, there is more freedom of design, though at the cost of increased print time. In particular, it can be used to fabricate filter elements such as thin septa and fins in horizontal layers, which are otherwise difficult to fabricate vertically with good quality. Ultimaker's support material is water-soluble PVA (polyvinyl alcohol).

In [A-55] can be found different surface roughness parameters found from measurements of PLA 3D prints with different shell thicknesses made by Ultimaker 3D printer. The measurements confirmed the surface becoming smoother as the printing temperature was increased from 210°C to 230°C.

Another model of high-end general-purpose desktop FDM 3D printer, 5th generation Makerbot Replicator, belongs to the University of Westminster Faculty of Architecture and the Built Environment (FABE). Moreover, they are also in possession of industrial-grade Dimension Elite FDM 3D printer. Dimension Elite is enclosed and uses soluble support technology.

Figure A.9. University of Westminster FST 3D printers: a) Ultimaker 2+ Extended; b) XYZprinting da Vinci 1.0A (left) and Ultimaker 3 Extended (right).

One of fabrication problems that can occur with FDM printing of larger base objects is bottom side bending (warping and sometimes curling are terms used in 3D printing community for this issue) due to too fast thermoplastic cooling [A-56]. Excessive cooling results in intense material contraction, which causes the print corners and edges to lift up from the build plate. Warping happened multiple times during project, especially when printing of low-profile resonator started, although the build plate was heated and fans were not switching on for the first layer. There are several other ways how this problem can be reduced like decreasing temperature, manually slowing down opening print speed or using adhesive (glue from a stick, hair spray) on the print surface. The most convenient (built-in features in Cura) and effective solution that has been applied is printing with a brim or raft.

Another typical problem with FDM prints is stringing – polymer threads that are left in the places where nozzle travels over open space. Stringing can be controlled by tuning filament retraction (pulling back) settings. For the filter insert PLA holders, stringing was minimized by changing insert geometry so that there are less disconnected surfaces within one layer.

SLA (stereolithography) technology uses photopolymer liquid resin which is hardened by being exposed to focused light, one point or entire layer at a time, the process known as curing. However, SLA here primarily refers to point-wise laser-based photopolymerisation method in contrast with layer-wise DLP (digital light processing) method. DLP projects mask with matrix of square pixels and has obvious advantage in speed, but details degrade for horizontally large prints as the pixels increase in size since their maximum number is limited. Moreover, SLA vector scanning is in general higher quality technology, and when used with

good optics for precision focusing, it can suppress DLP quality even if the laser spot size is not smaller than the DLP pixel size. SLA is not only one of the very oldest AM processes, but high frequency components including microwave filters were first produced by it more than 10 years ago [A-57], and is still the most popular 3D technology in microwave engineering research [A-58], [A-59]. This comes from combination of fine details and smooth surfaces it is able to fabricate with availability and usability, being second in widespread consumer popularity only to FDM. Main advantage in resolution SLA has over FDM is in horizontal direction (*xy*-resolution). First startup company dedicated to development and commercialisation of polymer SLA AM RF antennas, waveguides and filters has already appeared [A-60].

Most of commercially available SLA resins are epoxides with some acrylate content and react to light in the UV (ultraviolet) and visible spectrum regions. Unlike FDM filaments that are mostly in standard size and open form, SLA resin tanks are usually proprietary and cannot be refilled or exchanged with those from other vendors. Classical right-side up industrial SLA printers have light source on the top and new print layers are added above others, at the surface of the resin, while the build platform descends. Modern desktop SLA printers take upside-down (inverted) approach with light source on the bottom and new layers added under old ones through transparent non-stick tank bottom while the build platform ascends [A-61]. The main reason for this change is that the right-side up printing requires the resin tank to be filled at least as much as the printed object's height is. In addition, structures in SLA process are typically printed having certain acute angle to the platform and using vast support. The leftovers of the support are not easy to be completely removed, so the structure side attached to the support should not be the one requiring accuracy and smoothness.

However, there are engineered photopolymers highlighting different properties plastic print can have. For instance, one of the most affordable high quality SLA printers comes with a choice of materials simulating a range of injection-moulded plastics, such as durable resin (FLDUCL01) simulating PP, having impact resistance (IZOD impact strength test) of 109 J/m [A-62]. Of special interest is high temp resin (FLHTAM01), having Heat Deflection/Distortion Temperature (HDT) of 289°C at 0.46 MPa and of 130°C at 1.81 MPa. Post-cured high temp is also stiff with Young's Modulus of 3.6 GPa and flexural modulus of 3.3 GPa.

PolyJet, a material jetting technology, has been used to produce highest resolution and finest details [A-63], [A-64]. Common materials used for PolyJet 3D printing are UV light curable photopolymers VeroWhite and VeroClear, the former being opaque and the latter transparent. Unlike SLA, material is not cured inside vat, but first jetted in a similar way to inkjet printers. High quality (HQ) variants of Vero photopolymers ($\varepsilon_r \approx 2.86$ and $\tan \delta \approx 0.022$ at 10 GHz) have accuracy in *x* and *y* directions of about 100 μm and in *z* direction better than 10 μm. In addition, their horizontal surface roughness rms is about 5 μm.

Selective Laser Sintering (SLS), belonging to the powder bed fusion category, is a popular industrial AM method. Like SLA, SLS uses laser technology. However, lasers in SLS typically have several times higher power, which makes them less affordable than SLA. Standard polymer material choice is nylon (polyamide, PA), having excellent combination of strength, flexibility and durability. It is suitable for end products, rather than just for prototyping. There are different types of nylon to satisfy particular design requirements, such as nylon 11 and nylon 12, of which 11 is more elastic. Support can be removed very easily,

essentially without visible traces, and that powder reused. Since recently, SLS consumer printers are starting to be released [A-65].

FABE is in possession of two Z Corp 3D printers, Zprinter 250 and 450[25], which use Binder Jetting (BJ) process with two different materials involved. One of them is again the powder bed, but now there is also a liquid binder that comes out of an inkjet-like head to stick together the powder particles. In each successive step, a new powder layer is spread across the base with a roller and the build platform is lowered down by a single layer thickness after application of the adhesive binder where required by the structure geometry. Yet again, the rest of the powder filling what are supposed to be hollow volumes is removed and reused. Like in conventional inkjet printing, Zprinter 450 horizontal resolution is expressed in dots per inch, being 300 x 450 dpi, which is around 85 x 56 μm. Its single layer is 89 – 102 μm thick.

A.4.2 Metals

Full metal AM, although conceptually similar, is significantly more difficult and expensive than polymer AM, and at the moment it is not on the horizon for non-professionals. Typical raw material is metal powder, that is, powder bed fusion method is mostly used, but binder jetting has the metal printing capability as well. However, the printing requires much higher power (lasers are in hundreds of Watts) and has slower scanning speed than for polymers as the energy density required to melt a metal powder is much greater than for a polymer powder. As the direct consequence of this, there are rigorous requirements for temperature control and heat isolation. Furthermore, high temperature gradients around the melting area cause strong stress in the material requiring the print to be firmly metal connected with the build platform. Eventually, this support is removed by conventional metal machining techniques.

Possibility to make weight saving designs, prominently by using lattice structures, are of great aid for aerospace applications, where reduced fuel consumption implies massive cost benefit. Airframes on series production commercial aircrafts have already started being equipped with metal AM parts, and metal AM waveguide RF components including filters and antennas are planned to be used in satellite payloads [A-66]. Emphatic expectations from this branch of manufacturing are confirmed with acquisitions of the leading metal AM machine manufacturers by some of the best known names in the world of industry [A-67].

Selective Laser Melting (SLM) is the most popular metal AM technology for RF, principally equal of SLS for non-metal powders. Subtle difference between SLM and SLS is that SLM goes a step further, not only sintering, but melting the powder. SLM of microwave waveguide devices has been tested with aluminium alloy $AlSi_{10}Mg$ and titanium alloy Ti_6Al_4V (TC4) at Ku/K band [A-68]. Ti_6Al_4V had better surface finish ($Ra = 4\text{-}10$ μm compared to $Ra = 5\text{-}15$ μm) and higher manufacturing accuracy of the two (0.05 mm compared to 0.1 mm in the worst cases), but worse electrical resistivity (2.0×10^{-6} Ωm compared to 1.6×10^{-7} Ωm). Stainless steel SLM print of a mode converter, traditionally requiring difficult electroforming fabrication, is presented in [A-64], and its measured conductivity is 8.2×10^{-7} S/m. Cu-15Sn bronze (copper alloy) has also been a popular material of choice for SLM [A-69]. Another AM method from the powder bed fusion

---

[25] After Z corporation was acquired by 3D Systems in January 2012, Zprinter technology was rebranded as ColorJet, addressing its colouring capabilities inherited from 2D inkjet technology.

category that can be used for metal printing, but is not found so often in practice, is Electron Beam Melting (EBM).

The basic way of controlling surface roughness, but not trivial in practice as the parts can lose dimensional accuracy, is with temperature. The roughness increases with the rise of scanning velocity. In [A-69], after manual polishing, Cu-15Sn surface roughness was Ra = 2.79 μm. In TESAT [A-38], ultrasonic cleaning and chemical polishing are used at the stage one of the post-processing.

Binder jetting can be used with metal powders as well, and has lower cost than SLM or EBM. In addition to the adhesive jetting stage, common with the polymer printing, metals require the green part to go through several furnace cycles: to burn of the polymer binder, to lightly sinter the metal particles together and to improve density by infiltrating another metal into the material pores. In [A-70], waveguide circuits and antennas were fabricated using BJ technology at Ka band (WR-28 waveguide) from 316 stainless steel powder of 30 μm mean diameter. The surface roughness was Ra = 6.26 μm, and when steel was infiltrated with bronze, unloaded Q of almost cube shaped rectangular cavity resonator with resonant frequency of around 30 GHz was 466, whereas when steel was infiltrated with copper, unloaded Q increased to 616. In comparison, [A-69] gives Ra = 12.89 μm for the same material.

Since recently, there have been FDM PLA filaments with copper and other metal fills available from the leading electronic component distributors. However, apart from metal feel, colour and several times increased weight, these materials are essentially non-conductive even though metals have contents as high as 80% because metal particles are mutually separated with the PLA.

A.4.3 Ceramics

The temperature limitation encountered when using a conventional polymer can be shifted higher if it is replaced with a ceramic material, even though it is more difficult to have it processed. In addition, characteristic feature of ceramics is high hardness. Some of them have very high permittivity combined with very low losses, properties desired for dielectrics, especially resonators. Powder bed based AM processes have the widest range of materials available for manufacturing, and apart from plastics and metals, they can print ceramic objects as well. Some of the ceramic powders that can be consolidated by sintering are silica/glass and porcelain.

Nonetheless, in RF applications 3D printing from resins compatible with SLA process is preferred way of fabricating ceramic device parts. In [A-71] and [A-72], X and Ka band bandpass filters with spherical and hemispherical resonators were printed from Somos PerFORM resin [A-73] having HDT of 268°C at 0.46 MPa and of 119°C at 1.81 MPa. In addition, in the 25-60°C temperature range it had about 40% lower frequency shift compared to Accura Xtreme standard polymer resin. Similarly, Formlabs ceramic resin has HDT of 290°C at 0.46 MPa and of 104°C at 1.81 MPa [A-74]. At the cutting edge end, HRL Laboratories have produced polymer-derived ceramic with ten times improved strength, being able to withstand temperatures higher than 1700°C [A-75].

A.4.4   Flexible materials

Material flexibility can be realized by extruding thermoplastic elastomers (TPEs – materials having both thermoplastic and elastomeric properties), with NinjaTek [A-76] being notable manufacturer of thermoplastic polyurethane (TPU) filaments. Using the ring resonator setup for material characterization at 2.4 GHz and changing infill percentage of inner substrate layers from 40% to 100%, NinjaFlex showed shift of the relative dielectric permittivity from 2.32 to 2.98, at the same time having loss tangent increased from 0.034 to 0.061 [A-77]. Related NinjaTek Cheetah flexible filaments are optimized for user experience with fast and easy printing.

A.4.5   Printed Circuit Boards

One of the latest developments in additive manufacturing is 3D printing of professional multilayer PCBs [A-78]. DragonFly 2020 Pro 3D PCB Printer [A-79], [A-80] is available on the market for performing this task. It prints high resolution PCBs from nanotechnology based dielectric and conductive inks. In addition, it supports fabrication of full range of PCF features, including different types of vias.

A.5.   Metal plating and inkjet printing

Iron and steel sheets used to be coated with a thin layer of tin for corrosion prevention as far back as in thirteenth century in Bohemia. Splitting a structure into the support and metal coating segments, it is possible to independently optimize both of them with different objectives that can be mutually exclusive. In microwave devices, support may require sturdiness, lightweight, isolation and low cost characteristics, whereas metal surface may require smoothness, good electrical conductivity and low reactivity. Plating is used even for conventional metal waveguide filters with high performance demand (good example are satellite applications), when a layer of higher conductive metal, typically silver, is deposited over the walls of waveguide housing.

Silver is not the material with highest electrical conductivity – superconductors [A-81] can attain higher conductivity at low temperatures and graphene [A-82] at room temperature. Actually, at microwave frequencies superconductors do not have zero losses like at DC, but are still not less than an order of magnitude lower than for any standard metal conductor, with surface roughness depending on the square of frequency rather than on the square root like in standard conductors [A-83]. However, superconductor components are more expensive and require relatively complex cooling systems that consume energy and add volume and mass, even though high-temperature superconductors (HTS, now with critical temperatures reaching 133 K for HBCCO at ambient pressure and 203 K for H_2S under extremely high pressure [A-84]) have been available to replace low-temperature metallic superconductors, so significantly cheaper, less power-hungry and with larger heat vaporization high temperature cryogenics (liquid nitrogen cooling) can be used instead of liquid helium.

After the discovery of first high-temperature superconductor YBCO more than 30 years ago, there had been aggressive campaign for use of microwave superconductivity in space communications and surveillance systems led by High Temperature Superconductivity Space Experiment (HTSEE) program, and significant effort was made for application in mobile

telephony base stations too [A-85]. A number of microwave devices have been developed in the upcoming decades, most prominently microwave filters (HTS thin-film filters based on planar filters; hybrid dielectric/HTS filters, based on dielectric resonator filters; and HTS thick-film coated filters, based on full 3D microwave filters). Although there are still publications on this topic [A-86] and commercial production [A-87], the progress has largely diminished with superconductor microwave devices having additional issues in reliability, especially of the cryocooler technology, as well as power handling. Power handling capacity is limited by critical current density (10^6 A/cm^2 is its typical value for thin-films), which exceeding switches superconductors to the normal state. Surface resistance increase with the applied field causes nonlinearities that also reduce superconductor power handling capability.

With 2D zero-gap semiconductor graphene, record room temperature electrical conductivity was achieved in laboratory in small exfoliated pure graphene pieces having charge carrier mobility in excess of 200 000 cm^2/V·s [A-88]. Electron scatterers were largely reduced to intrinsic ones like phonons that cannot be removed at 300 K and gate voltage was 50 V. So far, this has not been even remotely replicated in real-life use conditions with graphene of larger size and custom-shape, because such an extremely thin material is very sensitive to effects that rapidly reduce electron mobility like charge impurities, microscopic ripples and substrate on which it is laid down. As an illustration, few-layer graphene in practice often shows better electrical performance than single-layer one, being more resilient to external influences, and graphite, although composed of stacked graphene layers, does not keep the same characteristics described in superlatives. Hence, silver is still the preferred choice in most wireless communications applications that demand maximizing electrical conductivity.

There are two kinds of electrochemical deposition of metals – electroplating and electroless plating [A-89], [A-90]. In electronics, electrochemical deposition has revolutionized IC manufacturing, enabling copper to replace aluminium for interconnections, and has numerous other applications like in deposition for magnetic recording devices. In a nutshell, in the electrolytic cell for electroplating, the component to be plated is the cathode, the metal used for plating is the anode, both electrodes are submerged into electrolyte solution, and there is external power supply keeping the ion current flowing between the anode and the cathode. The electrodeposition occurs as the metal cations are reduced on the structure acting as cathode, while at the same rate metal is oxidised at the anode and associated with the remaining anions in the solution to replenish the electrolyte, keeping the electroplating process going. Electroplating is often done in several stages and there are many aspects of electroplating process like plating solution type, electrolyte concentration, additives, temperature and electric current that can be varied to achieve desired results. For instance, thin initial layer with good adherence, called strike, is formed by a high cathode current density in a bath with low concentration of ions.

The most interesting metals for electroplating in microwave applications are copper, silver and gold, all chemical element in group 11 of the periodic table, which apart from being the most electrically conductive metals have excellent thermal conductivity and are unreactive. Copper plating is among the most widely used ones in general, with copper being only marginally worse conductor than silver, but significantly less expensive, hence being the electrical conductor of choice in most applications. As a plating material, copper has high plating efficiency, consequently having good coverage even on difficult-to-plate surfaces, and

is able to cover small imperfections in the base metal. Copper is also suitable for plating thermoplastics, because they have large coefficients of thermal expansion, and copper can absorb stress. Acid sulphate simple ion system is by far the most common copper plating solution, being low cost and easy to control. Other commercially used plating systems are fluoborate simple ion system as well as alkaline cyanide and pyrophosphate complex ion systems. Silver is the most electrically and thermally conductive metal. Cyanide baths, known since the 19th century, are still most frequently used silver plating solutions because of good stability and adhesion. There exists high demand for gold in electronics industry because of its high inertness (most noble metal) that prevents formation of surface oxides, excellent wear resistance, and because it is the most malleable metal. Therefore, it is common to see gold plated coaxial connectors and mechanical calibration kits for electronics measurement instruments. Similar to silver, cyanide plate solution is the most important one for gold. Needless to say, cyanide solutions are tried to be avoided if there is a good alternative available because of their toxicity (also, they are usually operated at temperatures of not less than 80°C), like it is the case with copper electrodeposition.

Electroplating is used for achieving high quality surface finishes in microwave components. In addition, electroplating can produce wide range of deposit thicknesses. The ability to produce thick finishes goes to the extent of electroforming – making entire parts on top of models. Rigid PCBs most often come with copper foils that are first electrodeposited on a titanium rotating drum attached to the cathode and immersed into copper sulphate electrolyte solution [A-91]. The drum rotation speed determines the cladding thickness. Copper clad lamination to the substrate usually occurs at the same time with substrate resin impregnation into glass cloth. In addition, copper electrodeposition is used for plating through, blind and buried holes. This used to be area for application of pyrophosphate solutions, but are now as well largely replaced by high-throw acid sulphate solutions. Naturally, at the same time additional layers of copper are deposited over laminated copper foils.

Presently, very interesting application of electroplating is for 3D printed components. In [A-69], gold electrodepositioning has improved 316SL stainless steel BJ AM surface roughness (R_q) from 16.10 μm to 6.73 μm and Cu–15Sn bronze SLM AM R_q from 3.52 μm to 1.67 μm. Engineers in Airbus Defence and Space have silver plated best samples of waveguide filters with enhanced performances using AM, under development for future satellite payloads [A-38]. Silver plated 3rd and 5th order direct coupled filter prototypes manufactured using laser melting of $AlSi_{10}Mg$ had measured insertion losses better than 0.3 dB. Another set of experiments with silver plated 1st order 3D printed filter by researchers from Consiglio Nazionale delle Ricerche found equivalent electrical surface resistivity droping from 20 to 8 μΩ·cm for $AlSi_{10}Mg$ SLM base and from 250 to 8 μΩ·cm for Ti_6Al_4V SLM base [A-38].

However, electroplating has limitation in that it cannot directly cover with metal non-conductive surfaces like polymers and ceramics. Nevertheless, electrodeposition can still be utilized even in these cases, provided that some other process is used to apply the initial conductive layer [A-92]. Electroless (non-galvanic) plating is suitable for the purpose of depositing thin layers of metal even to non-conductive surfaces. It is different from the electroplating in that there is no external power supply involved to be source of electrons, but it is reducing agent present in the solution instead. When apertures in PCB dielectrics need to

be plated, standard procedure used for decades is to first catalyse their surfaces using palladium [A-93]. Following this, formaldehyde oxidises on palladium catalyst generating electrons, which are then spent for the reduction of copper ions, that is, electrolessly plating the PCB dielectric. On the other side, in [A-94] is given overview of five microwave waveguide components 3D printed in SLA from polymers and electroplated with copper. An alternative to electroless copper plating, which is predominantly used for flexible circuits, is direct matallization with graphite colloids [A-95]. It offers reduced consumption of chemical and energy resources.

It should be added here that there are multiple other available methods of metal plating such as chemical vapor deposition (CVD, which is a popular way of graphene production), evaporation, and sputtering. They are used for high-quality thin-film deposition, but have higher process complexity and cost.

There exist conductive adhesive silver paints (RS Pro Silver, Maplin, Reichelt Elektronik, to name a few) designed primarily for repairing electrical connections, such as those on PCBs. Coating plastic 3D prints with them is good for small series prototyping, especially with Ferro 6290 0341 (L204N) silver conductive lacquer [A-64], because it has the highest conductivity from all the products in this range (20-60 $\mu\Omega\cdot$cm electrical surface resistivity). Another similar product are paints for electromagnetic shielding of electronic equipment, like Soliani emc electrically conductive paints with silver, copper (Figure A.10.) and nickel filler options [A-96]. If surfaces to be covered are not complex, inexpensive adhesive copper tape can be used as ad hoc solution for testing.
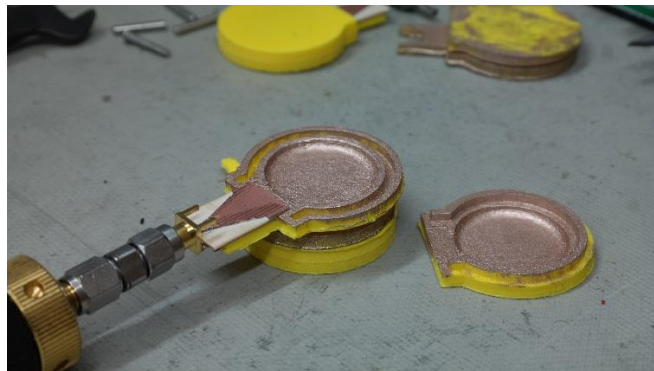
Figure A.10. Low-profile high Q integrated cavity, 3D printed from PLA and coated with Soliani emc conductive copper paint for single-port Q factor experimental verification.

Printed electronics methods can be considered as a special case of horizontally controlled additive metal plating. A popular choice is inkjet printing with conductive inks [A-97] on flexible substrates. In flexible circuits, cladding with copper is usually made independently from substrate formation, even when it is done with rolled annealed copper foils. Inkjet printers used vary from paper printers filled with conductive ink toner to industrial ones, most commonly used being Fujifilm Dimatix Materials Printers (DMPs) and Super Inkjet (SIJ) Technology printer. Compared to material jetting 3D printers, these printers are not designed for multilayer printing, although they have been used printing in several passes and same companies that produce 3D printers often produce conductive inks. It should be highlighted that inkjet printing is not exclusively combined with flexible substrates, but with others as well, such as 3D printed polymer ones [A-98].

In Figure A.11. a) are shown E-plane waveguide filter inserts with I-shaped insets printed using Dimatix DMP-3000 on 75 μm thick Kapton substrate (ε_r = 3.4). However, since the Sun Chemical nanosilver conductive ink (σ = 1.0-1.5 x 10^7 S/m) on them is only about 1 μm thick, which is less than the skin depth at 10 GHz, the experimental results did not show good filtering performance. To simulate this wave transmission effect in CST Microwave Studio, standard 'Lossy metal' model is not appropriate because it uses perturbation method, calculating the field distribution as if insert metal was opaque – PEC, and then independently adding losses assuming that the incident wave enters metal orthogonally and decays to zero inside it (metal surface impedance is reduced to the wave impedance inside it, $Z = (1 + j)\sqrt{\pi\mu f/\sigma}$ [1-1]). Instead, silver ink printed metal can be modelled as general full-wave analysed 'Normal' material, again inserting its conductivity value, or to have faster simulation, with 'Ohmic sheet' model [A-99]. However, for 'Ohmic sheet' resistance and reactance values (Ohm/sq) cannot be used the simplified expression from the 'Lossy metal' model, but they should either be calculated including finite material thickness and wave reaching the back side, or measured. This analysis found that for satisfactory filtering performance with the given silver ink conductivity at least 10 μm thick metallization is needed.

Figure A.11. Inkjet-printed E-plane inserts with I-shaped insets for compact waveguide filters: a) Kapton substrate, Dimatix DMP-3000 printer; b) PET substrate, Epson Stylus C88+ printer, without (up) and with (down) copper electroplating.

In Figure A.11. b) are shown inserts for the same filter implementation, but printed on PET flex material using Epson Stylus C88+ inkjet paper printer. (A problem with this low-cost approach is clogging after printing stops.) In addition, the problem with printed ink thickness (as well as to increase conductivity) was tried to be resolved by copper electodeposition [A-100], [A-101]. The electroplating was made at FST chemistry lab using $CuSO_4 \cdot 5H_2O$ solution (Figure A.12.). Although a much thicker layer of copper was coated, as it can be seen at the bottom of Figure A.11. b), the eventual substantial peeling of copper occurred and prevented any response improvement. One more approach used in printed electronics industry, and tested for RF circuits is combining inkjet printing- and electroless plating [A-102]. On the other side, screen printing using stencil, even though it is one of older printing technologies, is capable of directly depositing much thicker layers of conductive ink than other print methods, in [A-103] demonstrating range from 10.9 μm to 58.8 μm by a single print press.
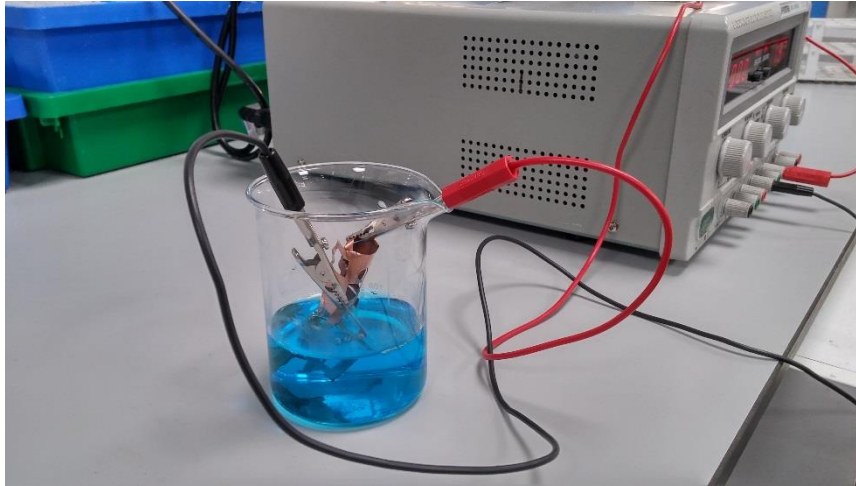
Figure A.12. Setup for copper electroplating: A vessel with $CuSO_4$ water solution (concentration of 100 gL^{-1}); Anode is residue of copper sheet used for filter insert fabrication; Cathode is the ink on thin PET foils that needs to be copper plated (area of several cm^2); DC bench power supply with controllable current output.

One recent cutting edge technology considering joining metals and plastics is Plasma-SealTight (PST) [A-104]. Direct bonding of finely tuned plastic compounds to metals in the injection moulding process is enhanced by atmospheric plasma coating.

References

[A-1]   LPKF Laser & Electronics AG, Osteriede 7, 30827 Garbsen, Germany, Available: www.lpkf.com

[A-2]   LPKF Laser & Electronics AG, "Manual CircuitCAM 5.0", English Version 1.0, Revision: 2.6.04, June 2004

[A-3]   Ucamco, "The Gerber Format Specification", Revision: 2017.11, November 2017, Available: https://www.ucamco.com/en/guest/downloads

[A-4]   J. Coates, "What's new in ODB++"", *The PCB Design Magazine*, I-Connect007, September 2014, Available: http://www.iconnect007.com/landing/design/pcb-design-magazine

[A-5]   "The Great Gerber vs. ODB++ Debate", *The PCB Design Magazine*, I-Connect007, September 2014, Available: http://www.iconnect007.com/landing/design/pcb-design-magazine

[A-6]   LPKF Laser & Electronics AG, "Brochure LPKF Drilling, Milling and Routing Tools", Available: www.lpkf.com /products/rapid-pcb-prototyping/tools

[A-7]   LPKF Laser & Electronics AG, "Manual BoardMaster 5.0", English Version 5.0, Revision: 14.6.06, June 2006

[A-8]   LPKF Laser & Electronics AG, "ProtoMat C60 Manual", English Version, March 1999, Available: www.lpkfusa.com

[A-9]   Rogers Corporation, "RO4000® Series High Frequency Circuit Materials Data-sheet", Available: www.rogerscorp.com/acs/literature.aspx

[A-10] Rogers Corporation, "RO4000® LoPro® Series High Frequency Circuit Materials Data-sheet", Available: www.rogerscorp.com/acs/literature.aspx

[A-11] Rogers Corporation, "RT/duroid® 5870 /5880 High Frequency Laminates Data-sheet", Available: www.rogerscorp.com/acs/literature.aspx

[A-12] LPKF Laser & Electronics AG, "In-House Rapid PCB Prototyping Product Catalog: Circuit Board Plotters", Available: http://www.lpkf.com/products/rapid-pcb-prototyping/index.htm

[A-13] K. Tavernirer, "PCB Fabrication Data: Design to Fabrication Data Transfer", V6, September 2016, Available: www.ucamco.com

[A-14] Eurocircuits, "Design Guidelines", July 2014, Available: www.eurocircuits.com

[A-15] Tenting – Plugging – Filling, Available: http://www.we-online.com/web/en/leiterplatten/ layout/design_tipp/design_tip_2.php

[A-16] Via In Pad - Conductive Fill or Non-Conductive Fill?, Available: www.4pcb.com

[A-17] W. S. Wong and A. Salleo (editors), "Flexible Electronics: Materials and Applications", Springer, 2009.

[A-18] J. Coonrod, "High-Frequency Flexible Circuits", *The PCB Design Magazine: Flexible Designs*, I-Connect007, June 2013, Available: http://www.iconnect007.com/landing/design/ pcb-design-magazine

[A-19] G. Oliver, "Using Flex in High-Speed Applications", *The PCB Design Magazine: Materials*, I-Connect007, March 2014, Available: http://www.iconnect007.com/landing/design/pcb-design-magazine

[A-20] Z. Yang, A. Takacs, S. Charlot and D. Dragomirescu, "Design of Kapton based passive circuits at microwave frequencies," *2015 European Microwave Conference (EuMC)*, Paris, 2015, pp. 873-876.

[A-21] D. C. Thompson, O. Tantot, H. Jallageas, G. E. Ponchak, M. M. Tentzeris and J. Papapolymerou, "Characterization of liquid crystal polymer (LCP) material and transmission lines on LCP substrates from 30 to 110 GHz," *IEEE Transactions on Microwave Theory and Techniques*, vol. 52, no. 4, pp. 1343-1352, April 2004.

[A-22] E. Arabi, G. McKerricher and A. Shamim, "Comparison of filters: Inkjet printed on PEN substrate versus a laser-etched on LCP substrate," *2014 44th European Microwave Conference*, Rome, 2014, pp. 1226-1229.

[A-23] Hong-Duc Nguyen *et al.*, "RF characterization of flexible substrates for new conformable antenna systems," *2016 10th European Conference on Antennas and Propagation (EuCAP)*, Davos, 2016, pp. 1-5.

[A-24] Rogers Corporation ULTRALAM® 3000 Liquid Crystalline Polymer Circuit Material Double-Clad Laminates, Available: www.rogerscorp.com/documents/822/acm/Fabrication-Guidelines-ULTRALAM-3000-LCP-Materials.aspx

[A-25] DuPont™ Pyralux® flexible circuit materials, Available: www.dupont.com/products-and-services/electronic-electrical-materials/flexible-rigidflex-circuit-materials/brands/pyralux-flexible-circuit.html

[A-26] J. Coonrod, "Different Copper Foils for Different Reasons", *The PCB Magazine: Imaging*, I-Connect007, April 2012, Available: http://www.iconnect007.com/landing/pcb/pcb-magazine

[A-27]   G. S. Cox, "Material Choices for High-Speed Flexible Circuits", *The PCB Magazine: High-Speed Materials*, I-Connect007, April 2017, Available: http://www.iconnect007.com/ landing/pcb/pcb-magazine

[A-28]   J. R. Walker and B. Dixon, "Machining Fundamentals", 9th edition, Goodheart-Wilcox, 2014.

[A-29]   Machinery News, Products and Features for Production Engineers, Available: www.machinery.co.uk

[A-30]   P. J. Bruneau, H. D. Janzen and J. S. Ward, "Machining of terahertz split-block waveguides with micrometer precision," *2008 33rd International Conference on Infrared, Millimeter and Terahertz Waves*, Pasadena, CA, 2008, pp. 1-2.

[A-31]   S. Franssila, "Introduction to Microfabrication", Second Edition, John Wiley & Sons, 2010.

[A-32]   Y. Wang, X. Shang and M. J. Lancaster, "Micromachined 3D millimeter-wave and terahertz devices," *2015 IEEE MTT-S International Microwave Workshop Series on Advanced Materials and Processes for RF and THz Applications (IMWS-AMP)*, Suzhou, 2015, pp. 1-3.

[A-33]   O. Glubokov, X. Zhao, B. Beuerle, J. Campion, U. Shah and J. Oberhammer, "Micromachined multilayer bandpass filter at 270 GHz using dual-mode circular cavities," *2017 IEEE MTT-S International Microwave Symposium (IMS)*, Honololu, HI, 2017, pp. 1449-1452.

[A-34]   T. Skaik, M. Lancaster, M. Ke and Y. Wang, "A micromachined WR-3 band waveguide diplexer based on coupled resonator structures," *2011 41st European Microwave Conference*, Manchester, 2011, pp. 770-773.

[A-35]   I. Gibson, D. Rosen and B. Stucker, "Additive Manufacturing Technologies: 3D Printing, Rapid Prototyping, and Direct Digital Manufacturing", Second Edition, Springer, New York, NY, 2015.

[A-36]   Additive Manufacturing Magazine, Available: www.additivemanufacturing.media

[A-37]   ASTM International: Standard Terminology for Additive Manufacturing Technologies, 2012

[A-38]   P. Martin-Iglesias, C. Miquel-Espana and J. Galdeano (organisers), "Additive Manufacturing for RF Passive Hardware", workshop WM03, *46th European Microwave Conference*, London, 2016

[A-39]   3D Manufacturing Format by 3MF Consortium - Enabling the full potential of 3D Printing, Available: www.3mf.io

[A-40]   Ultimaker Cura 3D Printing Software, Available: https://ultimaker.com/en/products/ ultimaker-cura-software

[A-41]   D. T. Pham, R. S. Gault, "A comparison of rapid prototyping technologies", *International Journal of Machine Tools and Manufacture*, Volume 38, Issues 10–11, 1998, Pages 1257-1287

[A-42]   C. R. Garcia, R. C. Rumpf, H. H. Tsang and J. H. Barton, "Effects of extreme surface roughness on 3D printed horn antenna," *Electronics Letters*, vol. 49, no. 12, pp. 734-736, June 6 2013.

[A-43] C. Tomassoni, R. Bahr, M. Tentzeris, M. Bozzi and L. Perregrini, "3D printed substrate integrated waveguide filters with locally controlled dielectric permittivity," 2016 46th European Microwave Conference (EuMC), London, 2016, pp. 253-256.

[A-44] E. Wheatley et al., "Practical design issues of low cost polymer waveguide filters", Workshop WMB: Filter II - Practical Aspects Of Microwave Filter Design And Realization, *2005 IEEE MTT-S International Microwave Symposium Digest*, Long Beach, 12-17 June 2005.

[A-45] B. Riddle, J. Baker-Jarvis and J. Krupka, "Complex permittivity measurements of common plastics over variable temperatures," *IEEE Transactions on Microwave Theory and Techniques*, vol. 51, no. 3, pp. 727-733, Mar 2003.

[A-46] P. I. Deffenbaugh, R. C. Rumpf and K. H. Church, "Broadband Microwave Frequency Characterization of 3-D Printed Materials," *IEEE Transactions on Components, Packaging and Manufacturing Technology*, vol. 3, no. 12, pp. 2147-2155, Dec. 2013.

[A-47] A. L. Vera-López, E. A. Rojas-Nastrucci, M. Córdoba-Erazo, T. Weller and J. Papapolymerou, "Ka-band characterization and RF design of Acrynolitrile Butadiene Styrene (ABS)," *2015 IEEE MTT-S International Microwave Symposium*, Phoenix, AZ, 2015, pp. 1-4.

[A-48] J. Castro, E. A. Rojas-Nastrucci, A. Ross, T. M. Weller and J. Wang, "Fabrication, Modeling, and Application of Ceramic-Thermoplastic Composites for Fused Deposition Modeling of Microwave Components," *IEEE Transactions on Microwave Theory and Techniques*, vol. 65, no. 6, pp. 2073-2084, June 2017.

[A-49] J. M. Felício, C. A. Fernandes and J. R. Costa, "Complex permittivity and anisotropy measurement of 3D-printed PLA at microwaves and millimeter-waves," *2016 22nd International Conference on Applied Electromagnetics and Communications (ICECOM)*, Dubrovnik, Sep. 2016, pp. 1-6.

[A-50] M. W. Elsallal, J. Hood, I. Mcmichael, T. Busbee, "3D Printed Material Characterization for Complex Phased Arrays and Metamaterials", *Microwave Journal*, 59. 20-34. Oct. 2016.

[A-51] Proto-pasta Composite PLA - Electrically Conductive Graphite, Available: www.proto-pasta.com/collections/new-releases-favorites/products/conductive-pla

[A-52] F. Castles *et al.*, "Microwave dielectric characterisation of 3D-printed $BaTiO_3$/ABS polymer composites", *Sci. Rep.* 6, 22714; doi: 10.1038/srep22714, Mar. 2016.

[A-53] Low Loss Polymer for High Performance Dielectric Applications, Available: www.zeonex.com/electronics.aspx.html#low-dielectric

[A-54] Ultimaker 2+, Available: www.ultimaker.com/en/products/ultimaker-2-plus/specifications

[A-55] D. Chaidas, K. Kitsakis, J. Kechagias and S Maropoulos, "The impact of temperature changing on surface roughness of FFF process", *2016 IOP Conference Series: Materials Science and Engineering*, Vol. 161, No. 1.

[A-56] How to fix warping, Available: www.ultimaker.com/en/resources/19537-how-to-fix-warping

[A-57] Bosui Liu, Xun Gong and W. J. Chappell, "Applications of layer-by-layer polymer stereolithography for three-dimensional high-frequency components," *IEEE*

Transactions on Microwave Theory and Techniques, vol. 52, no. 11, pp. 2567-2575, Nov. 2004.

[A-58] J. Maas, B. Liu, S. Hajela, Y. Huang, X. Gong and W. J. Chappell, "Laser-Based Layer-by-Layer Polymer Stereolithography for High-Frequency Applications," *Proceedings of the IEEE*, vol. 105, no. 4, pp. 645-654, April 2017.

[A-59] J. S. Silva, M. García-Vigueras, T. Debogović, J. R. Costa, C. A. Fernandes and J. R. Mosig, "Stereolithography-Based Antennas for Satellite Communications in Ka-Band," *Proceedings of the IEEE*, vol. 105, no. 4, pp. 655-667, April 2017.

[A-60] Swiss*to*12, Available: www.swissto12.com

[A-61] The Ultimate Guide to Stereolithography (SLA) 3D Printing, Available: www.formlabs.com/blog/ultimate-guide-to-stereolithography-sla-3d-printing

[A-62] Functional Prototyping Materials for Engineers, Available: www.formlabs.com/materials/ engineering

[A-63] Fan Cai, Wasif Tanveer Khan and J. Papapolymerou, "A low loss X-band filter using 3-D Polyjet technology," *2015 IEEE MTT-S International Microwave Symposium*, Phoenix, AZ, 2015, pp. 1-4.

[A-64] S. Johann *et al.*, "Plastic and metal additive manufacturing technologies for hyperfrequency passive components up to Ka band," *2016 46th European Microwave Conference (EuMC)*, London, 2016, pp. 373-376.

[A-65] Formlabs Fuse 1, Available: www.formlabs.com/3d-printers/fuse-1

[A-66] Metal AM, Vol. 3, No. 3, Autumn 2017, available: www.metal-am.com

[A-67] Metal AM, Vol. 2, No. 3, Autumn 2016, available: www.metal-am.com

[A-68] O. A. Peverini *et al.*, "Selective Laser Melting Manufacturing of Microwave Waveguide Devices," *Proceedings of the IEEE*, vol. 105, no. 4, pp. 620-631, April 2017.

[A-69] B. Zhang *et al.*, "Metallic 3-D Printed Antennas for Millimeter- and Submillimeter Wave Applications," *IEEE Transactions on Terahertz Science and Technology*, vol. 6, no. 4, pp. 592-600, July 2016.

[A-70] E. A. Rojas-Nastrucci, J. T. Nussbaum, N. B. Crane and T. M. Weller, "Ka-Band Characterization of Binder Jetting for 3-D Printing of Metallic Rectangular Waveguide Circuits and Antennas," *IEEE Transactions on Microwave Theory and Techniques*, vol. 65, no. 9, pp. 3099-3108, Sept. 2017.

[A-71] C. Guo, J. Li, D. D. Dinh, X. Shang, M. J. Lancaster and J. Xu, "Ceramic filled resin based 3D printed X-band dual-mode bandpass filter with enhanced thermal handling capability," in *Electronics Letters*, vol. 52, no. 23, pp. 1929-1931, 11 10 2016.

[A-72] J. Li, C. Guo, L. Mao and J. Xu, "3D printed bandpass filters using compact high-Q hemispherical resonators with improved out-of-band rejection," in *Electronics Letters*, vol. 53, no. 6, pp. 413-415, 3 16 2017.

[A-73] Somos® PerFORM, Available: www.dsm.com

[A-74] Formlabs Form X ceramic resin, Available: www.formlabs.com/materials/ceramics

[A-75] Z. C. Eckel et al., "Additive manufacturing of polymer-derived ceramics", *Science*, Vol. 351, Issue 6268, pp. 58-62, Jan. 2016

[A-76] NinjaTek, 311 W. Stiegel Street Manheim, PA 17545, USA, Available: www.ninjatek.com

[A-77] S. Moscato *et al.*, "Infill-Dependent 3-D-Printed Material Based on NinjaFlex Filament for Antenna Applications," *IEEE Antennas and Wireless Propagation Letters*, vol. 15, pp. 1506-1509, 2016.

[A-78] The PCB Magazine: 3D Printing and Structural Electronics, I-Connect007, Jan. 2015, Available: http://www.iconnect007.com/landing/pcb/ pcb-magazine

[A-79] Interview with Simon Fried, "Printing PCBs...in Your Office!", *The PCB Magazine: What's net in PCB fabrication*, I-Connect007, Feb. 2016, Available: http://www.iconnect007.com/ landing/pcb/pcb-magazine

[A-80] Nano Dimension, 2 Ilan Ramon St., Ness Ziona Science Park, 7403635, Israel, Available: www.nano-di.com

[A-81] K. K. Mei and G. C. Liang, "Electromagnetics of superconductors," *IEEE Transactions on Microwave Theory and Techniques*, vol. 39, no. 9, pp. 1545-1552, Sep 1991.

[A-82] A. K. Geim and K. S. Novoselov, "The rise of graphene," *Nat. Mater.*, vol. 6, no. 3, pp. 183–191, Mar. 2007.

[A-83] R. R. Mansour, "Microwave superconductivity," *IEEE Trans. Microw. Theory Tech.*, vol. 50, no. 3, pp. 750–759, Mar. 2002.

[A-84] A. P. Drozdov, M. I. Eremets, I. A. Troyan, V. Ksenofontov, and S. I. Shylin, "Conventional superconductivity at 203 kelvin at high pressures in the sulfur hydride system," *Nature*, vol. 525, no. 7567, pp. 73–76, Aug. 2015.

[A-85] M. Nisenoff, "Microwave superconductivity Part 2: Current and future applications," *2011 IEEE MTT-S International Microwave Symposium*, Baltimore, MD, 2011, pp. 1-4.

[A-86] R. R. Mansour and P. D. Laforge, "Multiband superconducting filters," in *2016 IEEE MTT-S International Microwave Symposium (IMS)*, 2016, pp. 1–4.

[A-87] Superconductor Technologies Inc., Available: www.suptech.com

[A-88] S. V. Morozov *et al.*, "Giant Intrinsic Carrier Mobilities in Graphene and Its Bilayer," *Phys. Rev. Lett.*, vol. 100, no. 1, Jan. 2008.

[A-89] M. Paunovic, M. Schlesinger, "Fundamentals of Electrochemical Deposition", Second Edition, John Wiley & Sons, Inc., Hoboken, New Jersey, 2006

[A-90] M. Schlesinger, M. Paunovic, "Modern Electroplating", Fifth Edition, John Wiley & Sons, Inc., Hoboken, New Jersey, 2010

[A-91] Copper Foils for High Frequency Circuit Materials, Available: www.rogerscorp.com/acs/ literature.aspx

[A-92] Making a PCB – PCB Manufacture step by step, Available: www.eurocircuits.com/making-a-pcb-pcb-manufacture-step-by-step

[A-93] A. J. Cobley, B. Abbas, A. Hussain, and B. Mkhlef, "The Effect of Low-Frequency Ultrasound on Catalysed Electroless Copper Plating", *The PCB Magazine: Plating and Etching*, I-Connect007, May 2014, Available: http://www.iconnect007.com/landing/pcb/ pcb-magazine

[A-94] C. Guo, X. Shang, J. Li, M. J. Lancaster, and J. Xu, "3-D printed lightweight microwave waveguide devices," *2016 IEEE 5th Asia-Pacific Conference on Antennas and Propagation (APCAP)*, 2016, pp. 47–48.

[A-95] M. Carano, "Graphite-based Direct Metallization for Complex Interconnects by", *The PCB Magazine: Plating and Etching*, I-Connect007, May 2014, Available: http://www.iconnect007.com/landing/pcb/ pcb-magazine

[A-96] EMC Electrically conductive paints, Available: www.solianiemc.com/products/emc-electrically-conductive-paints/emc-electrically-conductive-paints

[A-97] M. Singh, H. M. Haverinen, P. Dhagat, and G. E. Jabbour, "Inkjet Printing—Process and Its Applications", *Advanced Materials*, vol. 22, issue 6, pp. 673–685, Feb. 2010

[A-98] K. A. Nate, J. Hester, M. Isakov, R. Bahr and M. M. Tentzeris, "A fully printed multilayer aperture-coupled patch antenna using hybrid 3D / inkjet additive manufacturing technique," *2015 European Microwave Conference (EuMC)*, Paris, 2015, pp. 610-613.

[A-99] Modelling Thin Materials in CST Studio Suite Application Note, Available: www.cst.com

[A-100] P. Xu and M. C. Hamilton, "Reduced-Loss Ink-Jet Printed Flexible CPW With Copper Coating," *IEEE Microwave and Wireless Components Letters*, vol. 23, no. 4, pp. 178-180, April 2013.

[A-101] A. Sahu *et al.*, "Microwave characterization of ink-jet printed CPW on PET substrates," *2015 86th ARFTG Microwave Measurement Conference*, Atlanta, GA, 2015, pp. 1-4.

[A-102] A. Sridhar *et al*, "Inkjet-printing- and electroless-plating- based fabrication of RF circuit structures on high-frequency substrates", *J. Micromech. Microeng.*, vol. 19, no. 8, 2009.

[A-103] S. L. Merilampi, T. Bjorninen, A. Vuorimaki, L. Ukkonen, P. Ruuskanen and L. Sydanheimo, "The Effect of Conductive Ink Layer Thickness on the Functioning of Printed UHF RFID Antennas," *Proceedings of the IEEE*, vol. 98, no. 9, pp. 1610-1619, Sept. 2010.

[A-104] Plasmatreat® GmbH (equipment supplier) and AKRO-PLASTIC GmbH (compound producer), "PST – Plasma-SealTight®: Ultra-strong and media-tight", Available: www.akro-plastic.com

Appendix B: MATLAB Scripts

Synthesis of generalised Chebyshev filter function

```
f0=10e9; % center frequency
fu=10.13e9; % lower passband limit
fl=9.88e9; % upper passband limit
BW=fu-fl; % bandwidth
FBW=BW/f0; % fractional bandwidth
fz1=9e9; % lower stopband TZ
fz2=10.265e9; % upper stopband TZ
fNRN=6.29e9; % Nonresonant TM010 node


Omegaz1=1/BW*(fz1-(fu*fl)/fz1);
Omegaz2=1/BW*(fz2-(fu*fl)/fz2);
OmegaNRN=1/BW*(fNRN-(fu*fl)/fNRN);


Omega=(-25:0.01:25); %Lowpass prototype frequency, real numbers as in Chapter 6.3.1
N=uint8(4); %Filter order (unsigned 8-bit integer)
Ntob=4;


OmegaZ=[Omegaz1, Omegaz2, inf, inf]; %TZs p.227
P=poly(OmegaZ);
Ps=P; %initialization of Ps as analytic continuation of P
LP=length(P);
for i=1:LP
  switch rem(i,4)
    case 2
      Ps(LP+1-i)=-1j*Ps(LP+1-i);
    case 3
      Ps(LP+1-i)=-Ps(LP+1-i);
    case 4
      Ps(LP+1-i)=1j*Ps(LP+1-i);
```

```matlab
    end
end


% General Chebyshev polynomial synthesis
x=zeros(N,length(Omega)); %(6.40) initialization
C4=zeros(1,length(Omega)); %(6.36a) initialization
for i=1:N
 x(i,:)=(Omega-1/OmegaZ(i))./(1-Omega/OmegaZ(i)); %(6.40) for each TZ
 C4=C4+acosh(x(i,:)); %(6.36a) argument summation
end;
C4=cosh(C4); %(6.36a)
RL=20; % max return loss in the passband
eps=1/sqrt(10^(RL/10)-1); % ripple factor - same as for conventional Chebyshev (Ch 3.6.2; 3.7.1; (6.34))
figure
plot(Omega,10*log10(1./(1+(eps*C4).^2))) %(6.35) graph
xlabel('\Omega')
ylabel('S-parameters (dB)')
hold on
plot(Omega,10*log10(1-1./(1+(eps*C4).^2)))
```

Software references

[CST]   CST Studio Suite (Microwave Studio), CST, http://www.cst.com/

[SON]   Sonnet, Sonnet Software, http://www.sonnetsoftware.com/

[MWO] NI AWR Design Environment (Microwave Office), National Instruments, http://www.awrcorp.com/

[ADS]   Advanced Design System (ADS), Agilent Technologies, http://www.home.agilent.com/en/pc-1297113/advanced-design-system-ads

[EPF]   EPFIL, D. Budimir. "EPFIL: waveguide E-plane filter design software and user's manual", Artech House

[MLB]   MATLAB, MathWorks, http://www.mathworks.com/

Publications

[P-1]   U. Jankovic and D. Budimir, "A Fully Planar Substrate Integrated Probe-Based Wideband Orthomode Transducer", *12th European Conference on Antennas and Propagation (EuCAP 2018)*, London, 9-13 April 2018.

[P-2]   U. Jankovic, N. Mohottige, D. Budimir and O. Glubokov, "Hybrid Manufactured Waveguide Resonators and Filters for mm-Wave Applications," *IEEE MTT-S International Microwave Workshop Series on Advanced Materials and Processes (IMWS-AMP 2017)*, 20-22 September 2017, Pavia, Italy

[P-3]   U. Jankovic, N. Mohottige, and D. Budimir, "Design of ultra compact pseudo-elliptic inline waveguide bandpass filters using inductive bypass coupling for various specifications," *Active and Passive RF Devices (2017)*, p. 8 (6 .)–8 (6 .), Jan. 2017.

[P-4]   U. Jankovic and D. Budimir, "Compact Inline E-plane Waveguide Resonators and Bandpass Filters with I-shaped Resonant Insets", *2016 Asia-Pacific Microwave Conference*, December 5-9, 2016, New Delhi, India

[P-5]   N. Mohottige, A. Glubokov, U. Jankovic and D. Budimir, "Ultra Compact Inline E-Plane Waveguide Bandpass Filters Using Cross Coupling", *IEEE Trans. Microw. Theory Tech,* vol. 64, no. 8, pp. 2561–2571, Aug. 2016.

[P-6]   U. Jankovic and D. Budimir, "Stepped Bend Substrate Integrated Waveguide to Rectangular Waveguide Transitions", *2016 IEEE International Symposium on Antennas and Propagation and USNC-URSI National Radio Science Meeting*, June 26 - July 1, 2016, Fajardo, Puerto Rico.

[P-7]   U. Jankovic, N. Mohottige and D. Budimir, " E-plane resonators for compact inline waveguide filters," *IET Active and Passive RF Devices seminar*, February 17, 2016, London, UK.

[P-8]   N. Mohottige, U. Jankovic and D. Budimir, "Ultra compact E-plane waveguide multiplexers," *2015 European Microwave Conference (EuMC)*, 2015, pp. 964–966.

[P-9]   B. Bukvic, U. Jankovic and D. Budimir, "A magnetically biased graphene based CPW switch for microwave applications," *2015 IEEE International Symposium on Antennas and Propagation USNC/URSI National Radio Science Meeting*, 2015, pp. 1656–1657.

[P-10]   N. Mohottige, U. Jankovic and D. Budimir, "Ultra Compact Pseudo-elliptic Inline Waveguide Bandpass Filters Using Bypass Coupling", *IEEE MTT International Microwave Symposium (IMS2014)*, June 1- 6, 2014, Tampa, Florida, USA.

[P-11]   U. Jankovic, "Design of Waveguide Antenna Filters for Wireless and Satellite Applications," MRes thesis, University of Westminster, London, 2014.

[P-12]   N. Mohottige, U. Jankovic and D. Budimir, "Compact E-Plane Varactor – Tuned Bandpass Filters", *2013 IEEE International Symposium on Antennas and Propagation and USNC-URSI National Radio Science Meeting*, July 7-12, 2013, Lake Buena Vista, Florida, USA.

[P-13]   U. Jankovic, N. Mohottige, V. Petrovic and D. Budimir, "Electromagnetic Modelling of Dielectric-filled Waveguide Antenna Filter Arrays", *2013 IEEE International Symposium on Antennas and Propagation and USNC-URSI National Radio Science Meeting*, July 7-12, 2013, Lake Buena Vista, Florida, USA.

[P-14]   U. Jankovic, N. Mohottige, Z. Golubicic, V. Petrovic and D. Budimir, "Electromagnetic Modelling of Dielectric-filled Waveguide Antenna Filters", *IEEE 20th Telecommunication Forum (TELFOR 2012)*, November 20-22, 2012, Belgrade, Serbia.

Poster competitions

[Po-1]   U. Jankovic, N. Mohottige and D. Budimir, "Novel Hybrid Manufactured Waveguide Filters with 3D Printed Insert Dielectric", *5th IET Technical Enterprise Workshop: RF in Aerospace Applications*, London Metropolitan University, London, 5 April 2017. (Best Poster Prize Awarded to Uros Jankovic)

[Po-2]   U. Jankovic, N. Mohottige and D. Budimir, " Modelling of Dielectric-filled Waveguide Filtennas*", IET Technical Enterprise Workshop*, February 27, 2013, Queen Mary College, London, UK. (Uros has won the IET Best Student Poster Award for this poster)